UNIVERSITA' DEGLI STUDI DI PARMA

Dottorato di ricerca in
Scienza e Tecnologia dei Materiali

Ciclo XXIX

# Progress in photovoltaic cells based on Low-Temperature Pulsed-Electron-Deposited $Cu(In,Ga)Se_2$ films

Coordinator:
Chiar.mo Prof. Enrico Dalcanale

Supervisor:
Dott. Edmondo Gilioli

Candidate: Filippo Annoni

2017

*Alla mia famiglia*

The dissertation concerning this PhD thesis will be publicly exposed at Università degli Studi di Parma on Friday the 17th of March, 2017.

# Abstract


The aim of this thesis is to improve the efficiency of thin film solar cells based on $Cu(In,Ga)Se_2$ (CIGS) grown by Pulsed Electron Deposition (PED) at very-low temperature (250 °C) in a single-stage process. This goal was carried out by optimizing the sodium content inside the CIGS absorber and both the structure and the morphology of the window layers. Zn(O,S) as buffer layer and transparent conductive oxides (TCOs) as back contact were tested for advanced Cd-free devices and bifacial solar cells, respectively.

For what concerns the optimization of the CIGS absorber layer grown by the low-temperature PED process (LTPED), a controlled sodium doping was achieved thanks to the deposition of very thin NaF precursor layer (4:8 nm) and a longer annealing process (up to 80 minutes). The final devices were then fabricated by depositing both a resistive layer of undoped-zinc oxide and a front contact of Al-doped zinc oxide (AZO) by radio-frequency (RF) magnetron sputtering. With respect to previous cells where no shunt-preventing layer was applied and AZO was fabricated by PED, the new window layer improved the uniformity of the cell performances over a larger area (1 square inch). Solar cells with optimized sodium content and window layer have reached an efficiency of 17%.

Bifacial CIGS solar cells were fabricated onto TCO materials. Al-doped zinc oxide, indium-tin oxide (ITO) and commercial fluorine-doped tin oxide (FTO) were used as TCO substrates. Devices with FTO as back contact exhibited solar cell parameters comparable to the Mo references for front illumination. When simultaneously illuminated from top and rear surface (bifacial) these cells exhibited an overall efficiency of 17%, thanks to the same FF and $V_{oc}$ as the front illumination, while bifacial $J_{sc}$ was the arithmetical sum of front and rear ones. A non-intentional and non-optimized Ga grading in the CIGS layer lowered the FF of devices grown onto ITO, while devices deposited on AZO had extremely poor efficiency. On ITO and FTO, a thinner CIGS absorber improved the rear $J_{sc}$ and thus the bifacial one, but $V_{oc}$ and FF were limited by shunting apparently related to the droplets produced during the LTPED process.

In the final part of this work, Zn(O,S) deposited by Atomic Layer Deposition (ALD) was studied and optimized to be used as an buffer layer for LTPED-grown CIGS to realize Cd-free devices entirely fabricated by means of vacuum-based methods. Initially, Zn(O,S) was tested on co-evaporated CIGS, investigating both composition and thickness. The ALD recipe corresponding to Zn(O,S) buffer with S/[S+O]=0.38 and a thickness of 40nm was found to maximize both FF and $V_{oc}$, leading to a higher

efficiency than the CdS reference due to greatly larger $J_{sc}$. The same study was then repeated on LTPED-grown CIGS with GGI=37.5% and GGI=30%. With GGI=37.5%, Zn(O,S) exhibited a loss in FF of about 10 points with respect to the CdS reference, which is attributed to a Zn(O,S) nucleation much richer in S. Such a nucleation increases the conduction-band offset causing current blocking. Indeed, CIGS with GGI=30% exhibited higher $V_{oc}$ and same FF as CdS reference, hence slightly larger efficiency, for 40nm-thick Zn(O,S) buffer with S/[S+O]=0.38. For LTPED-grown CIGS buffered with Zn(O,S), $J_{sc}$ was limited by the large reflectance of the samples as highlighted by external quantum efficiency measurements. Calculated internal quantum efficiency, which simulates the device behaviour with an antireflection coating, showed a $J_{sc}$ increase of roughly 10%.

The results reported in the thesis show the potentiality of the LTPED process in the absorber growth for CIGS-based solar cells. 17% efficient cells were obtained by optimizing a single-stage deposition process at low temperature, without applying any intentional Ga grading, K-treatment nor anti-reflection coating.

**KEYWORDS**: CIGS; Solar cells; Thin film; Pulsed Electron Deposition; Low temperature; Bifacial devices; TCO; Alternative buffer layer; Zn(O,S).

# INDEX

# 1. Introduction

$Cu(In_{1-x},Ga_x)Se_2$ (CIGS) is a p-type semiconductor used as light absorbing material in thin-film solar cells (TFSCs). Because of its large theoretical conversion efficiency (close to 30%), CIGS is the most promising material for thin-film solar cells and therefore PV applications for which silicon-based devices are not suitable. These applications consist of flexible and/or portable devices, building integrated photovoltaics (BIPV), and solar cells for space applications.

Although the typical CIGS deposition techniques ("3-stages thermal co-evaporation" and sputtering) have reached efficiency exceeding 22% on lab-scale devices and 17% for PV module, to obtain such important results it is mandatory to operate at high temperature (>500 °C) and, in some cases, a "selenisation" or "sulphurisation" step (usually involving toxic $H_2Se$ or $H_2S$). These processes and the high temperature extend the industrial manufacturing time and cost and preclude the use of cheaper and flexible substrates (e.g. plastics). Nowadays several companies (Solar Frontier, AVANCIS, Solibro, Manz, and others) are producing high volumes of CIGS-based modules on glass substrates, but the manufacturing of flexible CIGS TFSCs is less mature despite promising efficiencies have been achieved on laboratory-scale devices. Obviously, a low-cost technique able to produce large-area CIGS thin films for high-efficiency solar cells, using neither high temperature (saving energy and allowing flexible substrates) nor hazardous gases (saving the cost of the safe-control systems and time for the production) would be a more proficient and thus desirable process for industrial mass production.

Recently, at IMEM-CNR in Parma, a novel technique called Low-Temperature Pulsed Electron Deposition (LTPED) has been applied for the fabrication of CIGS-based thin-film solar cells. PED takes advantage of pulsed electron beam with a huge power density to "ablate" the target material, i.e. to transformation of the solid-state matter into a cloud of plasma containing several atoms and ions species, and even clusters and particles. The transformation is far from the thermodynamic equilibrium, hence a congruent evaporation can be achieved even for materials with an incongruent melting point. It means the stoichiometric composition of the target is transferred into the plasma and then in the film, formed by the plasma condensation onto the substrate. The desired composition and phase of CIGS can be achieved with a simpler method and at much lower temperature than the classic techniques, without any post-deposition process like selenization. In fact, by means of LTPED, CIGS absorber can be grown in

the tetragonal phase at 250 °C, in a single-stage process and from a quaternary target. High efficiency ($\eta$=15.2%) has been demonstrated for non-optimized devices.

Another issue affecting the CIGS-based solar cell technology is the cadmium content due to the cadmium sulphide (CdS) buffer layer. CdS is far from being an ideal buffer layer in CIGS solar cells because it is suspected to be cancerogenic and has a low band gap, that leads to absorption in the blue region and consequently to current loss as a result of the poor charge collection efficiency in the n-region of these type of the solar cell. Only recently, alternative buffer layers capable to replicate the CdS properties have been produced resulting in highly-efficient and Cd-free solar cells (1).

The main purpose of this thesis is to develop several aspects of solar cells based on LTPED-grown CIGS: first an enhancement of the efficiency and the homogeneity of the LTPED-grown samples, then the fabrication of bifacial devices and, finally, the introduction of $Zn(O_{1-x},S_x)$ as an alternative buffer layer to test the efficiency of LTPED-based Cd-free solar cells.

In the first part of the experimental activity (chapter 5. ), how to enhance the CIGS quality and to improve solar-cells design were investigated aiming to boost the solar cell efficiency and to enlarge the area with uniform performance. A fine-tuning of the sodium content into CIGS was performed by optimizing both the thickness of the sodium-precursor layer (NaF), deposited before CIGS, and the duration of the annealing process, carried out after the CIGS deposition and at the same temperature. The introduction of a resistive layer made of undoped ZnO aimed to the reduction of the shunt behaviour of the solar cells, while aluminium-doped zinc oxide (AZO) deposited by radio-frequency (RF) magnetron sputtering was used as transparent conductive oxide (TCO) of the window layer, on the lookout for a better uniformity than the PED-deposited AZO.

In order to optimize the composition of CIGS grown by LTPED, two PED sources were used to simultaneously ablate a CIS and a CGS target, and thereby to deposit a CIGS film with a spatial distribution of Ga content (GGI). After the characterizations of the sample, solar cells were completed to determine how the GGI influences the open-circuit voltage and the short-circuit current density of the devices.

The second experimental section (chapter 6. ) is dedicated to a particular application of PV devices: bifacial solar cells, i.e. solar cells capable to produce power whether illuminated through the front and/or the rear contact. Their purpose is to use the albedo (light reflected from the environment) to increase the power generation without enlarge the area of the device. Bifacial solar cells are based on the concept that both the front and rear contact are transparent to the visible and IR radiation, i.e. in the spectrum region where the absorber works. Moreover, with the same system, PV windows can be realized simply thinning the CIGS absorber until the whole device is semi-transparent in the visible region. The only way to fabricate such systems is to use a back contact made of heavily-doped n-type TCOs. Because of the high temperature (usually T>500 °C) of the classic CIGS deposition techniques, the TCO material

constituting the back contact can be deteriorated. However, good efficiencies have been demonstrated by co-evaporation onto indium-tin oxide (ITO). Here, the PED process is exploited to grow CIGS onto several TCOs at 250 °C with the goal of fabricating high-performance bifacial devices onto In-free TCO, like fluorine-doped tin oxide (FTO). Thus, solar cells with CIGS grown by PED onto ITO, FTO or AZO back contact were measured under front, rear and bifacial illumination and compared to the reference solar cell with Mo as back contact.

Another important issue is the development of an alternative buffer layer to get rid of CdS and produce Cd-free solar cells with enhanced efficiency. $Zn(O_{1-x},S_x)$ was chosen to replace CdS because of its larger band gap and because of its tuneable conduction band through the sulphur content ($x$): exploring its composition, the band offset towards CIGS can be optimized. Zn(O,S) buffers were grown by means of Atomic Layer Deposition (chapter 7. ) during the internship at Ångstrom Laboratory of Uppsala University (Uppsala, Sweden). After a calibration of the ALD parameters, Zn(O,S) buffers were applied to co-evaporated CIGS and later on PED-grown CIGS with different GGI. The resulting solar cells were characterized to find out the best composition and thickness of Zn(O,S) buffer layer. In the best matching between CIGS-GGI and Zn(O,S) composition, Zn(O,S) demonstrated to be an efficient alternative to CdS.

# 2. Solar Cells

## 2.1. Photovoltaic as energy source

Currently, the average global demand of power is about 17.7 TW of power and the world electricity consumption is expected to increase by 56% between 2010 and 2040 (2). The electric energy is obtained from several sources: “fossil fuels” (like oil, coal and natural gas), “alternative” energies (such as solar, wind, hydropower, geothermal and others), bio-fuel and waste or nuclear plants. Fossil fuels are the most popular energy source but their drawbacks in terms of environment sustainability and in the social and economic spheres cannot be afforded anymore. The usage of fossil fuels has brought to severe pollution and climate changes, highlighted by the temperature increase, that impact on human health and society and planet life in general (3), as recognized by the Paris Agreement in 2015 (CP.21) (4). Moreover, their supplies are limited and controlled by few countries. Considering even the expected decrease of nuclear power generation, following the Fukushima accident, nowadays there is a more serious effort to find energy sources and related technologies which will not damage our environment and at the same time be cheaper and available everywhere in the world, to be able to keep our energy supplies balanced with the growing demand.

Among the alternative energies, photovoltaics (PV) is the most promising sustainable energy source. During 2015, PV total installed capacity had an impressive growth with about 50.7 GW of additional installed capacity worldwide (26.5% above 2014). The globally installed total PV capacity is estimated to be roughly 228 GW at the end of 2015 and therefore it is still a very small part of the global energy consumption. There is evidence of an accelerating cost reduction during 2016, in parallel with a trend towards higher overcapacities in the industry (5). Concerning PV generation costs, and more precisely recently contracted power purchase agreements, new record values below 0.03 USD/kWh have been reached (5), confirming what is achievable today under favourable market opportunities and insolation conditions. The other side of the coin is the observation that the PV manufacturing in concentrated in few countries (one sixth installed in Cina, Japan and USA alone in 2014) and large parts of the global

PV market (78%) are still driven by financial incentives, accompanied by an increasing share of self-consumption or net-metering (15%) and about 6% of the market coming from competitive tenders (5).

To help the photovoltaic market expansion, research is developing several technologies aiming to different application: solar cells for concentration in solar plants for massive energy production, cost-effective modules for stand-alone or grid-connected PV system, thin-films-based devices for building integrated and portable PV, and so on.

PV modules made of crystalline Silicon have dominated and will probably continue to dominate the market of large utility-scale power plants for the predictable future. However, Building Integrated Photovoltaics (BIPV), which was considered to be a small niche market, is now starting to emerge to such an extent that the European stakeholders of the PV sector have put BIPV at the top of their strategic vision. In fact, residential, commercial and public buildings use about 60% of the electric power distributed by the grid in Europe and 75% in the USA.

There is hardly any doubt that the most suitable technology for BIPV applications is thin-film PV. The low and still falling manufacturing costs, in combination with the wide range of possible solutions to incorporate thin-film solar cells in façades and other architectural elements, are the driving force of a major change in the photovoltaic sector. Several materials have been investigated for thin-film solar cells, like amorphous Si, CdTe and $Cu(In,Ga)Se_2$ (CIGS), and more recently perovskite-based materials and $Cu_2ZnSnSe_4$ (CZTS). The highest efficiencies have been obtained with CdTe and CIGS, and several companies are producing PV module with them. In the next page, the trend of the best lab-scale efficiency of several PV technologies is summarized by the National Renewable Energy Laboratory, for externally-certified results updated at November 2016 (6).

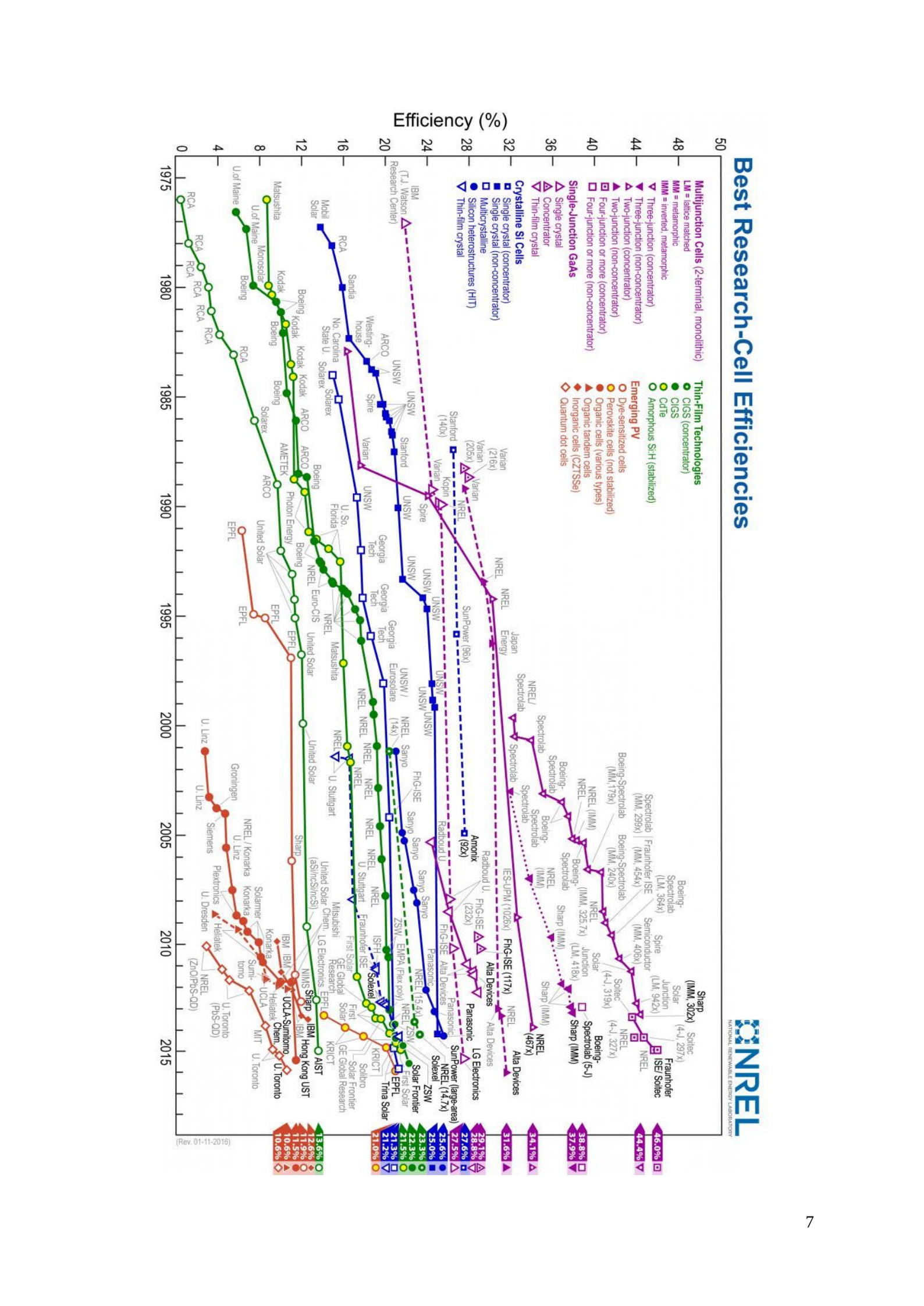
Best Research-Cell Efficiencies
NREL
NATIONAL RENEWABLE ENERGY LABORATORY
Efficiency (%)
Multijunction Cells (2-terminal, monolithic)
LM = lattice matched
MM = metamorphic
IMM = inverted, metamorphic
Three-junction (concentrator)
Three-junction (non-concentrator)
Two-junction (concentrator)
Two-junction (non-concentrator)
Four-junction or more (concentrator)
Four-junction or more (non-concentrator)
Single-Junction GaAs
Single crystal
Concentrator
Thin-film crystal
Crystalline Si Cells
Single crystal (concentrator)
Single crystal (non-concentrator)
Multicrystalline
Silicon heterostructures (HIT)
Thin-film crystal
Thin-Film Technologies
CIGS (concentrator)
CIGS
CdTe
Amorphous Si:H (stabilized)
Emerging PV
Dye-sensitized cells
Perovskite cells (not stabilized)
Organic cells (various types)
Organic tandem cells
Inorganic cells (CZTSSe)
Quantum dot cells
Sharp (IMM, 302x)
Soitec (4-J, 297x)
Fraunhofer ISE/ Soitec
46.0%
44.4%
Boeing-Spectrolab (5-J)
38.8%
37.9%
NREL (467x)
34.1%
Alta Devices
31.6%
29.1%
28.8%
LG Electronics
27.6%
SunPower (large-area)
27.5%
NREL (14.7x)
25.6%
25.0%
Solexel
ZSW
23.3%
22.3%
Solar Frontier
21.5%
First Solar
21.3%
EPFL
21.2%
Trina Solar
21.0%
AIST
13.6%
Hong Kong UST
12.6%
IBM
11.9%
UCLA-Sumitomo Chem.
11.5%
U. Toronto
10.6%
10.6%
(Rev. 01-11-2016)

## 2.2. Basic concepts

A solar cell is a device able to convert sunlight intensity into electric power. Solar cells technology is based on semiconductor materials faced together forming the so called “p-n junction” and on the photovoltaic effect, which is responsible for light absorption and free-carriers generation. The materials properties, and the interfaces between them, define the parameters which describe the behaviour of the solar cells and determine its efficiency, defined as the power generated per unit of area divided by the irradiating power density.

### 2.2.1. Semiconductors

Semiconductors are defined as materials with intermediate conductance between metals and insulators. This characteristic is due to the energy states the electrons can occupy inside the material structure. In a single atom, the electrons can occupy only precise energy states, therefore called “quantum” states, and, as stated by Pauli Principle, two electrons cannot occupy the same quantum level, thus cannot have the same energy. But when more atoms are bonded together forming an ordered structure, called crystal, the quantum level of the single atoms overlap forming energy bands. A band is a sort of continuum of electron-energy levels and the bands are separated each other by a gap: these gaps represent prohibited energy values for the electrons. Then, a density-of-states function define the number of electrons that can occupy the same level inside the band, thus having the same energy. Of course, the density of states inside the gap is zero. The density-of-states and the width of bands and gaps depend from the chemical elements composing the material and the order in which the atoms are packed in, i.e. the crystalline structure or lattice. Moreover, the electrons are characterized by a momentum-like vector (called k-vector) which depends from their position in the reciprocal lattice.

At 0 K, when no thermal energy is available, and without any external excitation, the electrons occupy the lowest energy states which are free, thus filling the lowest energy band first. In this condition, the highest energy level occupied is called Fermi level ($E_F$) at 0 K. The highest energy band with occupied states is defined Valence Band (VB) and in semiconductors its maximum ($E_V$) corresponds to $E_F$ at 0 K. The first band above the valence one is totally unoccupied at 0 K and is called Conduction Band (CB). Its lowest energy level is the conduction band minimum ($E_B$). The gap of forbidden energy between VB and CB is called band gap and its width, the Energy Gap ($E_G$), is defined by the difference $E_C - E_V$. This gap extension between the highest occupied level and the lowest unoccupied one define the conductance behaviour of the material. At room temperature (RT), if the electrons are provided by a thermal energy of $E_G$ or larger, some of them can jump from the VB to the CB where they are free to move thanks to the huge number of free states extended through the crystal, slightly separated in energy. In metals there is no band gap, hence whatever the temperature the electrons are free to move and current can flow. In insulators, indeed, the energy gap is huge and at RT no electrons are present in the CB, so the material

shows a great resistivity. Semiconductors are those materials with an energy gap comparable to thermal energy of electrons at RT, thus few free charge carriers allow the current flow, even if with greater resistivity than metals. In those semiconductors where $E_V$ and $E_C$ corresponds to the same electron k-vector in the reciprocal lattice, the band gap is called direct band gap. If the electron momentum is different, the gap is called indirect band gap: $E_V$ and $E_C$ are not faced together (different k-vector) in the reciprocal lattice and the transition, other than the energy, needs even for a momentum transfer. The required momentum is usually provided to the electron by turning on or off a quantum lattice-vibration wave (phonon).

Thermal energy is not the only way to excite electrons. Illuminating the semiconductor with a photon having energy $h\upsilon$ larger than the $E_G$ can cause two phenomena:

- Photoelectric effect: if the photon energy is even higher than the electron binding-energy to the material lattice, called work function ($W$), the electron absorbing the photon is ejected from the material surface. The energy exceeding the working function constitutes the kinetic energy of the free electron.
- Photovoltaic effect: if $E_G<h\upsilon<W$, the photon is absorber by an electron which is consequently transferred into the CB.

Photons with energy lower than the $E_G$ are not absorbed and can pass through the material giving rise to its transparency. The material absorbance is defined by the Lambert-Beer Law:

$$I_{(x,h\nu)} = I_{0(h\nu)} \cdot e^{-\alpha_{(h\nu)} \cdot x}$$

where $I$ is the light intensity at a depth $x$ into the material ($x \leq t$ thickness), $I_0$ the incident light intensity and $\alpha_{(h\upsilon)}$ is the absorption coefficient, which depends from the photon energy. For a direct band-gap semiconductor (CIGS, CZTS, CdTe, GaAs, etc.) in the approximation of parabolic bands and for band-to-band transition only, the absorption coefficient is ruled by the following equation:

$$\alpha_{(h\nu)} \propto (h\nu - E_G)^{1/2}$$

While for indirect bandgap semiconductors (as Si and Ge), in the same approximations as before:

$$\alpha_{(h\nu)} \propto \frac{(h\nu - E_G \pm E_P)^{1/2}}{\pm(e^{\pm\frac{E_p}{k_B T}} - 1)}$$

where $E_P$ is energy of the phonon assisting the transition, $k_B$ is the Boltzmann's constant and $T$ is the temperature. The ± symbol determine if the phonon must be created (−) or extinguished (+) and the denominator define the probability of this phenomenon.

Those electrons in VB which absorbed a photon with $h\upsilon>E_G$ are excited in CB at levels higher than $E_C$, and then lose part of their energy relaxing to empty states at lower energy. Even during this relaxing process the energy and momentum must be conserved, thus depending from the kind of band gap,

phonons may be created (indirect) or photons emitted (direct). Another mechanism is the energy transfer to other electrons.

As a consequence of an electron which moves into the CB, an electron vacancy is left in the VB: it can be represented by the presence of a positively-charged particle called “hole”. This fictitious particle is used to describe the electrons behaviour inside the VB when energy levels are freed therein by moved electrons. Since now there is a certain density of free states inside the VB, the electrons are free to move even there, but of course their mobility is different since the density of free states is different in the VB than in the CB. Therefore, the concept of holes can be introduced: their energy scale is the reverse of electrons and they have different mass with respect to electrons to describe their different mobility. Recombination between one free electron and one free hole may even occur: an excited electron relaxes down into the VB, filling a hole. It is a free-carrier recombination with band-to-band mechanism and usually generates a photon with energy equal to the energy lost by the carrier, $E_G$.

Summarizing, every time an electron has enough energy to transfer from the VB to the CB, a hole is created into the VB. A phonon is involved in the transfer process if the semiconductor has an indirect band gap. The two charge carriers are free to move within the material and thus the current can flow if a potential difference is applied. This the simplified description for an infinite crystal of “intrinsic” semiconductors, i.e. without defects and lattice variation, in which the free-hole density ($p_i$) is always equals to the free-electrons density ($n_i$).

Real materials are made by crystal grains merged together: each grain is oriented along a particular lattice direction and the jointing line between grains is a highly-disordered zone, full of defects. Moreover, since the materials are grown at a temperature higher than 0 K, entropy introduces defects even inside the crystal grains: atoms vacancies, interstitial atoms and substitutional atoms. In thin-film technology, other point defects are included in the crystals by impurities, which are almost impossible to be completely avoided, and line or volume defects may be created by a different lattice parameters between the material and the substrate. Each defect generates an energy level localized into the band gap of the semiconductors. Some defects can easily generate a free electron since their energy level is close to $E_C$, others are located just above $E_V$ and are likely to capture an electron from the VB and generate a free hole, others have an energy level situated in the middle of the band gap. These defects, especially the latter, change the normal behaviour of charge carriers since they allow carrier transitions at energy lower than the energy gap. Hence, another recombination mechanisms than the band-to-band process is possible: it is called Shockley-Read-Hall (SRH) recombination. In SRH mechanism electrons and holes are relaxed through mid-gap levels which are called deep-level traps. It is the dominant recombination mechanism in defected semiconductor materials, like CIGS thin-films for solar cells.

Intentionally-introduced impurities with a controlled density can be used to change the material property. Semiconductor doping is achieved introducing atoms of a new element in the lattice of the

material. This element can behave in two different ways. Introducing an atom that in the lattice is likely to lose an electron, hence called "donor", creates a level just below the $E_C$: the thermal energy at RT is enough to bring the electron in the free state. At the same time, a positively-charged ion is created and its position is fixed in the material lattice. The donor density ($N_D$) determine the density of electrons transferred in CB by this mechanism ($n$). Similarly, "acceptors" are atoms which creates an energy level just above the $E_V$ and, even at RT, can easily capture an electron from the VB thus generating a free-hole density ($p$) and negative ions in the lattice, in function of their density ($N_A$). Semiconductors doped with donor atoms are called "$n$-type" and are characterised by free-electron density larger than free-hole density ($n+n_i$)>$p_i$, thereby conductivity is mainly due to the electrons. On the contrary, semiconductors doped with acceptors are called "$p$-type" and have free-hole density larger than the electron one: ($p+p_i$)>$n_i$. Doped semiconductors are limited in carriers mobility due to modifications introduced by positively charged ions in the lattice: their electric field creates a distortion in the potential of the lattice which alters electrons and holes dynamics. Therefore, depending from the kind of doping and its density, conductivity of doped semiconductors is controlled by the trade-off between the increased carriers density and the reduced carriers mobility. Moreover, in doped semiconductors, the light absorption from free carriers becomes an important phenomenon: being in a quasi-continuum of energy levels, free carriers can absorb photons with almost whatever energy and be excited at higher energy level. Thus, the light transmission of the material is reduced since absorbance is increased especially for photons with energy lower than the semiconductors band gap. These photons are not absorbed in absence of free carrier.

If no doping is applied, the semiconductor is called intrinsic or undoped and $n_i$=$p_i$: $E_F$ is exactly in the middle of the band gap. With respect to a doped semiconductor, an intrinsic one has generally a lower conductivity due to the lower free-carrier density but higher transparency at photons with energy below $E_G$. However, materials may be unintentionally doped by stoichiometry variation: the semiconductor crystals grow with an excess or lack of one element thus creating "intrinsic" defects which are responsible for an enhanced free- electron or hole density.

In the case of extremely doped semiconductors, for high donors or acceptors concentration, the Fermi level can be pushed into the CB or the VB respectively. In this cases, the semiconductors are addressed as $n^+$-type or $p^+$-type and behave almost like a metal thanks to the huge free-carrier density.

### 2.2.2. The p-n junction

After the absorption of a photon with appropriate energy, an electron is excited into the CB and a hole is created in the VB. The two charged particles are likely to recombine soon with the band-to-band mechanism since they are attracted each other by their own electric field. This means they cannot be collected and used to produce an output power. To separate them, an electric field must be introduced.

The simplest way to introduce an electric field into the device is to create a p-n junction: a p-type semiconductor is chemically jointed with a n-type semiconductor. When such a structure is fabricated, at the junction the excess of free holes due to the acceptors in the p-type material diffuses towards the n-type side, and likewise the excess of free electrons due to the donors in the n-type semiconductor crosses the junction towards the p-type side. As a result, holes and electrons recombine creating a region dried of the free carriers introduced by the doping. This region extends on both sides of the junction and has an uneven charge distribution: negatively charged ions into the p-type and positively charged ions into the n-type side. For this reason, it is called "space charge region" (SCR) or depletion region. Inside it, an electric field is built in by the separated fixed ions and it gets stronger as the recombination proceeds. At the same time, the electric field causes the drift of the carriers which hinders their diffusion. Soon an equilibrium is reached, consisting in a steady state with a defined width of the SCR where the drift current equals the diffusion current: electrons and holes currents across the junction are both zero. The integrated electric field in the SCR is the built-in potential of the p-n junction $V_{bi}$ and depends on the $E_G$ and on the doping density of the p-type and n-type sides:

$$q \cdot V_{bi} = E_G - kT \cdot \ln\left(\frac{N_{CB} \cdot N_{VB}}{N_A \cdot N_D}\right)$$

where $q$ is the electron charge, $N_{CB}$ and $N_{VB}$ the density of states in the conduction band and in the valence band respectively. An example of p-n junction is sketched in Figure 2.1.

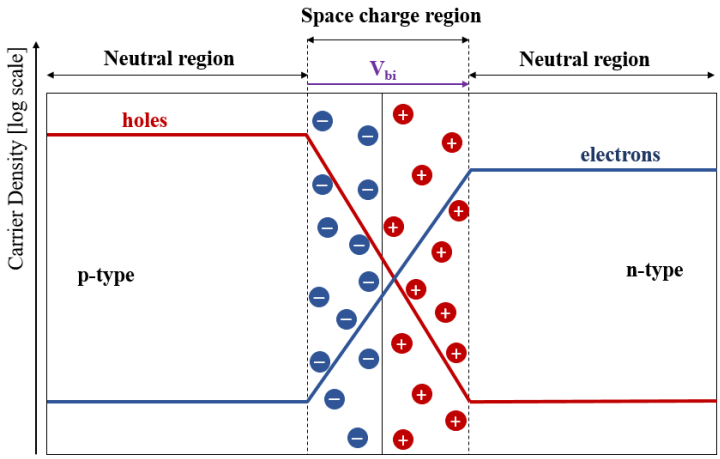


*Figure 2.1 - Steady state of a p-n junction. The red and blue curves represent the trends of holes and electrons density in it.*

The Fermi level must be constant through the p-type and the n-type semiconductors. This cause the band bending in correspondence of the p-n junction, as shown in Figure 2.2.

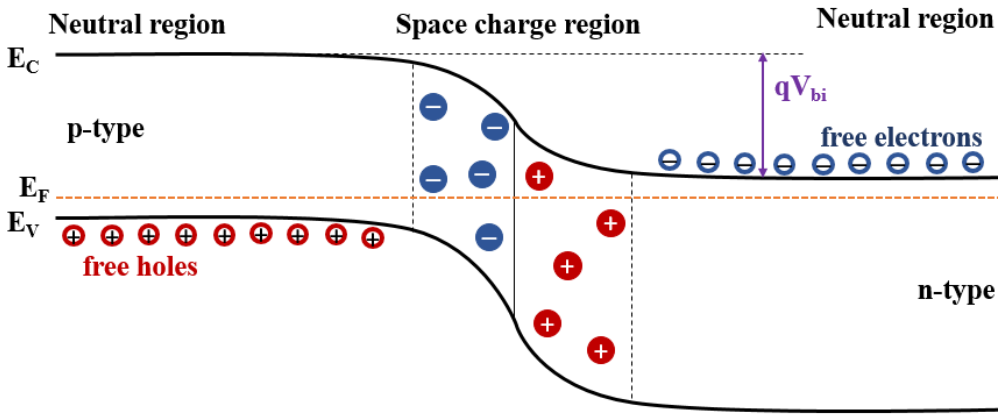


*Figure 2.2 - Schematic representation and banding in a p-n junction.*

P-n junctions are the basis of diode devices which can create a photogenerated current driving it in a preferential direction. Solar cells are diodes properly realized to produce power absorbing light in the most efficient way. The p-n junctions, and solar cells as well, are divided in:

- Homo-junction: the p-type and the n-type are the same semiconductor material, doped in two different ways. However, they have the same lattice and $E_G$.
- Hetero-junction: two different materials make up the p-n junction. They have different $E_G$ and the interface between them becomes a crucial feature for the diode behaviour, and hence solar cells efficiency, since it is filled of defects due to the different lattice parameters.

### 2.2.3. Working principles of solar cells

The solar cells take advance of semiconductors capability to absorb the light producing free electrons and free holes and of the p-n junction structure which can separate the two kind of carriers by means of its electric field. By means of opportunely fabricated contacts, the carriers are then extracted and power is generated. The IV characteristic of a solar cell in dark condition is the same as a diode. When illuminated, it is shifted ad its characteristics depends from its feature and from the incident light.

The emission spectra of the sun can be approximated to the black-body radiation at 5762 K, but then part of the light is absorbed by the Hearth atmosphere before reaching the solar cell. Air Mass (AM) is an index determining how atmosphere absorption influences the light spectrum and the intensity of the light reaching the Hearth surface:

$$AM = 1/\cos(\theta)$$

where $\theta$ is the incident angle. AM value is always ≥1. The standard spectrum to test solar cell is AM1.5, corresponding to $\theta$=48.6°, normalized for the power density of 1 kW/m$^2$. This spectrum is calculated on the sea level and considers the light absorption of some chemical compound (mainly $H_2O$ and $CO_2$). Usually, tests refer to AM1.5d (direct) which consider the direct light only, or to AM1.5g (global) which

consider even the diffuse light from the roundabouts and the environment. Solar spectrum along with AM0 and AM1.5g are shown in Figure 2.3.

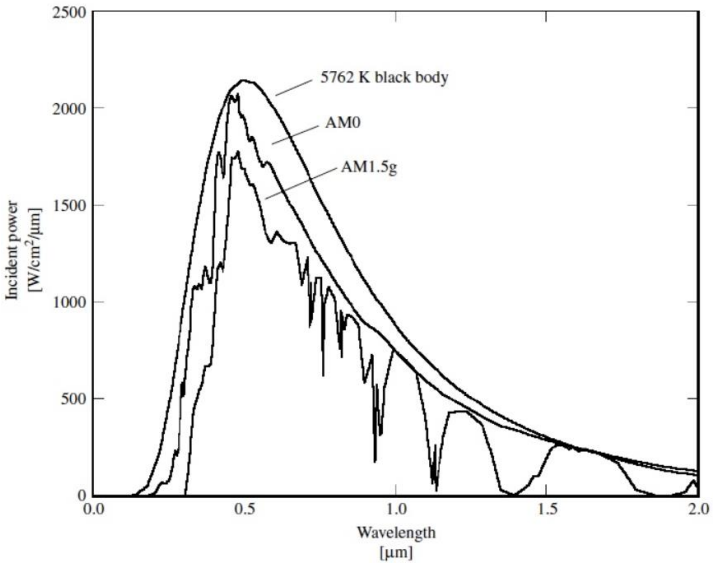


*Figure 2.3 - Calculated emission spectrum of a black body at 5762K and AM0 and AM1.5g spectra.*

When a semiconductors p-n junction is illuminated with these kind of spectrum, it produces a current which depends from the applied potential as:

$$I = I'_{SC} - I_{01} \cdot \left(e^{\frac{q(V+I\cdot R_S)}{kT}} - 1\right) - I_{02} \cdot \left(e^{\frac{q(V+I\cdot R_S)}{2kT}} - 1\right) - \frac{V + I \cdot R_S}{R_{sh}}$$

where $I_{01}$ and $I_{02}$ are the saturation currents, due to the recombination, in the neutral region and in the SCR; $R_S$ is the series resistance of the device, due to the contacts and the resistivity of materials; $R_{Sh}$ is the shunt resistance of the device, i.e. the resistance which is in opposition to internal currents short-circuiting the junction.

With a current-voltage (IV) measurement in standard condition (illumination with AM1.5g at 25 °C), it is possible to determine the characteristics of a solar cell:

- The open-circuit potential $V_{oc}$ which is the maximum tension the solar cells can produce;
- The short-circuit current density $J_{sc}$, which is the maximum current ($I_{sc}$) the solar cell can give per unit of illuminated area;
- The fill factor FF, which take in account the resistive and shunt losses and is defined as the ratio between the maximum output power ($P_M$) the solar cell can generate and the product of $V_{oc}$ with $I_{sc}$:

$$\mathrm{FF} = \frac{P_M}{I_{sc}\cdot V_{oc}} = \frac{I_m\cdot V_m}{I_{sc}\cdot V_{oc}}$$

where $I_m$ and $V_m$ are the current and the voltage corresponding to the working condition with the maximum output power.

An example of IV curve is shown in Figure 2.4.

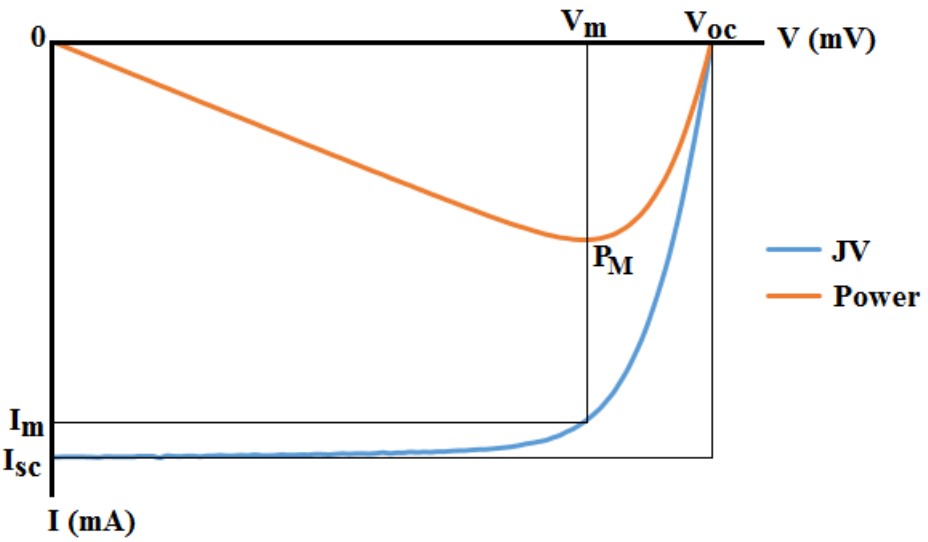


*Figure 2.4 - IV curve of a solar cell (blue curve) and its power trend as a function of voltage (orange curve). The ratio between the areas of the outer rectangle (defined by $V_{oc}$ and $I_{sc}$) and of the inner one ($V_m$ and $I_m$) defined the FF value.*

In general, the parameters of a solar cells are functions of three variables:

- Intensity and composition of the irradiating light: it does not affect the $V_{oc}$, but determine the $J_{sc}$ since the number of photogenerated carriers is correlated to the number of absorbed photons.
- The temperature, which affect the energy gap of the semiconductors composing the solar cells, thus slightly changing the $J_{sc}$ but heavily influencing the $V_{oc}$, which is inversely proportional to the working temperature.
- The device area with the same features, that determine the output current.

In the end, the solar cells efficiency $\eta$ is determined from the IV curve as:

$$\eta = \frac{P_M}{E \cdot A} = \frac{I_m \cdot V_m}{E \cdot A} = \frac{I_{sc} \cdot V_{oc} \cdot FF}{E \cdot A} = \frac{J_{sc} \cdot V_{oc} \cdot FF}{E}$$

in which $E$ is the irradiating power density ($W/m^2$) in standard condition and A the surface area of the solar cell ($m^2$). The efficiency represents the ratio between the generated electric power and the illuminating power. Several phenomena are limiting the efficiency of a solar cells, like:

- Transmitted light, i.e. the part of the spectra with energy lower than the energy gap of the absorbing material, which cannot be absorbed and thus cannot create electron-hole pairs in the junction;
- Light absorbed outside the p-n junction: the light absorbed by the front contact and in the neutral region of the semiconductors produces electrons and holes outside the electric field of the p-n junction, hence cannot be separate and recombine soon.

- Recombination: caused by defects state in the middle of the energy gap. SRH take place in the bulk of semiconductors, but even the interface plays an important role, especially highly-defected ones. For instance, the recombination at the physical junction of the p-n junction drastically lowers the $V_{oc}$ and thus plays a crucial role in hetero-junction based devices
- Dissipated energy by carriers thermalization.
- Parasitic resistance.

References related to semiconductor physics and devices are (7) (8) (9) (10).

# 3. CIGS-based Thin-Film Solar Cells

## 3.1. State-of-the-art of CIGS technology

$Cu(InGa)Se_2$ (CIGS)-based solar cells are considered as one of the most promising technologies for cost-effective and green power generation. This consideration is partly due to the advantages of thin-film technology, which can potentially allow low-cost deposition over large area to fabricate monolithically interconnected modules, using few amounts of materials.

Even more important, very high efficiencies have been achieved with CIGS for both lab-scale cell and PV module. Currently, the highest solar cell efficiency is 22.8% with 0.5 $cm^2$ total area fabricated by Solar Frontier (11), but several others laboratories has reached the 21% or hit the 22% (12). Furthermore, several companies have demonstrated sub-module efficiency above 16% and module efficiency exceeding 15% for $1m^2$ device (1). Key advantages of CIGS compared with other conventional PV technologies, include high energy-yield (kWh/KWp installed), low temperature coefficient of power loss, low sensitivity to shadowing (larger response at the IR radiation), and short payback time (13) (14). Cost-projections down to 0.35 €/Wp have been announced for the current technology, with potential for further reduction upon scale-up, allowing a significant saving of the total system cost (15).

Finally, CIGS technology has shown excellent long-term stability in outdoor (16) or damp-heat testing with encapsulation (17). Thanks to these features, CIGS-based PV modules have already hit the market. In addition to its potential advantages for conventional application, CIGS can be coupled with flexible substrates or deposited onto building blocks (cement or ceramic), which can be cheaper and/or more suitable than glass and allow innovative applications like portable devices or building-integrated PV (BIPV). Among these substrates, CIGS-based solar cells on plastics are very promising for power generation in space since they are very light-weight and with much higher radiation resistance than silicon. Other applications for CIGS would be transported-integrated PV and bifacial solar cells.

## 3.2. Material properties

$Cu(In,Ga)Se_2$ is a ternary material made by four elements, in whose structure indium and gallium occupy the same site. It is a solid-state solution of $Cu_2Se$, $In_2Se_3$ and $Ga_2Se_3$ where the Cu content define the phase and Ga/In ratio its electrical properties.

CIGS has a very complicated phase diagram characterized by an incongruent melting point. Several phases can be formed depending from its Cu content and the formation temperature, as sketched in the pseudo-binary equilibrium phase diagram of $In_2Se_3$-$Cu_2Se$ of Figure 3.1-a. The α phase is the chalcopyrite phase which results in p-type CIGS, the one the solar cells technology aims for. Its tetragonal unit cell is shown in Figure 3.1-b. The β phase, indeed, has a chalcopyrite lattice structure too, but is characterized by an ordered insertion of intrinsic defect which turn CIGS into n-type. This phase is called ordinary defect compound (ODC) and may have different compositions: $Cu_2In_4Se_7$, $CuIn_3Se_5$, $CuIn_5Se_8$. The phase δ has a sphalerite structure that is formed at high temperature and gives an n-type semiconductor. Other phases like $Cu_2Se$ are n-type as well. This makes the fabrication of good quality CIGS very important since the α-phase must be formed alone. Moreover, this phase exists only for slightly Cu-poor material (Cu content <25%): Cu/[Ga+In] ratio, called CGI, controls the phase formation in a narrow region corresponding to value just below 1. One of the essential feature of CIGS is that α-phase can be grown even with relatively large composition variation: its stability region is narrow (wider at higher temperatures) but the material can accommodate Cu vacancies still resulting in good quality absorber for solar cells without differences in its optoelectronic properties.

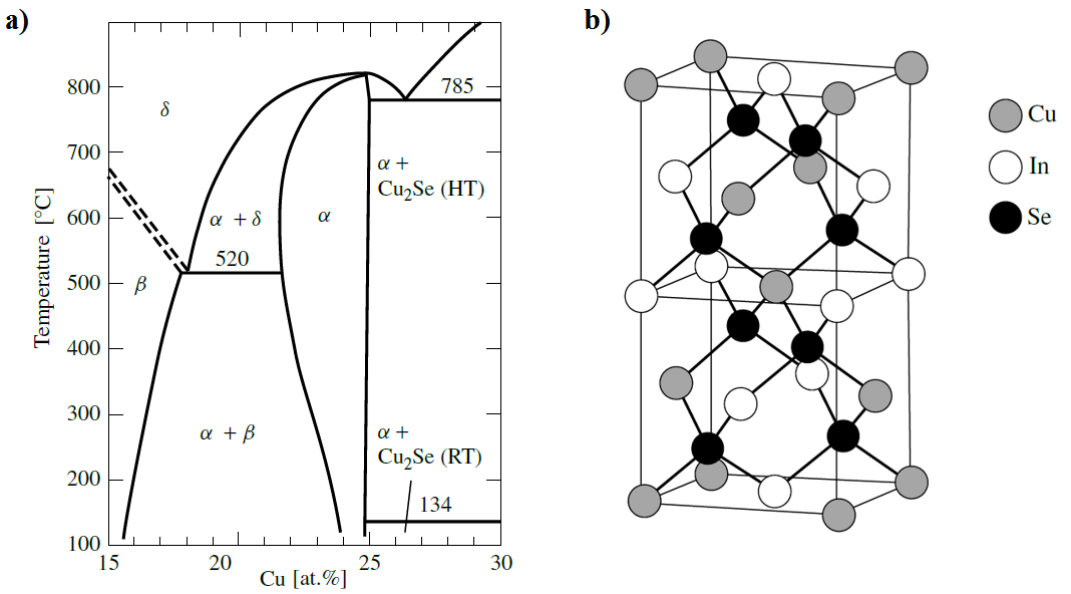


*Figure 3.1 - a) Pseudo-binary equilibrium phase diagram of $In_2Se_3$-$Cu_2Se$ for composition around the CIS chalcopyrite phase α (18). b) Unit cell of chalcopyrite structure. (19)*

CGI tolerance range is between 0.7 and nearly 1.0 to avoid the formation of phase β and to produce high efficient solar cells. Electrically inactive $2V_{Cu} + In_{Cu}$ defect complex is believed to be responsible for

the phase stability of Cu-poor and In-rich CIGS due to its very low formation energy, without affecting the solar cells behaviour. But decreasing too much the CGI, below 0.7, the $In_{Cu}^{2+}$ antisite defects would become predominant increasing the donor density which compensates the free holes of CIGS. The introduction of Ga into the CIS system leads to a larger chalcopyrite stability region due to the lower formation energy of $Ga_{Cu}^{2+}$ than $In_{Cu}^{2+}$. Moreover, the introduction of sodium into CIGS is very healthy for the absorber. Na is expected to occupy the Cu vacancies reducing the antisite defect density and so the compensation of CIGS, both at the grain boundaries and inside the grains.

Several defects are present in CIGS layers. For CIS, the most important ones are resumed in Table 3.1 along with their formation energy and their position inside the band gap (i.e. their activation energy). The defects distribution is even strictly correlated to the CIGS stoichiometry: since the absorber material is In-rich and Cu-poor, the defect density of $Cu_{In}$ would be lower than $In_{Cu}$ even if they have almost the same formation energy. The introduction of Ga in the CIS lattice gives rise to the same kind of defect as In but with different formation energy: for instance, $Ga_{Cu}$ has a larger formation energy than $In_{Cu}$ thus reducing the compensating contribute. This is the reason why Ga tends to stabilise the α-phase and increase the p-type nature of CIGS. Other defects are present in CIGS other than the ones listed in Table 3.1, but their formation energy is larger thus they influence in the solar cells performance plays a secondary role.

*Table 3.1 - The most important intrinsic defects affecting CIS and their characteristics.*

| Intrinsic Defect | Formation energy (eV) | Energy position | Type |
|---|---|---|---|
| $\mathbf{V_{Cu}}$ | 2.6 | $E_V$ + 0.03 eV | Shallow acceptor |
| $\mathbf{In_{Cu}}$ | 1.4 | $E_C$ − 0.25 eV | Compensating donor |
| $\mathbf{V_{Se}}$ | 2.4 | $E_C$ − 0.10 eV | Compensating donor |
| $\mathbf{Cu_{In}}$ | 1.5 | $E_V$ + 0.29 eV | Acceptor/Recombination centre |

The energy gap of CIGS is determined by the ratio between gallium and indium and is defined as GGI=Ga/[Ga+In]. Increasing the Ga content raises the conduction band while the valence bad is constant, thus increasing the band gap. This allows the band gap engineering since it is possible to tune the energy gap value playing with composition of the material. The energy gap depends from the Ga content with the following trend:

$$E_{G,CIGS}(x) = (1-x)\cdot E_{G,CIS} + y \cdot E_{G,CGS} - b \cdot x \cdot (1-x)$$

where $x$=GGI, $E_{G,CIS}$=1.01 eV, $E_{G,CIS}$=1.65 eV and $b$ is the bowing factor usually in the range of 0.15-0.24 eV.

The typical free hole concentration of polycrystalline α-CIGS films is in the order of $10^{15}cm^{-3}$-$10^{17}cm^{-3}$ and may be increased simply changing the intrinsic composition or with an extrinsic doping, for instance adding sodium which can enhance the doping level up to one order of magnitude.

The absorption coefficient $\alpha_{(h\nu)}$ of CIGS is among the highest for semiconductors. For photons having energy 0.2 eV larger than the CIGS energy gap $\alpha^{CIGS}=2\cdot10^5$ cm$^{-1}$. It is two orders of magnitude larger than the silicon one, $\alpha^{Si}=1\cdot10^3$ cm$^{-1}$, hence allowing the CIGS to absorb the whole light of the solar spectrum with a layer one hundred times thinner than Si. This explain why solar cells can have efficiency above 20% with CIGS absorber layer as thin as 1-2.5 μm, instead of 200-300 μm of silicon. Figure 3.2 provides an overview of the absorption coefficient trend as a function of the photon energy for several materials used as absorber of solar cells. CIGS shows the highest curve in the IR and visible region, thus enabling the larger current and efficiency among the thin film PV technologies. The photons with higher energy are absorbed in the first few tens of nanometres of CIGS, while the IR ones, with larger wavelength, penetrate deeper inside the CIGS layer.

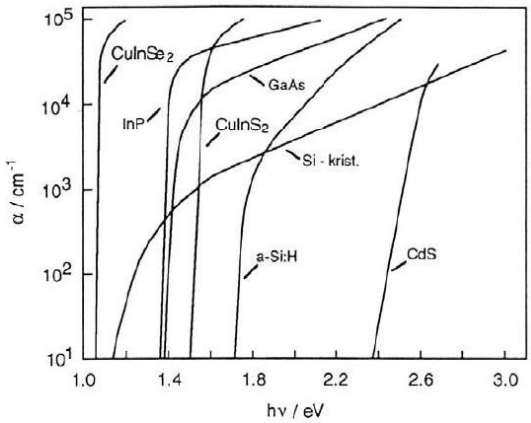


*Figure 3.2 - Absorption coefficient α as a function of photon energy, for several materials used as absorber in solar cells.*

## 3.3. CIGS devices

This section provides a brief overview of the layers and the materials composing the CIGS-based TFSCs. Figure 3.3 shows examples of the solar cell stack, while Figure 3.4 shows the bands line-up for a classic CIGS-based solar cells.

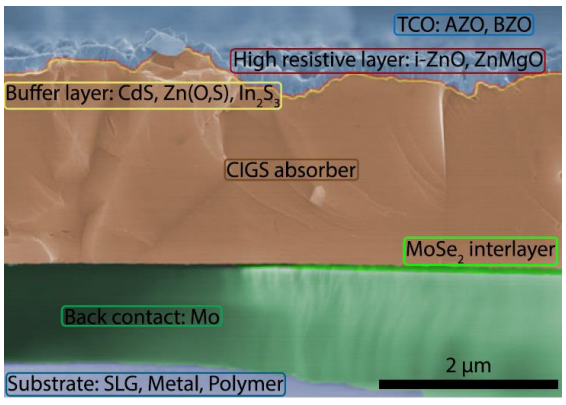


*Figure 3.3 - Basic structure of a typical solar cell based on CIGS absorber, with examples of commonly used materials. (1)*

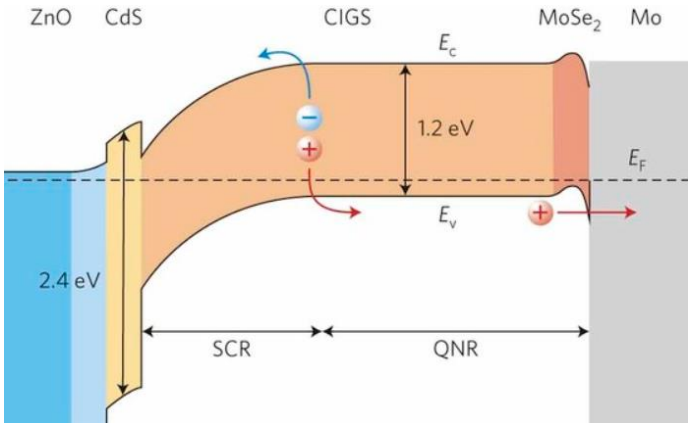


*Figure 3.4 - Bands line-up in a classic CIGS-based solar cells. (20)*

### 3.3.1. Substrate

The substrate is the physical support of the solar cell. The layers constituting the thin film solar cell are sequentially deposited on the substrate mainly by vacuum-based processes. Therefore, the first important features for its choice are the chemical, thermal and vacuum stability of the material: it must not melt, break down, deteriorate, degas or react with the other materials at the temperatures and in the environments it will be processed (several hundreds of °C, vacuum, water solution at high pH, etc.). The thermal expansion coefficient must be very close to the one of the other materials, to avoid the collapse of the device caused by layer exfoliation during the depositions at high temperature (see Table 3.2). Moreover, the substrate surface must be very flat and clean in order to allow a homogeneous and conformal growth of the device layers.

*Table 3.2 - Coefficient of thermal expansion (CTE) and density of several substrate and materials used in CIGS-based TFSCs.*

| Material | CTE ($10^{-6}K^{-1}$) | Density ($g/cm^3$) |
|---|---|---|
| Substrates | | |
| SLG | 9 | 2.5 |
| Steel | 11-16 | 7.8 |
| Ti | 8.6 | 4.5 |
| Al | 23.1 | 2.7 |
| Polyimide | 12-24 | 1.5 |
| Insulating layers | | |
| SiOx | 1-9 | 2.2-2.7 |
| $Al_2O_3$ | 6-8 | 3.9 |
| Solar cells layers | | |
| Mo | 4.8 | 10.2 |
| CIGS | 8-11 | 5.9 |
| CdS | 4.5 | 4.8 |
| ZnO | 4.75 / 2.9 | 5.6 |

Sodium-rich glass, soda-lime glass (SLG), is the most used substrate since it can resist to the high temperature of the process, do not degas or decompose neither in vacuum nor water solution, whatever its pH. Moreover, during the high temperature steps of the solar-cell fabrication, it naturally supplies the

absorber with sodium, essential for the CIGS doping. The main limits of glass substrate are the fragility and the non-flexibility (although very thin glass can be considerably bended). Additionally, its price greatly affects the solar cells overall cost. Cheaper substrates, like plastics, would reduce the TFSCs production cost.

Ceramic or cement substrate would be more suitable for the building integrated PV, while substrates like thin metal foils or plastic materials are very crucial for flexible applications and/or extremely-light solar cells. The main problem for the formers, usually porous or grainy materials, is the extreme roughness of the surface: treatment like glazing are necessary. Indeed, plastics are very flat but decompose above relatively low temperatures: only few poly-imides (Upilex, Kapton) can resist up to almost 300°C, whereas classic CIGS deposition techniques need temperature rarely below 500 °C to produce high-efficiency devices. Metal foils (Ti, Mo, Cu, Stainless-steel, etc.) may be a solution, besides more expensive and rough: lapping is needed. Anti-diffusion and insulating layer, called blocking layer (usually $Al_2O_3$ or nitrates), must be applied to avoid metal atoms to migrate into the absorber layer, creating detrimental defects in the CIGS lattice, and/or to electrically isolate the device from the substrate. On the other side of the coin, with respect to glass, the alternative substrates need a further step to provide the right amount of sodium to the CIGS absorber: it usually consists in applying a very-thin layer of sodium precursor material (like NaF) prior the CIGS or on its top.

### 3.3.2. Back contact

The back contact is in charge to collect the carriers produced by the pn junction of the device. Metal are preferred because of their large conductivity. Among them, molybdenum has been chosen because at high temperature and in presence of Se it gives rise to a $MoSe_2$ layer between CIGS, which makes the CIGS/Mo contact ohmic and with a reduced resistance. Moreover, Mo is known to efficiently reflect the light that CIGS has not absorbed back into the absorber layer. Mo is usually deposited by sputtering at a thickness of 300nm-1000nm, in a bi-layered configuration to maximize the adhesion to the substrate and the conductivity.

Recent studies introduced the concept of rear-contact passivation: a thin layer of dielectric like $Al_2O_3$ is deposited on the top of Mo, prior CIGS growth, in order to reduce the defect density that enhances the carrier recombination. The CIGS/Mo contact is guaranteed by patterned holes whose density and dimension must be optimize to maximize the efficiency gain.

Transparent conductive oxides (TCOs) could be used to produce semi-transparent or bifacial solar cells, i.e. devices that produce power even if not the whole light intensity is absorbed or being illuminated from both sides simultaneously. The outcome of solar cells with TCO back contact would be applications like smart windows and BIPV. The p-type TCOs are rare and do not provide the necessary electrical performance. Thus, the only TCOs used for these purposes are n-type semiconductors. To avoid the formation of a parasitic junction at the back contact, due to the p nature of CIGS and the n of

TCO, the latter must be very doped, i.e. with a huge free carrier density, to behave like a metal and ensure an ohmic contact towards CIGS. The conditions of the following-layer deposition are crucial since the high temperature can deteriorate the TCO or the interface, creating phases between CIGS and TCO (like $Ga_2O_3$) which would be detrimental for the device. Among the oxides developed, indium-tin oxide (ITO) and fluorine-doped tin oxide (FTO) have the highest carrier density and hence are the most suitable as back contact.

### 3.3.3. CIGS absorber

In the solar cells of this thesis, CIGS is the p-type material of the p-n junction. Since its doping level is usually between $1 \cdot 10^{15} cm^{-3}$ - $5 \cdot 10^{16} cm^{-3}$, orders of magnitude lower than the topmost materials, the junction is called p-$n^+$ junction and almost the whole SCR is located inside CIGS. This make CIGS the absorber layer, i.e. the layer supposed to absorb the light, create electron-hole pairs and separate the carriers.

There are several advantages in using CIGS as absorber material for TFSCs: above all, its highest theoretical efficiency (up to 30%), due to the highest absorption coefficient, and the tuneable band-gap from 1.01 eV to 1.68 eV through the control of its GGI.

Although GGI=65% provides the optimal band-gap value for the best conversion efficiency as theoretically predicted from the solar spectra (21), the actual Ga content in the current record efficiency devices is definitely lower, about 30%. This difference implies that, in addition to the band gap, there are other factors playing major roles in the conversion efficiency.

CIGS thin-films for absorber purpose usually have a thickness of 1-2.5 μm and are poly-crystalline films with grain dimension from few hundreds nm to 1 μm. The grain boundaries between these crystals are critical for the solar cells behaviour: they are made of extended defects which diminish the carrier diffusion length increasing the recombination probability and may be even turned to n-type introducing parasitic junction inside the absorber, if not properly passivated. Even interfaces between absorber and the other materials are key regions for the device functioning.

Recombination of the charge carriers is one of the main limits of solar cells based on CIGS. The recombination may take place in several regions of the absorber and hence is divide in three typologies (22) as sketched in Figure 3.5.

- Recombination in the in the quasi-neutral region (QNR): it depends from the diffusion length of the carriers into the CIGS and from its thickness. The recombination of carriers is due band-to-band mechanism or to deep-levels located in the bulk of the material, created by point defects in the lattice of the crystals or by grain boundaries and acting as traps and recombination centres (SRH mechanism).

- Recombination in the SCR: due to SRH recombination promoted by centres located in the SCR or to the tunnelling enhanced recombination. Tunnel effect is due to high carrier density at the p-n junction interface and it causes the bulk carriers to be captured by interface states or, vice versa, to interface carriers to be captured by bulk states in the SCR. These kinds of recombination affect the $V_{oc}$.
- Interface recombination: due to high defect density at the p-n junction interface. It strongly reduces the $V_{oc}$.

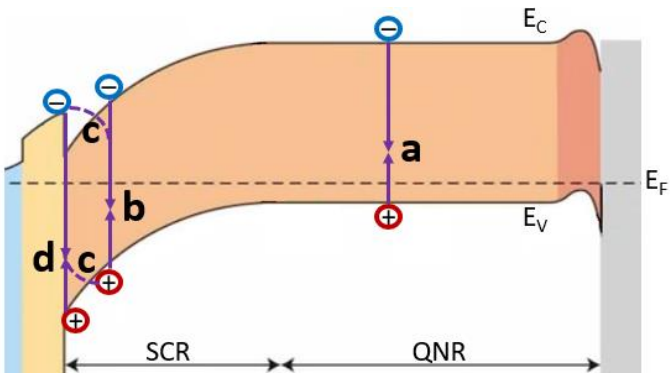


*Figure 3.5 - Recombination mechanisms in a CIGS solar cell: a) in the quasi-neutral region, b) in the space charge region, c) tunnelling enhanced in the SCR and d) at the interface.*

To lower the defect density and the compensation into the CIGS layer, it is necessary to reduce the defect density at the interfaces and inside the absorber: passivation is crucial for high efficient solar cells.

Sodium incorporation has been an important step towards high efficiency solar cells based on CIGS. Na slightly improve the p-type doping inside CIGS grains, acting as a donor replacing In and Ga, but its main role is played at the grain boundaries, where it has been found to diffuse. There, Na inhibits the formation of $In_{Cu}^{2+}$ defects thus reducing the compensating-defect density. This GB passivation results in incredibly-healthy effect on $V_{oc}$ and FF. Moreover, sodium has been observed to reduce the dimension of CIGS grains and to increase their orientation along the (112) direction, if available during the CIGS growth. Sodium is commonly incorporated by diffusion from the SLG substrate, promoted by high temperature of deposition process, or depositing a very-thin precursor layer (e.g. NaF) before or after the CIGS growth. (23) (24) (25)

To reduce the back-contact recombination, an extremely thin layer of dielectric material (e.g. $Al_2O_3$) can be grown between CIGS and the back contact. It is called passivation layer because it reduces interface recombination by chemical (reduction of interface trap density) and field-effect passivation (reduction in surface minority-carrier concentration), while point openings allow for contacting (26) (27). Similarly, front contact passivation can be approached by means of a thin ZnS layer (28) or other materials (29), or sulfurizing the surface (30).

Recent advancements in CIGS-based solar cells have been obtained by introducing a KF post-deposition treatment. The growth of a thin KF layer on the top of CIGS resulted in a more homogeneous buffer and improved interface, which rose both FF and $V_{oc}$. (31)

To facilitate the extraction of carriers, bands grading has been introduced in CIGS layer. By means of Ga grading it is possible to change the level of $E_C$ and thus create a slope in the $E_C$ along the CIGS growth axis. First, a back-surface field is created by larger Ga content close to the back contact ("back grading"), to assists the drift of photo-generated electrons towards the p-n junction. It improves the collection of free electrons, especially for photon energy in the near IR, which generates free carriers deeper in CIGS and outside the SCR. Another advantage consists in the presence of a low-bandgap ("notch") region close to the front surface, enhancing the absorption of low energy photons. Larger Ga content at the front interface of the absorber than in the notch ("front grading") is needed for improved junction quality. Similarly, introducing S at the interface creating a topmost layer of $Cu(In_x,Ga_{1-x})(Se_{1-x},S_x)$, it is possible to lower the $E_V$ and facilitate the collection of photo-generated holes towards the back contact. (32)

### 3.3.4. Buffer layer

The buffer layer is part of the so called "window layer" of the solar cell along with the transparent conductive oxides (TCO). Window layer is aimed to complete the p-n junction, to maximize the light to the deeper absorber and to conduce the carriers.

The buffer layer purpose is to guarantee good interfacial properties between the absorber and the TCO, in terms of both band line-up and lattice matching, meanwhile minimizing losses due to light absorption and obstacles in carrier collection.

CIGS-based thin-film solar cells are heterojunction-based devices in which the role played by buffer layer is of extreme importance. Despite homojunction solar cells, in which the same semiconductor is used to realize both the sides of the pn-junction, in heterojunction two different materials complete the structure. The latter system is preferred in TFSCs technology to have a wider-band-gap semiconductor as buffer, with respect to the absorber. Being transparent in the IR region and in most of the visible spectrum, it reduces the light absorption and allows the most of the incident light to reach the absorber material, increasing the $J_{sc}$.

As a drawback, the interface turns to be a critical point in heterojunctions. The physic interface between buffer layer and absorber coincides with the pn-junction electrical interface. This enhances the interface recombination: the non-perfect matching of the material lattices results in different kind of defects, many of which having an energy located in the middle of the band gap. These defects are electrically active and operate as recombination centres. Their presence where the charge carriers are created and separated has dramatic effect on the solar cell performance.

Moreover, the two materials have different $E_V$ and $E_C$. In fact, another critical point to be taken in account in heterojunction solar cells is the band alignment between buffer layer and absorber. To have high efficiency, it is essential to have a good matching between the bands of the junction materials. The band bending across the whole device must be maximized to enhance carrier extraction: conduction-band and valence-band energies should decrease towards the top-most window layer to support electron collection from the front contact and hole collection from the rear one. For this reason, more than the width of the band gap, the relative positions of valence band and conduction band are of leading importance. The value of buffer CB ($E_{C,buffer}$), in function of the one of CIGS ($E_{C,CIGS}$), create an offset (conduction band offset, CBO) which gives rise to a cliff or a spike:

- *If* $E_{C,buffer}<E_{C,CIGS}$, CBO<0: a deep well is formed. It enhances the recombination probability lowering the device $V_{oc}$.
- *If* $E_{C,buffer}>E_{C,CIGS}$, CBO>0: the bands originate a barrier for the electrons which brings to current blocking and FF loss first, and even $V_{oc}$ decrease later. However, for slight positive CBO (<0.3eV) a small improvement is expected due to the reduced recombination and to the small spike which can be overstepped by free electrons.

Thus, not only $J_{sc}$ but even $V_{oc}$ and FF are correlated to the buffer material, strictly depending from the CBO value. Therefore, it is an essential point to find a proper buffer-layer material, along with a deposition process, that minimizes the interface recombination and result in a good band-alignment structure.

At the beginning, the pn-junction CIGS-based solar cells, at the beginning, was completed evaporating a thick layer of cadmium sulphide (CdS). Later, chemical bath deposition (CBD) was introduced for CdS growth, the layer was thinned (up to few tens of nm) and followed by sputtering deposition of undoped zinc oxide (i-ZnO). ZnO was preferred to substitute CdS because of its wider band gap (3.3 eV instead of 2.4 eV). The resulting window structure, with a very thin CdS and the resistive i-ZnO layer, is the configuration that still gives the best results for CIGS solar cells, despite in the past years many efforts have been spent researching on alternative buffer layers. There are probably several causes at the base of the CBD-CdS success: good conduction-band alignment and good lattice match, Cd-indiffusion within the first CIGS layer (turning it to n-type and forming the widely discussed buried junction), CIGS surface etching in the wet environment followed by S-passivation, prevention of sputter damage to the absorber.

Therefore, in CIGS technology, the most used buffer is a 40nm-100nm CdS layer grown by means of CBD. To avoid the presence of cadmium, both in the PV modules and in the industrial production waste, alternative buffer layers (like Zn(O,S), (Zn,Mg)O, Zn-Sn-O, $In_2S_3$, Zn-In-Se, etc.) are being studied. Their band gap is even larger than the CdS one (2.4 eV), thus the short wavelength (blue) response is increased and they allow a considerable current-density gain. Moreover, changing their composition or

growth condition, it is possible to tune the conduction band and thus the CBO to find the best condition towards CIGS. The deposition methods have been diversify seeking vacuum-based processes not to interrupt the vacuum-chain of the industrial production, like puttering, atomic layer deposition, chemical vapour deposition, and so on.

### 3.3.5. Front contact

The front contact is constituted by three different layers: a resistive one to reduce the shunts, the TCO to collect the carriers and a metal contact to efficiently extract them.

The resistive layer is usually made of undoped ZnO or (Zn,Mg)O with a thickness of few tens of nm, which are almost transparent in the visible region of the spectra having a large bandgap (above 3.2 eV). They have a high sheet resistance and thus avoid carriers to move back into the buffer and recombine. Therefore, the presence of resistive layer reduces the shunt behaviour and increases the FF.

The front TCO indeed must have a low sheet resistance to reduce the resistive loss. To achieve the correct conductivity, highly doped oxides are used, like indium-tin oxide or aluminium-doped zinc oxide, but the free-carrier absorption below their energy gap lowers the device current. Thereby, a compromise between the light absorption and the sheet resistance is obtained at a certain thickness. New solutions take advantage of transparent oxides with lower free-carrier density and larger carrier mobility (like boron-doped zinc oxide by CVD) to achieve the same sheet resistance with reduced light absorption.

The front metal contact is needed to reduce the series resistance of the device and increase the FF. It is most important in large area devices and modules. Of course, the surface covered with the metal contact is a dead zone from the solar cell point of view: all the light is absorbed by the metal and the solar cells below it is completely shadowed and does not produce power. Simulations are used to find out what is the best geometry of the metal contact to obtain the best compromise between current density and fill factor and therefore to maximize the efficiency.

Eventually, an anti-reflection coating could be applied to reduce the light intensity reflected by the TCO and increase the current density.

## 3.4. Classic CIGS deposition techniques

The most suitable technology for CIGS-thin-film production on large area are thermal co-evaporation and sputtering. They are both applied by company to fabricate PV module which already hit the market. Both have different strategy for the CIGS growth, but their common features are a multi-stage process depositing precursors layers and the high temperature (450°C-600°C) involved for the formation of the chalcopyrite p-type structure and to avoid other phases. A selenization process is required to reintroduce

the Se which has evaporated from the CIGS lattice or even to form the CIGS material. In some cases, this process in performed by means of an atmosphere of toxic $H_2Se$.

### 3.4.1. Thermal co-evaporation

The most spread technique is thermal co-evaporation. It is based on the simultaneous evaporation from several heated sources of the elements composing CIGS. Their evaporation rates can be adjusted during the growth as well as the substrate temperature. The schematic representation of a vacuum system for the growth of CIGS thin-film is illustrated in Figure 3.6.

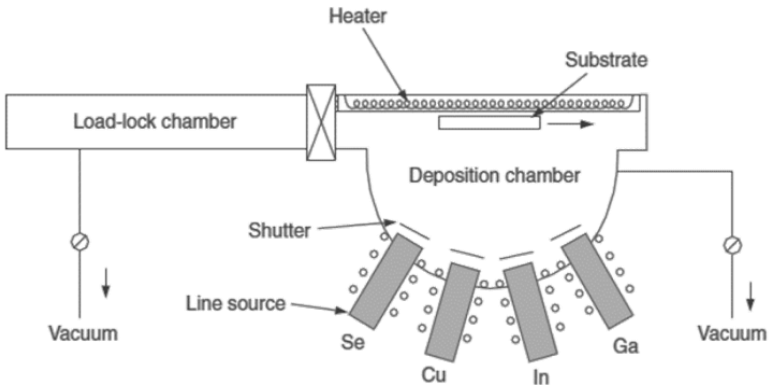


*Figure 3.6 - Schematic representation of a vacuum chamber equipped for CIGS thin-films deposition by means of thermal co-evaporation technique.*

Several strategies have been exploited to improve the quality of the CIGS absorber deposited by thermal co-evaporation. The first and simplest way consisted in keeping the evaporation rates of the elements and the substrate temperature constant for the whole process. Then other methods have been developed variating the element deposition rates and thus creating precursor layers with different stoichiometry, in the extreme case of 3-stage co-evaporation $Cu_2Se$ and $(Ga,In)_2Se_3$, as shown in Figure 3.7. In these cases, the temperature is risen from initial low values (250°C-400°C) up to 500°C-600°C for the final selenization and annealing steps. Such high temperature is unavoidable for this kind of deposition since there is no other way to form the CIGS α phase.

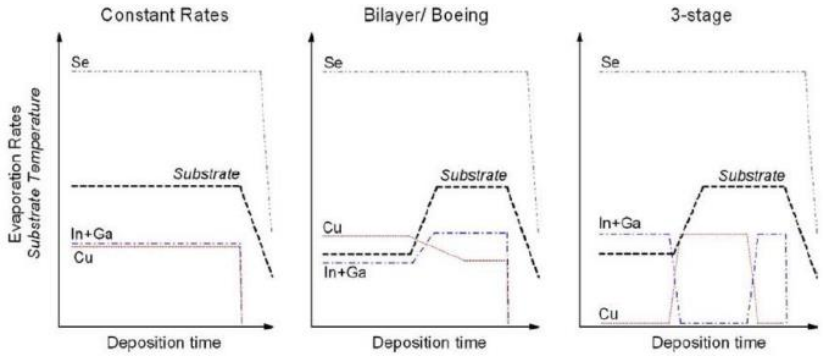


*Figure 3.7 - Evaporation rates of Cu, In, Ga and Se, along with the substrate temperature, during CIGS deposition by co-evaporation for three different growth strategies. (33)*

The 3-stage deposition process introduced by (34) has been observed to provide the best crystallinity of the CIGS absorber and to naturally result in a double grading profile of Ga inside it (35) (36). The Ga grading is now usually controlled adjusting the In and Ga evaporation rates during the deposition, to optimized the conduction and valence band shape of the absorber.

An additional step consisting in high temperature annealing in $H_2S$ atmosphere, can be used to form a $Cu(In,Ga)(S,Se)_2$ surface layer.

### 3.4.2. Sputtering

The sputtering technique is used to fabricate CIGS absorber as well, but generally leads to lower device efficiency with respect to thermal co-evaporation. In particular, results of sputtering deposition from quaternary CIGS target are extremely poor. Therefore, sequential sputtering from targets with different composition is used to deposit precursor layers, with different stacks as shown is Figure 3.8. Later a high temperature annealing (around 500 °C) is performed ex-situ in atmosphere of $H_2Se$ or $Se_2$, to introduce Se in the material and form CIGS.

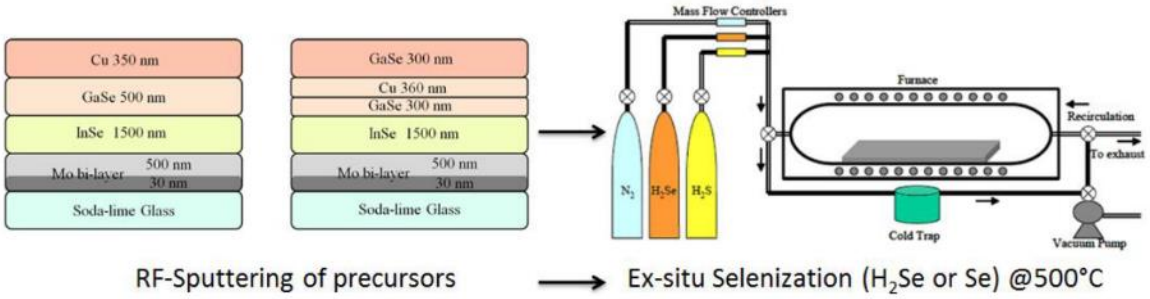


*Figure 3.8 - Schematic representation of two CIGS growth processes by means of sputtering technique: first precursor layers are deposited (left) and then annealed in $H_2Se$ (or mixture of it with $H_2S$) or Se atmosphere at 500 °C to form the CIGS α phase (right).*

# 4. The Pulsed Electron Deposition technique

## 4.1. Introduction

In recent years, important progress has been made towards the development of thin film solar cells based on $Cu(In,Ga)Se_2$. The efficiency has been improved for both lab-scale devices and industrial modules. Several companies are currently producing CIGS modules but their spread on the market is still limited by the competitiveness and robustness of silicon-based technology. An opposition between the two technologies into the same field is not what the thin-film PV is aiming for. Thin film solar cells, and CIGS-based ones *uber alles*, should look for innovative applications, i.e. planar silicon cells are not suitable for building-integrated, flexible devices or for power generation in the outer space. These applications involve the same structure of the CIGS-based solar cell, except for the substrate material. Building integration is aiming to save the installation cost that silicon cannot avoid. To achieve this purpose, research is trying to deposit CIGS-based solar cells directly onto building blocks, which would be used as construction units of the outer walls. Cement blocks and ceramic tiles are considered good substrates for both edifice façade and roof, while glass (coupled with transparent back contact, such as TCO) is the only alternative to fabricate PV windows. In these cases, the substrate would still be an important part of the overall cost of the PV module. More affordable substrates would be plastic materials, which are very cheap, light and easy to install. Moreover, flexible devices may be fabricated with plastics foils or tapes. Very-light substrates are even preferred for space application, where the most important parameter is not power-per-cost but power-per-weight. Unfortunately, CIGS has an incongruent melting point and its classic deposition techniques, mainly co-evaporation and sputtering, must involve temperature between 450 °C and 600 °C to form the p-type α-phase of CIGS. At such a high temperature, no plastic material can be used as substrate. Poly-imides have the highest degradation temperature among plastics, resisting until about 300 °C. At such a low growth temperature, co-evaporation and sputtering form films with a mixture of α- and β-CIGS phase. The latter phase exhibits a n-type conductivity and causes parasitic junctions inside the absorber, whose effects on the solar-cell performance are very detrimental. Moreover, CIGS growth at high temperature over back contact made by TCOs is affected by the formation of $Ga_2O_3$ at the interface. Gallium oxide is a wide bandgap semiconductor (≈4.9 eV) whose conduction and valence bands do not match with the ones of CIGS and

TCOs, thus causing the block of the current. Thus, the CIGS deposition by means of classic methods involving high temperature limits the efficiency of bifacial solar cells or PV windows.

In order to exploit very cheap and light substrates and to grow CIGS onto TCOs, it is essential to find deposition techniques capable to grow good-quality CIGS at lower temperature. An alternative cost-effective method combining low temperature and high-quality-CIGS growth is supposed to be promptly and gladly accepted by the industry. Pulsed electron deposition has the potential to be the right candidate.

In this chapter, the working principles of pulsed electron deposition (PED) are described. The deposition of CIGS at very-low temperature (250 °C), from a single target and without any selenization process is described in chapter 5. , as well as the milestones achieved during the development of CIGS-based solar cells by means of PED. The best solar cell obtained during this PhD project has a remarkable efficiency of 17.0% despite the lack of several optimization steps both in CIGS (no Ga grading applied, neither sulphurisation of the surface nor KF treatment) and in the other layers (standard CdS/i-ZnO/Al:ZnO window layer). The features of this record cell are presented in section 5.4.

## 4.2. The PED process

Pulsed electron deposition (PED) is a physical vapour deposition technique (PVD) capable to grow good-crystalline films at low temperature and from a single target. PED most important feature is to transfer the stoichiometry of the target into the deposited film, independently on the material phase diagram. By means of pulsed electron beams with a huge power-density (some $10^8$ W/cm$^2$), the technique delivers an astonishing amount of energy to the target material in a very short time (in the order of 100 ns). The PED power density is orders of magnitude higher than the one necessary to evaporate materials ($10^5$-$10^6$ W/cm$^2$), so bringing to non-equilibrium heating of the target surface. Therefore, the target material is suddenly transformed into plasma without undergoing any phase transition: congruent evaporation is achieved even for incongruent melting point material. This phenomenon is called "*ablation*". In this way, the composition of the target is transferred to the plasma and then to the film. Since temperature of the plasma is incredibly high (thousands of K), plasma species are extremely energetic (up to 10 eV). When these particles approach the substrate, the film grows with a good crystallinity even for low substrate temperature, since the inner energy of the species is sufficiently high for increasing the adatom mobility. For this reasons, PED is most suitable for those multi-component semiconductors, complex metal-oxides and alloys which usually form different phases, or solid state solutions of these phases, in function of the composition and the growth temperature. Incongruent-melting-point material cannot be grown by means of co-evaporation or sputtering methods without applying the right temperature to form the wanted phase and neither from a single target with a good control in the composition. Indeed, by means of PED it is possible to grow the correct phase by a stoichiometric single target and at a lower temperature. A small thermal evaporation

process occurring at the target surface is unavoidable, but it can be minimized by maximizing the power density of the e-beam.

Several materials had been reported to be deposited by means of pulsed electron deposition: ZnO-based semiconductors (37), composites $CoFe_2O_4$-$BiFeO_3$ (38), hydroxyapatite (39) and other oxides (40), $FeS_2$ (41), ionic conducting glasses, and even polymeric materials, such as hydro- and fluoro-carbon polymer films (PTFE). More similar to CIGS, high-temperature superconductors (HTS) $YBa_2Cu_3O_{7-x}$ (YBCO) (42), $GdBa_2Cu_3O_7$ and $(Gd_xEu_{1-x})Ba_2Cu_3O_7$ are among the most interesting materials successfully deposited by PED, despite their incongruent melting point and very intricate phase diagrams. Before PED, Pulsed laser deposition (PLD) was exploited to deposit HTS films. The two techniques have several similarities (ablation of the target, plasma features, composition conservation etc.). The most important difference lies in the mean used to ablate the target material (laser beam or electron beam) and in the equipment cost: a laser source is awfully more expensive than a pulsed electron gun. A basic comparison between PED and PLD is made in the section 4.2.4. In the past few years, thin-film group at IMEM-CNR of Parma developed a very-low-temperature pulsed-electron-deposition (VLTPED) process to grow CIGS for thin film solar cells, demonstrating it is suitable for high-efficiency devices.

This section is aimed to give a deeper description of how pulsed electron deposition works and what kind of features the grown film has.

### 4.2.1. Spark generation and discharge dynamics

The PED source is a hollow cathode electron gun which works in pulsed mode to maximize the power of the electron beam. High tension is used to accelerate the electrons (over 10 kV), but the most important characteristics are the huge current density (up to $10^5$ A/cm$^2$) and the short time of the discharge (≈100ns). A background low pressure of inert gas is necessary for the beam propagation. The discharge breakdown voltage is function of both gas nature and pressure. The resulting electron beam is focused on the target and is composed by electron with different kinetic energy. Figure 4.1 shows a schematic representation of the PED set-up and the geometries of the system. (43)

High currents are generated by means of a special hollow cathode. The so-called "*transient*" hollow cathode works in pulsed mode and consists of a metal tube with a narrow exit, installed in front of a planar anode. An electrolytic capacitor is connected in series to the cathode: it provides the electrical charge to the cathode. The pulse rate is controlled by a pre-discharge trigger circuit which ignites the plasma. Special cathode geometries and reduced electric field inside it promote plasma oscillations and slow movements, thus enhancing the probability of ion-impact ionization of the background gas. This increases the number of free electrons before the spark escapes the cathode through its narrow exit.

Then, the propagation of the electron discharge needs for collimation and acceleration towards the target material. They are obtained thanks to a configuration called "*channel-spark*": an insulating tube

constricts and stabilizes the discharge, which is accelerated by the anode-cathode electric field and magnetically self-pinched. (44)

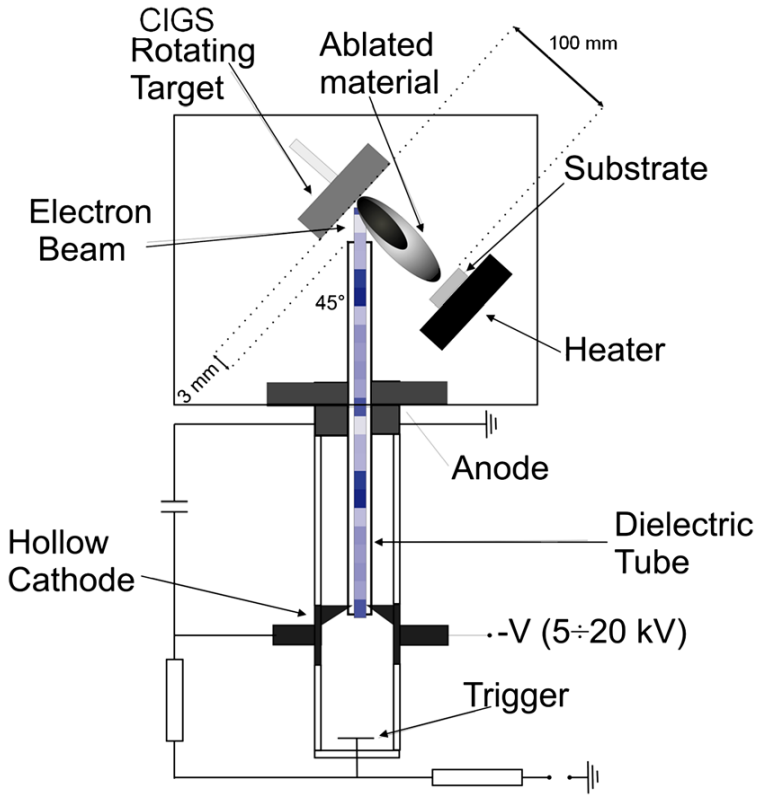


*Figure 4.1 – Schematic representation of a pulsed-electron-beam source (45)*

The breakdown tension ($V_B$), i.e. the tension required to have the discharge, is controlled by the constricted discharge law:

$$V_B \cdot P \cdot 2r = cost$$

where $P$ is the background pressure of the gas and $r$ the dielectric tube radius. The constant product of the three elements depends on the kind of gas used. An example is shown in Figure 4.2. Note that the distance between the cathode and the anode, or target, plays a minor role. Usually, it is preferred to work at higher tension and lower pressure to maximize congruent evaporation of the target and minimize interactions of plasma particles with the background gas.

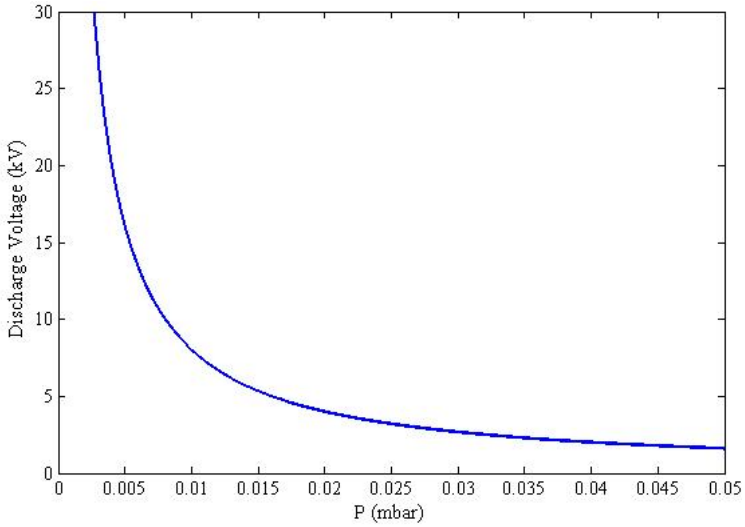


*Figure 4.2 – Example of breakdown voltage trend as a function of gas pressure for an electron-beam source. The curve is calculated by the equation:* $V_B \cdot P \cdot 2r = cost$

During its propagation inside the dielectric tube, the beam is made by a channel of ionized gas through which the electrons pass. The head of the beam ionizes the gas particles it meets, creating a nearly space-charge-neutralized column. Lower-energetic electrons, mainly due to secondary ionizations and to electron extraction from the tube inner-wall, are lost during the propagation: they are repelled radially outward leaving a path of positively charged ions in which the electron beam propagates. The magnetic field of the discharge itself contributes to the electron collimation. The propagation of the discharge is then a collective process.

The electron beam of PED is a poly-energetic beam since the electrons in it do not have everyone the same energy. Different energy means different velocity, so the electron energy and beam power is function of the time. The beam can be divided at least into three contributions as a function of the electron energy, as determined by (44) and shown in Figure 4.3:

- the head of the beam contains few electrons with the highest energy;
- a second pack of electrons with intermediate energy and still low current follows the head;
- the tail of the beam has the highest current but the lowest energy.

This energy distribution of the electrons into the beam is crucial for the ablation process: lower-energetic electrons may cause only heating of target material, resulting in incongruent melting, while extremely energetic ones may penetrate too deep in the target, originating ablation far below the surface.

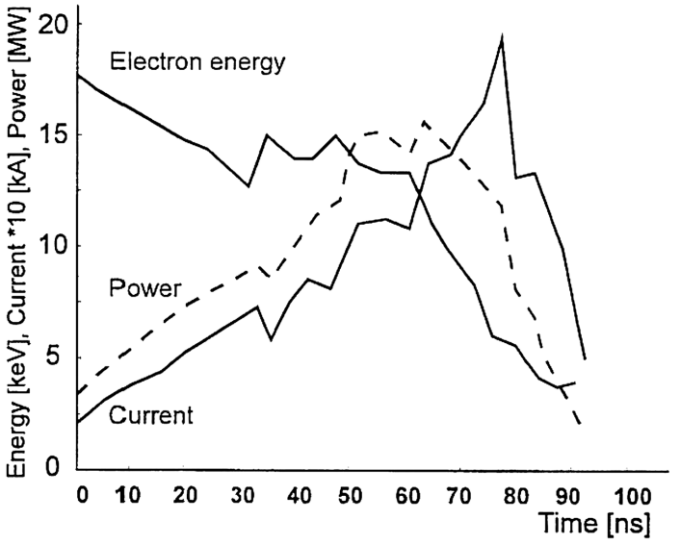


*Figure 4.3 – Electron energy, current and power of a single electron-beam pulse accelerated by 20 kV tension as determined by (44).*

Due to extra-long operating times or bad cooling system, the electron flux distribution can be modified by overheating of the PED source. The hollow cathode is very sensitive to temperature and its heating causes electron emission by thermo-ionic effect. These electrons have low energy, extending the discharge tail, thus enhancing the incongruent evaporation. To allow the cathode cooling between two consecutive pulses, commercial PED sources usually limits their own operating power reducing the pulse repetition rate in function of the accelerating voltage. An example is shown in Figure 4.4, where the electron gun is limited to operating power of 15W: at a voltage of 14kV the repetition rate can be up to 10Hz, while at 20kV the rate is limited at 5Hz.

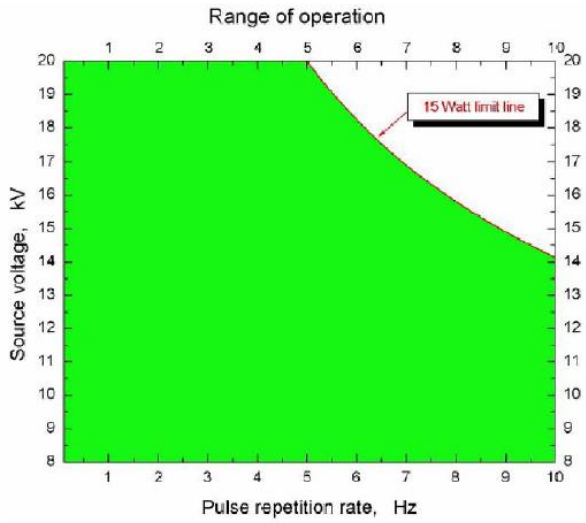


*Figure 4.4 – Maximum PED voltage of a Neocera PEBS20 source as a function of pulse frequency to keep the power limited at 15W.*

The operating power of a PED source is the power consumption, which is just few watts, while the power supplied in each pulse is very high because of the extremely short discharge duration.

### 4.2.2. Interaction with target material and plasma plume formation

The interaction between the electron beam and the target material is very complicated and particularly important for the characteristics of the deposited film, both in terms of composition and morphology. The most important parameters are the distributions of power and of electrons energy in the beam. They control the ablation and the penetration of the beam inside the target, respectively. To achieve the ablation, it is necessary to overcome a power level, the *ablation threshold* which depends on the target material (1-5·$10^7$ W/$cm^2$). If the beam power is below this threshold, the material is not ablated but only incongruent evaporation will occur. On the other hand, very energetic electrons penetrate deeper into the target giving rise to ablation below the surface, which may remain solid. The plasma expansion below the surface would cause *macroscopic splashing* phenomena, transferring solid particulate onto the substrate. These solid debris are detrimental because they create an uncontrolled and significant variation of the film thickness. It is mandatory to find the right trade-off between these two phenomena in order to obtain a good-quality film. The acceleration voltage at which PED works is the crucial parameter to be optimized.

When the electron beam hits the target, energy is transferred through inelastic collision between electrons and atoms. The electrons trajectory is influenced by Coulomb scattering and follows a zig-zag line. Part of the incident electrons are even reflected at the surface because of the scattering. The penetration range into the target δ is roughly approximated as:

$$\delta[\mu m] \approx 5.37 \cdot E \cdot \left(1 - \frac{0.9815}{1 + 0.00031 \cdot E}\right) \cdot \frac{1}{\rho} \cdot \cos\left(\frac{\alpha}{2}\right)$$

$$for\ 1keV \leq E \leq 20MeV \quad and \quad 0° < \propto < 60°$$

where $E$ is the energy of the electron expressed in keV, $\rho$ is target density in g/$cm^3$ and $\alpha$ the angle between the beam direction, determined by the dielectric tube, and the plane of the target surface. (44) (46)

An example of the penetration range as function of the electron energy is shown in Figure 4.5.

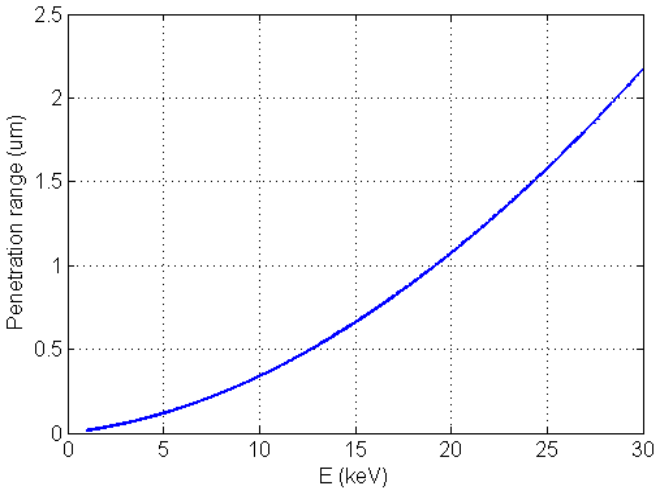


*Figure 4.5 - Electron range as a function of its energy, in a target material with ρ=7g/cm³ and with impingement angle α=45°.*

The electron range should be larger than the thermal diffusion length $\delta_T$, which depends from the thermal conductivity of the target $A$ and the pulse duration $\tau$:

$$\delta > \delta_T = 2 \cdot \sqrt{A \cdot \tau}$$

If this condition is not verified, incongruent evaporation may significantly affect the film stoichiometry and at the same time the deposition rate will be lower because of less ablated volume. To impose this condition at the system, it is possible to operate in two ways: maximize the penetration depth of the electrons, increasing the PED accelerating voltage, or minimize the thermal diffusion length, shortening the pulse duration. The former solution is limited by macroscopic ablation, while the pulse duration is an intrinsic parameter of the electron source and cannot be controlled. From the experimental point of view, it is necessary to find the discharge voltage that gives the best compromise between the composition and the morphology of the film. (43)

Efficiency of energy-transfer from the electron beam to the target is about 30%. In fact, electrons approaching the target transferred their energy in several ways and originates several phenomena:

- reflected electrons (about 25%);
- energy used for the ablation or evaporation, linked to the material ablation threshold or heat of evaporation, respectively;
- X-ray and other radiations production;
- thermal diffusion;
- negative charging of the target surface, which lowers the potential for the following electrons, and so their kinetic energy.

The power density absorbed by the target is not distributed uniformly along the penetration depth of the electron, but follows approximately the expression:

$$\frac{P(z)}{P_{max}} = 1 - \frac{9}{4} \cdot \left(\frac{z}{\delta} - \frac{1}{3}\right)^2 \qquad z < \delta\,, \qquad P_{max} = \frac{4}{3} \cdot (1 - \zeta) \cdot V \cdot \frac{j}{\delta}$$

where *P(z)* is the power density along the electron range in W/cm$^3$, $P_{max}$ is the maximum power density, $\delta$ the electron range into a target, *j* the electron beam current density in A/cm$^2$, *V* the accelerating voltage of the PED ($q \cdot V$ is the uniform electron energy) and $\zeta$ an empiric factor expressing the power loss. The current density propagating inside the target depends from current of the electron beam *I*, the beam-spot area on the target *S* and the impingement angle $\alpha$: $j = I/S \cdot cos(\alpha)$. The factor $\zeta$ comprehends reflected power due to target morphology or surface charging and takes into account the target thickness and composition, as well as its electric and thermic properties. Moreover, since the electron source may change its behaviour for long operating time due to the over-heating of components, $\zeta$ even considers the power variation of the beams from pulse to pulse. (44) (47)

The power-distribution equation is approximated for mono-energetic electrons, thus all of them having the same penetration range. The trend of the normalized power density as a function of the depth across the penetration range is shown in Figure 4.6.

Since the electrons of the beam have different energy and different penetration range during the time of the pulse (see Figure 4.3), the total absorbed power density is the integration in time and depth of the power profile: *P(z,t)*. For a channel-spark pulse, the resulting power transfer is maximized at the target surface and gradually drops becoming zero at longest electron range. Unavoidably, part of the beam energy is transformed into heat and conducted deeper inside the target, depending from the thermal conductivity of the solid material. Therefore, the power profile results more spread in depth. The thickness of the ablated layer is determined by the depth *z* at which the absorbed power equals the ablation threshold. Below that layer, incongruent evaporation take place. For materials with poor thermal-conductivity, it is possible to minimize the amount of target incongruently evaporated so having negligible composition variation in the deposited film.

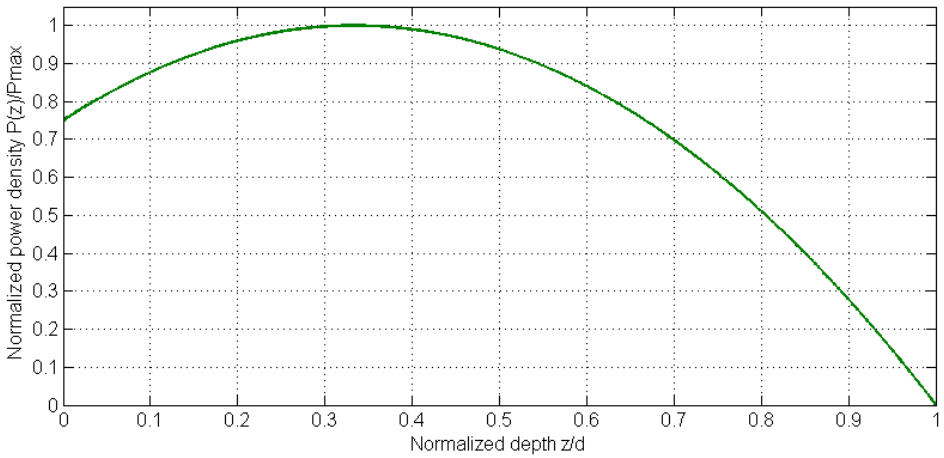


*Figure 4.6 – Normalized power density transferred to the target as a function of depth normalized to the electron range (z/δ).*

The energy of electron beams with power density above the ablation threshold is transformed first into electronic excitation of the target. Then, it is converted into thermal, chemical and even mechanical energy involving both processes at the thermodynamic equilibrium and far away from it. But numerical simulations show that only a relatively small part of the total power of the beam is used for ablating the material, i.e. to transform it in the plasma state. The most of the energy is loaded into the ablated particle as inner energy, stored both in excited states and expansion velocity. This unconventionally-huge inner energy is very important to grow the film without heating too much the substrate. The temperature of the target surface and of the plasma is a good indication of how much energy is stored in the ablated particles. The target-surface temperature is expected to change as:

$$\frac{dT}{dt} \propto \frac{P}{C \cdot \rho \cdot (\delta_T + \delta)}$$

where $P$ is the integrated power density, $C$ and $\rho$ the thermal capacity and the density of the target material, $\delta$ and $\delta_T$ the electron range and thermal diffusion length into the target. Simulations suggest the temperature of the target surface increases up to several thousands of Kelvin (7000K-10000K), during the first 200 ns after the beam hits the target. This means a high melting temperature of a material is not an impediment for the ablation, if its thermal conductivity is low enough. The highest temperatures are reached thanks to the contributions of the beam bulk and the beam head, which carry the highest power density (see Figure 4.3). After the beam is absorbed by the target, the surface temperature drops immediately (in few ns) to 1000K-2000K and then thermalizes over a longer time, in the range of milliseconds. During the cooling, incongruent evaporation phenomena may take place. (46) (47)

The huge high temperature localized in few hundreds of nm or few μm causes the surface-layer ablation, i.e. the sudden transformation of the solid material into a vapour/plasma state, maintaining the same composition. The known ablation mechanisms are classified in four categories:

1) *Collisional* ablation: provided by massive-particles collisions with the target, whose atoms are ejected from the surface due to simple momentum transfer. It is typical of sputtering deposition. Different elements have different sputtering yields and the sputtered particles has lower inner energy than the other ablation methods.
2) *Thermal* ablation: energy is transferred by the coupling of the beam with vibrational and electronic modes of the target material. It is the main ablation mechanism for PLD process with nanoseconds pulses and is a secondary one in PED process.
3) *Electronic* ablation: it is the PED most important mechanism. The beam interacts with the atoms of the target and their electron shells, ionizing and exciting them, and creates electron-hole couples in the lattice. It is dominant even in PLD with picoseconds pulses.
4) *Macroscopic* ablation: a main issue in PLD and PED process. Solid particulate with striking dimension (even tens of micrometres) is originated by the interaction of a very-energetic beam

with the target and then deposited onto the substrate. This mechanism affecting the target surface morphology is can be classified in two cases:

i. *Exfoliation*: thin layers are peeled off from the target surface, because of high thermal expansion coefficient and high sublimation temperature of the material (high ablation threshold);
ii. *Hydrodynamic ablation*: evaporation of the matter take place below the surface, which remains liquid or partially solid. These particulate is then transported onto the substrate by the supersonic expansion of the plasma below it. It is called "subsurface super-boiling" when irregular-shaped particulate is ejected from the target, or "splashing" when a sort of surface explosion occurs, shooting droplets of different dimensions towards the substrate.

Macroscopic ablation is inevitable for both PLD and PED and is the reason why it is very hard to grow nanostructured layers by means of these pulsed energetic techniques. Fortunately, thanks to the poly-energetic feature of the electron beam, hydrodynamic mechanism could be avoided during PED ablation acting on the acceleration voltage of the electron beam. Indeed, the splashing phenomenon is always present in the pulsed electron deposition. It creates rounded particles with dimension from few nanometres to the micrometre order of magnitude. The dimension of these particles and their density (number per unit of area) should be controlled to preserve the film morphology. The target preparation is very important to avoid larger particles: using dense targets without cracks and micro-voids is mandatory. Moreover, applying a potential between the target and the substrate has been found to lower both the density and the dimension of the droplets affecting the film morphology, but at the same time it reduces the deposition rate. Remarkably, droplets preserve the target composition: during the flight from the target to the substrate, more volatile elements evaporate from the molten surface only, causing a stoichiometry variation of less than 5% once onto the film. Droplets with diameter of tens of nanometres (nano-droplets) are therefore very important for the film growth, providing a good deposition rate and low composition variation from the target content.

Along with splashing, the other main contribute to the material deposition in PED process is the electronic ablation. It forms a dense layer of plasma, called "plasma plume", which contents a multiplicity of super-energetic particles: ions in different charge states, free electrons, excited atoms, molecules, clusters, etc.. The plasma plume expands in direction of the largest pressure gradient, hence perpendicularly to the target surface. The mean free path of the particles inside the plasma is very short. The great number of collisions minimizes the divergence of the plasma plume and so the material is not spread on an angle as large as in a classic thermal evaporation. Therefore, the deposition is very straightforward. The geometry of the system is important as well, especially the impingement angle $\alpha$ between the dielectric tube and the target surface. The best deposition condition has been determined to

be for $\alpha$=45°, at which the waste of power density due to current reflection is not an issue and the plasma shape is optimal for an expansion perpendicular to the target.

Optical Emission Spectroscopy analyses of the plume reveal a "white-hot" plasma with a Bremsstrahlung emission in the very first millimetre. After expansion of few millimetres, the plasma shows a wide range of emission lines due to the highly-ionized species. Later, the ions reduce their charge with the cooling of the plasma, so the spectral intensities drop as a function of the distance and the time of expansion. During this adiabatic expansion in vacuum, the thermal and excitation energy is transformed into kinetic energic, speeding up the particles. Plasma particles velocity is described by:

$$v = \left(\frac{2}{\gamma - 1}\right) \cdot \sqrt{\frac{\gamma \cdot k_B \cdot T}{m}}$$

where $\gamma$ is the ratio between the specific heats at constant pressure and volume of the plume ($C_P/C_V$), $k_B$ the Boltzmann constant, $T$ the temperature of the specie and $m$ its mass. Each particle has its own velocity, but their distribution is well approximated by the Maxwell-Boltzmann distribution:

$$f(v) = v^3 \cdot e^{-\frac{m \cdot (v - v_{cm})^2}{2 \cdot k_B \cdot T_{eff}}}$$

where $v_{cm}$ is the centre of mass velocity. Since there is no momentum transfer from the electronic beam and because of the collisions inside the plasma, the ejected species maintain a velocity directed perpendicular to the target surface: the only driving force is the pressure gradient between the dense plasma and the low vacuum of the deposition chamber. The energies of the ablated species are stabilized after the initial spot and so their velocity is frozen for long distances. Average velocity of double or higher charged atoms escaping the surface is up to $10^4$ m/s in the centre of the plasma plume, while the one of nano-droplets is $10^3$ m/s. The velocity of the species decreases linearly with the distance of the particle from the plasma centre, while the plasma density decreases exponentially with the distance from the centre. An example of plasma plume expansion in space and time is shown in Figure 4.7.

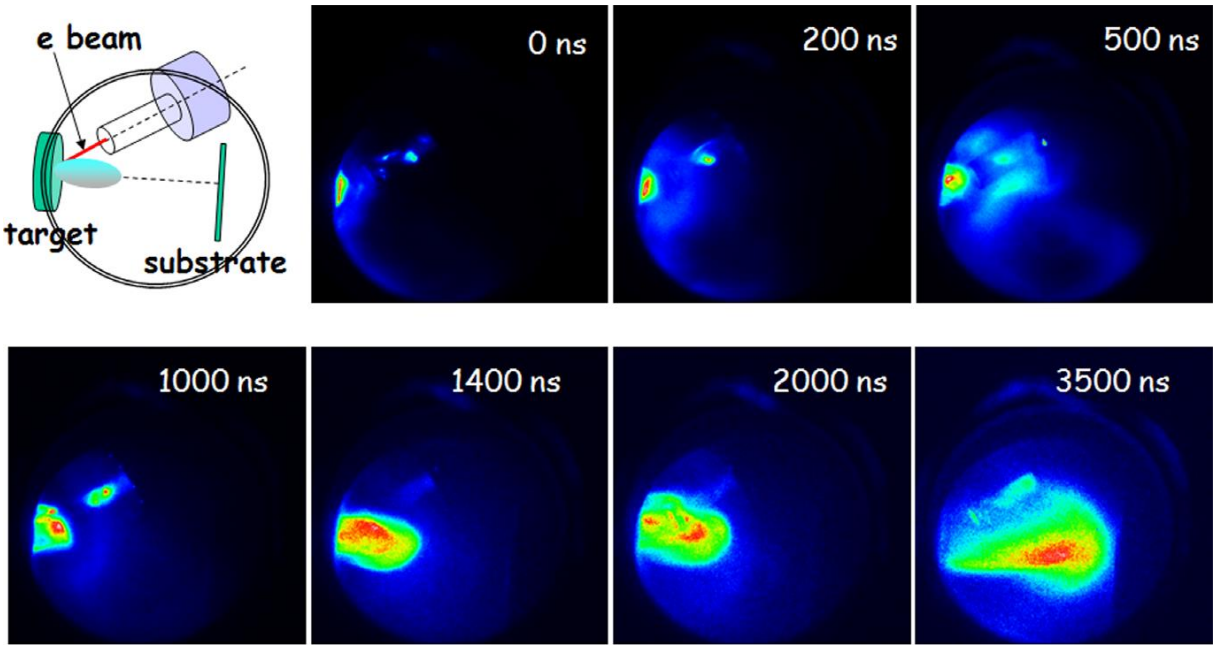


*Figure 4.7 –Hydroxyapatite plasma plume expansion in Ar background gas after PED ablation, at several different times. (40)*

However, theory describes the presence of a very-dense plasma layer immediately above the surface, which is stable for all the pulse duration. It is called "Knudsen layer" and has a crucial part in limiting the ablated-particles velocity. Each particle ejected from the target surface must cross the Knudsen layer, in which undergoes to an incredible number of collisions due to the high density of the layer. Because of these collisions, the particles velocity is asymptotically decreased to a value close to the plasma sound velocity. Therefore, the plasma expansion speed $u$ is limited to a value close to the local sound velocity of the plasma $a$ and we referred to it by the plasma number of Mach $M$:

$$M = \frac{u}{a} \quad , \quad a = \sqrt{\frac{\gamma \cdot k_B \cdot T}{m}}$$

Remarkably, enhancing the accelerating voltage of the electron beam does not cause any increment in the ablated-particles velocity. The consequent increase of their inner energy is always compensated by an augmented number of collisions inside the Knudsen layer. This phenomenon mitigated the velocity of the particles escaping the Knudsen layer at a constant value, whatever the working voltage of the PED system and the power density of the electron beam. In the case of PED and PLD, the Mach number is around or higher than 1, meaning the plasma has a supersonic expansion. For classic evaporation by means of effusive source, the number of Mach is close to 0 because the particles have very low kinetic energy.

Even the background gas plays a role during the plasma expansion. It brings to scattering and thermalization of the plasma and so affects the kinetic energy of the plasma species, the spatial distribution and the deposition rate of the ablated material. In general, the higher the pressure, the more

confined and slower the plume. Nevertheless, the pressure variation of the background gas in the $10^{-4}$-$10^{-2}$ mbar range seems to cause slightly changes in the plasma features, hence it has negligible effects on the quality of the deposited film. Reactive scattering to form new molecules is even possible if the gas used is not an inert one: $O_2$ may be used for oxides deposition. Otherwise, noble gases like Ar or He are preferred.

### 4.2.3. Thin-film growth

As a consequence of target ablation and plasma plume propagation, the matter condensates onto the substrate positioned exactly over the target. The most important parameters of thin-film growth are the composition and the deposition rate, which are both function of the accelerating voltage and the distance from the centre of the deposition. The substrate temperature plays a minor role in PED deposition.

The angular distribution of the plasma plume causes an angular profile of the film thickness and of the composition. The deposition is very peaked on the axis of the plasma plume, that for a beam-target impingement angle of 45° means just over the point in which the electron beam hits the target. The angular distribution of the thickness must take in account both congruent-ablation and incongruent-evaporation contributes, mediated by an opportune coefficient, since they are always present at the same time but with different intensity. Evaporation and ablation give rise to different angular distribution, so the "Comsa-David Model" describes these two contributes during a PED or PLD deposition (48) (49) (50), by means of a two-cosine function:

$$F(\theta) = a \cdot \cos(\theta) \ + (1 - a) \cdot \cos^{\mathrm{p}}(\theta) \quad , \quad p > 1$$

where $\theta$ is the angle from the plasma plume axis and $a$ is the coefficient that weight the contributes from the evaporation at thermodynamic equilibrium and ablation. Evaporation has a broad distribution, dispensing the matter on a large angle with low deposition rate, so it is described by a $cos(\theta)$ function. Ablation indeed is very forward-peaked and its distribution is better described by $cos^{p}(\theta)$, in which $p>1$ indicates how great is the drop of deposited thickness from the centre of the deposition. For very-high accelerating voltages that allow an almost pure ablation of the target and negligible evaporation, the coefficient $a$ tends to zero and the angular distribution is approximated as:

$$F(\theta) \approx \cos^{\mathrm{p}}(\theta)$$

Considering the deposition usually takes place on flat substrates, a geometric correction must be applied:

$$D(\theta) \approx \cos^{\mathrm{p}+3}(\theta)$$

The coefficient $p$ is related to the target material and the plasma features from the relation:

$$p = 1 + 2.13 \cdot \frac{M \cdot \sqrt{\gamma}}{1 + M \cdot \sqrt{\gamma}} + \gamma \cdot M^2$$

where $\gamma$ is the ratio between the specific heats of the plume and $M$ is the plasma velocity expressed in Mach number. For $M$=1, $p$ value is about 4. Note that $p$ does not depend from the accelerating voltage since the plasma diffusion velocity is not, for power density above the ablation threshold.

The contribution fraction of the first cosine term ($f$) in Comsa-David Model is determined by (51) as:

$$f = (p \cdot a + a)/(p \cdot a - a + 2)$$

and it corresponds to the fraction of the deposited mass with a stoichiometry different than the target material.

Once the species arrive on the substrate, it is necessary they have a certain "surface mobility" to grow a film with good crystalline properties, i.e. the right structure and low defect density. The adatom diffusion length onto a surface is a function of its own energy $kT$ and of the activation energy for the diffusion $\varepsilon_D$:

$$D = D_0 \cdot e^{-\frac{\varepsilon_D}{kT}}$$

$\varepsilon_D$ is usually in the order of 2-3eV. Classic deposition techniques working at the thermodynamic equilibrium, like thermal evaporation, produce species with inner energy in the same order of the thermal energy for melting or sublimation (0.01-1eV). This value is lower than the diffusion activation energy so it is straightforward to heat the substrate in order to promote the diffusion and to have a crystalline film. Unfortunately, increasing the growth temperature the thermal disorder or entropy is higher, so the defect density inside the material is increased. Indeed, particles produced by ablation approach the substrate with energy from few eV to 10eV, high enough to activate the diffusion process with no need of external energy to be provided.

### 4.2.4. PLD and PED comparison

Pulsed laser deposition and pulsed electron deposition share several features, like the plasma formation and the transfer of stoichiometry from the target to the film. Their core difference lies in the mean used to provide the ablation: pulsed laser beams or pulsed electron beams, respectively. Hence, the beam characteristics and its interaction with the target are different.

In the PED process, the beam power density is controlled by the acceleration voltage, while the current is an intrinsic characteristic depending on the geometry of the e-beam source. The electrons of the beam do not have the same energy, so it is a poly-energetic beam whose power density is distributed for a certain length inside the target. The maximum power transfer is always at the surface, so phenomena like subsurface super-boiling is avoided and the deposition can be controlled to obtain a good thickness homogeneity.

In PLD, the beam energy density, called "fluence", is controlled by laser intensity, so changing the number of photons per pulse. It is not possible to act on the photon energy and all the photons have the same energy. The peak of the transferred power density for PLD is always below the target surface, its

position depends from the material absorption coefficient and on the laser wavelength and cannot be controlled in depth. The latter feature means subsurface super-boiling is a major issue with PLD and severe problems arise in the film morphology due to large particulate deposited onto the substrate.

For PED, problems during the power transfer, the ablation and/or the film growth occurs for materials:

- with high electron or thermal conductivity: since the energy is quickly distributed over a larger volume, the ablated matter is drastically reduced and PED process is turned into a sort of electron-beam evaporation;
- made by atoms with elevate atomic number: it increases the reflected part of the electron beam and the power density for the ablation is drastically decreased;
- having huge specific latent heat of evaporation: the most of the energy is spent for the ablation and the plasma formation, so the particles composing the plasma have lower inner energies and thus film quality is poorer.

PLD suffers the same problems as PED for materials with high thermal conductivity and elevate specific latent heat of evaporation, but in addition is not able to ablate those materials transparent to the laser wavelength.

Nevertheless, the cost of the equipment is very important especially for the industrial point of view. Since both PLD and PED have a small deposition area, due to the plasma plume characteristics, to grow on large area several sources are needed. A PED source costs about 50k$, while PLD sources capable to reach the fluence to activate the ablation are in the range of 500k$-1M$. For the industrial scale-up, PED would be preferred since the cost of the installation equipment is 10-20 times lower than PLD.

# 5. CIGS by Low-Temperature PED for TFSCs

## 5.1. Equipment

A brief explanation of the experimental equipment for CIGS deposition, available at IMEM-CNR of Parma, and the targets preparation methods.

### 5.1.1. Experimental set-up

CIGS absorber for TFSCs were grown by means of a commercial PEBS-20, Neocera Inc. This PED source works with acceleration voltage of 8-20 kV at the repetition rate of 12-8 Hz. The channel-spark system was realized by an alumina tube having inner diameter of 3mm. The source was installed in a vacuum chamber, kept at a base pressure of $1 \cdot 10^{-7}$ mbar by means of turbopumps. The samples were introduced by means of a magnetic feedthrough from a load-lock pre-chamber, to preserve the vacuum in the deposition chamber. A $1 \cdot 10^{-3}$-$1 \cdot 10^{-2}$ mbar background pressure of Ar (5N purity) was then introduced in the main chamber for the PED functioning.

In the deposition chamber, the substrates were loaded 3 cm beneath the heaters. Heaters were graphite susceptors warmed up by halogen lamps positioned inside them. Two heaters were used, one for the deposition and one for the post-deposition annealing treatment. In this way, the sample was heated from the back side by the thermal radiation emitted from the graphite susceptors. As long as the graphite blocks are larger and longer than the sample, a homogeneous temperature profile is obtained on the substrate. For 2.5cm-wide and 8.5cm-long sample, no appreciable temperature variation was observed onto the front side of substrate.

The targets of the PED process were glued to copper holder by means of conductive past and then installed on a rotating carousel. This carousel could host up to four targets and could be externally rotated to switch from one target to another during the process. Moreover, every target rotated in order to homogenize the erosion and minimize target heating and macroscopic ablation. It is very straightforward to avoid incongruent evaporation, target surface degradation and bad film morphology. Target rotation speed can be tuned according to the material and the pulse rate. The selected target was positioned 2 mm below the alumina tube exit. The PED source position can be slightly change, without breaking the vacuum, to adjust the alumina tube position at the height of the target. The same distance and angle

between the alumina tube and the target must be maintained not to alter the ablation process from deposition to deposition, when the targets are thinned. An impingement angle of 45° was used. The process gas was introduced into the chamber by means of a capillary positioned close to the target, facing the alumina tube exit, and its flux was controlled by means of a flowmeter.

The samples were placed 8cm over the target surface and the deposition were centred just over the point in which the electron beam hit the target. Samples holders were made of steel in two different shapes: one with three 1"×1" (2.6cm×2.6cm) slots, the other arranging one 1"×3" (2.6cm×7.8cm) sample. The temperature of the downward face of the samples was calibrated by means of both thermocouples and thermo-imaging, as a function of the graphite heaters temperature.

The deposition chamber was equipped with two windows: a transparent glass and a ZnS window. The former was meant for OES analyses of the plasma plume; the latter was used to focus the substrate with IR pyrometer of IR camera placed outside the chamber. They were used to determine the temperature interference caused by the growing film, which gives an indication of the film thickness.

### 5.1.2. Target preparation

The targets used for pulsed electron depositions were synthesized all at IMEM-CNR. The materials were NaF and Cu(In,Ga)$Se_2$ with variable Ga content, produced with the following methods:

- NaF: 0.5cm-thick sodium fluoride disks with diameter of 40 mm were formed by cold pressing NaF powders (5N) at 200 bar for 10 minutes and by sintering the pellets at high temperature: 900 °C for 12 h. It resulted in a dense and compact target suitable for efficient PED ablation.
- CIGS: targets with different composition from $CuInSe_2$ to $CuGaSe_2$ were grown by means of a modified Liquid Encapsulated Czochralski method (LEC). BY LEC technique, elements (5N) in perfect stoichiometric ratio (Cu=25%, (In+Ga)=25%, Se=50%) were melted together at 1170 K by means of radio-frequency heating, under pressure in a semi-closed system inside a quartz tube. The obtained melt phase was then cooled down to room temperature in 2 days, after which the CIGS phase was formed. The fabricated ingot had a diameter of 1" and was eventually cut into 1cm-thick slices (disks) to obtain the PED targets.

The target disks were preserved in a low-humidity cabinet before the use. They were glued to the copper holder by means of a conductive paste which is dried by heating at 200 °C.

## 5.2. Very-low temperature CIGS deposition by PED

As already described in chapter 3. , CIGS has the highest absorption coefficient and the largest theoretical efficiency among semiconductors for TFSCs. CIGS technology has greatly been improved in the last few years but it is still limited by the high temperature involved in the deposition process. New applications and cheaper devices will be possible if CIGS is grown at lower temperature than the classic deposition technique. Low-Temperature Pulsed Electron Deposition (LTPED) has been exploited for this reason at IMEM-CNR of Parma.

The core of the LTPED process is the interaction between a high power pulsed electron beam and a few millimetres thick CIGS target, having the stoichiometry to be reproduced in the thin film. Each pulse lasts about 200 ns during which an average power of $10^8$ W/cm$^2$ is dissipated in a volume of a few mm in diameter and 1μm in depth. As a result, a significant portion of the bombarded material is ablated and gives rise to a plasma containing all the elements of the compound in essentially the same proportion as in the original target. Then, the elements contained in the plasma condensed on the substrate forming the film. Some variations in CIGS composition can be performed by increasing the temperature, due to the re-evaporation of more volatile elements, and specific grain orientations can be selected.

Whatever the back contact used (Mo or TCOs), the best experimental conditions for CIGS deposition were found to be at an Ar pressure of $5 \cdot 10^{-3}$ mbar with a PED voltage of 16 kV and a repetition rate of 9 Hz. The substrate temperature during the growth was 250°C-280°C and its distance from the target was fixed at 8cm. An example of PED functioning is showed in Figure 5.1.

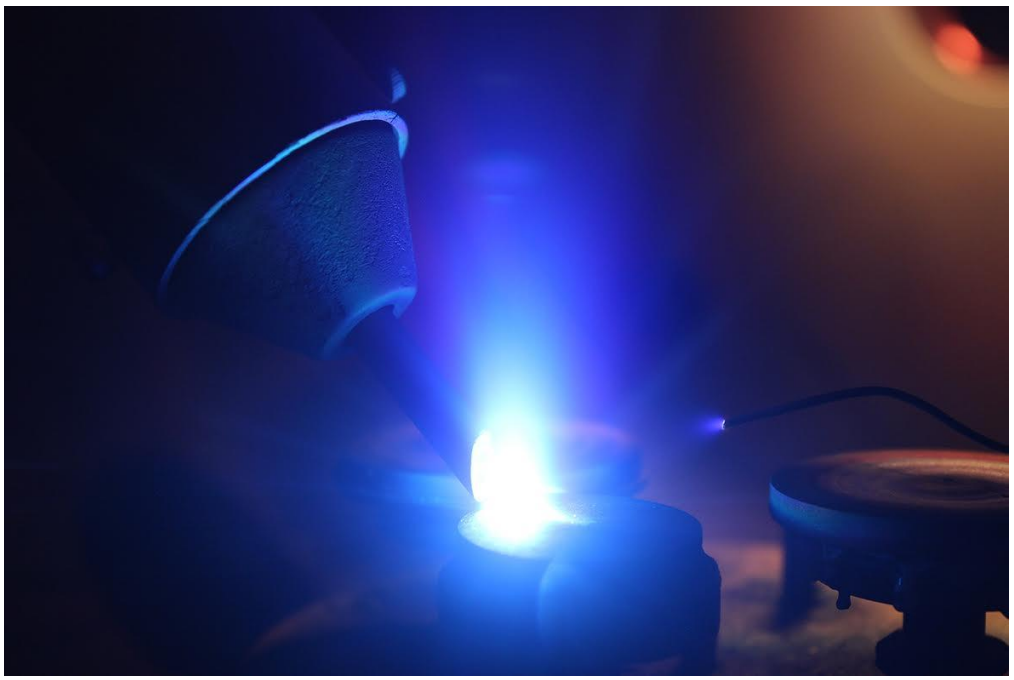

*Figure 5.1 - Plasma plume formed by PED ablation of a CIGS target. The electron gun is on the left and its alumina tube drives the electron beam to hit the target surface with an angle of 45°. The glowing shape of the plasma reflects its forward expansion. On the right, a small pipe is continuously providing Ar gas, necessary for the discharge propagation. Behind, two NaF targets can be seen.*

NaF precursor layer was deposited prior to CIGS as described in section 5.3.2. Then, CIGS target was cleaned by means of 2k pulses with the substrate still in the load lock. Later, the substrate is introduced in the deposition chamber and placed beneath the graphite block and over the target, to be heated before the deposition. The substrate temperature was checked by pyrometer or thermo-camera and when it saturated, the deposition was performed. The growth was interrupted at the CIGS thickness of 1.6 μm and immediately after the sample underwent an annealing treatment at the same temperature as the CIGS deposition, in vacuum (Ar pressure of $5 \cdot 10^{-3}$ mbar) for 80 min. The annealing is performed to enhance the CIGS crystallinity and orientation, but mainly to diffuse the Na across the CIGS layer. A long annealing time was needed because of the low temperature.

The CIGS thickness was determined in-situ by means of a pyrometer and/or a thermo-camera (see Appendix I - Thin-film characterization methods). Raytek Marathon MM pyrometer detects the radiation wavelength of 8 μm and the interference maximums and minimums allow to discriminate the CIGS thickness (with a refractive index n≈2.5) every 800 nm of deposited material. At the first maximum, CIGS thickness would be 800 nm, at the first minimum it would be 1600 nm. The PED deposition was hence stopped when the pyrometer indicated the temperature interference caused the first minimum, as shown in Figure 5.2. Then, the thickness of CIGS film was exactly 1.6 μm as confirmed by SEM cross-section images.

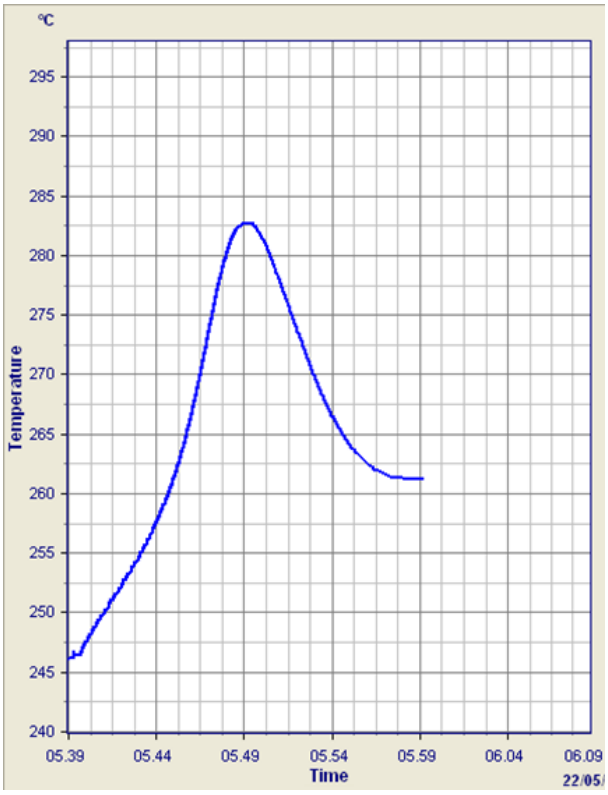


*Figure 5.2 – Interference fringes of a CIGS film grown onto Mo substrate by means of LTPED. The deposition was stopped at the first minimum, i.e. at CGS thickness of 1.6 μm.*

During the deposition, thermography measurements were carried out by means of a FLIR Thermocamera T450SC. Two-dimensional images were used to determine the temperature variation of a wide area of the sample, in real time. The thickness of different sample region can be investigated at the same time during the deposition, and it is possible to determine temperature gradients through thermal mapping prior of the deposition. Two example of thickness determination by means of IR camera are shown in Figure 5.3.

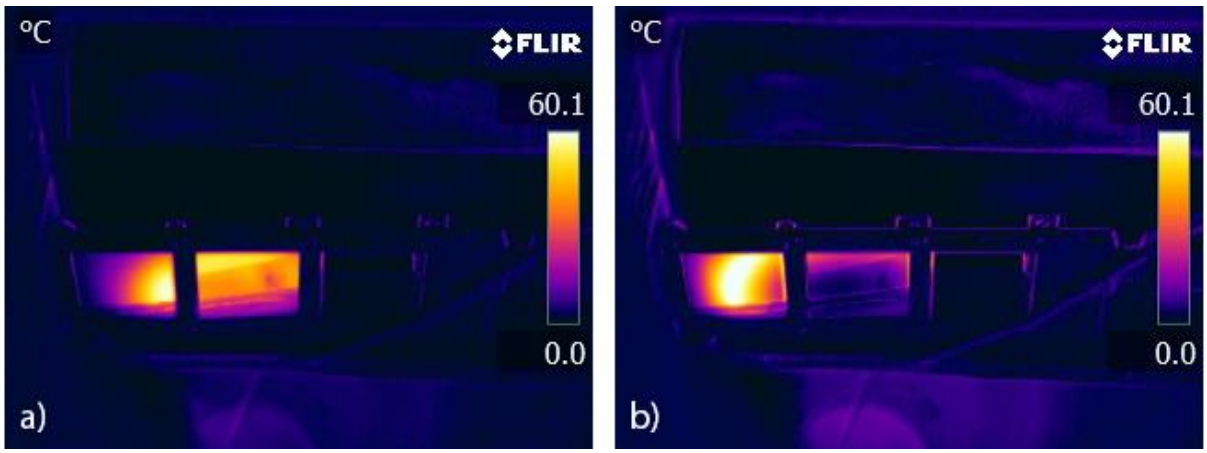


*Figure 5.3 – Substrate temperature variation during CIGS deposition. Two samples are loaded on the holder, one in the left slot, one in the central one. The deposition is centred on the central sample. Temperature variation due to interference can be observed in both the images. The highest temperature corresponds to the maximum interference, so a thickness of 80 0nm, and the lowest temperature indicates the minimum interference, i.e. no material deposited or 1600nm-thick CIGS. Image a) was taken just after the maximum interference onto the centre of the central sample, while image b) was shot at the end of the deposition. In the latter image, the central sample has a uniform thickness distribution, while the left sample has huge thickness variation from one side to other.*

### 5.2.1. Effects of PED voltage on CIGS films

For CGS, the ablation mechanism became dominant with respect to the thermal evaporation one over the accelerating voltage of 11.5 kV, since the ablated mass was proportional to the square of the accelerating voltage, as shown by Figure 5.4.

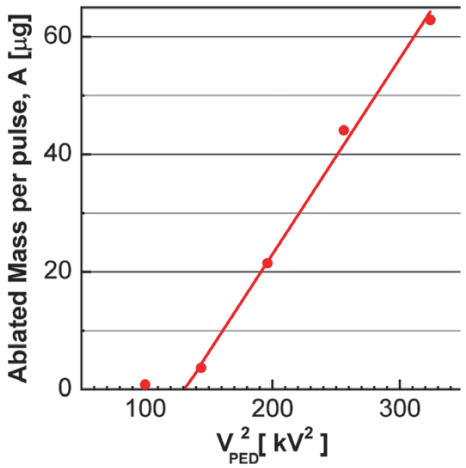


*Figure 5.4 – Trend of ablated mass from a single pulse on CGS target as a function of the PED voltage squared. (52)*

At 11.5kV, the Neocera-PEBS-20 electron source produced electron beams with current density of ~1· $10^4$ A/cm$^2$ and a duration of about 200ns. The resulting power density of each beam of ~1· $10^8$ W/cm$^2$ can be considered the ablation threshold for CGS. Actually, incongruent evaporation took place even increasing the voltage above 11.5 kV due to the heating of the target, but its contribution was lower and lower.

Accelerating voltage of 16 kV has been found to be the best compromise between optimal CIGS composition and optimal film morphology. As shown by Figure 5.5, higher voltage causes increased number and size of the droplets due to macroscopic ablation, while lower ones give rise to a flatter film but with bad stoichiometry.

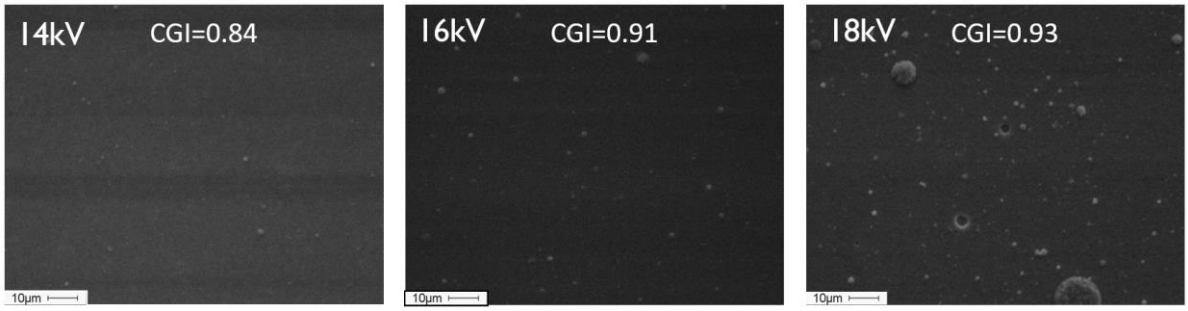


*Figure 5.5 – Surface morphology and CGI variation of CIGS samples grown at different PED voltage from the same target.*

Average lattice parameter of CGS was in good agreement with Cu/Ga ratio, as a function of the accelerating voltage (as shown in Figure 5.6), meaning the ablation was becoming predominant above 14 kV.

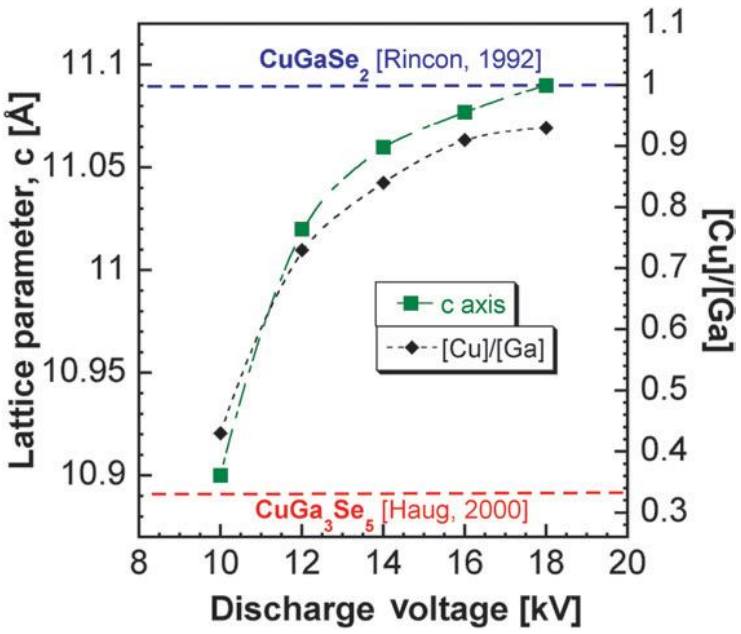


*Figure 5.6 – Lattice parameter c (green squares) and Cu/Ga ratio (black diamonds) of CIGS grown at 300 °C in function of PED acceleration voltage. (52)*

### 5.2.2. Angular distribution

Working at 16 kV, about 8500 PED-pulses were necessary to grow CIGS film with a thickness of 1600 nm. At a pulse rate of 9 Hz, the absorber deposition over a 1"×1" area was performed in roughly 16min when using one electron source. In this condition, the bi-cosine angular distribution of Comsa-David model was found to have a coefficient $p$=3.8, thus resulting in:

$$F(\theta) = 0.03 \cdot \cos(\theta) + 0.97 \cdot \cos^{3.8}(\theta)$$

The CIGS thickness variation is plotted in Figure 5.7 and, over 2.5cm-wide sample, it was lower than 8% at the edge of the substrate.

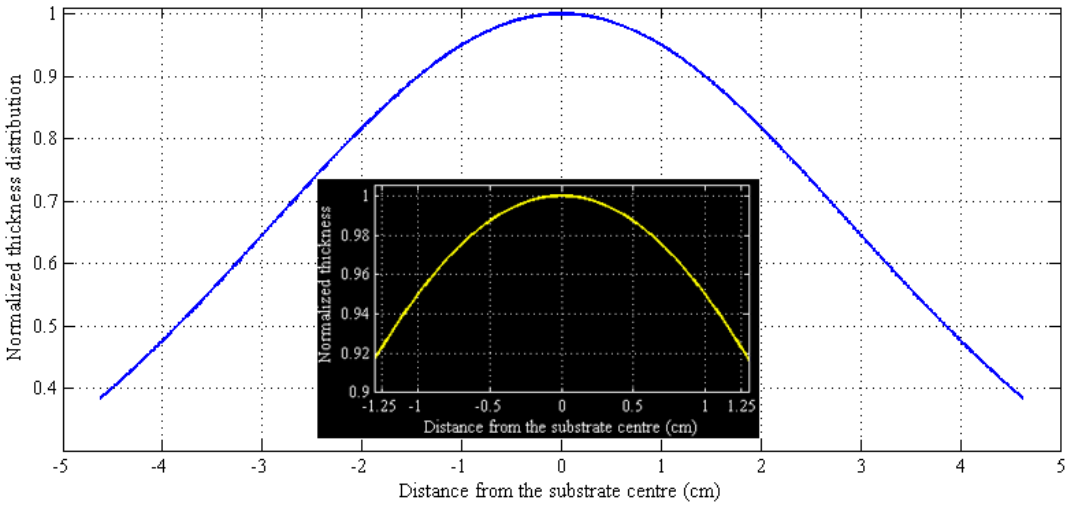


*Figure 5.7 – Thickness distribution of CIGS grown by PED at 16kV and 300°C. The black insertion is a zoomed part around position zero representing the standard sample width of 2.5cm.*

The contribution of incongruent evaporation $f$ to the deposited mass was determined to be 0.069 of the deposited film. This estimated value agreed with EDS-SEM measurements, which revealed a mole fraction of the odd or OVC phase, $CuGa_3Se_5$, of about 0.07. Thereby, CGS films grown at 300 °C by PED at 16 kV and 9 Hz had the chemical formula: $CuGa_3Se_5 + 14CuGaSe_2$.

Remarkably, the parameter $p$ is almost constant at ~4 for accelerating voltage > 12 kV. The plasma velocity of the PED process was determined from $p \approx 4$ and considering $\gamma = C_P/C_V = 1.67$ for a monoatomic gas resulting in a Mach number $M \approx 1$, in agreement with the formation of the Knudsen Layer in the ablation process. Thus, for CGS the plasma expansion velocity is limited to the plasma speed of sound for PED voltages > 12 kV. (52)

### 5.2.3. Effects of substrate temperature

During the PED ablation at 16 kV, the CIGS target is heated up to 300 °C (measured by pyrometer) thus leading to unavoidable incongruent evaporation. For CIGS grown by PED with substrate at room temperature, the film composition was extremely different than the target one, meaning the evaporation

at the thermodynamic equilibrium played a central role. In fact, the film was richer in volatile elements, mainly Se but even Ga and In, and highly Cu-poor (CGI≈0.60). Increasing the substrate temperature, a re-evaporation of the more volatile elements from the film compensated the stoichiometry variation due to incongruent evaporation from the target. For growth temperature of 250°C-300°C, the CIGS film had the optimal composition for solar cells: slightly Cu-poor (CGI≈0.90), Se content near to 50% and the same GGI as the target.

The energy of the plasma generated by the electron beam ablation of CIGS targets is of the order of 1–10 eV and may cause the formation of crystalline films even when the substrate is at room temperature. X-ray diffraction measurements showed that CIGS deposited directly on glass at room temperature exhibited an amorphous phase, mainly due to a large presence of selenium which segregated at the grain boundaries. Just above the room temperature, CIGS crystallized in tetragonal phase with prevalent crystalline orientation along (220). Then CIGS preferential orientation strongly depended on the growth temperature. Increasing the substrate temperature, the density of (112) grains increase until this orientation prevailed over the (220) one. The crossover temperature appeared to increase with the Ga content of CIGS, being lower than 270 °C at GGI=0.30 and about 450 °C at GGI=1. The size of the grains may vary from tens of nm at room temperature to 1–2 μm above 400 °C. The solar cell efficiency does not seem correlated with either the relative density of (220) and (112) grains or the size of the grains. XRD measurements of CIGS with GGI=0.30 at different growth temperature are shown in Figure 5.8. (45) (53)

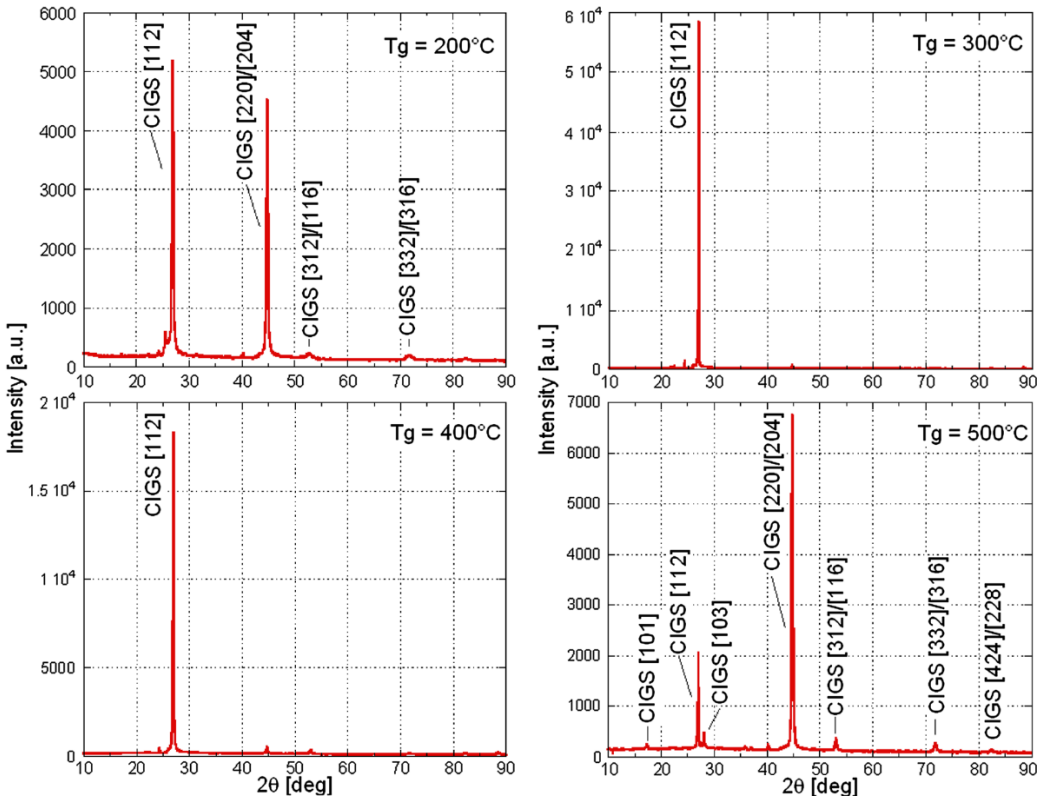


*Figure 5.8 – θ/2θ XR diffraction patterns of CIGS films grown by PED on soda lime glass at different substrate temperature $T_g$ from 200 °C and 500 °C. (45)*

Selenium re-evaporation is the most critical effect which makes single stage CIGS deposition so difficult to obtain with techniques requiring high deposition temperatures. The metallic selenium melting point is about 220 °C and its vapour pressure is 4 mbar at 300 °C and reaches about 70 mbar at 500 °C. Thanks to the good crystalline quality obtained even below the selenium evaporation temperature, LTPED can minimise the problem of selenium depletion from the deposited film. In fact, 15% to 17% efficient basic solar cells were obtained with substrate temperatures between 250 °C and 270 °C. At temperature higher than 300 °C, the effects of selenium depletion can be clearly seen in the J-V curves of basic solar cells, as in the example shown in Figure 5.9 deposited at 500 °C. Se-poor interface is well known to affect the solar cells behaviour, causing a roll-over effect that lowers FF and $V_{oc}$. (54)

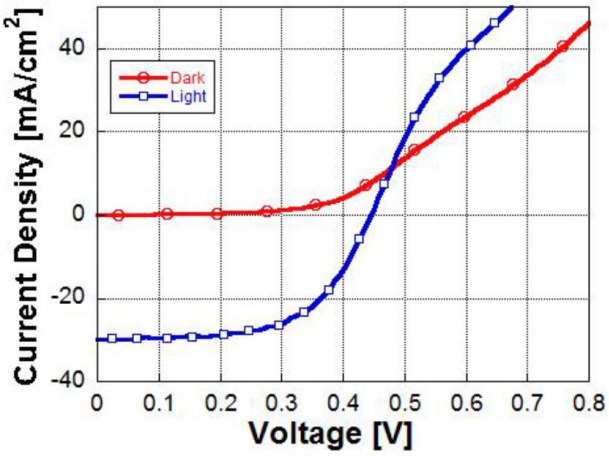


*Figure 5.9 – Dark (red circles and line) and illuminated (blue squares and line) characteristics of a CIGS solar cell where the absorber layer is deposited at 500°C. The corresponding cell parameters are: Voc=444 mV, FF=58.6%, Jsc=30.1 mA/cm2, η=7.8% (55)*

The re-evaporation of Se from the CIGS interface layer at high temperature and its correlation with the roll-over effect were confirmed by photo-luminescence (PL) emission, Figure 5.10. Low-temperature PL investigations of devices with CIGS grown by PED at high ($D_1$, red curve) and low ($D_2$, blue curve) temperature showed different emissions:

- CIGS absorber grown at 500 °C had a broad emission spectrum, at which several defect states were contributing. The one at about 80 meV from the band edge (~1.15 eV) was attributed to Se depletion (56). The other main emission may be due to the deep donor defect related to In and Cu, which is expected to be at about 250 meV below the conduction band of CIGS (56).
- CIGS absorber grown at 250 °C showed a single emission band, thus marking a point for the good interplay between low growth-temperature and sodium doping, which hinders the formation of $In_{Cu}^{2+}$.

As a result, the efficiency of solar cells with CIGS grown 250 °C were not affected by the roll-over problem, while the ones with CIGS grown at 500 °C were. For this reason, both FF and $V_{oc}$ were increased at 250 °C if compared to 500 °C, resulting in higher efficiency: fill factor from ~55% to >70% and open-circuit voltage from ~450 mV to > 600 mV.

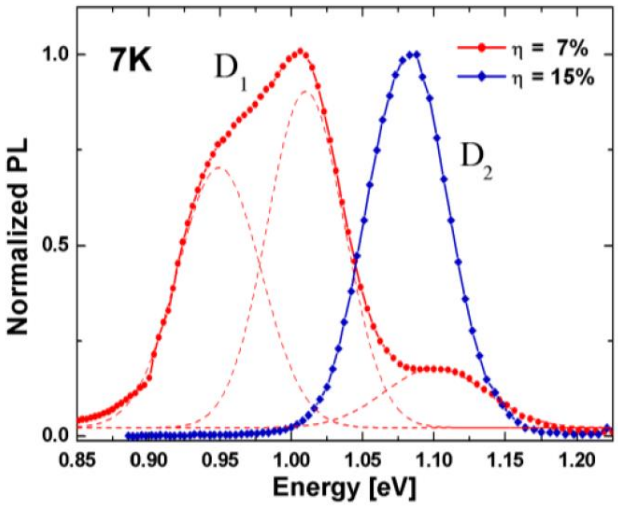


*Figure 5.10 – Low temperature (7K) photoluminescence spectra of two CIGS samples grown by PED with different substrate temperature: $D_1$ (red dots and curve) was deposited at 500 °C, $D_2$ (blue dots and curve) at 270 °C (LTPED).*

To avoid Se re-evaporation and hence high density of Se vacancies at the absorber-buffer interface, the annealing treatment which followed the CIGS deposition was usually carried out at the same temperature used for the growth (250°C<$T_g$<300°C). The duration of this thermal process was found to highly affect the solar cells behaviour in all its parameters (voltage, current, FF), as shown in Figure 5.11, and is believed to be correlated with the very slow Na diffusion from the precursor layer. Thus, long annealing time should be applied to compensate the low temperature: best conditions were found for annealing of 80 min.

SIMS analyses confirmed the sodium profile inside the CIGS was not flat even after annealing lasting 80 min (Figure 5.12, red curve). A larger Na content was found in the first CIGS region close to the Mo, i.e. where NaF layer was deposited and sodium diffused from.

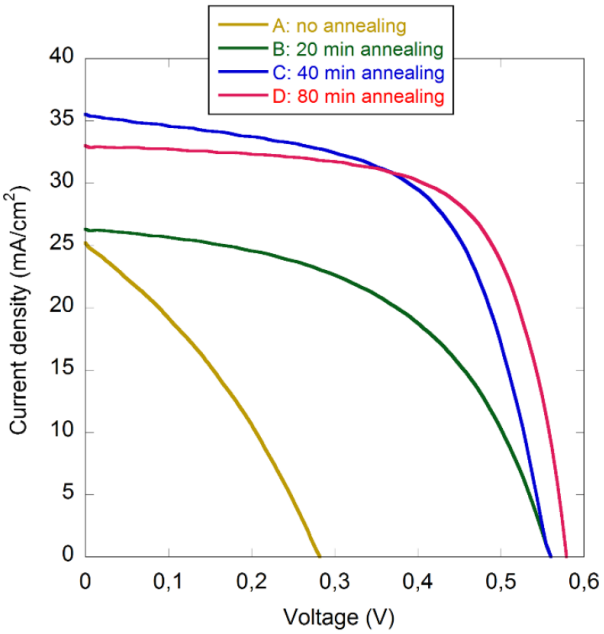


*Figure 5.11 – JV measurements of solar cells as a function of the absorber annealing time. (57)*

### 5.2.4. CIGS composition profile

SIMS analyses (Figure 5.12) demonstrated no variation of CGI or GGI was performed during the CIGS deposition of standard devices: Cu, In and Ga had a flat profile along the growth axis. It is in agreement with a constant evaporation rate from the target and a constant re-evaporation rate from the substrate. No Ga gradient in the CIGS film can be realized on purpose without changing the substrate temperature, but this will affect even the CGI, or switching from target to target with different Ga content during the deposition. By this latter strategy, it would be possible to obtain a CIGS absorber with a variable GGI along the growth axis to increase the solar cells performance.

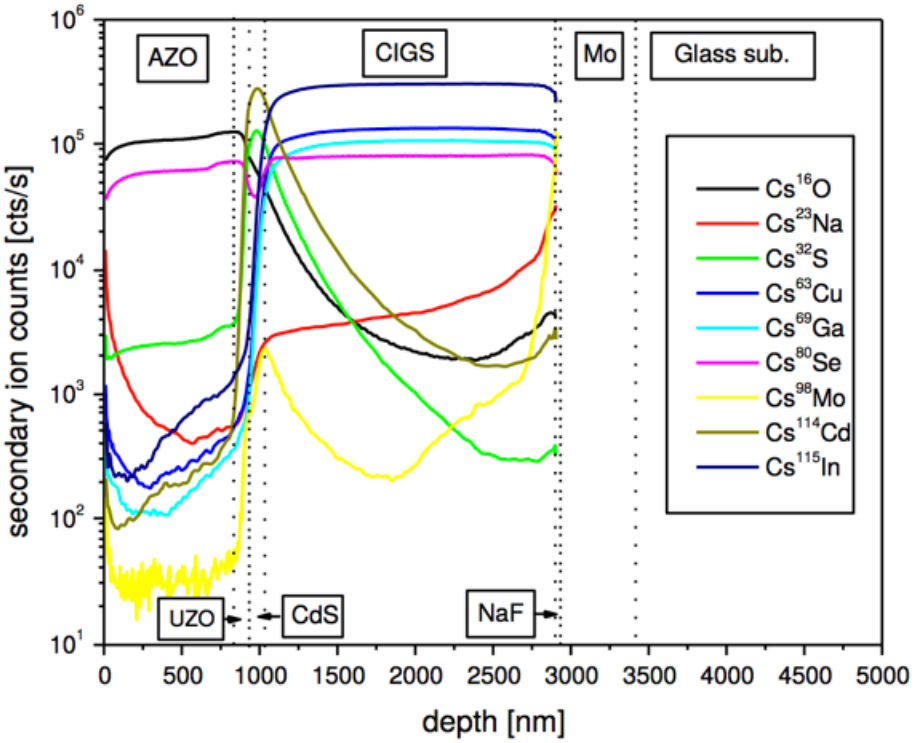


*Figure 5.12 – SIMS analysis of a standard solar cells from IMEM-CNR of Parma. The CIGS was grown by PED at the acceleration voltage of 16 kV, with a substrate temperature 270 °C, and after underwent an annealing treatment at 270 °C for 80 min.*

### 5.2.5. Electrical properties of LTPED-grown CIGS

CIGS thin films are very resistive and Hall Effect measurements were very complicated. Thus, it was not possible to measure the electron mobility of the absorber material. The electrical resistivity was measured by means of Van der Pauw technique with 4-points probe, and the free carrier density of CIGS films could be estimated by considering a mobility of 10 $cm^2/Vs$. CIGS resistivity was found to be directly correlated to the NaF thickness, ranging from $4x10^3$ Ωcm to 2 Ωcm, and its free carrier density was thus estimated to vary from $1.5 \cdot 10^{14}$ $cm^{-3}$ to $3 \cdot 10^{17}$ $cm^{-3}$. These values are not highly reliable since there are not certain data about the hole mobility in CIGS. The increase of the Ga content was observed to significantly enhance the resistivity and lower the free carrier density. The higher concentration of

Cu vacancies into CIGS than CGS may be the reason of the improved doping in CIGS, since these defects are the main diffusion sites for Na. (57) (58)

The best way to investigate the free carrier density of CIGS was found to be capacitance-voltage measurements. Solar cells were completed with the structure presented in section 5.3. The electrical properties of LTPED-grown CIGS solar cells were comparable to the state-of-the-art results published in the literature (59). Figure 5.13 (left) shows the CV plot at 120 K and 300 K of a representative solar cell based on LTPED-grown CIGS at 250 °C. From the minimum of the typical u-shaped curve at 120K (60) a rough estimation of the CIGS free carrier concentration was found to be of the order of $10^{15}cm^{-3}$.

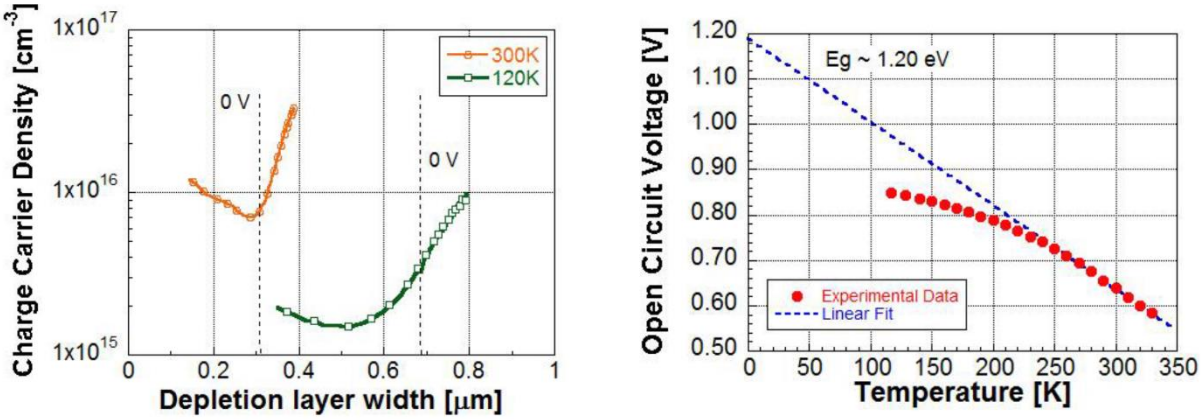


*Figure 5.13 – Left: capacitance-voltage profile of a representative solar cell with CIGS grown by LTPED, measured at 300 K and 120 K. The test signal frequency is 1 MHz. (55) Right: Temperature dependence of $V_{oc}$ of a typical CIGS solar cell fabricated by LTPED. The extrapolated value of $V_{oc}$ at 0 K corresponds to $E_g/q$, where $E_g$ is the absorber bandgap and q the electron charge.*

The cell ideality factors, obtained from the dark I-V curves at room temperature, are typically around 1.5–1.6 indicating that the dark current is dominated by SRH recombination in the space charge region (61). The open circuit voltage as function of temperature for a typical cell is shown in Figure 5.13 (right), together with a linear fit performed in the linear temperature regime of 230K–330K. The T=0 K intercept of this fit is close to 1.2 V, indicating an energy barrier for recombination of approximately 1.2 eV. As this value is near to the bandgap-energy of the CIGS absorber, the obtained result indicates that recombination in the bulk of the absorber is the dominant recombination mechanism. (55)

## 5.3. PED-CIGS solar cells architecture

In this thesis, the structure of devices based on CIGS grown by LTPED were changed in function of the study carried out. The classic CIGS-based solar cell structure is shown in Figure 5.14.

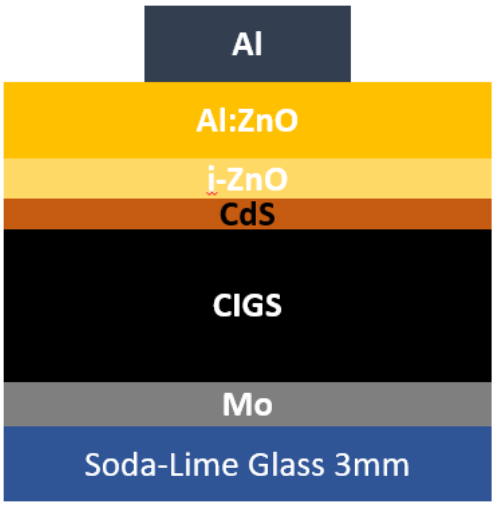


*Figure 5.14 – Classic structure of a solar cell based on CIGS.*

Here, the materials stacked up in typical architecture are described, along with their deposition processes. This classic structure is used to fabricate the present LTPED record solar cell and for the combinatorial PED study.

Architecture variations are performed to realize bifacial solar cells and Cd-free devices. The characteristics and deposition methods of TCOs as back contact and Zn(O,S) buffer layer are described in chapter 6. and chapter 7. , respectively.

### 5.3.1. Substrate and back contact

The substrates were commercial 2mm-thick 2.5cm×2.5cm (6.25 $cm^2$) soda-lime glass, covered with $Si_3N_4$ and Mo, supplied by Singulus Technologies. $Si_3N_4$ had a thickness of 100 nm and acted as blocking layer to avoid sodium diffusion from the glass into the CIGS, thereby the sodium content was controlled by the NaF precursor layer only. Mo layer is 700nm-thick deposited by sputtering and was the back contact of the solar cells, with a sheet resistance of 35 μΩ/sq.

For the TCO study of chapter 6. , Al:ZnO and ITO by RF-Magnetron sputtering on SLG and commercial FTO on SLG were used as back contact.

In the study about the alternative buffer layer, for co-evaporated CIGS only, Mo back contact was DC-sputtered onto SLG.

### 5.3.2. Sodium precursor

The low temperature of PED process was found to start an uncontrolled and non-optimized Na migration from the SLG substrate, through the Mo back contact, into CIGS. Therefore, to control the supply of sodium to the absorber, NaF was deposited by PED directly onto the back contact, immediately before the CIGS deposition. The NaF thickness determined the amount of sodium incorporated in the CIGS. A $Si_3N_4$ diffusion barrier was introduced between SLG and Mo to avoid any glass contribution.

NaF was deposited on Mo using PED voltage of 14 kV with a repetition rate of 10Hz, at an Ar pressure of $5 \cdot 10^{-3}$ mbar. The substrate temperature was kept at 80 °C and the distance target-substrate is the same as CIGS: 8 cm. Target cleaning was performed shooting 2k pulses before the deposition, the substrate still parked in the load lock. From time to time, a thickness calibration was carried out to determine any variation in the NaF deposition rate, mainly due to the target getting thinner: 5k pulses were shot on glass and the film thickness was measured by profilometer. The NaF deposition rate was about 0.02 nm/pulse. A calibrated thickness of 8-10 nm was then deposited onto Mo in a few hundreds of pulses.

The low temperature of Mo substrate during the CIGS deposition does not allow the formation of $MoSe_2$ compound between CIGS and Mo, as SIMS analyses of Figure 5.12 confirmed: no peak of Se signal (pinkish curve) was observed close to the Mo layer. The interface CIGS/Mo is known to be a Schottky barrier to holes, whose large height affects both FF and $V_{oc}$ of the solar cells. Then, $MoSe_2$ layer is very important because it attenuates the band distortion at the interface lowering the barrier height, hence forming a quasi-ohmic contact which minimizes the losses. (62) (63) (64) In PED deposition of CIGS, a new route to obtain an ohmic contact must be applied. The deposition of NaF prior to the CIGS growth was found to be a good alternative to the $MoSe_2$ layer. To investigate the electrical behaviour of CIGS/Mo back-contact, Au/CIGS/Mo and Au/CIGS/NaF/Mo structures on glass substrates were prepared. The Au/CIGS contacts were used to ensure a sufficient ohmic characteristics of the top contact (65) and to allow the detection of the resistivity changes at the back contact. The measured JV curves of both structures are reported in Figure 5.15 and clearly show the transition from rectifying to ohmic behaviour when introducing the NaF layer. These results explained why series resistances as low as 0.2 $\Omega/cm^2$ can be achieved in solar cells grown at substrate temperatures as low as 250 °C, in the presence of a NaF buffer layer on top of the Mo back-contact. Coupled to the poor sodium diffusion due to the low temperature, the NaF layer provides a high sodium content into the first CIGS region, increasing the free-hole density therein. The proposed mechanism supposes that the high doping of CIGS can thin the barrier enough to be tunnelled by carriers. This could be the reason why good device quality (as shown in the next sections of this chapter) could be obtained with the LTPED growth of CIGS on Mo, even if $MoSe_2$ is not formed.

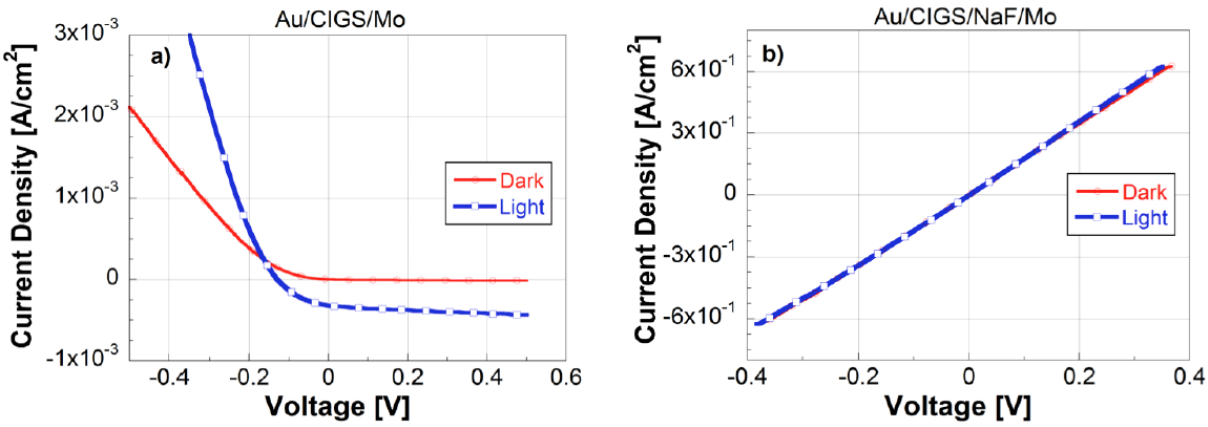


*Figure 5.15 – Current density vs voltage behaviour of a) Au/CIGS/Mo structure and b) Au/CIGS/NaF/Mo one. The introduction of the sodium precursor layer(NaF) turned the CIGS/Mo rectifing junction into ohmic contact, for both dark (red curve) and illuminated line (blue curve). (55)*

If the low substrate temperature is not a problem for the formation of the back ohmic contact, sodium diffusion into the CIGS film at 250 °C is much less effective compared to CIGS cells grown and annealed at temperatures as high as 600 °C. Increasing the thickness of the NaF buffer layer to enhance Na diffusion is not an option as CIGS adhesion on Mo is compromised by a NaF thickness exceeding a critical value of about 30 nm. In the case of the basic CIGS solar cells, the CIGS film thickness was limited to 1.6 μm even to ensure an optimum sodium diffusion through the whole absorber, for 8-10 nm of NaF. Alternative solutions were explored at IMEM-CNR to incorporate Na or to tune its diffusion profile and extend the diffusion range, without exceeding the critical Na concentration in CIGS:

- providing NaF after the CIGS deposition has resulted in a poor contact between Mo and CIGS and might even cause a high doping of CIGS in the space-charge region, which lowers the SCR extension.
- NaF inclusion into the CIGS target was a good solution to ablate both the materials at the same time and to build a flat sodium profile inside the CIGS, but had been found to result in bad target homogeneity: NaF phases has separated from CIGS and the evaporating ratio of the two materials was completely random.
- Introducing sodium into the middle of CIGS had caused both bad contacts towards Mo and huge problems to mechanical stability of CIGS: an incomplete NaF diffusion had probably resulted in great quantity of sodium at the grain boundary, that later caused the peel off. The thickness limit for NaF layer included into CIGS film must be very thin not to cause grains disaggregation.
- A more elegant approach to overcome the poor Na diffusion can be the deposition of a NaF/CIGS multilayer structure by PED, maintaining low temperatures and avoiding long-time annealing process. Its aim is to create a sodium profile providing NaF where it is necessary and taking advantage of the low diffusion to have different content inside CIGS in function of the depth. Preliminary study confirmed that alternating nano-layer of NaF at the CIGS deposition provides an easy way to carefully control the Na content and gradient along the CIGS-growth

direction at temperature as low as 250 °C. Of course, the NaF layers thickness, the distance between them, their number and their position inside CIGS are the parameters to be adjusted to create a Na gradient. This Na gradient could be useful to select the doping of CIGS as a function of the depth from the surface and the width of the space charge region. We believe it is a fundamental step for the optimization of high-quality and large-area thin-film solar cells based on CIGS by PED. This strategy is currently being developed at IMEM-CNR of Parma. (66)

### 5.3.3. CIGS absorber

The CIGS absorber is grown by the single-stage LTPED process with the set-up described in section 5.1 and the deposition parameters described in section 5.2.

### 5.3.4. Buffer layer

CdS by chemical bath deposition was used as buffer layer for the solar cell of this chapter and for the study about back contacts made by TCOs. Reference solar cells of Zn(O,S) series were buffered with CdS as well.

CdS grown by CBD has great inclusion of oxygen and hydroxide groups (up to 10% of overall atoms), so the buffer material actually is Cd(S,O,OH). Other impurities like C and N are present in the lattice due to reaction by-products. Both the amount of this impurities and the morphology of CdS depends on the deposition condition: temperature, precursor compounds and their ratio, CIGS surface, and so on. Post deposition treatment of CIGS with KF nucleates a more uniform film of CdS, thus increasing the $V_{oc}$ and allowing to thin the buffer for a slight enhancement of $J_{sc}$. In the present thesis, no KF treatment was applied.

CdS was grown by an in-house CBD process. Stock aqueous solution of 0.1 M cadmium chloride ($CdCl_2$), 0.1 M thiourea ($CS(NH_2)_2$) and 16.8 M ammonia ($NH_3$) were stored in tightly closed bottom. The freshly-grown CIGS sample was introduced into a 100-ml flat-bottom borosilicate-glass beaker containing a room-temperature solution of bi-distilled water (43 ml) and ammonia (15.4 ml) having pH=12, for 5 minutes. Later, the two chemical precursors for CdS deposition were added, still at RT: first $CdCl_2$ (1.4 ml) followed by thiourea (20 ml) after 2 minutes, with a concentration ratio of about 1:14. Then, the beaker containing sample and solution was introduced in the hot bath at 80 °C to start the CBD process. The beaker was magnetically stirred and after 10 min, the sample was extracted from the solution and the procedure was repeated with a fresh solution. At the end of the second stage, a 90-100nm-thick film of CdS was grown.

The reaction steps are illustrated in Figure 5.16. As soon as the CIGS sample was exposed to air, it was introduced into the ammonia solution with pH=12 for 5 min at room temperature. $NH_3$ is believed to "clean" the CIGS surface from $CO_2$ deposition and from oxidation occurred during the unavoidable air exposure. Later $CdCl_2$ was introduced in the solution to start the formation of Cd-ammine ion complexes

onto the CIGS surface, which are essential for the CdS nucleation. After 1 min, the solution was putted into the hot bath at 80 °C and thiourea was added. $S^{2-}$ ions are created by the interaction of thiourea with $OH^-$ of the solution and when the temperature is risen enough, CdS is formed at a $Cd^{2+}$:$S^{2-}$ ratio of 1:2. The nucleation started with islands and their growth brings to the film formation. After about 10 min, the CdS layer was not yet fully covering but big clusters were formed inside the solution and floated on the surface. Their dimension was not comparable to CdS buffer thickness, thereby the sample was extracted from the solution to avoid their inclusion in the film and very-bad buffer morphology. A second deposition with the same parameters was then carried out to obtain a fully covering layer with a thickness of about 90nm. The sample was cleaned with de-ionized water and dried by means of Ar flow.

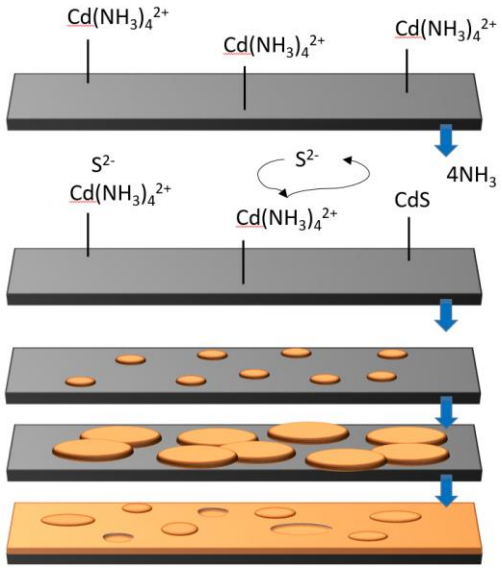


*Figure 5.16 – Growth mechanism of chemical bath deposited CdS (orange) over CIGS (dark grey substrate).*

Thickness of 90nm-100nm were found to be the optimal compromise between light absorption and shunt resistance. Lower thickness caused more shunted solar cells, so FF loss. Thicker film indeed enhanced the light absorption of the buffer, hence decreasing the $J_{sc}$.

### 5.3.5. TCO

The shunt-preventing layer of the solar cells was made by ~100 nm of i-ZnO, while roughly-800nm-thick film of Al-doped ZnO was the front transparent contact of the devices. They were deposited by means of RF-Magnetron sputtering, using cathode fabricated by Angstrom Science. Commercial targets by Testbourne Ltd. were used, produced by Hot Isostatic Press, 0.5cm-thick and with a diameter of 2". Al:ZnO (AZO) target composition was 98%ZnO-2%$Al_2O_3$ in weight.

Before each deposition, whether i-ZnO or AZO, the chamber was previously pumped down to at least $5 \cdot 10^{-6}$ mbar by means of a turbopump and then Ar was introduced as process gas. The targets underwent a cleaning process before the growth, avoiding deposition onto the sample by means of a shutter. Once the cleaning was over (roughly 20 min at different power and pressure), the shutter was opened to start

the deposition. Series to optimize i-ZnO and AZO layers were conducted, in function of distance, sputtering power, Ar pressure and temperature. RT depositions were preferred to avoid element inter-diffusion at the interfaces which were detrimental for the device behaviour. The best growth conditions are shown in Table 5.1:

*Table 5.1- Deposition parameters for RF-Magnetron sputtering of i-ZnO and AZO.*

| Material | Distance (cm) | Power (W) / Power density ($W/cm^2$) | Pressure (mbar) | Deposition Temperature | Deposition Rate (nm/min) |
|---|---|---|---|---|---|
| **i-ZnO** | 8 | 100 / ~5 | $5 \cdot 10^{-3}$ | RT | 15.4 |
| **AZO** | 8 | 120 / ~6 | $5 \cdot 10^{-3}$ | RT | 32.0 |

With these settings, the materials were adjusted for the solar cells, both in terms of electrical properties and optical ones. The intrinsic ZnO layer was very resistive, $R_{sheet} > 2 \cdot 10^6$ Ω/sq. The AZO resistivity was strongly decreased heating the substrate up to 250 °C, but the solar cells suffered of great FF and $V_{oc}$ drops when heated, so TCO sputtering depositions were performed at room temperature. The best results for AZO deposition at RT by sputtering ($R_{sheet}$=10-22 Ω/sq for a thickness of 890 nm, transmittance) are shown in section 5.4.1, along with a comparison with AZO grown by PED.

Unfortunately, in the middle of the PhD project, following to a failure of the cooling system, the cathode overheated and the magnetic field was modified. The new deposition condition resulted in a bad film properties at the centre of the deposition: more resistive Al-ZnO film and highly-stressed i-ZnO, which often ended up in cracks and film crumbling. Thus, from then, the sputtering growths of both materials were carried out in off-axis configuration. Off-axis deposition with the sample centre shifted 2.5 cm from the deposition centre allowed good conductive AZO and resistive i-ZnO without structural problems. Of course, because of the off-axis position, the film thickness was not homogeneous on the surface: the deposition angle from the axis changed from 8.5° on one side of the sample to 25.5° on the other side. As a result, the AZO thickness over the sample varied from 850 nm to 700 nm and its sheet resistance from 45 Ω/sq to 25 Ω/sq (resistivity from $3.8 \cdot 10^{-3}$ Ωcm to $1.7 \cdot 10^{-3}$ Ωcm). The thickness variation of i-ZnO was from 100nm to 85nm, and no appreciable variation was observed in its resistivity. The average optical transmittance of the i-ZnO/AZO bilayer was 85±3%, significantly affected by reflectance due to the thickness of the total window layer (950nm-800nm). In this configuration, small variation in the solar cell behaviour were due to the bad uniformity of TCO thickness and sheet-resistance.

The samples with alternative buffer layer had TCO deposited by DC-sputtering, following another process as described in chapter 7.

### 5.3.6. Front contacts

Aluminium contacts were thermally evaporated onto the Al:ZnO in a specific chamber. Their thickness is 2 μm. Aluminium (5N) rods for a weight of 0.3 g were loaded in a Ta boat supplied with a DC power of about 400 W. Under these conditions, at a pressure $<5 \cdot 10^{-6}$ mbar, the rods are melted and Al starts to evaporate towards the sample, located at 10 cm from the boat crucible. The sample is placed under a metal shadow mask with different geometries; the most used one for this thesis were made by a circular dot, with a diameter of 1 mm, and one 3mm-long thin finger. The solar cells were then mechanically scribed in rectangular 0.5 $cm^2$, 0.1 $cm^2$ or 0.2 $cm^2$ area with the Al contact in the middle.

The samples with alternative buffer layer and co-evaporated CIGS (section 7.4) had contacts made by Ni/Al/Ni structure in fork geometry. This structure is aimed to reduce the contact resistance between the materials and to prevent Al oxidation, thus giving good and stable contacts over a long time.

Note that no antireflection coating was applied for any solar cells of this thesis.

## 5.4. Achievements in CIGS solar cells by LTPED

Throughout the PhD project, the best solar cell fabricated by means of LTPED showed an efficiency of 17.0%. This value was achieved on small area by means of a lab-scale process and without K-doping, intentional Ga grading and antireflection coating. We consider this result to be a crucial milestone along the path to the industrial scale-up of LTPED and it was published in (55).

Earlier top efficiency of LTPED solar cells was 15.2% ($V_{oc}$=584 mV, $J_{sc}$=37.5 mA/$cm^2$, FF=69.4%), as published in (67), demonstrating high-efficiency CIGS-based solar cells can be grown at low temperature in a single-stage process by means of PED. At that time, solar cells had been completed by means of CdS as buffer layer and 250nm-thick AZO by PED as TCO. A more performant TCO was necessary to improve the uniformity and to increase the efficiency.

### 5.4.1. TCO improvements

To improve the solar cells behaviour, the introduction of i-ZnO resistive layer and a more uniform AZO film were needed. During the PhD project, we performed a comparison of AZO features as a function of the deposition method, PED or RF-Magnetron Sputtering, which was published in (68).

AZO targets for PED were home-made starting from highly-pure commercial powders (Sigma Aldrich, 5N) of ZnO mixed with $Al_2O_3$ 2wt%. The mixture was finely grinded in a ball mill in iso-propanol and then pressed in a free-standing pellet of $2.8 \cdot 10^7$ Pa for 5 min at room temperature. Then, the targets were sintered at 1000 °C for 12 h. Eventually, the pellet (diameter of 40 mm and thickness of 2 mm) was polished to obtain smooth and uniform surface and glued with silver paste on a rotating target holder

inside the PED chamber. To ablate the target, PED acceleration voltage of 14 kV at a repetition rate of 10 Hz was used.

AZO deposition by RF-Magnetron sputtering is described at section 5.3.5.

The TCO-AZO by PED demonstrated lower resistivity than the sputtered one, especially at room temperature ($3.7 \cdot 10^{-4}$ Ωcm instead of $1.1 \cdot 10^{-3}$ Ωcm, for 550nm-thick film deposited on glass). Unfortunately, its uniformity was very poor: the film growth was strongly affected by macroscopic ablation process tacking place at the target surface, which deposited large droplets. From time to time, these particles were removed from the target because of their poor adhesion and merging to the film, causing pinholes: important shunts paths were randomly distributed on the surface. The morphology of PED-gown AZO was an insurmountable issue. Thereby, with PED-AZO, the device area allowing efficiency as high as 15.2% had just been a small part of the whole samples: roughly 0.15 $cm^2$ over ~5 $cm^2$. RF-Magnetron sputtering, instead, gave rise to very flat and uniform AZO film, thus more suitable for solar cells application. Morphology of AZO films grown by PED and sputtering are compared in Figure 5.17.

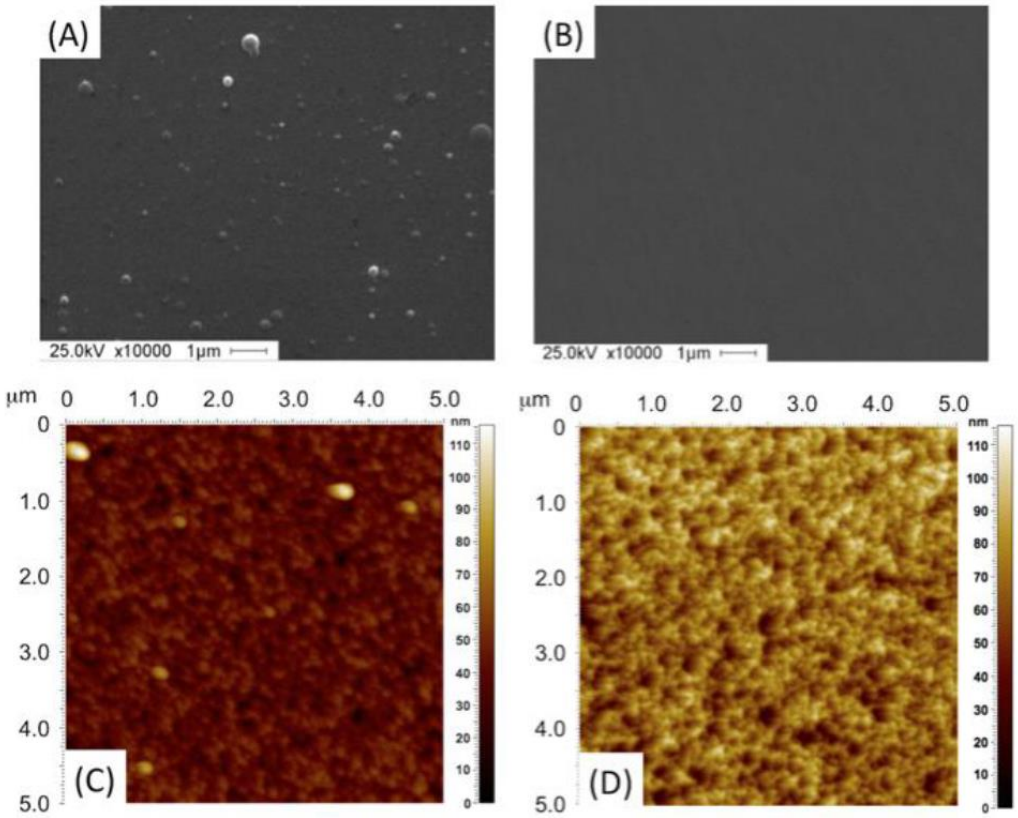


*Figure 5.17 - Surface images by SEM (top ones) and AFM (bottom ones) of 550nm-thick AZO film grown by PED (A and C) and RF-Magnetron sputtering (B and D). Large particles, with dimension comparable with the film thickness were observed in PED-grown CIGS.*

On the other hand, as shown in Table 5.2, to obtain the same resistivity as with PED, AZO by sputtering must be heated up to 250 °C during the growth. The grains of both the AZOs were mainly oriented along

the (002) direction, with a small (100) contribute which is higher in the PED-grown one. PED films showed higher transparency in the visible region than sputtered ones.

*Table 5.2 – Summary of physical properties of 550nm-thick AZO films grown by means of PED and sputtering techniques*

| Growth temperature (°C) | PED-grown AZO | | | Sputtering-grown AZO | | |
|---|---|---|---|---|---|---|
| | Resistivity (Ωcm) | Average Transmittance (%) | (002) texture coefficient (%) | Resistivity (Ωcm) | Average Transmittance (%) | (002) texture coefficient (%) |
| **RT** | $3.7 \cdot 10^{-4}$ | 100 | >90 | $1.1 \cdot 10^{-3}$ | 95 | 85 |
| **100** | $5.2 \cdot 10^{-4}$ | 100 | >90 | $6.1 \cdot 10^{-4}$ | 100 | 82 |
| **150** | $3.5 \cdot 10^{-4}$ | 100 | >90 | $5.8 \cdot 10^{-4}$ | 100 | 84 |
| **200** | $7.1 \cdot 10^{-4}$ | 99 | 88 | $3.9 \cdot 10^{-4}$ | 100 | 80 |
| **250** | $4.3 \cdot 10^{-3}$ | 100 | 83 | $3.7 \cdot 10^{-4}$ | 100 | 86 |

Having higher transparency and same resistivity actually means the PED-grown AZO had larger electron mobility and lower carrier density, thus absorbing less portion of the radiation with energy below the energy gap. Additionally, the rougher surface of PED-AZO, due to the large droplets presence, may partially reduce the light intensity reflected by the films.

The AZO deposition to complete the solar cell by both PED and RF-Magnetron sputtering was preferably performed at RT in order to avoid a detrimental inter-diffusion of chemical elements through the junction, in particular of Cd and Na. Solar cells based on PED-grown CIGS has extensively demonstrated to have huge drop in the performance if annealed or heated after the CdS deposition at temperatures above 100 °C.

According to Table 5.2, to obtain devices with an equivalent sheet resistance <15Ω/sq at room temperature, we reduced the thickness of PED-AZO to 250 nm and increased the one of Sputtered-AZO to 890 nm. The thicker AZO grown by Sputtering gave rise to much more refection than the PED one, whatever the growth temperature, due to the interference fringes as shown in Figure 5.18.

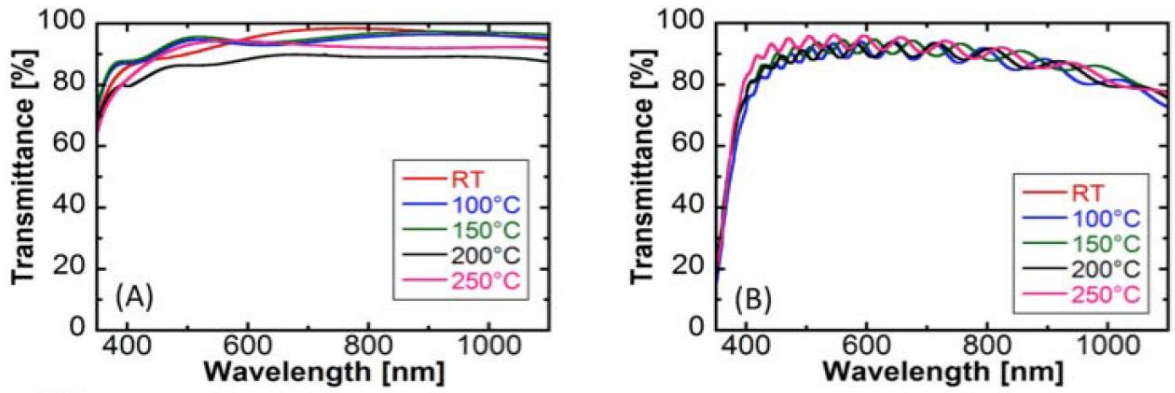


*Figure 5.18 - Transmittance spectra of a 250nm-thick AZO film grown by PED (A) and of an 890nm-thick AZO film grown by RF-Magnetron sputtering, at several substrate temperatures (B). The interference due to the thickness is more evident in B. PED-AZO had an absorption edge shifted at smaller wavelength, due to a slightly larger bandgap, and lower absorption in the IR region.*

AZO thickness and resistivity spatial variation onto the sample is shown in Figure 5.19. The sheet resistance was varying from 22 Ω/sq in the deposition centre to about 10 Ω/sq at 3 cm aside it.

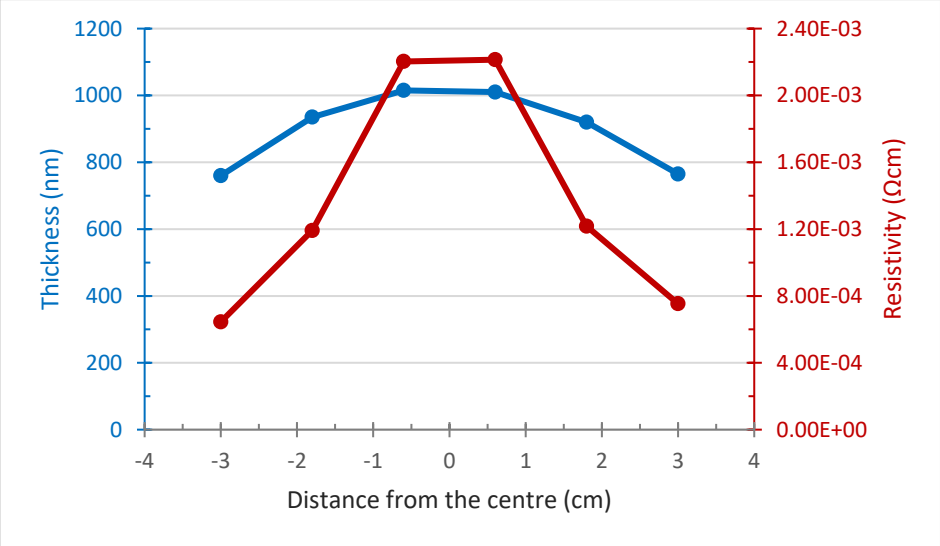


*Figure 5.19 - Thickness (blue dots and line) and resistivity (red ones) trends onto the glass substrate, as a function of the distance from the centre of the deposition. The AZO film was sputtered at 120 W for 30 min in Ar pressure of $5 \cdot 10^{-3}$ mbar.*

### 5.4.2. 17%-efficiency record device

Because of the good uniformity and morphology of AZO by RF-Magnetron Sputtering, we decided to apply this technique for the deposition of ZnO-based TCO. The choice led to a compromise since we wanted to increase the lateral uniformity, even if current-density loss was expected due to the reduced transmittance. However, the introduction of the intrinsic ZnO layer was essential to increase the FF of the devices. With the new i-ZnO/AZO bilayer grown by sputtering, it was possible to repetitively obtain solar cells based on LTPED-grown CIGS with FF above 70%, and up to 76%, over a larger area than before (almost the whole sample, 6 $cm^2$).

Other improvements were applied to the solar cells, such as a reduced NaF-layer thickness (from 30 nm to 4nm-8nm) and a longer annealing time (from 20 min to 80 min). We found out 8nm of NaF coupled with 80 min of annealing maximized the $V_{oc}$ and the FF. Probably, in this conditions the sodium profile inside CIGS optimized several absorber characteristics: the ohmic contact Mo/CIGS, the doping and grain-boundaries passivation and the width of the space charge region.

The best solar cells fabricated during this thesis showed efficiency of 17.0%: in Table 5.3 the improved solar cells are compared with the best previous results.

*Table 5.3 –Comparison between solar cells based on CIGS-GGI=30% grown by LTPED at 270°C-250°C, fabricated prior or during the PhD. Modification in the sodium precursor layer, annealing time and TCO structures allowed higher efficiency and improved uniformity. The current densities were determined on illuminated area of 0.20cm²-0.15cm².*

| | NaF thickn. (nm) | CIGS annealing time (min) | i-ZnO resistive layer | AZO as TCO by means of | $V_{oc}$ (mV) | $J_{sc}$ (mA/cm²) | FF (%) | η (%) | Ref |
|---|---|---|---|---|---|---|---|---|---|
| **Prior results** | 30 | 20 | NO | PED | 584 | 37.5 | 69.4 | 15.2 | (67) |
| **This PhD** | 8 | 80 | YES, by RF-Magnetr. Sputtering | RF-Magnetr. Sputtering | 674 | 33.6 | 75.2 | 17.0 | (55) |
| | Uniformity of 2.5cm×2.5cm: Std. Dev. | | | | 1.5% | 3.8% | 2.1% | 4.9% | |

As expected the current density of the new devices was lower, but the improvements of open-circuit voltage and fill factor were greater enough to rise the efficiency up to 17.0%. The $V_{oc}$ enhancement was surely due to a better sodium diffusion into the grain-boundaries close to the CIGS surface and to lower shunt behaviour thanks to the introduction of i-ZnO layer. The additional FF was a consequence of the new bi-layered i-ZnO/AZO TCO.

JV and EQE measurements of record devices fabricated during the PhD are shown in Figure 5.20. The CIGS had a GGI content of 0.30 (measured by SEM-EDX) and was grown with the same parameters as described in section 5.2. Light I-V curve was obtained under 1 sun illumination produced by a class-A solar simulator, which was also used for the collection of the QE spectrum in combination with a set of 16 narrow-band filters (FB350/1100-10, Thorlabs Inc., Newton, NJ, USA) and a silicon photodiode (Thorlabs FDS-1010-CAL) for the calibration.

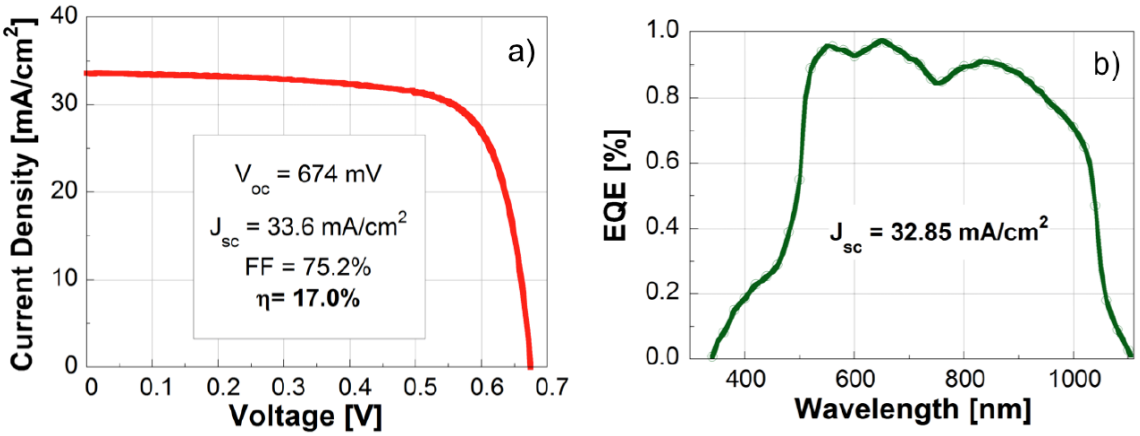


*Figure 5.20 – JV (a) and EQE (b) measurements of the record solar cells.*

SIMS analyses of the record devices (Figure 5.21) were performed revealing several absorber features:

- The thickness of the absorber layer is congruent with the expected one (1.8 μm).
- The sodium content (red line) in the CIGS, as expected, is not constant but has a bulge at the back contact. The Na content at the CIGS/Mo interface is almost one order of magnitude greater than in the bulk and decreases rapidly but with a sort of step, becoming constant after the first

600 nm of CIGS. The Na profile looks modified by the new NaF thickness and annealing duration with respect to the one of previous samples shown in Figure 5.12.

- The Se, In and Cu contents (pink, dark blue and blue curves) seem to slightly increase towards the CdS interface but they are almost flat in the bulk. The high Se content in the ZnO window layer is an artefact due the overlapping of the Zn and Se signal.
- The calculated CGI is almost constant along the whole growth axis (Figure 5.22, red line).
- Large amount of oxygen is detected inside the CIGS, gradually decreasing towards the Mo back contact and may be due to a memory effect caused by the erosion of the crater walls. Anyway, it was found to increase again in correspondence of the Mo surface, hint of a presence of molybdenum oxide, and its trend reveals a peak even at CIGS surface.
- The Ga/In ratio in the CIGS appears higher at the Mo interface than at the CdS interface: an unexpected grading was performed.

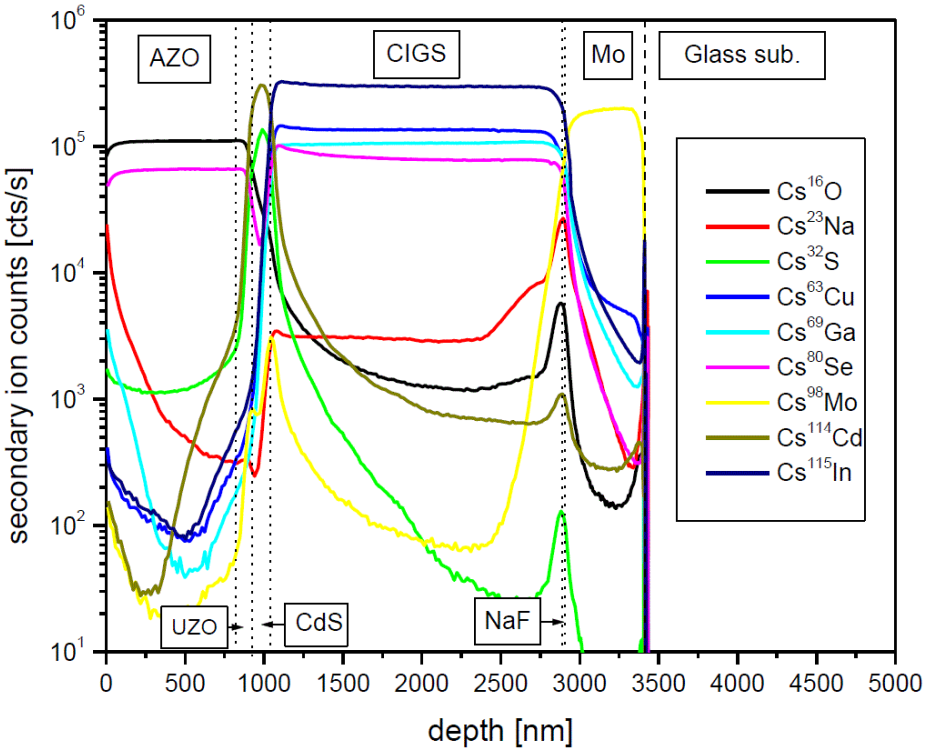


*Figure 5.21 - SIMS analysis of one of the record devices.*

As already said, this record device was fabricated with no intentional Ga grading along the CIGS growth axis. But from both SIMS and Raman analyses, a variation of the Ga content was found along the CIGS thickness. By means of SIMS, it is not possible to calculate the absolute Ga and In content, therefore it is not possible to determine the exact value of GGI. However, from the variation of the ratio between the Ga signal and the sum of Ga and In signals, the relative variation of GGI can be estimated. In Figure 5.22, GGI represents this signal ratio (blue line), while CGI is determined in the same way but for Cu content (red line). The GGI determined by Raman analyses is shown in Figure 5.23. Both the methods

revealed an increasing GGI moving towards the Mo back contact. The relative variation from the surface to the bottom of CIGS was ~17% for SIMS and ~20% for Raman. It was totally unintentional and therefore non-optimized: it is difficult to evaluate its influence on the device behaviour.

Moreover, SIMS and Raman analyses may be affected by errors that enlarged the degree of uncertainty. SIMS erosion from the crater wall and/or grains detachment may bring to memory effect which altered the data. Indeed, Raman shift is related to GGI by means of a model (see Appendix II - Solar-cells characterization methods): the constants of this model may not be the same for CIGS grown with different techniques, thus bringing to a systematic error. This may explain why Raman revealed GGI moving from 0.39 to 0.51 when SEM-EDS measurements revealed an average CIGS composition with GGI=0.300±0.005, the same as the target.

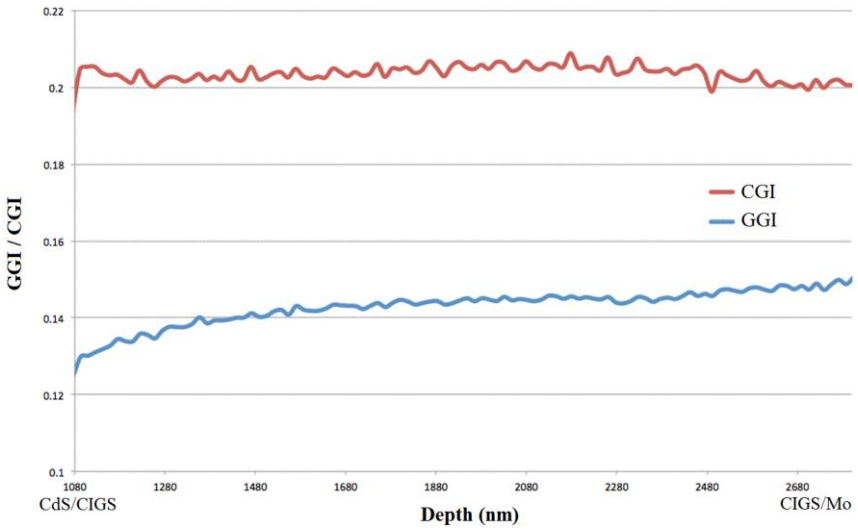


*Figure 5.22 - Here, CGI and GGI represents the ratio between Ga or Cu SIMS signal and the sum of Ga and In SIMS signals. Their variation along the CIGS thickness provides an indirect measurement of the GGI or CGI relative variation between the CIGS bottom (close to Mo) or front (close to CdS). CGI is almost constant, while GGI shows a 17% variation.*

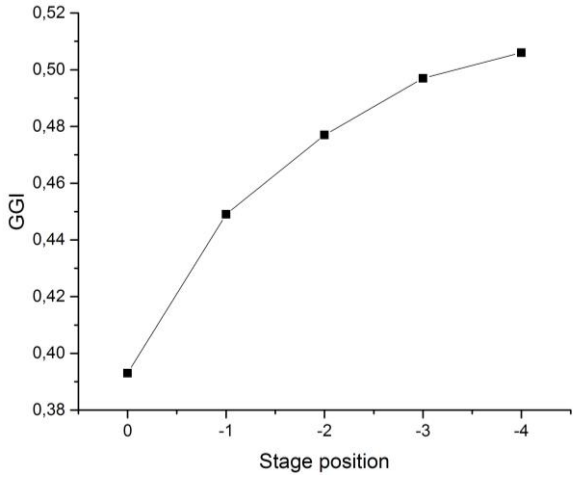


*Figure 5.23 - GGI along the CIGS thickness determined by the peak shift of Raman analyses. The Raman peak was determined scanning in deep from the CIGS surface (stage position=0) to the region close to Mo (stage position =-4). Each stage position unit corresponds to roughly 400 nm.*

The unintentional Ga grading is still under investigation. At the same time, intentionally graded CIGS sample are on the way with a double meaning: sharpening the Raman analysis to adapt the model to LTPED-CIGS and understand the feasibility of an intentional double grading of CIGS absorber by means of the LTPED process.

## 5.5. Combinatorial PED

Research and development of thin film solar cells is directed to a better comprehension of the material characteristics and to squeeze the technology for their best exploitation, to enhance both the device efficiency and the materials properties. Of course, the features of the light absorber material are the most important ones, the ones most affecting the device behaviour. Among all the improvements in the absorber quality, one of the most effective methods to enhance the solar cell efficiency is the introduction of a Ga grading along the CIGS growth direction. With this trick, the conduction band of CIGS are smoothly increased towards the back contact thus "driving" the electrons towards the pn junction with the band potential and promoting an enhanced electrons collection. However, this approach is particularly appropriate for high temperature deposition process such as co-evaporation where the deposition steps are well defined and the temperature must be varied during the process. Very Low-Temperature Pulsed Electron Deposition needs to apply innovative and simpler solutions since the cost-effectiveness and the ease of the solar cell production are the main goal for the future.

As a first step towards the Ga grading, it is necessary to find the PED-CIGS composition that maximize the solar cells efficiency, with the classic CdS buffer layer. To identify the optimal composition of the absorber layer, a study of a multi-sample growth was carried out in a single step: the CIGS-GGI ratio was continuously varied from 0 to 1 between the sample edges, by means of a combinatorial deposition. Combinatorial deposition is a powerful method frequently applied in material science: by the deposition of a library of materials, it allows to study and understand the properties of different materials depending in the variation of a parameter. In our case, this parameter is the composition, the ratio of elements constituting the compound. It can be considered as a way to explore the phase diagram of CIGS at a constant growth temperature. Thanks to this route, phase diagram of a complex compound can be studied in thin film form (69) (70) by using multi sources deposition systems (71) (72) (73).

In this work, simultaneous depositions were carried out ablating in an independent way two different targets, with two distinct Pulsed Electron Deposition sources. The two electron guns were ablating one target each one at the same time and the distance between the two tubes was 7 cm. The substrate is a placed 8 cm over the targets and consisted of a single 75mm×26mm glass, covered with 100nm-thick $Si_3N_4$ as blocking layer and 700nm-thick Mo as back contact. First, NaF precursor layer was deposited as described in section 5.3.2. Then, the target-holder carousel was rotated to position a CIS target and a CGS target below the alumina tubes of the two PED guns to perform concurrent growths of $CuInSe_2$

and $CuGaSe_2$. Both the PED sources worked at 16 kV and the substrate temperature was 270 °C. The set-up of this experiment is schematized in Figure 5.24.

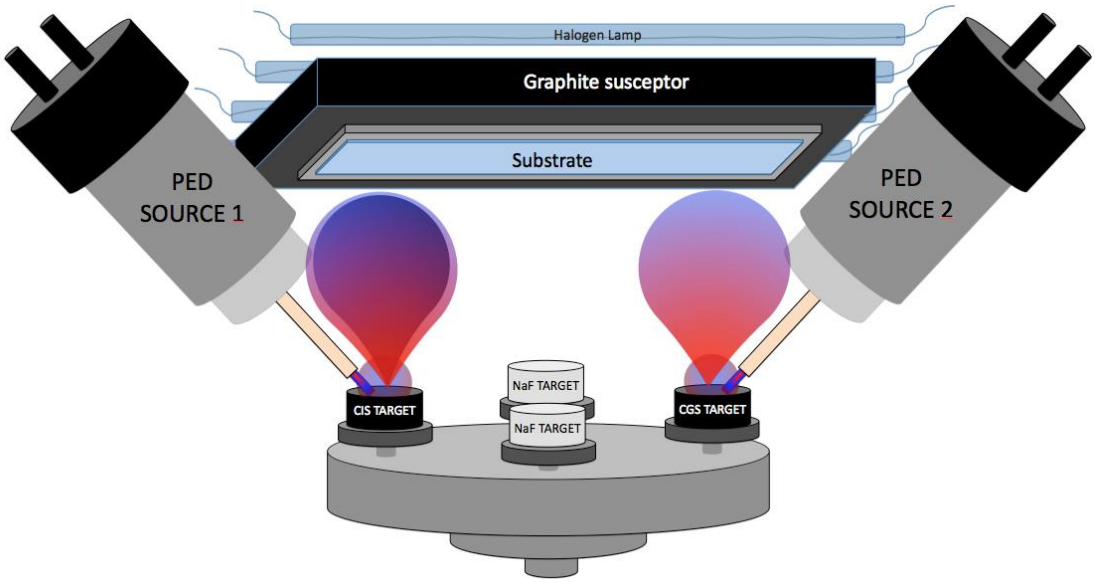


*Figure 5.24 – Scheme of set-up for CIGS deposition with two PED sources. Here, one CIS and one CGS targets are used.*

With this combinatorial deposition, $Cu(In_{1-x}Ga_x)Se_2$ was deposited in 1.6μm-thick film, with x varying between <0.1 on one side of the sample and >0.9 on the other side. The system geometry allowed thickness uniformity distribution of CIGS as shown in Figure 5.25: variation along the sample length was about 2% in the centre and up to 7% at the substrate edges. Thus, the edges were not considered in the solar cells study. Devices with comparable characteristics were investigated from a ~5cm-long central part of the sample.

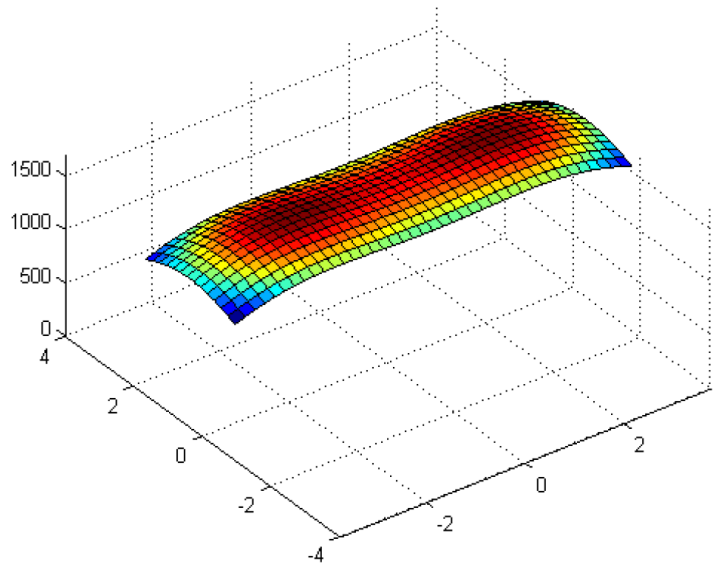


*Figure 5.25 – Simulated thickness distribution by Comsa-David model for samples realized with the combinatorial PED set-up. The film thickness was 1.6 μm over the two targets, had a small decrease (2%) between them and dropped at the edges (7%).*

First of all, compositional and structural features of the whole length-graded CIGS sample were studied in 35 points and are reported in Figure 5.26. The structural properties of the samples were characterized by X-ray diffraction (XRD), performed with a Siemens D500 (Siemens, Berlin, Germany) system in Bragg–Brentano geometry. Morphological and compositional analyses of the samples were conducted by scanning electron microscope (SEM, model Philips 515, Eindhoven, The Netherlands) operating at 25 kV and equipped with an Energy Dispersive X-Ray Spectrometer (EDS) "EDAX" detector. Compositional analyses by SEM-EDS, made along the whole sample length, indicated the measured data (blue diamonds) had exactly the same trend as the values calculated via the bi-cosine formula of Comsa-David model (green triangles), for the ablation plume distribution applied to a PED system based on 2 guns and 2 different compound as targets. GGI was even calculated from lattice parameters derived by XRD analyses: the c and a axes (red squares and orange crosses, respectively) and the lattice volume (blue crosses). GGI from structural investigation exhibited a very similar trend as SEM-EDS and simulated data, but a little bit shifted towards higher values. Moreover, XRD-GGI were more scattered especially around GGI of 0.6. Some structural modifications, maybe due to strain effects, might be occurred.

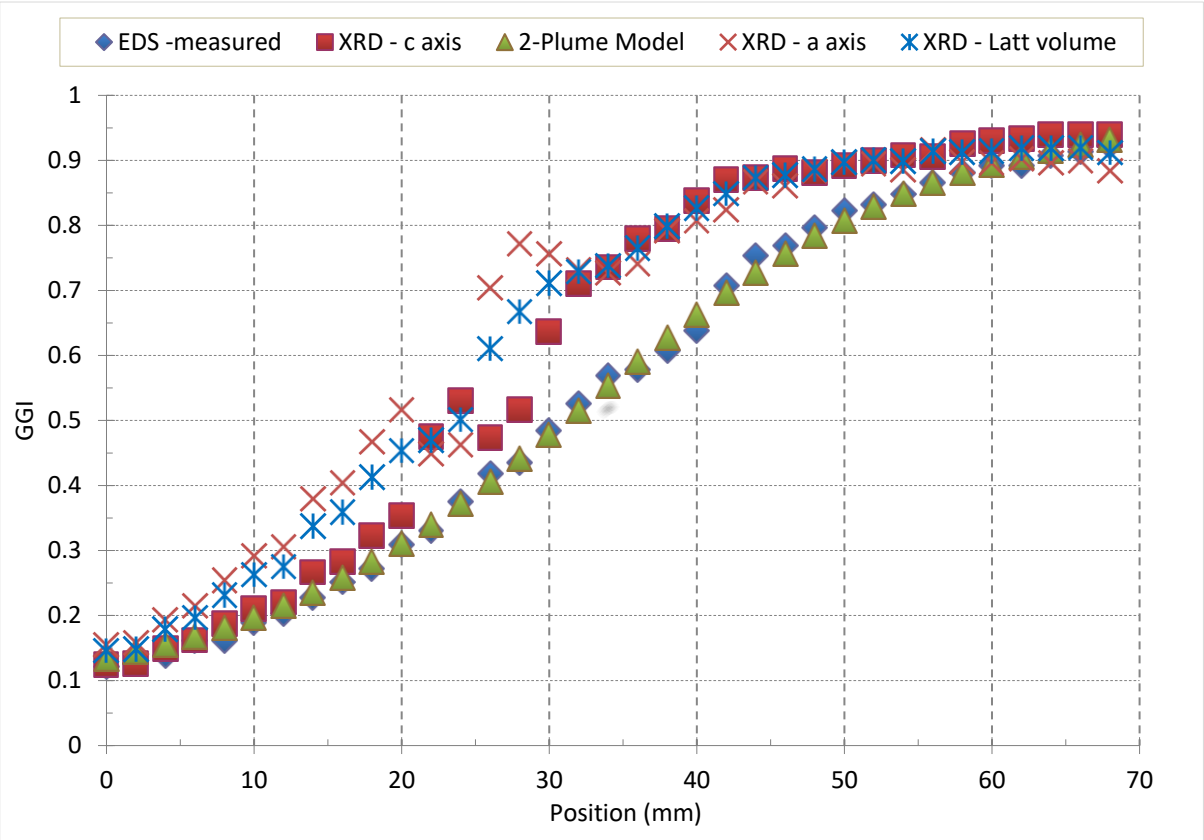


*Figure 5.26 – GGI data as measured by SEM-EDS (blue diamonds), simulated by Comsa-David model for two PED sources in the experiment geometry (green triangles) and derived by XRD measurements (orange crosses for a axis, red squares for c axis and blue crosses for lattice volume).*

Later, solar cells were realized in the classic solar cell architecture of Figure 5.14 depositing the other layers. CdS was applied in one CBD run on the whole sample, with a thickness of 120 nm. Later, the

sample was cut in 3 pieces and the solar cells were completed in three different runs depositing 120 nm of i-ZnO and 800 nm of AZO by RF-Magnetron sputtering, in off-axis configuration. The samples were then prepared for electrical characterizations completing the structure with 2µm-thick aluminium contacts by thermal evaporation and scribing them into 20 devices, with an area of 0.21 $cm^2$ each. These 20 solar cells represented CIGS with the GGI from 0.18 to 0.85, as determined by SEM-EDS and Comsa-David simulation. Then, the effect of Ga content on the solar cells behaviour was investigated, studying the parameters of devices with different GGI, all grown in one single deposition run.

Solar cells performance was tested by current–density vs. voltage with a Keithley 2635 system under 1 sun illumination, supplied by a ABET SUN 2000 solar simulator at standard test conditions (AM1.5g at 25 °C).

JV curves showed low values of $J_{sc}$, $V_{oc}$ and especially FF. The structure was not optimized since thicker CdS and i-ZnO layers were deposited, to avoid any shunts paths and study the sample in its full length. Moreover, before CdS growth, the sample underwent compositional and structural analyses during which CIGS surface may be deteriorated. In fact, the aim of this study was not to fabricate high-efficiency solar cells, but to obtain comparable devices grown in the same CIGS run and to find the GGI at which solar cells parameters, like current density and voltage, are maximized. $J_{sc}$ and $V_{oc}$ trends as a function of GGI are shown in Figure 5.27: $J_{sc}$ (blue squares) has maximum at GGI≈0.3, while $V_{oc}$ (red dots) is maximized at GGI≈0.57.

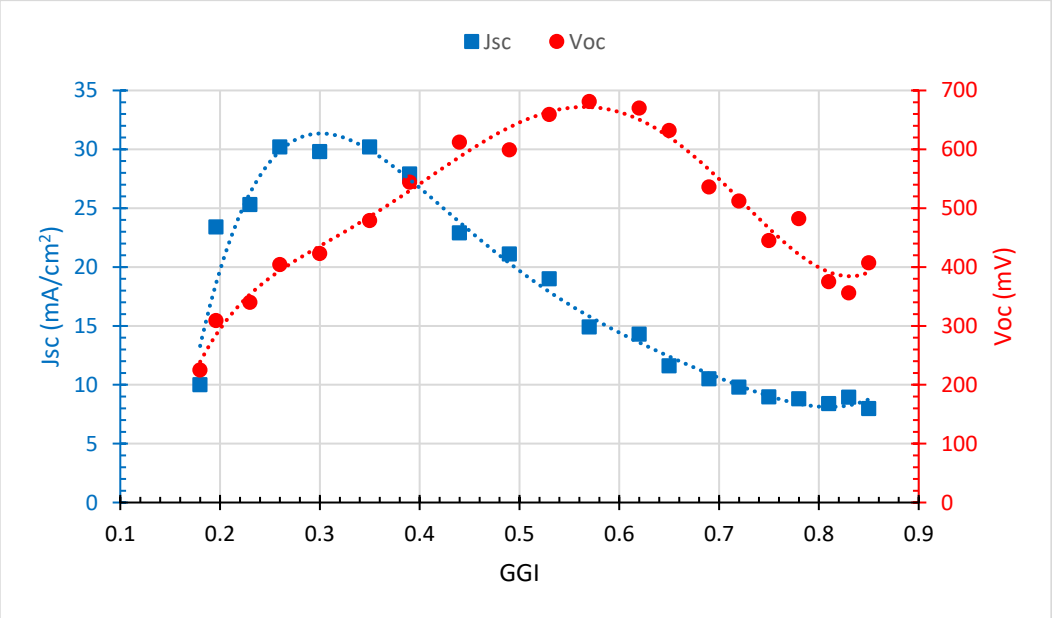


*Figure 5.27 - Experimental values of $J_{sc}$ (blue squares) and $V_{oc}$ (red dots) as a function of the GGI, the dotted lines represent their trends.*

Since the Ga content determines the band-gap width of CIGS, even if not linearly, the $V_{oc}$ would be maximized for CGS material, i.e. at GGI=1. However, the high amount of Ga brings to stoichiometry variation resulting in lower quality of the absorber material due to other phases formation and high

defect density. Interface recombination becomes the dominant recombination mechanism in CGS devices due to increased defects density at the interface, increased tunnelling and negative CBO in the CdS/CGS pn-junction (74). A further $V_{oc}$ drop for large In content (i.e. towards CIS) is indeed caused by the enhanced SRH recombination due to the lower $E_G$.

As said, GGI affects both $V_{oc}$ and $J_{sc}$, therefore the most important parameter to be taken in account is the product between $J_{sc}$ and $V_{oc}$, called power density. Power density as a function of GGI was calculated and its normalized values are plotted in Figure 5.28. From the trend, power-density behaviour could be foreseen and optimal Ga concentration determined. The maximum value of power density was expected for a Ga concentration of 37.5% in the CIGS target, corresponding to $Cu(In_{62.5}Ga_{37.5})Se_2$ absorber.

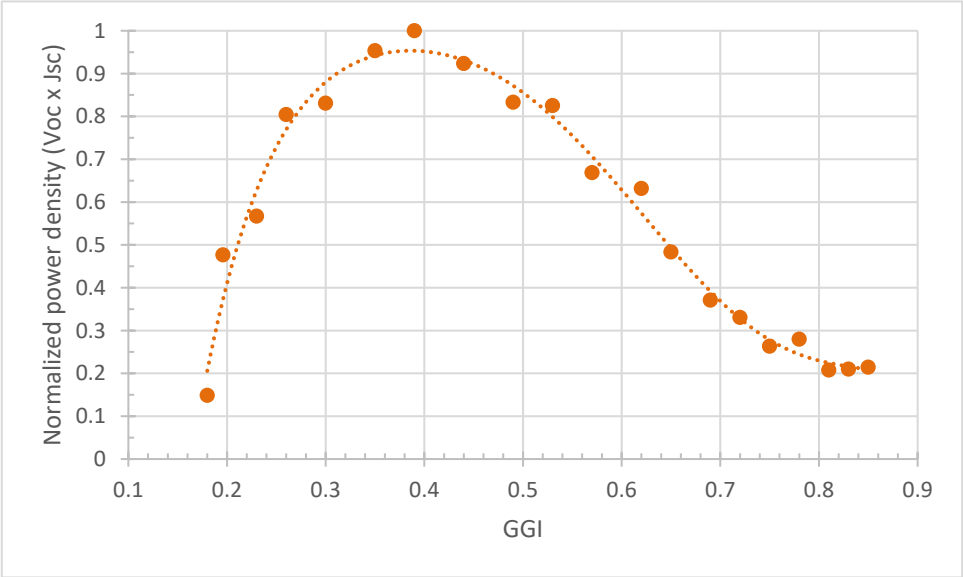


*Figure 5.28 - Normalized power density as a function of GGI on the sample. The dots are experimental points while the dotted curve corresponds to their fitting.*

This result was an important step for the optimization of solar cells based on CIGS fabricated by means of the LTPED process developed at IMEM-CNR of Parma. Target with composition of $Cu(In_{62.5}Ga_{37.5})Se_2$ were synthetized and CIGS with GGI=37.5% is currently studied to boost the solar cells efficiency over the present record.

## 5.6. Conclusions

Although the important 17.0% and good-uniformity result, optimizations are needed to reach the same level of CIGS record devices and face the industrial scale-up. The importance of the role of Ga grading in the final efficiency is still under investigation. Thin-Film group at IMEM-CNR of Parma is currently developing a LTPED process with takes advantages of several CIGS targets to gradually change the CIGS composition during its growth. In this way, a good control of the Ga grading can be applied to realize the Ga profile simulations suggest to maximize the efficiency.

External quantum efficiency measurement of the record device bares its limits and shows where the improvements are required and may be mostly effective. Collection efficiency at both short and long wavelength is yet poor. An alternative buffer layer with wider band gap than CdS would be a great step for enhancing the device current density, shifting the absorption QE drop from ~510 nm to 350nm-400nm. More transparent, thinner and more conductive TCO would help to increase the QE at short wavelength, as well, and in the whole spectra. Applying an antireflection coating would increase the current too. For what concern the CIGS absorber, potassium doping of the CIGS surface has still to be studied and the Ga grading is currently being developed.

Additionally, we demonstrated that with LTPED it is possible to create a library of CIGS absorber varying its Ga content along the sample surface, by means of two PED sources ablating two different targets. The experiment proves the reliability of the Comsa-David model for the LTPED deposition, with calculated GGIs corresponding to the ones measured by EDX, while structural modifications appear to modify the lattice parameters for intermediate compositions. The devices array obtained with this experiment allows to explore the $V_{oc}$ and $J_{sc}$ trends as a function of the GGI in a single sample.

# 6. Bifacial Solar Cells with LTPED

In this chapter, I report on bifacial solar cells based on CIGS grown by LTPED process at 250 °C onto $SnO_2$:F, Sn:$In_2O_3$ and Al:ZnO back contacts. The experimental work was published in the paper (75).

## 6.1. Bifacial solar cells

In the last years, impressive progresses were achieved by the photovoltaic industry in terms of both production capacity and cost reduction. They pushed the progress of new installations, especially in those countries which adopted a feed-in tariff scheme. On the technological front the most visible result has been mainly limited to the steady increase in the efficiency of solar cells and modules. So far, no real breakthrough has yet been achieved in terms of product innovation: the market is still dominated by conventional flat panels with no significant differentiation between crystalline Silicon and thin film technologies. Among the most interesting innovations being explored and developed by the research community, bifacial solar cells (BFSCs) can play an important role in the take-off of building integrated photovoltaics (76).

### 6.1.1. Principles of bifacial solar cells

BFSCs are a pioneering solution able to generate power from radiation illuminating either or both the front and the back side of the device. Thus, it can increase electricity production per square meter of the PV-module through the absorption of the albedo. Thanks to this property, BFSCs are very promising for the integration in a built environment where vertical architectural elements are illuminated from different sides during the day and where albedo is an important component of the overall illumination. Moreover, an increase of 50% in electric power can be achieved in rooftop PV installation using concentrators to focus albedo on the back of the device (77). The albedo irradiance and spectral distribution depends from the surroundings of the solar cells, Figure 6.1 shows few examples.

Consequently, the power density of PV modules can be increased using bifacial solar cells instead of the traditional mono-facial ones, while reducing costs related to the covered area of the PV systems. The idea to collect the light from both the side of the devices came in the 60's (78) and since then BFSCs have been fabricated on a number of different cell architectures, as polycrystalline silicon (79) (80), dye-

sensitized devices (81), perovskite thin-films (82), kesterite-based structures (83) and SnS solar cells (84). An overview of the achievements of several PV technologies exploited for bifacial solutions is shown in Table 6.1, provided by (85). Silicon-based devices are the most used and studied ones for bifacial applications, being silicon the most mature PV technology, but several other technologies have been recently tested because of the promising outcome and the predicted market-share increase (86). Furthermore, the practical advancements in BFSCs can even be applied to sharpen other PV solution, like tandem solar cells.

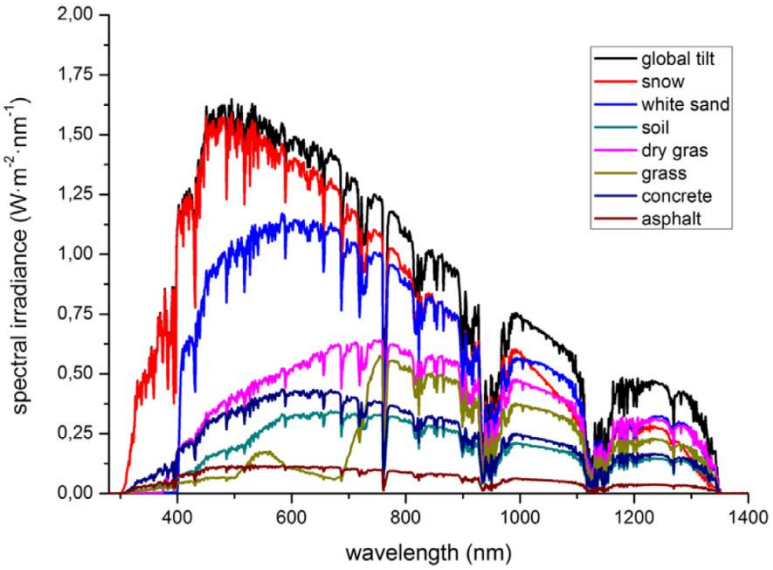


*Figure 6.1 - Albedo irradiance from different grounds compared to the solar spectral irradiance (black curve). (87)*

*Table 6.1 - Bifacial solar cells technologies and their conversion efficiency, as summarized by (85)(references therein).*

| Description | Concentration (Sun) | Efficiency (front or front/rear) |
|---|---|---|
| Buried[a] (independently confirmed) | 1 | 21.9 |
| Fz-Si p-type triode structure (independently confirmed) | 1 | 21.3/19.8 |
| Fz-Si (a-Si:H rear surface passivation) (independently confirmed) | 1 | 20.1 |
| Fz-Si (independently confirmed) | 1 | 19.4/16.5 |
| Fz-Si symmetrical (independently confirmed) | 1 | 18.4/18.1 |
| MISIL (independently confirmed) | 1 | 17.1 |
| Flexible c-Si (thickness: 110 μm, AM0)[a] (independently confirmed) | 1 | 14.7 |
| CdTe ($Cu_xTe$ back contact, 40–60% transmission) (independently confirmed) | 1 | 13.9 |
| Si-HJT cell on commercial CZ c-Si 6" wafer using busbar-less front side metallization | 1 | 23.14 |
| GaAs thin film (thickness: 5 μm) | 1 | 22.6/12.9 |
| Zebra (n-type c-Si) | 1 | 21.3 |
| nPERT | 1 | 20.63 |
| n-type HIT screen printed | 1 | 20.2 |
| Sliver® solar cells | 1 | 19.4 |
| Remote plasma CVD | | > 18/ > 18 |
| (ITO)/($p^+nn^+$)Cz-Si/(IFO) Cu contact 25 × 25 $mm^2$ | 3 | 17.9/17.0 |
| (ITO)/($p^+nn^+$)Cz-Si/(IFO) Cu contact 25x25 $mm^2$ | 1 | 17.6/16.7 |
| Cz-Si p-type SiNx PECVD and screen printed, industrial process | 1 | 16.6/12.8 |
| $p^+nn^+$[a] | 7 | 16.5/13.6 |
| $p^+nn^+$[a] | 1 | 15.7/13.6 |
| GaAs thin film (thickness: 1.5 μm, AM0) | 1 | 15.4 |
| CIGS | 1 | 15.2 |
| POWER cell (16% transparency) | 1 | 12.9 |
| CdTe/CdS (ITO back contact) | 1 | 10.3/2.1 |
| Flexible dye-sensitized (if 90° bending: −6%) | 1 | 6.8 |
| Dye-sensitized (Ti foil based flexible) | 1 | 6.55/4.79 |
| Dye-sensitized (polypyrrole counter electrode) | 1 | 5.74/3.06 |
| Ultra-thin CdTe (0.68 μm) | 1 | 5.7/5.0 |
| Solid-state dye-sensitized solar cell (tandem – no color distortion) | 1 | 3.3 |
| Organic (50% transparency) | 1 | 3.24 |
| Simulated n-type HIT | | 27.02 |

[a] Not under standard test conditions.

Contrary to standard solar cells, there is not a prevalent way accepted by the scientific community to measure the efficiency of bifacial devices. In the past years, several ways have been proposed in literature to evaluate the behaviour of BFSCs, since it is not so straightforward to define their conversion efficiency (85). The simplest way, as in Table 6.1, is to report the efficiency obtained illuminating only the front, as if the device was a classic solar cell, or the efficiencies obtained illuminating independently both the sides of the solar cells. In the latter case, it is called "equivalent efficiency". "Bifaciality factor" is commonly used to refer to BFSCs efficiency. It is defined as the ratio between the of the independent illumination of the front and the one of the back:

$$Bifaciality\ factor(\%) = \left\{\frac{\eta_{front}}{\eta_{rear}}\right\} \cdot 100$$

But since the most-important feature of BFSCs is to be able to absorb the light and generate power being irradiated from both the sides *at the same time*, other methods would be preferred to determine the actual bifacial operation. The following have been proposed:

- "Equivalent efficiency": the efficiency of a standard monofacial solar cell able to produce the same power density as the bifacial cell at the same test conditions. It represents the sum of rear and front efficiencies in respect of the irradiance on each side of the BFSC. (88) (89)
- "Separation rate": based on the short-circuit current density of the device, which contrarily to the open-circuit voltage has a linear trend with the light intensity and is not influenced by external resistance, as indeed the maximum output power and efficiency are. (90)

$$Separation\ rate(\%) = \left\{\frac{J_{SC\ front+rear}}{J_{SC\ front} + J_{SC\ rear}}\right\} \cdot 100$$

- "Absolute bifacial influence": $\Delta$ on any parameter ($X$) of the bifacial solar cell, such as $J_{sc}$, $V_{oc,}$ efficiency (85):

$$\Delta = X_{front+rear} - \{X_{front} + X_{rear}\}$$

Even the irradiance should be classified, especially for the rear illumination which can be obtained by the simple albedo or using mirrors. With this purpose, (87) have defined the "irradiance gain" $g$ as:

$$g = \frac{G_{front} + G_{rear}}{G_{front}}$$

where $G$ is the irradiance, and the "irradiance factor" $x$ as:

$$x = \frac{G_{rear}}{G_{front}} = g - 1$$

Thus, the bifacial *1.x* efficiency is the efficiency obtained irradiating the front with 1 sun and simultaneously the rear with a light intensity of $x$ times the one at the front. Also, the gain due to the bifacial solar cells as compared to the monofacial one, called "gain-efficiency product" (GEP), is simply

the product of *g* and the *1.x* efficiency. Figure 6.2 shows an example of GEP as a function of irradiance gain for two fictitious solar cells.

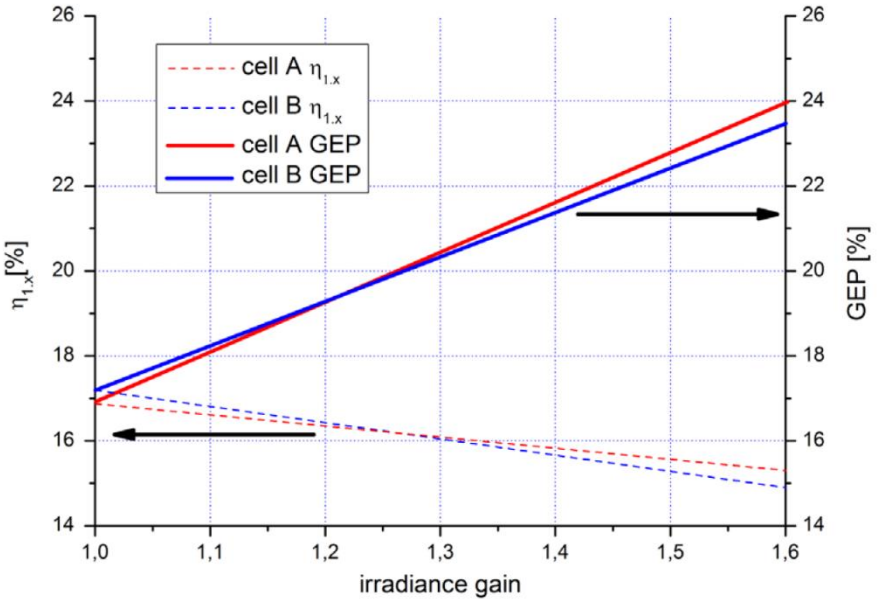


*Figure 6.2 - Simulated bifacial 1.x efficiency and gain-efficiency product for two fictitious bifacial solar cells with different electrical parameters as a function of the radiance gain. (87)*

### 6.1.2. CIGS bifacial solar cells

In BFSCs based on thin films the light absorbing layer is sandwiched between two transparent electric contacts. One is the standard n-type transparent conducting oxide (TCO), while the other must be either a p-type TCO or a very highly doped n-type TCO, which can essentially behave as a metal. $CuInGaSe_2$ is an ideal candidate as light absorbing layer in a BFSCs because of the high photovoltaic conversion efficiency reached with the classic structure. Moreover, semi-transparent bifacial solar cells can be fabricated for PV-window applications simply thinning the absorber (up to few hundreds of nanometres for the CIGS).

An obvious solution to make a CISG-based BFSC is to replace the opaque Mo back contact with a highly conductive TCO (carriers density $>10^{20}$ $cm^{-3}$), like Fluorine-doped Tin Oxide $SnO_2$:F (FTO) or Indium-Tin Oxide Sn:$In_2O_3$ (ITO) or Al-doped Zinc Oxide Al:ZnO (AZO). Good ohmic CIGS/FTO and CIGS/ITO contacts can be obtained at temperature up to about 550 °C and solar cells with efficiencies exceeding 15% can be fabricated thanks to the low sheet resistance of the TCO layer (91) (92). At temperatures above 520 °C, TCO back contacts deteriorate affecting the BFSC, consequently it has been suggested that the performance of CIGS bifacial solar cells could be improved by inserting a thin Mo layer between the TCO and CIGS absorber (93). On the other hand, it is well known that most of the CIGS deposition processes including co-evaporation and all the technologies based on post-deposition selenization or sulphurization (94), require growth or annealing temperatures close to or exceeding 550 °C, to optimise the crystalline and the electrical quality of the light-absorbing layer. This also

imposes a limit on the type of substrate of bifacial cells, for instance most of the flexible polymeric substrates, like PET, being unsuitable for high-temperature deposition. Thus, even for BFSCs, low-temperature CIGS deposition process would be preferred.

Here, good ohmic contacts between CIGS and ITO or FTO were obtained at low temperatures by means of LTPED. Exploiting the low temperature and the high CIGS quality of LTPED, results comparable to the best ones found in literature were achieved at much lower temperature (250 °C) and can open the door to lightweight, flexible and cheaper substrates for bifacial solar cells.

## 6.2. TCO substrates

To study bifacial solar cells based on CIGS absorber grown by LTPED, at temperature as low as 250°C, three different TCO materials were chosen as back contact for their large n-type doping, good conductivity and high transparency: $SnO_2$:F (FTO), Sn:$In_2O_3$ (ITO) and Al:ZnO (AZO).

- FTO: very stable and robust oxide, FTO is one of the most conductive oxides known, it is less expensive than ITO and therefore ideal for a wide range of application from opto-electronics to RFI/EMI shielding and touch-screen displays. Here, one-inch square FTO/glass substrates were cut from the same 10cm×10cm 2mm-thick commercial batch. Their average optical transparency was ≈80% in the visible region, energy gap ≈4.2 eV and electrical resistivity about $3\times10^{-4}\Omega$cm.
- ITO: it is used in several touch-screen and display technologies, such as LCD, OLED, plasma, electroluminescent and electrochromic displays, and other applications as infrared reflecting coating. Here, ITO layers were deposited on heated glass substrate by RF Magnetron Sputtering from commercial targets with $In_2O_3$-$SnO_2$ 90–10wt% composition and diameter of 2" (Testbourne Ltd.).
- AZO: aluminium-doped zinc oxide is cheaper than ITO and FTO, but has the poorest electrical properties, due to the lower carrier density and mobility. For this study, AZO films were grown on glass substrate at high temperature by RF-Magnetron Sputtering from commercial targets with ZnO-$Al_2O_3$ 98–2wt% composition and diameter of 2" (Testbourne Ltd.).

The substrates for ITO and AZO were 1mm-thick transparent soda-lime glass. Immediately before the TCO deposition, they were sequentially cleaned in ultrasonic bath by means of 10%wt-HCl solution, distilled water, acetone, ethanol and iso-propanol (3 min each treatment). Afterward, they were dried with compressed air and then placed on a hot plate at 200 °C for 5 min and finally mounted on the sample holder. The back side of the glass substrate was directly in contact with a graphite susceptor, heated by halogen infrared lamps, and IR thermography was used to monitor the temperature of the substrate surface during the deposition. The distance between substrate and target was set to 8 cm for

both ITO and AZO. The chamber pressure was pumped down to $5.0\times10^{-6}$ mbar before Ar was loaded at a working pressure of $5.0\times10^{-3}$ mbar, whether the target material. Before the deposition, the plasma discharge was ignited with the shutter closed and a 20 min pre-sputtering stage of the ceramic target was performed to remove the contaminants and clean the surface of the target. Note that no diffusion barrier was applied between glass substrate and the TCO: the unique limits to the sodium diffusion from SLG into CIGS were the low temperature and the TCO layer itself.

The optimization of conductivity and transparency of AZO films at RT is exposed in chapter 5. . AZO as back contact of BFSCs was grown sputtering the ceramic target with a power of 120 W (~6 W/cm$^2$) at Ar pressure of $5.0\times10^{-3}$ mbar, heating the substrate at 250 °C. (95) The ohmic behaviour of the CIGS/AZO contact was tested by IV characterisation of Au/CIGS/NaF/AZO/glass structure, which is shown in Figure 6.3.

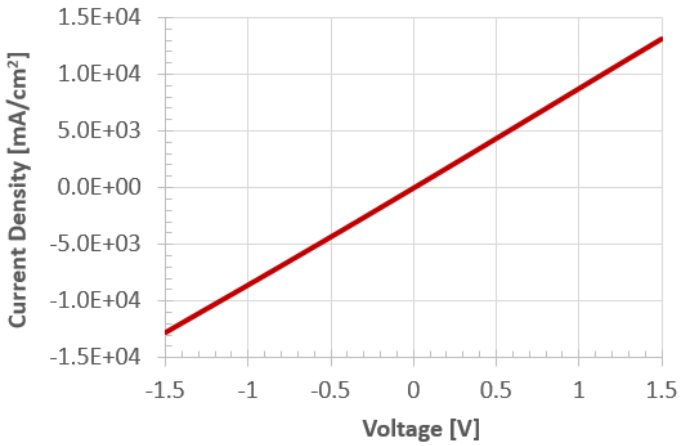


*Figure 6.3 - JV of Au/CIGS/NaF/AZO/glass structure, confirming the ohmicity of CIGS/AZO contact in this study.*

The evolution of ITO properties and its interface with CIGS was studied to optimise the film for the subsequent LTPED deposition. First the electrical conductivity and the optical transparency of the ITO back-contact were investigated in function of sputtering power, substrate-target distance and gas pressure at room temperature: the best conditions were found at a power of 20 W (~1 W/cm$^2$) and Ar pressure of $5.0\times10^{-3}$ mbar, with a distance of 8 cm. Then, a range of temperatures between room temperature and 315 °C was explored: the resistivity of the ITO films decreased monotonically with increasing temperature, as shown in Figure 6.4-a, and reached a minimum value of $1.08\cdot10^{-4}$ Ωcm at 315 °C, corresponding to an n-type carrier concentration of $2\cdot10^{21}$ cm$^{-3}$ and a mobility of 30 cm$^2$V$^{-1}$s$^{-1}$. At this temperature, a thickness of 280nm-300nm was found to be the best compromise between substrate transparency and sheet conductivity. Figure 6.4-b shows that a 280nm-thick ITO layer transmitted more than 85% of the visible light while the sheet resistance did not exceed 3.5Ω/square.

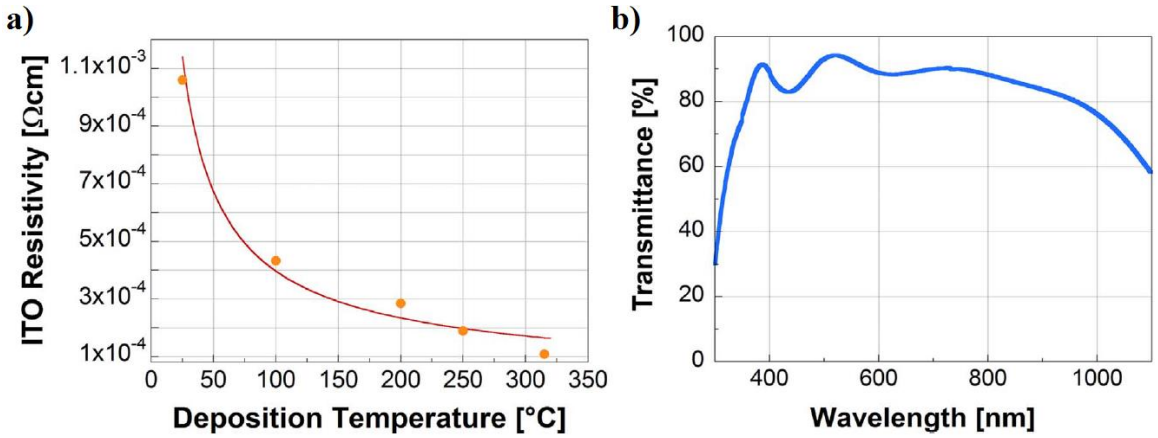


*Figure 6.4 - a) Variation of ITO resistivity as a function of the substrate temperature during the RF-Magnetron sputtering deposition. The red curve is a guideline for the eye. b) Optical transmittance spectrum of a 280nm-thick ITO layer grown onto glass at 315 °C.*

The ohmic characteristics of the CIGS/ITO interface were then assessed by preparing an Au/CIGS/NaF/ITO/glass test structure, where the Au top contact was deposited to have a negligible contact resistance with CIGS. The I-V curve in Figure 6.5 confirms the ohmic behaviour of the contact between the LTPED-grown CIGS and ITO, which was also observed to remain stable at room temperature over the typical lifetime of a test device.

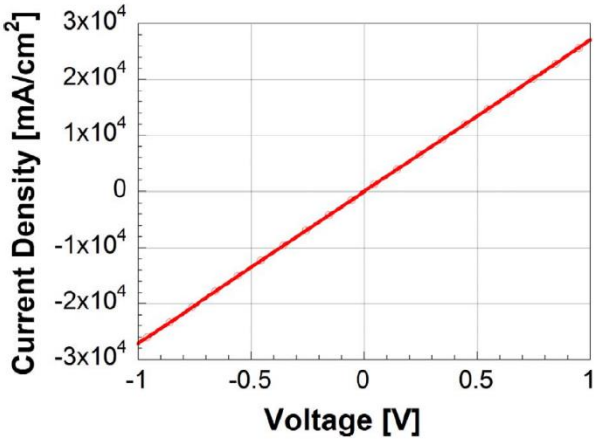


*Figure 6.5 - JV characterization of Au/CIGS/NaF/ITO/glass test structure revealing the ohmicity of the CIGS/ITO contact.*

Electrical and optical properties of the TCOs used as back contact for bifacial solar cells in this thesis, are summarized in Table 6.2.

*Table 6.2 - TCOs used as back contact for BFSCs based on LTPED-grown CIGS.*

| TCO | Sputtering param. | | Thickn. (nm) | Average optical transp. (%) | Resist. (Ωcm) | Sheet Resist. (Ω/sq) | Carrier Mobility ($cm^2/Vs$) | Carrier Density ($cm^{-3}$) |
|---|---|---|---|---|---|---|---|---|
| | Power (W) | Temp. (°C) | | | | | | |
| **AZO** | 120 | 250 | 850 | ≈83 | $5 \cdot 10^{-4}$ | 5.0 | 36 | $5 \cdot 10^{20}$ |
| **ITO** | 20 | 315 | 280 | ≈85 | $1 \cdot 10^{-4}$ | 3.5 | 30 | $2 \cdot 10^{21}$ |
| **FTO** | Commercial | | 600 | ≈80 | $4 \cdot 10^{-4}$ | 3.0 | 30 | $5 \cdot 10^{20}$ |

## 6.3. Experimental

Solar cell samples were deposited on 25mm×25mm glass substrates and mechanically scribed into 16 test devices. A picture of a final device with TCO as back contact is shown in Figure 6.6.

*Figure 6.6 - Standard test sample, later mechanically scribed into 16 solar cells of area=0.05 cm$^2$. The brownish frame is due to the CdS deposition: it was etched on one edge to realize the contact with the TCO at the back, by means of Ag paste.*

The architecture of these cells is sketched in Figure 6.7, where the back-contact pad is shown at the edge on top of the back TCO layer (CdS is scratched from the frame to expose the TCO).

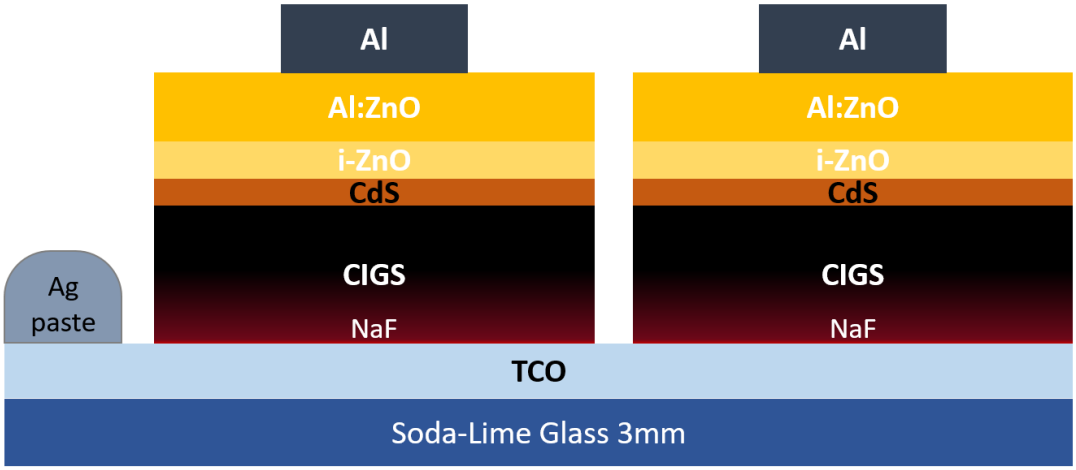


*Figure 6.7 - Example of materials stack in bifacial solar cells of this thesis, where TCO may be either AZO, ITO or FTO.*

Three sets of samples were prepared, one on commercial FTO-coated glass, one on glass sputtered with ITO and one with sputtered AZO, using the specific recipe developed for the subsequent LTPED deposition of CIGS. CIGS depositions were carried out in the same period, thus all sample were comparable among each other. Two different CIGS thickness were applied for FTO and ITO back contact.

The CIGS light-absorbing layers were deposited by Low-Temperature Pulsed Electron Deposition in a home-made deposition machine fitted with commercial Neocera PEBS-20 source, the same equipment described section 5.1. Both the growth temperature and the CIGS thickness were monitored in situ by IR thermography. Sodium doping was obtained by initiating the LTPED process with the deposition of

10nm-thick NaF at a substrate temperature of 80 °C, which was later raised to 250 °C for CIGS growth without breaking the vacuum. Following the result of section 5.5 on the CIGS composition study, the polycrystalline CIGS targets for LTPED were synthesised with the following atomic composition: Cu=25.0%, In=15.7%, Ga=9.3%, Se=50.0%, as determined by SEM-EDS analyses. Then, CIGS films were deposited with an electron beam accelerating voltage of 16 kV and a repetition frequency of 9 Hz, at a substrate temperature of 250 °C. With these parameters and the above specified target composition, we deposited CIGS films having GGI=0.375±0.005 and a bandgap of about 1.2 eV. No intentional grading of the CIGS composition was performed during the deposition, in order to independently understand the influence of the substrate on the structural and compositional properties of LTPED-deposited CIGS films. For each set of samples, cells with two different CIGS thicknesses were realized:

- 1.85µm-thick CIGS absorbers (from now "Thick-CIGS"), designed to be compared with standard LTPED-grown CIGS cells on Mo back contacts;
- 1.20µm-thick CIGS absorbers (called "Thin-CIGS"), made to study the potential application of this low-temperature technology for the preparation of efficient bifacial solar cells.

All the rest of the cell architecture was the same as described in section 5.3 for all the devices of the study: 90nm-thick CdS by CBD and RF-Magnetron Sputtered 120nm-thick i-ZnO and 800nm-thick AZO. Basically, the solar cells had the same structure as the classic CIGS ones, but the back contact.

## 6.4. Results

First of all, the CIGS morphology was investigated to correlate the growth characteristics to the TCO material used as substrate. With ITO and FTO, the CIGS morphology looked very similar to the case of LTPED growth on Mo substrates, with an average grain size of 800nm-1000nm. Therefore, the growth kinetics did not appear to be affected by the replacement of Mo with ITO or FTO. Besides, CIGS deposited on AZO back-contact grew with a great density of smaller grains (200nm-400nm). Figure 6.8 and Figure 6.9 show SEM cross-sectional images of two complete solar cells grown on ITO or AZO coated glass substrates, respectively.

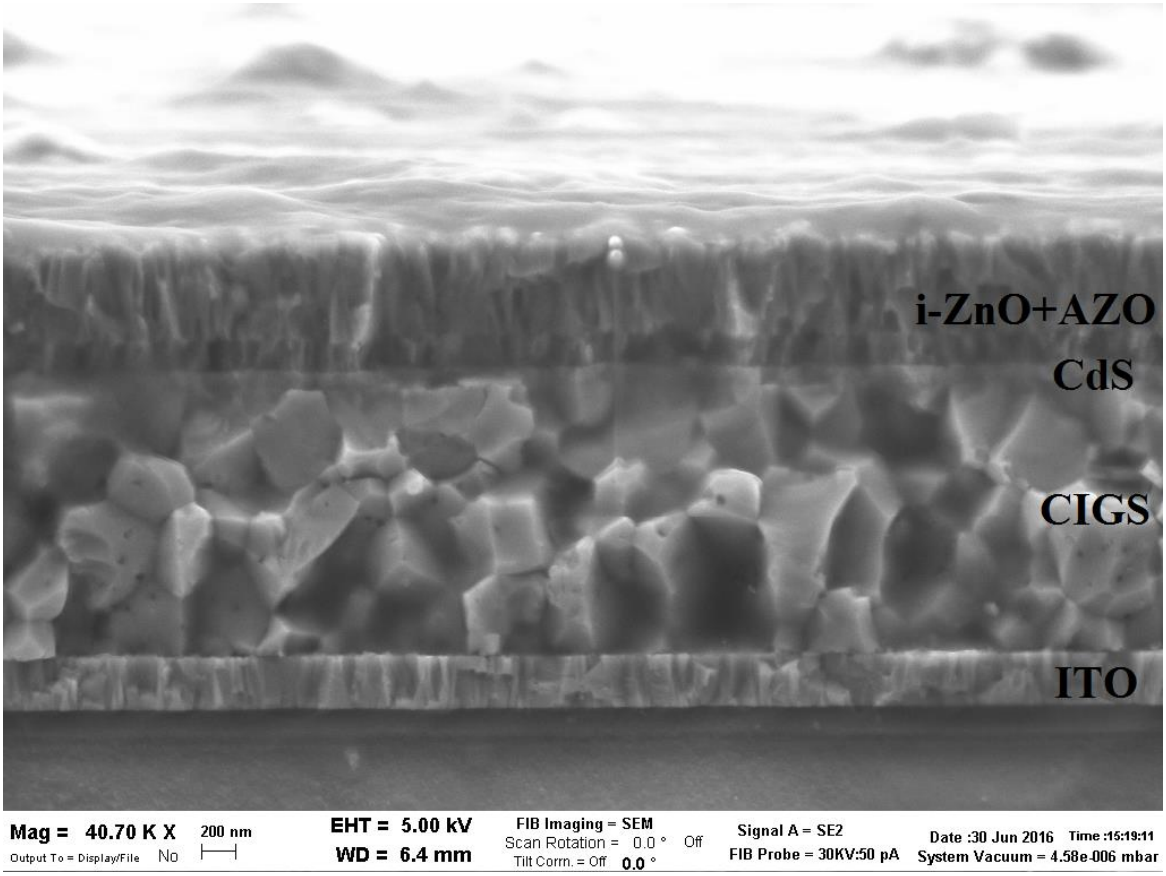


*Figure 6.8 - SEM cross-sectional image of a solar cell with 1.80µm-thick CIGS grown onto ITO back-contact, by LTPED.*

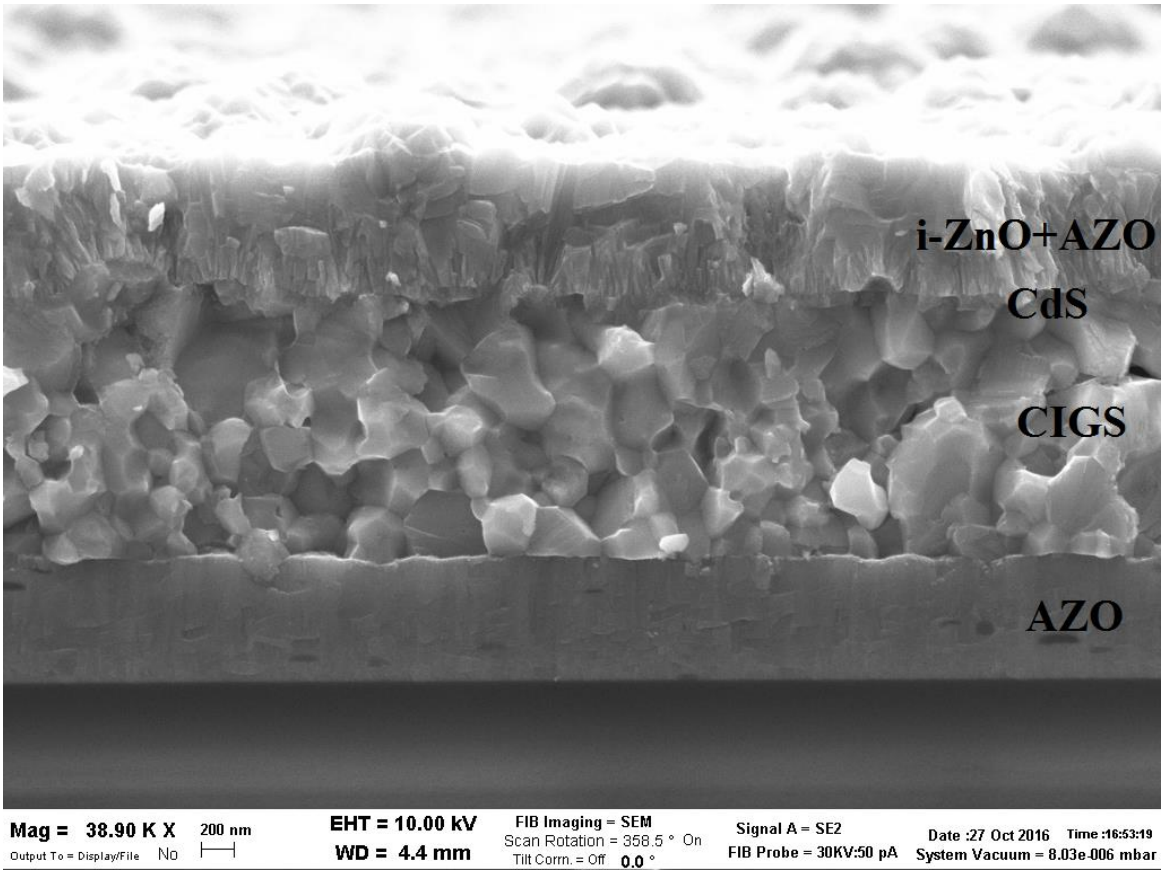


*Figure 6.9 - SEM cross-sectional image of a solar cell with 1.80µm-thick CIGS grown onto AZO back-contact, by LTPED.*

Test devices for I-V and other electrical characterisation were obtained by mechanical scribing around the top metal contacts. The active area of each independent device was about 0.05 $cm^2$. SEM imaging (e.g. Figure 6.10) confirms that the same mechanical scribing procedure used for standard cells on Mo back contacts can be used to cut efficiently through all the layers except for the TCO back contact, thus guaranteeing both a good electrical insulation between one solar cell and the other and the back-contact continuity over the whole sample.

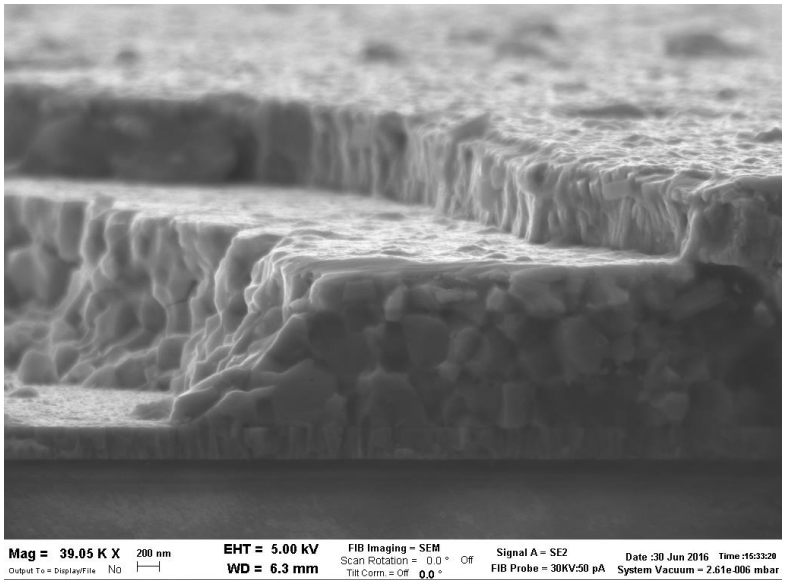


*Figure 6.10 - SEM cross-section of a solar cell with CIGS grown by LTPED on ITO, taken in correspondence of a scribing line. On the left of the image, the complete scribing of the solar cells is obtained, saving the only TCO back contact.*

The I-V parameters of the solar cells grown on TCOs were measured under front, rear and bifacial illumination at 25 °C using a solar simulator. The standard illumination of the cell under the solar simulator through the top contact is defined as "front-illumination", while in the "rear-illumination" configuration solar cells are turned upside-down and irradiated through the glass and the TCO. In both configurations, the cells were placed on black sample holders to avoid any non-absorbed light to be reflected back into the active region of the cell. The “bifacial measurement” was obtained under one-sun illumination from both sides of the cells at the same time using a concave glass to reflect the light at the back of the sample, as shown in Figure 6.11. In this conditions, the irradiance factor was 1, the irradiance gain equal to 2 and thus in this study bifacial 1.1 efficiencies were measured. As usual, dark measurements were used to extract information on both the shunt and the series resistance of the devices.

External Quantum Efficiency (EQE) measurements were carried out under the solar simulator with a set of 16 narrow-band filters and a Silicon photodiode for the calibration.

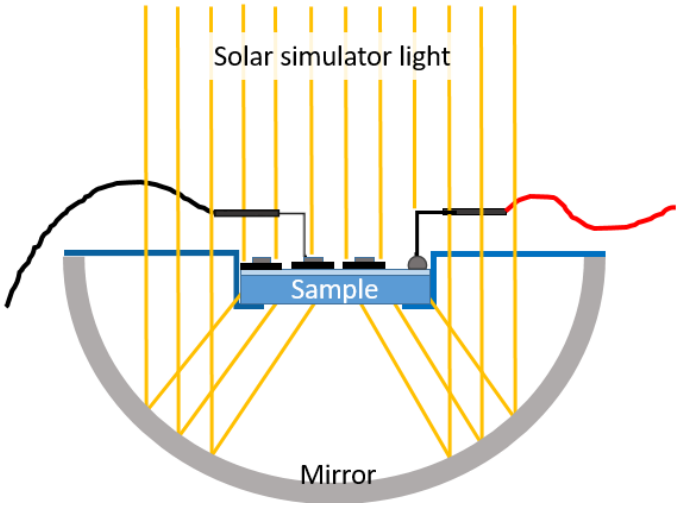


*Figure 6.11 - Geometry adopted for bifacial illumination of solar cells with TCO back contact.*

Table 6.3 reports the results for the best 25×25 $mm^2$ samples from the statistical point of view. Each datum is the average over the 16 devices contained in the sample, each one having an area of 0.05 $cm^2$. The relative standard deviations of the key cell parameters in the best samples on FTO and ITO were 1.5% for the $V_{oc}$, 2.1% for the fill factor, 3.8% for the $J_{sc}$ and 4.9% for the efficiency (in relative %).

*Table 6.3 - Average electrical parameters of the best 25mm×25mm bifacial solar cell samples. Each datum is the mean of the value from the 16 devices of the samples. The bifacial efficiency was measured under illumination of 1sun from the front and 1sun from the rear, therefore it is called bifacial 1.1 efficiency. For AZO only, the data are related to one of the best solar cell.*

| Cell type | Illumin. mode | Voc (mV) | Jsc ($mA/cm^2$) | FF (%) | η (%) | $R_s$ ($\Omega cm^2$) | $R_{sh}$ ($\Omega cm^2$) | Separation rate (%) | Δη |
|---|---|---|---|---|---|---|---|---|---|
| **Thick CIGS/FTO** | Front | 627 | 30.3 | 70.1 | 13.3 | | | 100.0 | +1.1 |
| | Rear | 537 | 8.1 | 59.9 | 2.6 | | | | |
| | Bifacial | 637 | 38.4 | 69.4 | 17.0 | | | | |
| | Dark | | | | | 1.2 | 899 | | |
| **Thin CIGS/FTO** | Front | 489 | 29.0 | 50.2 | 7.1 | | | 97.6 | +1.1 |
| | Rear | 450 | 17.3 | 39.4 | 3.1 | | | | |
| | Bifacial | 493 | 45.2 | 50.9 | 11.3 | | | | |
| | Dark | | | | | 1.4 | 576 | | |
| **Thick CIGS/ITO** | Front | 636 | 29.0 | 59.0 | 10.9 | | | 100.0 | +1.1 |
| | Rear | 525 | 7.0 | 43.5 | 1.6 | | | | |
| | Bifacial | 639 | 36.0 | 59.0 | 13.6 | | | | |
| | Dark | | | | | 0.5 | 563 | | |
| **Thin CIGS/ITO** | Front | 521 | 29.6 | 41.7 | 6.4 | | | 101.1 | +1.2 |
| | Rear | 423 | 14.6 | 36.7 | 2.3 | | | | |
| | Bifacial | 502 | 44.7 | 44.1 | 9.9 | | | | |
| | Dark | | | | | 2.5 | 155 | | |
| **Thick CIGS/AZO** | Front | 421 | 18.3 | 45.8 | 3.5 | | | ND | ND |
| | Rear | 421 | 6.1 | 41.1 | 1.1 | | | | |
| | Dark | | | | | 2.44 | 284 | | |

JV curves of representative devices of the Thick-CIGS/FTO and Thick-CIGS /ITO samples, under front, rear and bifacial illuminations, are shown in Figure 6.12 and in Figure 6.13, respectively.

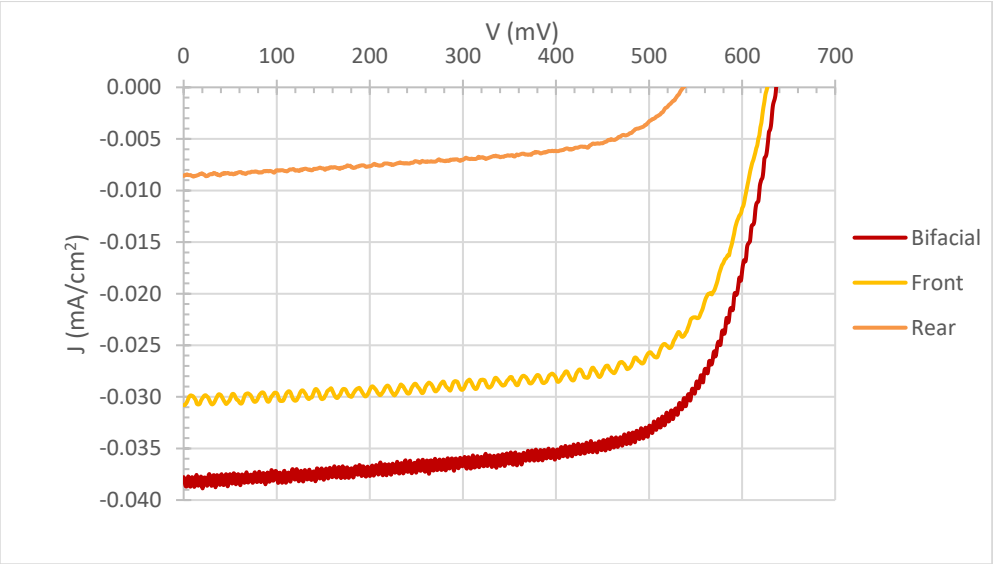


*Figure 6.12 - JV measurements in front, rear and bifacial illumination of a representative solar cell based on 1.80µm-thick CIGS grown onto FTO. The noise of the curves was due to an interference effect of the experimental set-up.*

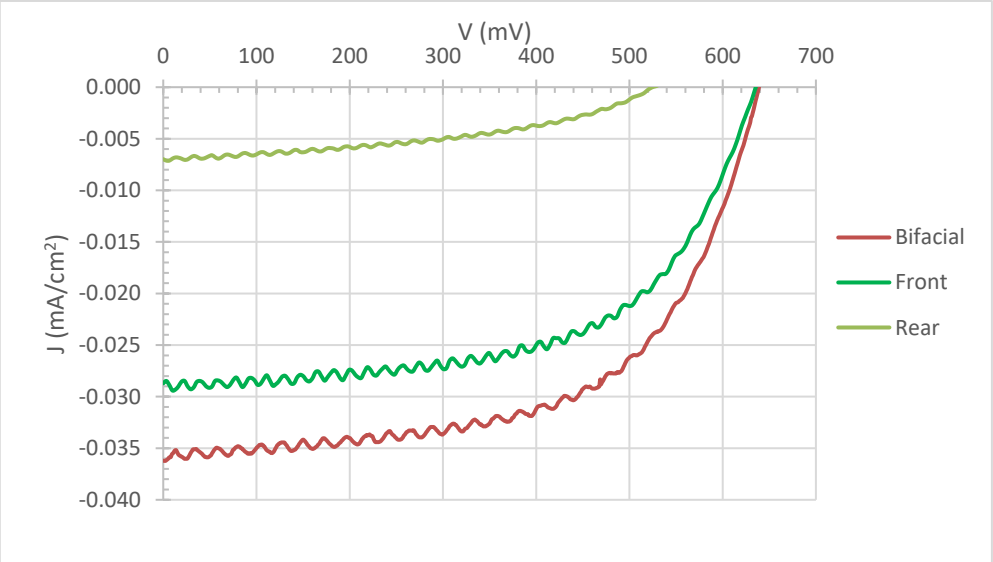


*Figure 6.13 - JV measurements in front, rear and bifacial illumination of a representative solar cell based on 1.80µm-thick CIGS grown onto ITO. The noise of the curves was due to interference effect of the experimental set-up.*

Not surprisingly, all solar cells exhibited lower efficiencies under back illumination with respect to front illumination. This is a typical feature of bifacial solar cells, reported both on Si (96) and CIGS-based (97) devices, which is due to the dominance of carrier generation in the neutral region of the junction over the contribution of the space-charge region. The most of the electron-hole pairs are created outside the depletion region and hence cannot be separated by its electric field and quickly recombine, if the diffusion length of the generated carrier is lower than their distance from the p-n junction. Since the estimated width of the depletion layer at short circuit, as obtained from dark C-V measurements, is about 350nm, the minority carrier diffusion length in LTPED-grown CIGS must be significantly lower than 1µm in all cells. This would explain the poor current density obtained with the rear illumination, and its great increase when the CIGS absorber was thinned.

Noticeably, the device current density under bifacial illumination was almost the arithmetical sum of the front and rear ones, with a separation rate around 100% for both ITO and FTO. Moreover, the FF and $V_{oc}$ produced by the solar cell in bifacial illumination were close or higher than the ones in the front illumination. In the end, the efficiency of bifacial devices appeared always at least 1 absolute% larger than the arithmetical sum of front and rear efficiencies.

The top efficiencies measured under front-illumination for Thick- CIGS/FTO, CIGS/ITO and CIGS/AZO cells are reported in Table 6.4 alongside with results obtained with a nominally-identical-CIGS solar cells on Mo back contact. The record devices on ITO and FTO were not found in the best samples of Table 6.3 but in samples with lower average efficiency and higher standard deviation.

*Table 6.4 - Electrical parameters from front illumination of the record LTPED-grown solar cells with no intentional bang-gap grading of CIGS, for different back contacts.*

| Cell type | Voc (mV) | Jsc ($mA/cm^2$) | FF (%) | η (%) | $R_s$ ($\Omega cm^2$) | $R_{sh}$ ($\Omega cm^2$) |
|---|---|---|---|---|---|---|
| **CIGS/Mo/glass** | 659 | 30.4 | 73.5 | 14.7 | ~1 | ~1000 |
| **CIGS/FTO/glass** | 652 | 30.8 | 73.3 | 14.7 | 1.2 | 900 |
| **CIGS/ITO/glass** | 641 | 29.9 | 61.5 | 11.8 | 1.3 | 710 |
| **CIGS/AZO/glass** | 421 | 18.3 | 45.8 | 3.5 | 2.4 | 280 |

The results in Table 6.3 and Table 6.4 raised several topics which appeared to be specifically related to the LTPED process: the extremely-good properties of CIGS grown onto FTO, the performance gap between Thick- and Thin-CIGS, the low FF of CIGS/ITO devices and the very poor characteristics of CIGS/AZO solar cells.

### 6.4.1. FTO: the astonishing back-contact

The first point is the surprising behaviour of solar cells with back contact made of FTO. The performance of the cells grown on FTO-coated glass was almost the same as the Mo-benchmark, not only in terms of $V_{oc}$ and $J_{sc}$ but mainly in terms of FF: both >73%, with very close $R_s$ and $R_{sh}$. This confirms that the low-temperature Na-doping of CIGS in the LTPED process, which was optimised for the Mo back contacts, worked also for FTO-coated substrates without any modifications. As pointed out in the literature, the ohmic behaviour can be explained by trap-assisted tunnelling or tunnel-enhanced recombination of carriers through a very thin potential barrier at the interface between $p^+$-type CIGS and $n^+$-type TCO. The extreme doping of CIGS could be only explained by massive Na content at the interface with the TCO back contact. Figure 6.14 is a SIMS analysis of a Thick-CIGS/FTO solar cell from the same sample of Table 6.1. It shows large Na inclusion in the first absorber region, and confirmed no gallium oxide was formed at the interface with FTO (towards the back contact, Ga signal drops exactly as Cu and Se ones; In decreases and then stabilized at a higher value because of FTO).

For what concerns CIGS layers and the following ones, the SIMS spectra of CIGS/FTO solar cell is indeed very similar to the ones of the samples grown onto Mo (see chapter 5. ).

Remarkably, the current density of FTO solar cells, were even higher than the Mo reference, while the $V_{oc}$ lost a few mV. In the end, the power density of devices with FTO or Mo back-contact was the same.

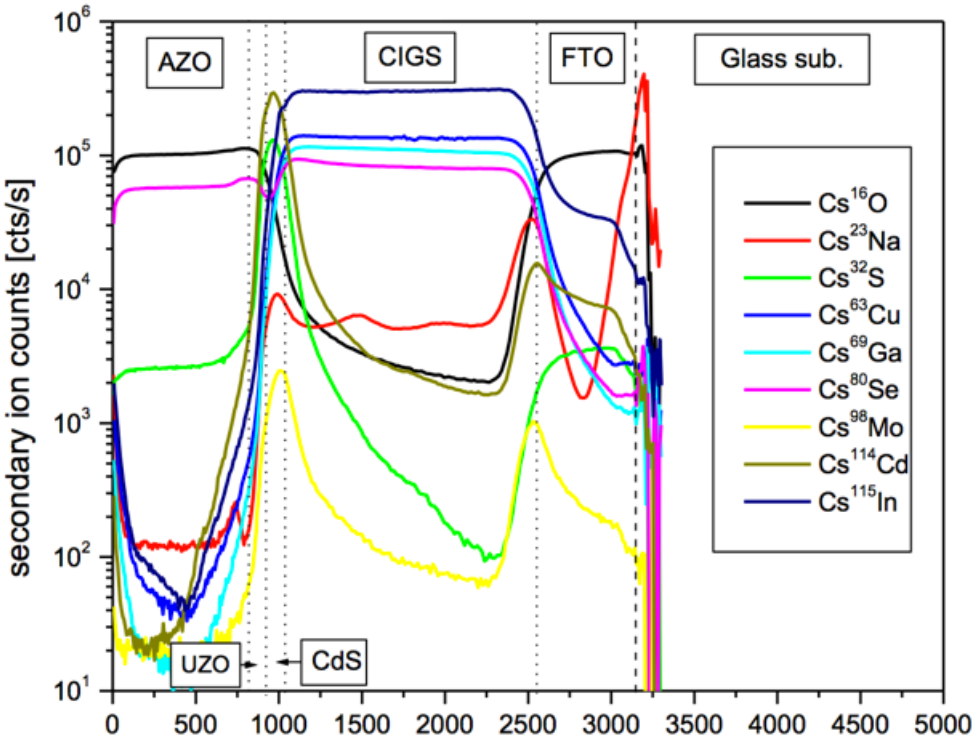


*Figure 6.14 - SIMS analysis of Thick-CIGS grown onto FTO back-contact. Se signal in the ZnO window layer is an artefact due the Zn which here is detected as Se.*

### 6.4.2. Thick-CIGS vs Thin-CIGS

An open question was the dramatic performance difference between thick and thin solar cells, independently of the substrate. Under front illumination all Thick-CIGS solar cells exhibited a much higher efficiency with respect to Thin-CIGS cells (+87% for CIGS/FTO and +70% for CIGS/ITO). This was not due to the absorbance of the cells as the short-circuit current density did not vary significantly between the two sets of devices. For instance, in the case of ITO, the thinner CIGS had even larger front current-density than the thicker one (+0.6 mA/cm$^2$). The deterioration of the efficiency in thinner devices was associated to a reduction of the $V_{oc}$ (~−25%) and, most of all, the FF (~−40%). In fact, the shunt resistance values as obtained from the dark I-V curves pointed towards the presence of a higher density of low-resistance shunting paths in Thin-CIGS cells compared to Thick-CIGS ones. Probably, the most important cause of the increase of shunting paths through the active region of the cells was the incorporation of sub-micron size debris generated by the ablation of the CIGS target during the LTPED deposition. Some of these small grains can be weakly attached to the substrate at the end of the deposition and were likely to be removed during the CBD deposition of the CdS buffer layer or during

the subsequent sputtering deposition of ZnO. Electron Beam Induced Current (EBIC) imaging confirmed the presence of debris and craters in the CIGS film. In Figure 6.15, the craters appear as bright spots in the EBIC image taken at a beam voltage of 20 kV at which most the electron-hole pairs were generated inside the ZnO layers if the film was flat and regular. As the EBIC gain (number of electron-hole pairs generated per incident electron) is almost double in CIGS with respect to ZnO, the bright spots were regions where the ZnO came off partially or completely together with some CIGS particulate. The impact of the debris was statistically reduced as the particulate was gradually buried in the CIGS film as the deposition proceeded and the thickness increased. This means that the reduction of the amount of particulate or the size of the debris is one of the main challenges on the path to the LTPED deposition of solar cells with a medium to high degree of transparency, i.e. ultra-thin (~300 nm) CIGS for semi-transparent solar cells.

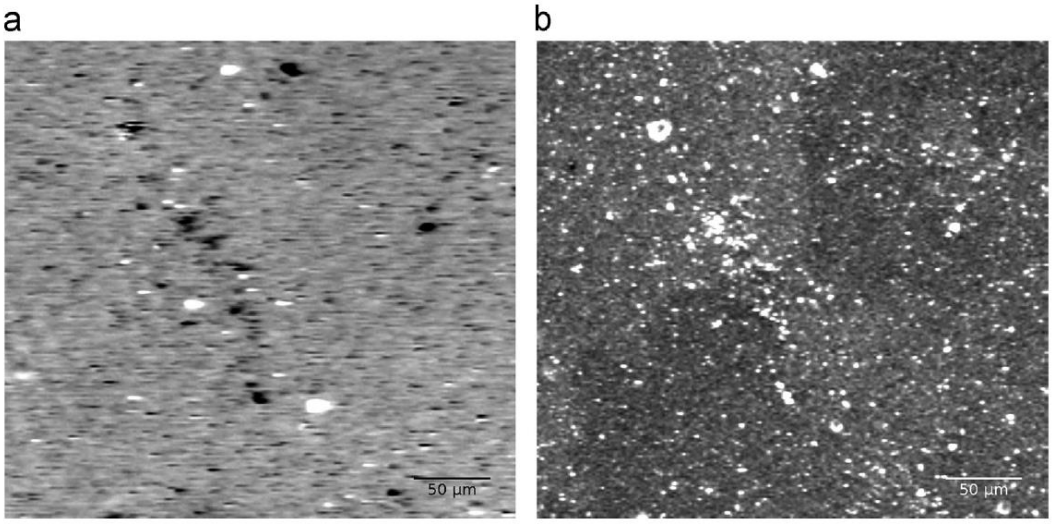


*Figure 6.15 - a) Plan-view EBIC image of a CIGS/ITO solar cell, at 20 kV and 10 pA electron-beam current. Bright spots correspond to areas where the EBIC signal is about double the background. b) Secondary-electron image of the same area.*

### 6.4.3. Why does ITO back-contact limit the FF?

Another important issue was the performance gap between FTO and ITO-coated glass substrates. As pointed out in the introduction, it is well known that the CIGS/ITO interface is difficult to optimise particularly at the typical growth temperatures required by thermal co-evaporation of CIGS and by the post-growth thermal treatments used also in the case of sputtering + selenization processes. Even if the LTPED growth temperature was 250 °C, the comparison between the sets of substrates indicated that the low FF and $V_{oc}$ exhibited by the cells deposited on ITO must be related to the characteristics of the CIGS/ITO interface. The ohmicity of the contact was not an issue (see Figure 6.5). More information about the quality of the CIGS layer in the solar cells can be obtained from the EQE data. The spectra obtained under front and back-illumination for typical Thick- and Thin-CIGS/ITO devices are shown in Figure 6.16 a) and b), respectively.

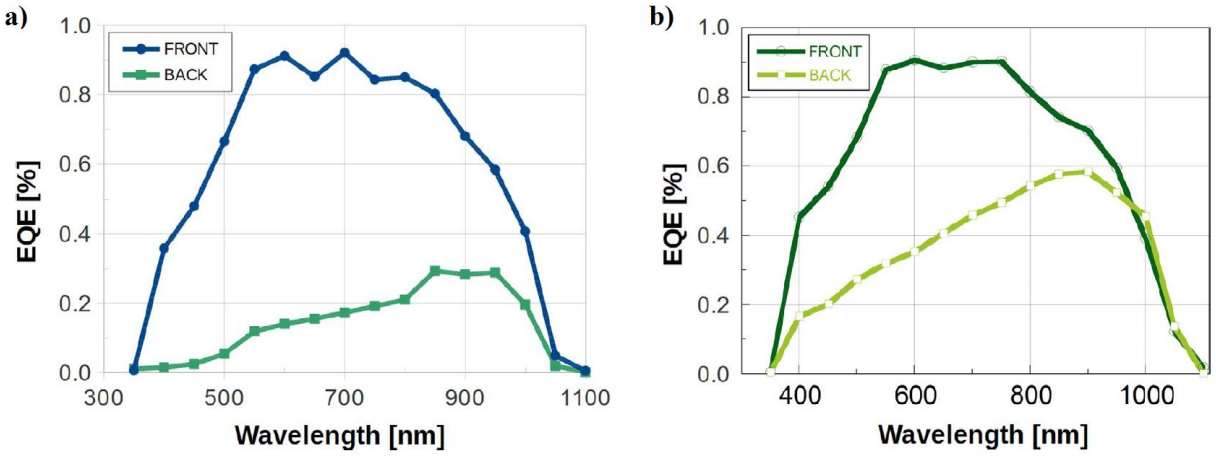


*Figure 6.16 - External quantum efficiency measurements of representative Thick- (a) and Thin- (b) CIGS/ITO solar cells, under front and back illumination. Calculated currents were almost the same as the ones determined by JV measurements.*

Under back illumination, for both samples the quantum efficiency increased almost linearly with increasing wavelength between 400 nm and 900 nm and the ratio between the two average slopes was about equal to the inverse of the ratio between the CIGS thicknesses. Both curves have a maximum between 900 nm and 950 nm. Fitting the quantum efficiency spectra by using the absorption spectrum of the standard LTPED-grown CIGS on Mo back contacts ($E_g$=1.2eV), it was not possible to find a collection-efficiency depth-profile which provided a good fit of both the front and the rear illumination spectra at the same time. The only way to find a match between the calculated EQE spectra and the experimental data was to drop the assumption that the absorption coefficient was uniform along the growth direction. In fact, the best fit between the calculated and the experimental spectra was found by assuming that high-bandgap (>1.45 eV) CIGS was formed at the interface with the ITO back contact. Both in the case of Thin- and Thick-CIGS samples, the best fit between the calculated EQE spectra and the experimental data was found for a depletion layer width of about 600 nm.

A clear confirmation of the presence of a major unintentional grading of the CIGS composition was obtained by means of depth-resolved RAMAN spectroscopy, using a micro-Raman apparatus equipped with a confocal microscope (lateral spatial resolutions of approximately 1 µm). The spectrometer is calibrated at the silicon Raman peak of 520.6 $cm^{-1}$ before each measurement. The spectra were recorded at different sample depths for 30 s and 4 repetitions, while the peak fitting was carried out using a Lorentzian function. Figure 6.17 a) shows the peak-shift of the A1 vibrational mode of CIGS, while sampling the film along the growth direction of a Thin-CIGS/ITO cell from the CdS interface towards the back contact. As widely reported in the literature (98) (99), a change in the Raman Shift value of this peak corresponds to an almost linear variation of the gallium content, ranging from a minimum value for CIS to a maximum value for CGS with a total variation of about 10 $cm^{-1}$. Thus, the shift in Figure 6.17 a) corresponds to a variation of about 22% of the GGI index. A similar behaviour can be observed in Figure 6.17 b) for a Thick-CIGS/ITO cell, corresponding to a GGI variation of about 27%. Hence, LTPED-grown CIGS onto ITO seemed to nucleate with larger Ga content than expected and to

gradually diminish its GGI during the growth, until it stabilised after deposition of about 1µm-thick film. On the contrary only a negligible fluctuation in GGI value is observed in a typical cell deposited on a FTO back contact as reported in Figure 6.18 (Ga 2%-richer region in the centre of the absorber).

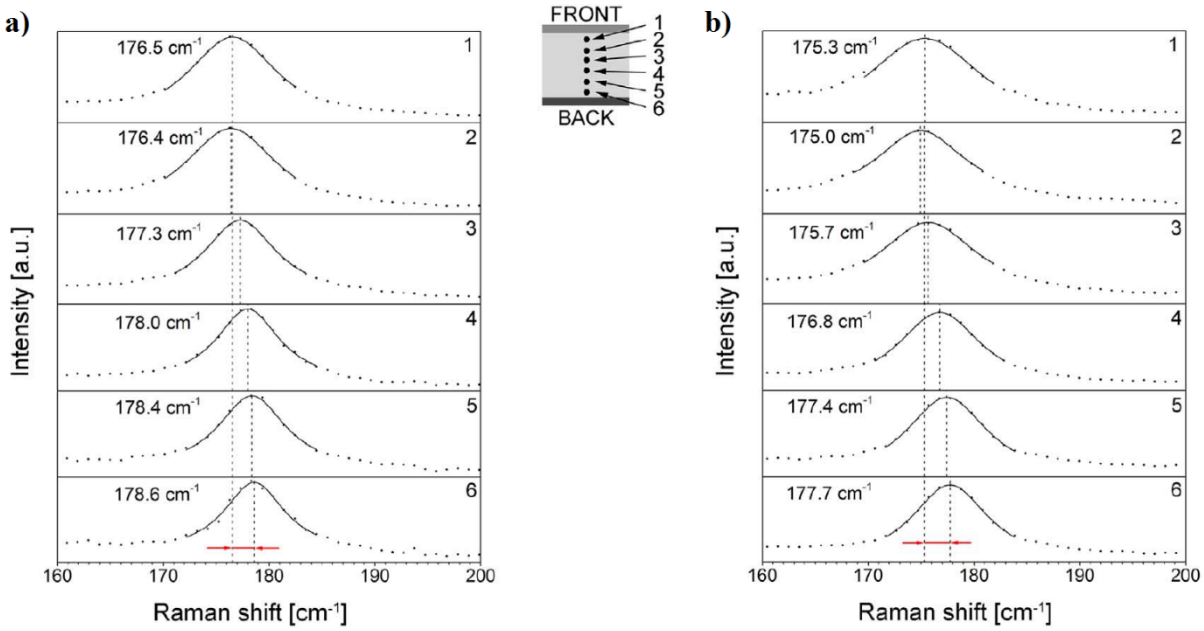


*Figure 6.17 - Normalized Raman spectra of a solar cell obtained by focusing the laser spot at different depths in the CIGS film, as depicted in the scheme at the top in the centre. Spectrum 1 refers to a region close to the front contact, spectrum 6 to the back contact. a) Thin-CIGS/ITO: the separation between the minimum and the maximum shift is about 2.2 $cm^{-1}$; b) Thick- CIGS/ITO: the separation between the minimum and the maximum shift is about 2.7 $cm^{-1}$*

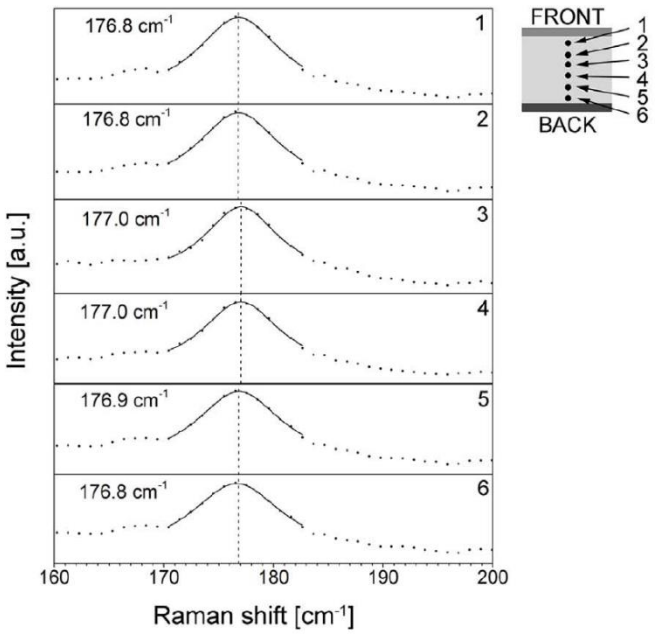


*Figure 6.18 - Normalized Raman spectra of a Thick-CIGS/FTO solar cell obtained by focusing the laser spot at different depths in the CIGS film, as depicted in the scheme at the right top corner. With FTO back-contact, no peak shift was observed along the growth axis of CIGS.*

This means that the unintentional grading of LTPED-grown CIGS is peculiar effect occurring in films grown on ITO back contacts. The unintentional increase of the gallium concentration in the CIGS films towards the CIGS/ITO interface is possibly related to the preferential reaction between gallium and oxygen reported, among others, by (100) (101).

Since the series resistance of the CIGS/ITO cells appeared to be comparable to the cases of CIGS/FTO and CIGS/Mo (Table 6.3 and Table 6.4), gallium oxide was not expected to be formed at the interface between CIGS and ITO. On the other hand, the same preferential reaction could favour the formation of a Ga-rich CIGS phase which was then likely to propagate along the growth direction despite the PED plume being much richer in Indium. This "memory" effect has been observed in PED growth of monocrystalline CIGS on Ge substrates (102) and it is likely to be strain-driven, as it has been in that case, due to the 3% lattice mismatch between CIS and CGS. Lattice relaxation at the scale of single grains and the propagation of defects, other than the grain boundaries, towards the active region of the solar cells could then explain the increase of the dark current and the consequently reduction of both FF and $V_{oc}$ with respect to a standard LTPED-grown solar cell. Preliminary admittance measurements as a function of temperature seemed to confirm that the density of electrically active defects in CIGS/ITO cells was much larger than in CIGS/Mo and CIGS/FTO solar cells.

### 6.4.4. The AZO affair

Among the TCO studied as back contact for bifacial solar cells, AZO was the only one showing awfully poor device quality with the Thick-CIGS absorber. As resumed in Table 6.3 and Table 6.4, these kinds of solar cells had series resistance double than ITO and FTO cases, while the shunt resistance is several times lower. As a consequence, they impacted the FF limiting it to maximum values of about 46%. $J_{sc}$ and $V_{oc}$ were affected as well. The reason of this behaviour is still an open question and therefore under investigation. Preliminary analyses seemed to confirm no gallium oxide is formed at the interface and CIGS grew with just a slightly Ga-richer first layer on AZO. The doping level of AZO back contact was close to ITO and FTO ones, so an ohmic contact was expected, as even suggested by JV characterisation of Au/CIGS/NaF/AZO/glass structure in Figure 6.3. The main suspects were pointing towards an Al diffusion into CIGS which may compensate the hole concentration and, in extreme cases, turning CIGS grains or grain boundaries into n-type. But, on the other hand, Al content is straightforward to achieve high doping level in order to create the $n^+/p^+$ ohmic tunnel junction. Sputtering depositions from AZO target with 5wt% alumina content (instead of 2wt%) were carried out too, but the absorbance of the resulting films below the band gap of the material was dramatically increased. Ongoing study about deposition of AZO with 5wt% alumina by means of PED demonstrated improved conductivity and light transmittance. Preliminary results with PED-grown AZO as back contact showed solar-cells front efficiency above 9%, close to the ITO case.

## 6.5. Conclusions

In this part of the thesis, bifacial CIGS solar cells with different absorber thicknesses were realised by means of Low Temperature Pulsed Electron Deposition on $n^+$-type FTO, ITO and AZO back contacts deposited on glass. Efficiencies up to 14.7% under 1 sun front illumination were achieved in the case of 1.85μm-thick CIGS absorbers deposited on FTO back contacts at 250 °C. Comparable results reported in the literature (91) have been obtained at growth temperatures >500 °C. LTPED showed that CIGS grown at 250 °C had front efficiency higher than CIGS grown by co-evaporation at 450°C-500°C onto FTO (η=13.7%) and close to the one grown at 520 °C on ITO (η=15.2%), as determined by (93). Simultaneous 1sun-front and 1sun-rear illuminations of the FTO devices showed equivalent efficiency up to 17%. Neither gallium-oxide formation nor TCO degradation was observed with the LTPED process.

The significant degradation of the cell fill factor with decreasing CIGS thickness to just above 1μm was found to be related to the presence of craters left behind by micro-fragments of CIGS target. These particulates, generated by a particular ablation mechanism (macroscopic ablation) of the CIGS targets, can be weakly incorporated in the film during the LTPED growth and removed during the subsequent process steps. A solution to reduce the particulate has been studied in past (103) and is currently being developed for deposition of ultra-thin (~300 nm) CIGS by LTPED process aiming to semi-transparent solar cells.

The low-temperature deposition of CIGS on ITO back contacts was found to induce an unintentional compositional grading of the gallium content of the CIGS films with a GGI variation as large as 27% between the CIGS/ITO interface (Ga rich) and the CdS/CIGS interface (closer to the composition of the target). This unintentional grading did not appear to affect the series resistance of the cell but to reduce both the shunt resistance and the Voc, possibly because of a high density of electrically active deep levels in the CIGS film. The lattice mismatch between the Ga-rich phase formed at the ITO interface and the stoichiometric phase associated with the composition of the ablation plume can provide the driving force for the formation of these defects. Future developments of this work will include high resolution analytical mapping of the CIGS/ITO interface by means of High-Resolution Transmission Electron Microscopy (HR-TEM).

Solar cells grown with AZO back contact had a very bad quality and their behaviour is under investigation. However, the devices obtained growing CIGS at 250 °C by LTPED on sputtered AZO showed efficiency larger than the ones grown at temperatures of 500 °C (0.04%) (93), which have had even poorer FF and almost negligible current since gallium oxide was formed at the interface and AZO deterioration occurred, increasing its resistivity probably because of Se incorporation.

Despite of these open problems, LTPED is on route to become a viable and low-cost production process for high-efficiency bifacial and semi-transparent CIGS solar cells. LTPED demonstrate FTO can be an

In-free alternative to ITO for TCO back contact. The results reported here were obtained on glass substrates as a first step towards the realisation of bifacial CIGS devices on lightweight, highly flexible and transparent substrates, like plastic materials or thin glass.

# 7. Zn(O,S) as Alternative Buffer

## 7.1. Alternative buffers

Until few months ago, the most efficient $Cu(In,Ga)Se_2$ solar cells necessitate a CdS buffer layer grown by chemical bath deposition. From early years of 2000', alternative buffer layers have been extensively studied by researchers to eliminate Cd content, avoid non-vacuum techniques, decrease absorption in 300nm-500nm spectral region and passivation of CIGS surface. Thanks to great efforts, up-to-date results show solar cells with alternative buffers at the top positions of the CIGS record board. Solar Frontier has recently achieved the stunning efficiency of 22.8% with Cd-free buffer layer (11). Other laboratories have demonstrated alternative buffered CIGS solar cells could reach high efficiency as shown in Table 6.1.

*Table 7.1 - List of high-efficiency Cd-free alternative-buffered CIGS solar cells (grey lines), with device parameters and manufacturers, compared to CdS best results (white lines). Data are related to small-area devices.*
*° not externally certified efficiency*

| **Producer** | **Year** | ***Buffer material*** | **Deposition technique** | $J_{sc}$ (mA/cm$^2$) | $V_{oc}$ (mV) | **FF** (%) | **η** (%) | Ref. |
|---|---|---|---|---|---|---|---|---|
| Solar Frontier | 2016 | ***Zn(O,S,OH) + (Zn,Mg)O*** | CBD + ALD | 41.4 | 711 | 77.5 | **22.8°** | (11) |
| | 2016 | ***Zn(O,S,OH)*** | CBD | 39.4 | 716 | 77.9 | **22.0** | (11) |
| | 2016 | CdS + *(Zn,Mg)O* | CBD + ALD | 41.6 | 714 | 77.4 | **22.7°** | (11) |
| | 2015 | CdS | CBD | 39.4 | 722 | 78.2 | **22.3** | (104) |
| ZSW | 2015 | ***Zn(O,S,OH) + (Zn,Mg)O*** | CBD + RF-Sputtering | 37.2 | 717 | 78.6 | **21.0** | (105) |
| | 2014 | ***$In_xS_y$*** | Evaporation | 34.8 | 655 | 74.9 | **17.1** | (106) |
| | 2016 | CdS | CBD | 37.8 | 741 | 80.5 | **22.6** | (12) |
| Uppsala University and Solibro | 2006 | ***Zn(O,S)*** | ALD | 35.5 | 689 | 75.8 | **18.5** | (107) |
| | 2010 | ***$Zn_{1-x}Mg_xO$*** | ALD | 35.7 | 668 | 72.2 | **18.1** | (108) |
| | 2013 | ***$Zn_{1-x}Sn_xO_y$*** | ALD | 35.1 | 689 | 75.3 | **18.2** | (109) |
| HZB | 2014 | ***Zn(O,S)*** | Sputtering | 38.4 | 654 | 72.8 | **18.3** | (110) |

A wide-ranging and updated overview of different buffer-layer and window-layer technologies are given in (111) and (1).

## 7.2. Buffer engineering

The fine tuning of the buffer layer properties to adapt it in the best way to the CIGS absorber is known as “buffer engineering”. When absorber and buffer are faced together, the properties of the resulting heterojunction are mainly influenced by the energy-bands structure and the physical interface. Each of these factors deserves detailed analysis since they are combinations of various aspects and may affect fill factor as well current and voltage output of the solar cell. Consequently, the deepest understanding of the materials and the finest control in their depositions are necessary to reach higher efficiency of alternative-buffered devices.

### 7.2.1. Band alignment at the pn-junction

The energy-band structure of a junction strictly depends on its materials. Despite silicon, CIGS is a direct band-gap semiconductor: no phonons are involved in the charge-carriers transitions and conduction and valence bands extremes are related to the same reciprocal-lattice orientation. The main phenomena to be considered in the study of the band line-up are the band bending, typical of pn-junction, and the band discontinuities, which are unavoidable in heterojunction solar cells for both conduction and valence band. Since absorber, buffer and TCO are not the same material, the energy gap and electron affinity of p-type and n-type semiconductors are obviously different, thus bringing to energy discontinuities at the interface. The CIGS absorber is the smaller bang-gap material of the solar cell, while the TCO has the wider energy gap. Between them, the buffer layer plays a central role in the device behaviour creating, towards the absorber, the so-called Conduction Band Offset (CBO): discrepancy in the conduction band of two facing materials. CBO is probably the most important energetic aspect of the junction, managing the electron transfer through it and hence affecting the nature of the solar cell, i.e. its efficiency. The offset may be either positive or negative, in some cases even zero. Figure 7.1 shows the band alignment for positive and negative CBO.

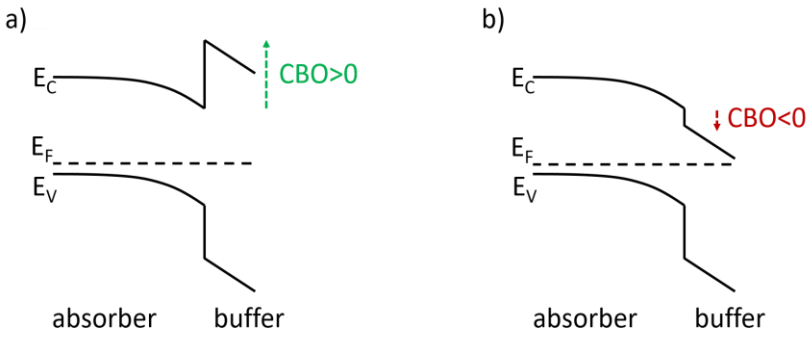


*Figure 7.1 - Examples of a positive (a) and a negative (b) conduction band offset between absorber and buffer layer*

A large positive CBO would be detrimental for the performance, introducing a high barrier for the electrons and consequently reducing their probability to overcome the obstacle, if not providing

additional energy to drive them towards the n-type TCO. On the other side, for negative CBO, theory predicts an increment of recombination probability due to the junction moved towards the physical interface.

However, theory suggests that excellent performance of solar cells can be achieved with a zero or small positive CBO between the CIGS and the buffer. $V_{oc}$ and FF are maximized for 0<CBO<+0.4eV. This CBO values are extremely healthy since CBO pushes the electrical pn-junction slightly into the CIGS, away from the physical material interface, without blocking the current. Moving the electrical junction below the surface of the absorber means turning the CIGS upper part into n-type, as pointed out by the position of the Fermi level. The new situation forming a CIGS homojunction is called "buried junction" and it is supposed to lower the interface recombination since the hole concentration at the interface is reduced. Actually, the CIGS surface has been observed to be already turned into n-type. Two different mechanisms have been proposed: Cd diffusion into the CIGS surface layer and Se vacancies ($V_{Se}^{+}$) at the CIGS surface. Se vacancies in the topmost layer could pin the Fermi level close to the conduction band. The CIGS surface would be turned n-type and the built-in electric field could be able to drive the migration of Cu atoms towards the CIGS bulk, generating Cu-poor phases called order vacancy or order defect compound (OVC or ODC). The inverted top-layer is expected to be thinner than 15nm and with doping level of $10^{11}$-$10^{12}$ $cm^{-3}$, orders of magnitude lower than the typical CIGS doping density of $10^{16}$ $cm^{-3}$, but comparable with a reasonable surface states density of $10^{12}$ $cm^{-2}$ necessary for the surface inversion. However, the CIGS exposure to air induces the passivation of $V_{Se}$ by oxygen which reduces the inversion. (112) (113) (114) (115) (116) (117) (118) (119)

In conclusion, for low positive or zero barrier height in the conduction band, the energy provided by the space-charge-region electric field to the electrons is enough to guarantee negligible losses during their extraction. At the same time, the further sink of electrical junction minimizes recombination at the interface. The bands alignment in CIGS solar cell is illustrated in Figure 7.2. It is remarkable to point out that CdS buffer layer provides a small positive CBO towards CIGS absorber, for a wide range of Ga content. The success of CIGS/CdS solar cells can be attributed to both favourable CBO and good interface properties. Unfortunately, enhancing the GGI ratio results in larger band gap, raising the $E_C$ of CIGS only, which brings to non-favourable CBO and lower efficiency devices. This might be the main reason for which CIGS solar cells buffered with CdS work so well for all CIGS compositions except the Ga-richer ones. (120)

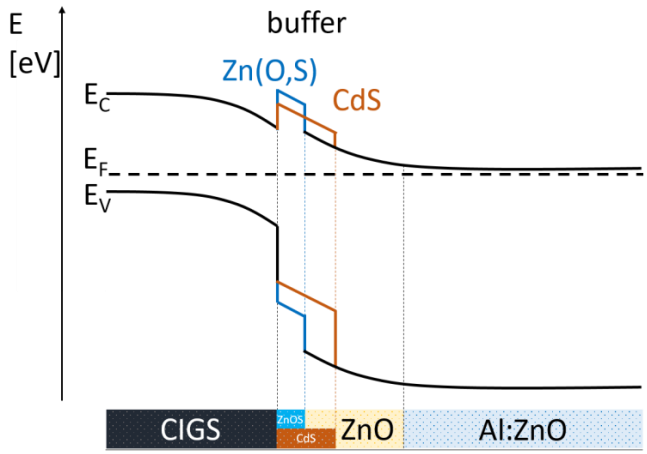


*Figure 7.2 - Typical CIGS solar-cell bands line-up with CdS or Zn(O,S) buffer.*

$Zn(O_{1-x},S_x)$ is a promising candidate to substitute CdS thanks to its tuneable band gap. Changing the composition, it is possible to vary the CBO (and energy gap) and find the most fitting one for the CIGS absorber. Considering the sulphur content *x* as the variable, one can range over from 3.2eV for *x*=0 (ZnO) to 3.6 eV for *x*=1 (ZnS), with a minimum of 2.6 eV at about *x*=0.45 due to the bowing. But the most interesting characteristic is the trends of valence band and conduction band, which are not linear with the sulphur content. Remarkably, the conduction band value is almost constant from *x*=0 to about *x*=0.45 and then starts to increase, while the valence band has the opposite trend increasing with the S content until *x*=0.5 and then remaining constant, as shown by Figure 6.3. (121) (122)

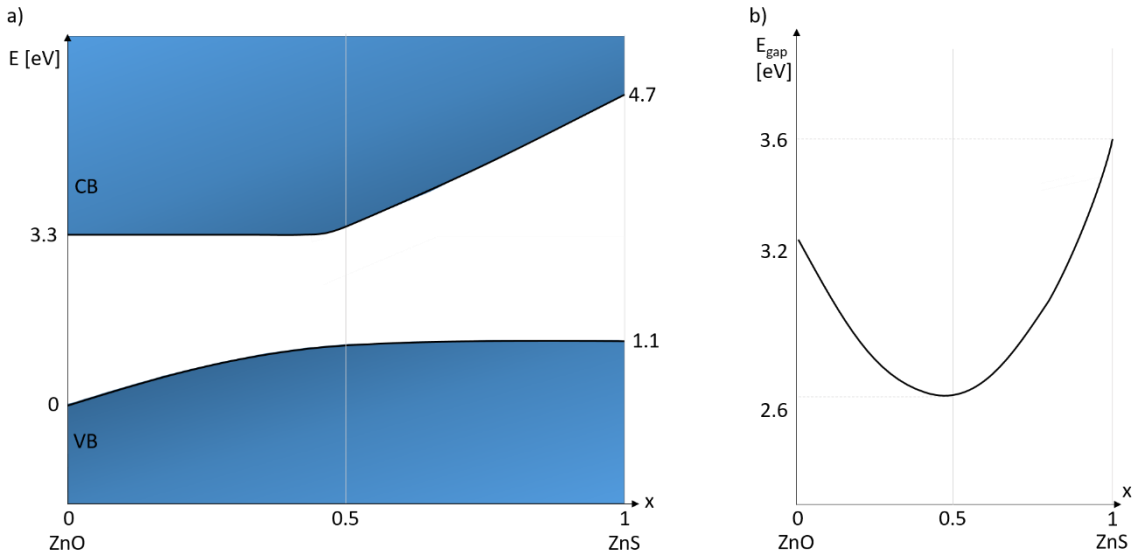


*Figure 7.3 – Schematic representation of $Zn(O_{1-x},S_x)$ valence and conduction bands (a) and energy gap (b) in function of its composition x (sulphur content), as found in literature: (121) (122)*

The CBO formed by Zn(O,S) towards CIGS depends both from the buffer composition (S content) and the absorber composition (Ga content) at the interface. Table 2 gives an overview of $Zn(O_{1-x},S_x)$-CBOs in function of its composition for a CIGS-GGI of 30%, compared with CdS buffer. ZnO has a negative

CBO towards CIGS. Increasing the S content, CBO turns positive only for *x*>0.5. The same CBO height of CdS (+0.3 eV) is reached for S content slightly higher than 0.7. Later, the CBO abruptly rises, following the increasing of the Zn(O,S) conduction band and causing the current block for CBO >0.5 eV. This phenomenon is highlighted in the JV measurements by the so called "roll-over-effect", which is tremendously detrimental for the device behaviour, since causes the FF dropping and may even result in $V_{oc}$ and $J_{sc}$ loss. (121) (122) (123)

*Table 7.2 – Energy gap and relative CBO formed towards CIGS-GGI=30% of ZnO, CdS and Zn(O,S) buffer layers.*

| Buffer | S content (x) | Buffer $E_G$ (eV) | CBO (eV) |
|---|---|---|---|
| CdS | - | 2.4 | +0.3 |
| ZnO | - | 3.3 | -0.2 |
| $Zn(O_{1-x},S_x)$ | 0.3 | 2.7 | -0.2 |
| $Zn(O_{1-x},S_x)$ | 0.5 | 2.6 | -0.1 |
| $Zn(O_{1-x},S_x)$ | 0.7 | 3.0 | +0.2 |
| $Zn(O_{1-x},S_x)$ | 0.8-0.9 | 3.2 | +0.7 |
| ZnS | 1 | 3.6 | +1.2 |

### 7.2.2. Physical interface

The conduction band offset is probably the most important parameter to be taken in account when studying the improvement of buffer layer in CIGS-based solar cells, but it is not the only one. Several other factors should affect the CIGS/buffer interface formation and the role they play is strictly connected to the material used as buffer and the deposition technique and process applied.

Among the huge variety of interface features, the key parameters to obtain high-efficiency CIGS-based solar cells are:

- post-deposition treatment with alkaline compounds;
- CIGS surface sulfurization to passivate Se vacancies and lower the position of the absorber $E_V$;
- enhanced inversion of the absorber interface region due to the doping (by Cd or Zn) of CIGS surface;
- low Ga content in the uppermost CIGS layer to reduce the point-defect concentrations;
- lattice matching between CIGS and buffer layer;
- alkaline (Na or K) doping of CIGS grains close to the surface to control the CIGS doping in the SCR;
- CIGS roughness, to be reduce to avoid shunt paths due to non-conformal growth of the buffer.

All of them are suggested to play a crucial part in the success of CIGS/CdS-junction solar cells. For this reason, it is highly recommended to understand how their role changes when using alternative buffer layers and processes different then chemical bath deposition.

## 7.3. Zn(O,S) by Atomic Layer Deposition

This project of doctoral research on Zn(O,S) buffer layers grown by atomic layer deposition was carried out at the Ångström Laboratory at Uppsala University, Sweden. The internship in the Thin Film Solar Cells Group of Solid State Electronics division and the relative period in Uppsala were financially supported by C.M. Lerici Foundation. The absorber material deposited by means of co-evaporation was provided by Solibro Research AB. The CIGS grown by PED was fabricated at IMEM-CNR of Parma.

### 7.3.1. The ALD technique

Atomic layer deposition (ALD) is a low-vacuum chemical thin-film growth technique capable to deposit materials with unique properties. Atomic-level control and robustness of the ALD process result in films with extremely high thickness uniformity, composition homogeneity, total absence of pinholes and negligible stress. Additionally, the excellent reproducibility makes the ALD technique suitable for industrial production if the lowered growth rate associated with ALD can be managed.

ALD is based on an iterated sequence of self-saturated chemical reactions between the substrate and gas species. Each iteration is called deposition "cycle". Gas species, known as "precursors", are injected one at a time in the growth chamber so that they are delivered to the substrate separately in order to avoid them to mix and react with each other. Each injection is called "pulse". The first precursor gas reacts with the substrate surface, depositing a single material layer. Then, the gas is pumped away and the chamber is purged with an inert gas to remove any excess of the first reactant except for a chemisorbed layer. Later, the second precursor is pulsed into the chamber, followed by another cleaning process, and ALD cycle is completed. The purge pulses are intended to avoid the precursor species to be present at the same time in the deposition chamber. This will cause a chemical vapour deposition (CVD) type process, which results in loss of process control of film thickness and uniformity. The system is designed to let the precursor gas flow in a uniform laminar manner over the surface of the heated substrate, until it reaches the exhaust pipe to be pumped away. In this way, the precursor interacts with the substrate and chamber walls only, reacting uniformly on the whole substrate surface. Besides the reactor geometry, other important parameters for the film growth in ALD process are:

- the choice of precursors, which determines the film composition;
- the pulse duration, to originate a self-terminating chemical reaction;
- the number of ALD cycles, determining the thickness of the film;
- the substrate temperature, that controls the activation of the chemical reactions and the film microstructure. Good film properties can be obtained at different temperatures, but the precursor must be able to react (enough temperature) and to not decompose or desorb from the sample surface (too high temperature).

At a suitable condition, the ALD process produce a reaction between substrate and precursors to nucleate a layer avoiding any decomposition, desorption, incomplete reactions, etc. Several ALD cycles perform a layer-by-layer deposition, where the resulting film is highly conformal even on rough substrate materials such as solar cell absorbers.

Precursors are volatile compounds stocked in bottles, where liquid or gas state precursors with higher vapor pressure are usually easier to control. During film growth, they are transported by a carrier gas which carries the source molecules into the deposition chamber. Here metal-organic compounds are necessary as metal source materials due to the lower deposition temperature aimed for, despite of their cost.

The ALD system utilized for this study is a home-built machine with a process chamber of stainless steel. The maximum sample dimension is 12.5 × 12.5 $cm^2$ and once the sample holder is loaded in its position it is part of the rear side of the deposition chamber, resulting in a gas volume with 2 mm height over the entire size of the substrate. The inner walls of the camber and the substrate are warmed up by external heaters at temperature of 125 °C. This temperature is kept constant for all the duration of the ALD growth and it is the same for each sample of this project. For the Zn(O,S) growth, Diethyl Zinc ($Zn(C_2H_5)_2$, DEZ) is used as zinc precursor and water vapour ($H_2O$) and hydrogen sulphide ($H_2S$) as oxygen and sulphur suppliers, respectively. During the ALD process, nitrogen ($N_2$) is used as carrier gas resulting in a nominal pressure of 2 mbar. The introduction of the precursor gases into the $N_2$ steam is obtained by means of fast switching valves. The chamber is flooded with nitrogen for 5 seconds after every precursor pulse in order to purge the system, i.e. to remove excess of precursor between one pulse and the other. The amount of precursor compound injected into the reaction chamber for each pulse is proportional to the opening time of its valve, which are 250 ms for DEZ and 500 ms for $H_2O$ and $H_2S$. The pulses sequence of an ALD cycle for a single-layer deposition of ZnO is DEZ/$N_2$/$H_2O$/$N_2$ and for ZnS is DEZ/$N_2$/$H_2S$/$N_2$, as shown in Figure 7.4. Zn(O,S) film are grown alternating these two kinds of ALD cycles, whose ratio determines the buffer composition or sulphur content, which is called a super cycle approach. (107)

Before the deposition, a starting procedure is carried out to keep the system always in the same condition. Once the sample is introduced into the system and closed off from the load compartment, the chamber is pumped down to a base pressure of $5\times10^{-6}$ mbar by means of a turbopump. Then it is flooded to 20 mbar of $N_2$ and 20 minutes are waited in order to let the sample thermalize at the desired temperature of 125 °C. Later, the system is pumped to 2mbar before starting the cycles of ALD growth.

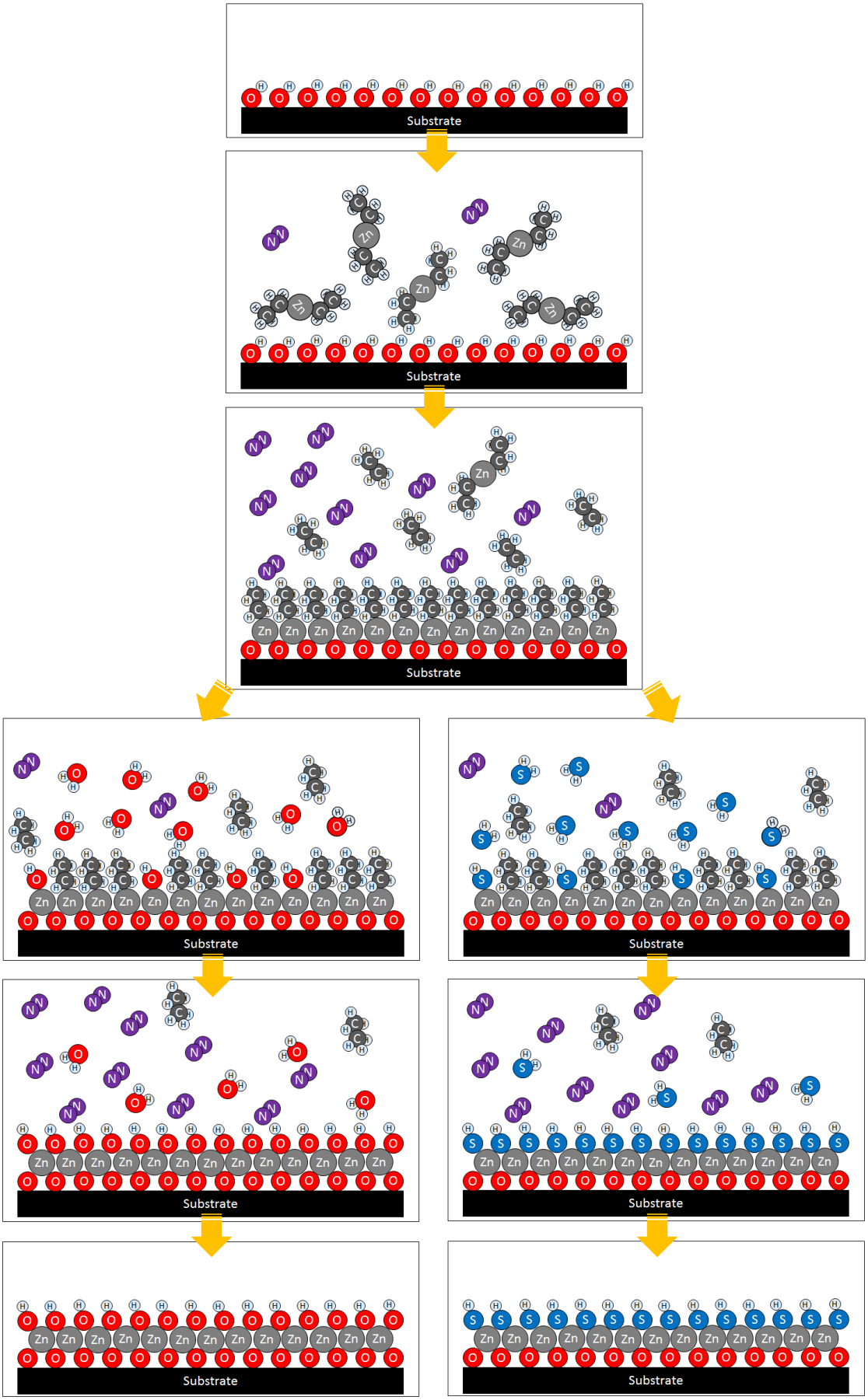


*Figure 7.4 – Schematic representation of an ALD cycle for depositing a ZnO (left branch) or a ZnS (right branch) layer.*

### 7.3.2. Preliminary results

Preliminary studies were carried out to determine the parameters of ALD growth, such as growth per cycle (GPC) and sulphur content in function of the precursor ratio. The $Zn(O_{1-x},S_x)$ layer composition ($x$) was controlled by the ALD pulsing sequence: the ratio between the number of cycles with $H_2O$ and the number of cycles with $H_2S$. The thickness of the buffer layer was indeed determined by the total number of cycles. Preliminary runs on 12.5 × 12.5 $cm^2$ soda-lime-glass substrates were performed in order to evaluate possible CVD growth, determine the deposition rate and find out how $Zn(O_{1-x},S_x)$ composition varies in function of $H_2S/H_2O$ cycles ratio.

CVD phenomena during an ALD process are detrimental. They are due to precursor gases not removed during the purging: if the two precursors, DEZ and $H_2O$ or $H_2S$, are mixed together in the chamber, they may react with each other on the substrate or in the gas phase and form additional ZnO or ZnS deposits on the substrate. This means atomic layer deposition unique advantages (uniform films with good step coverage and accurate thickness control) are lost in favour of a time-dependent fast growth process. Moreover, compositional control may be lost as well. CVD is usually observed by a much-increased deposition rate (thickness/time) and large differences in film thickness over the substrate surface. A series of depositions with constant $H_2S/H_2O$ cycles ratio (1/6) verified that the thickness of Zn(O,S) layer had a linear relation with the number of cycles, with an incubation period of about 3-4 cycles (see Figure 7.5) and a GPC compatible with an atomic layer deposition, and thus demonstrating negligible nucleation and CVD phenomena were occurring.

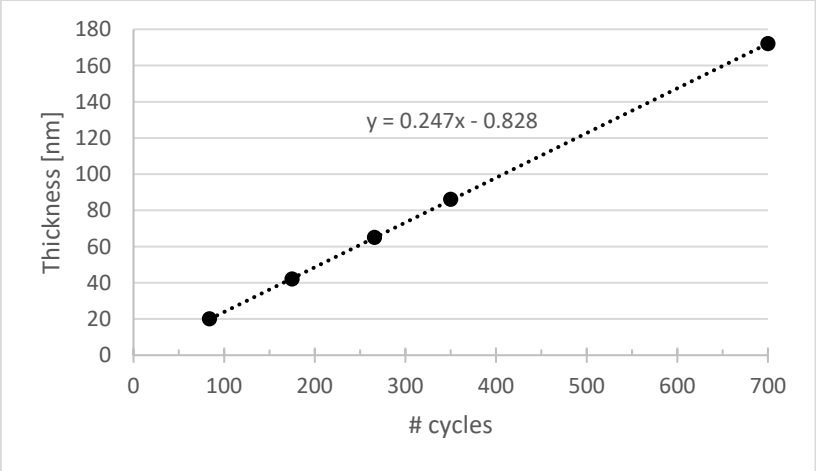


*Figure 7.5 - Zn(O,S) thickness by profilometer vs number of ALD cycles*

From the same series, the GPC for $H_2S/H_2O$ cycles ratio of 1/6 was calculated to be 0.25 nm/cycle. The thickness was evaluated by profilometry analyses of etched steps in films grown on glass substrate. Zinc and sulphur contents were determined by means of X-Ray Fluorescence (XRF), subtracting the glass contribution, and exhibited linear trends in respect of the number of ALD cycles (See Figure 7.6).

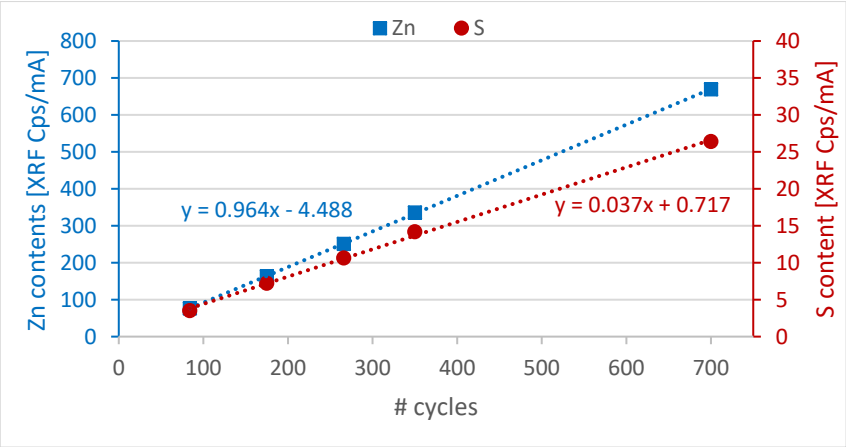


*Figure 7.6 - Zinc (blue squares, left axis) and sulphur (red circles, right axis) XRF counts vs number of ALD cycles.*

Figure 7.7 shows that S/Zn ratio was not constant changing numbers of ALD cycles, even if the same ALD recipe ($H_2S/H_2O$ cycles ratio of 1/6) was applied: sulphur content seems to increase in the thinner films. However, a sulphur gradient have been observed in Zn(O,S) thin films and could be attributed to an interface region slightly more richer in sulphur (122).

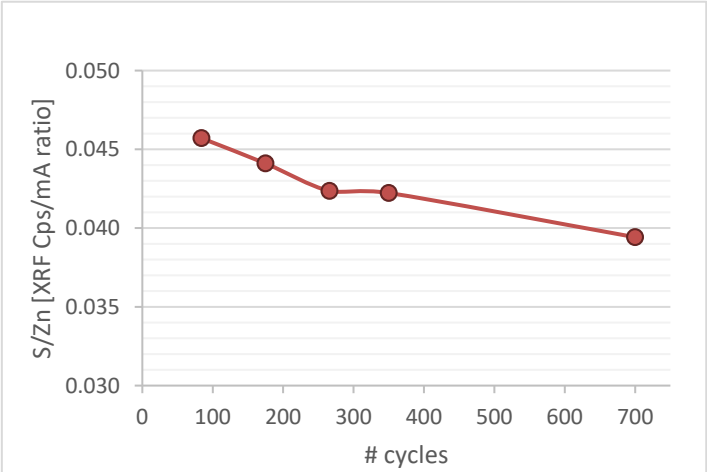


*Figure 7.7 - Ratio between sulphur and zinc XRF counts in function of the number of cycles, for as detected and glass-contribution corrected data.*

For the 12.5 × 12.5 $cm^2$ soda-lime-glass substrates used in this study, the Zn(O,S) homogeneity was good in terms of both thickness and composition, except for two corner regions affected by more than 5% absolute variation of sulphur content. Bad precursor diffusion during the $H_2S$ and $H_2O$ pulses should be the cause. However, a central area of about 5 × 5 $cm^2$ was found to have the best homogeneity and therefore was the one used for the sulphur content determination and the further depositions on CIGS.

The $Zn(O_{1-x},S_x)$ composition was evaluated using the S/Zn XRF-counts ratio for films on soda-lime glass substrates. The sulphur content *x* was calculated from XRF data on samples grown with different $H_2S/(H_2S+H_2O)$ cycles ratio (from now on *precursor ratio* or *ALD recipe*). Starting from a pure ZnS deposition, in which no water pulse was applied, the overall $H_2O$ cycles (i.e. the oxygen dose) was increased until the precursor ratio of 1/25, maintaining the same number of cycles for each recipe.

Following the results of Platzer-Björkman in (122), the S/Zn XRF-counts ratio of the pure zinc sulphide was kept as reference to calculate the compositions obtained with the other recipes:

$$S/Zn^{XRF}{}_{(ZnS)} : 1 = S/Zn^{XRF}{}_{(recipe)} : x_{(recipe)} \longrightarrow x_{(recipe)} = \frac{S/Zn^{XRF}{}_{(recipe)}}{S/Zn^{XRF}{}_{(ZnS)}}$$

This calculation is made assuming to have always stoichiometric compounds, that means the same number of cations and anions in the Zn(O,S). In this hypothesis, oxygen compensates the lack of sulphur so that in the material the ratio between Zn and (O+S) is always 1:1. The sulphur content in function of the precursors ratio is shown in Figure 7.8: it increased rapidly for lower $H_2S$ doses, then the trend slope is abruptly lowered after $H_2S/(H_2O+H_2S)$ cycles ratio of about 0.3, at which the S content was already approximately 0.8. Reproducibility study revealed compositional error is within 4% for each recipe.

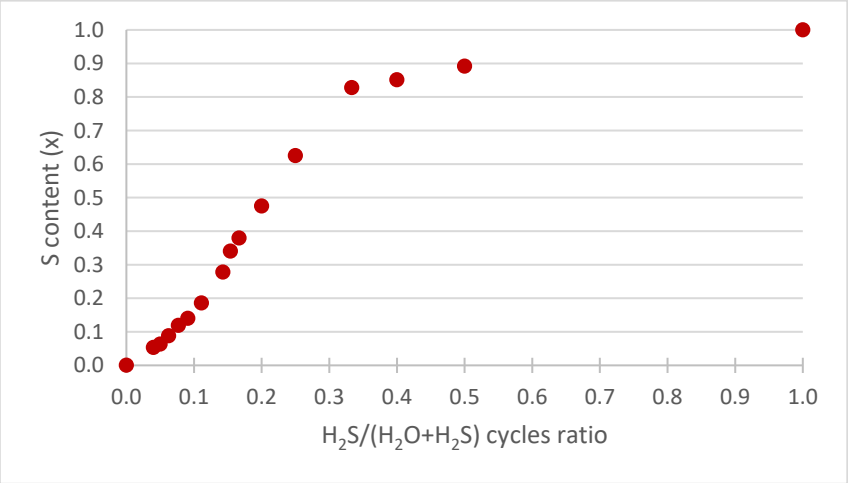


*Figure 7.8 - $Zn(O_{1-x},S_x)$ sulphur content x in respect of precursor ratio, for films grown with approximately 175 ALD-cycles.*

For this compositional study, the thickness of the films, measured by profilometer and XRR, showed a trend in function of the Zn(O,S) composition: starting from poor S content GPC slightly decreased, until it dropped at high sulphur inclusion, $x$>0.85 (see Figure 7.9). Moreover, the Zn deposition rate (evaluated by its XRF counts per cycle) revealed that the more sulphur in the film, the thinner the film itself. This could be caused by different reaction kinetics of $H_2S$ and $H_2O$. However, the Zn rate dropped much more than the deposition rate, in fact $Zn(O_{1-x},S_x)$ density depends on the composition since crystalline ZnO grains have a density of 5.6 g/cm$^3$ and ZnS phases of about 4.0-4.1g/cm$^3$.

Pure ZnS films showed better homogeneity on the whole 12.5 × 12.5 cm$^2$ soda-lime-glass samples than Zn(O,S) and ZnO ones: variations of Zn rate and S/Zn ratio were determined to be below 5% absolute. Therefore, the higher discrepancies in the corner regions of Zn(O,S) samples could be imputed to the water flux in the ALD chamber. For the 5 × 5 cm$^2$ central area, reproducibility of Zn(O,S) layers was found to be good, the error in the S content was evaluated to be about ±2% (absolute) for each recipe. This study was a necessary starting point to test the atomic layer deposition of Zn(O,S) on commercial

co-evaporated CIGS by Solibro Research AB company and on pulsed electron deposited CIGS by IMEM-CNR of Parma.

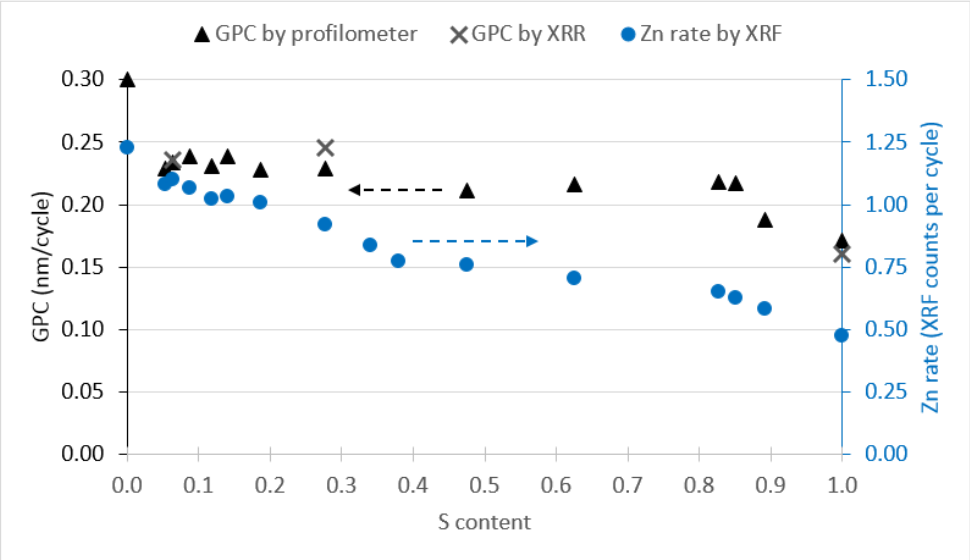


*Figure 7.9 - GPC (black triangles for thickness determined by profilometer and black cross for XRR, on the left axis) and Zn-content rate (determined by XRF, blue circles, right axis) in function of S content.*

### 7.3.3. State-of-the-art of ALD-Zn(O,S) grown on CIGS

The Ångström Laboratory of Uppsala University has developed atomic-layer-deposited Zn(O,S) buffer layer for Cu(In,Ga)$Se_2$ solar cell, demonstrating the high potential of this technology. Material and electrical properties of the resulting junction have been investigated. The ALD recipe for the growth of Zn(O,S) have been adjusted changing the precursor ratio to optimize the CBO for different Ga content of CIGS: interestingly, moving the absorber GGI from 0 to 1, the maximum in device efficiency have been found for the same ALD Zn(O,S) recipe for all GGI values. ALD-Zn(O,S) buffered solar cells and mini-modules have shown efficiency comparable or higher than CdS ones, mainly due to a current increase. These important results have been obtained despite a particular growth mechanism that has been proposed by Hultqvist (124). The hypothesis, supported by experimental evidence, suggests that thin films of ALD-Zn(O,S) grow with two main characteristics: a larger S content at the interface with CIGS and a structure composed by two different phases.

TEM measurements have revealed Zn(O,S) films grown on CIGS are a mixture of hexagonal ZnO grains, containing some sulphur, and a S-rich amorphous phase. These two phases have different electrical properties, which differently affect the pn-junction and thus also the solar cell behaviour. The hexagonal oxygen-rich Zn(O,S) grains form a negative CBO towards CIGS, whereas the sulphur-rich phase forms a positive CBO with CIGS and is assumed to have better electrical surface-passivation properties (125) (30). Moreover, the first layer of Zn(O,S) corresponding to the interface region, which has the stronger influence on the device quality, has been found to have larger sulphur content than the

one revealed in the rest of the film and expected by the applied ALD recipe. Thus, a sort of bilayer is formed, the interface layer having larger inclusion of amorphous phase than the top one.

The nanostructure of ALD-grown Zn(O,S) film on CIGS is tentatively described by Figure 7.10. Starting from a pure ZnO deposition and increasing the S dose (i.e. the $H_2S/H_2O$ cycles ratio), the oxygen-rich grains gradually decrease and the sulphur-rich phase expands in both the interface and top layers. Initially, it pushes up both $V_{oc}$ and FF because of enhanced surface passivation by S (126) (127) and of lower recombination, due to less junction area with negative CBO. At a certain point, the increasing S content causes the S-rich phase to be predominant and to have a high CBO barrier towards CIGS. The outcome is first a FF and $V_{oc}$ decline and later, when too many or all the oxygen-rich grains disappear (in the case of deposition of pure ZnS), a $J_{sc}$ drop. Accordingly, there is a trade-off in the S content and thus an optimal precursor ratio, which could maximize FF and $V_{oc}$.

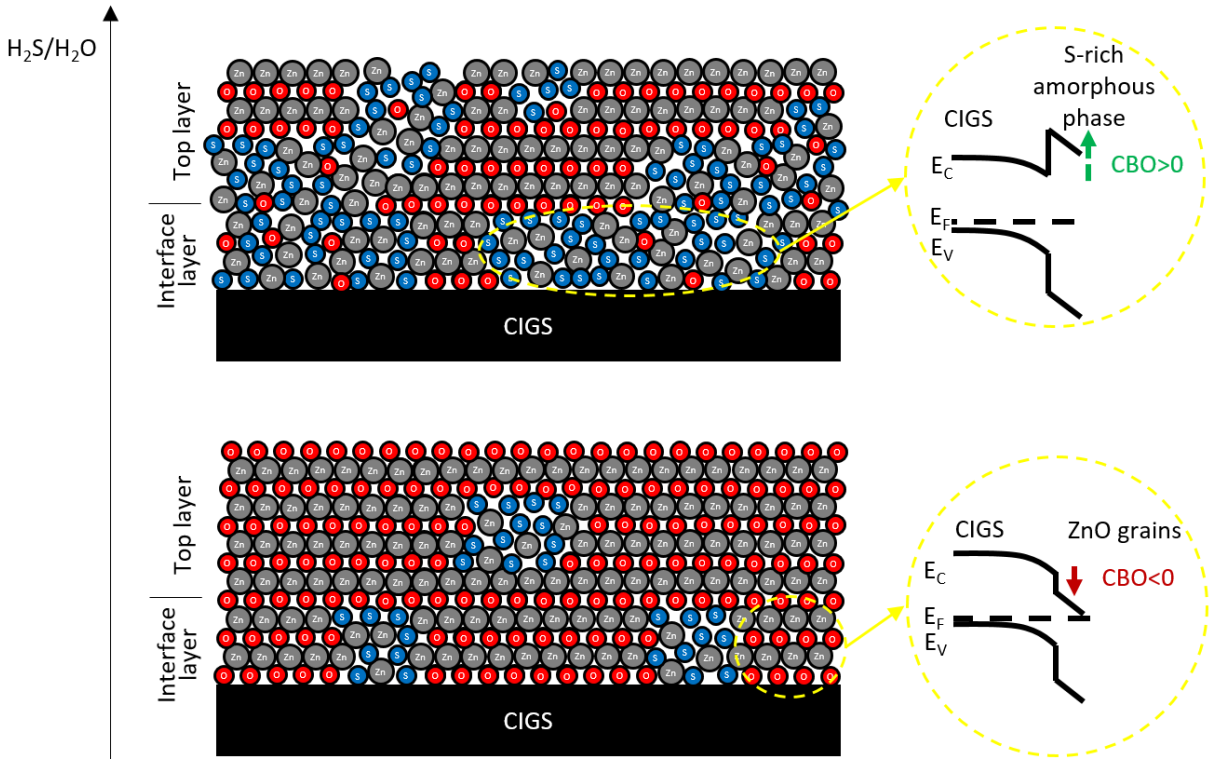


*Figure 7.10 - Illustration of the growth mechanism for the hypothesized Zn(O,S) bilayer and the resulting CBO towards CIGS for the two phases. Blue, red and grey circles indicate sulphur, oxygen and zinc atoms respectively. It is assumed that, enhancing the ratio of ALD-cycles with $H_2S$, the increasing S content promotes interface layer with higher S-rich amorphous phase to the detriment of hexagonal ZnO grains and consequently forming larger junction area with positive CBO.*

The S-rich amorphous phase in the interface region is expected to have higher S content than the top layer, hence the CBO of the junction is greater than the expected one by the applied recipe. Figure 7.11 shows a schematic representation of how the junction bands offsets in CIGS solar cells should be when buffered with ALD-Zn(O,S), because of the bilayered structure. (128) (129) (130) (131) (132) (133) (134) (135)

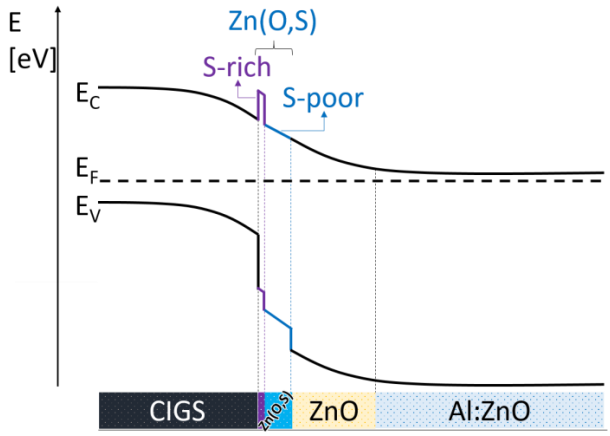


*Figure 7.11 - ALD-Zn(O,S) band alignment towards CIGS.*

## 7.4. ALD-Zn(O,S) buffer layer for co-evaporated CIGS

Atomic-layer-deposited Zn(O,S) buffer layer were grown on co-evaporated CIGS. Varying Zn(O,S) composition and thickness, the best ALD buffer recipe was found to result in solar cells more efficient than the CdS reference. Moreover, pure ZnS thickness study and Zn(O,S) interface variation were carried out. Hypothesis on the buffer growth was proposed to describe the composition and thickness trends.

The CIGS used for this study is commercial material provided by Solibro Research AB Company, grown on Mo-coated glass substrate by a co-evaporation process. No further detail about the absorber material can be released. Each CIGS sample was part of the same production batch so elevate uniformity from sample to sample was assumed. CIGS had been covered with a 30nm-thick capping-layer of CdS by CBD, with the same processed used for in-line solar-cells industrial production, and then stored under constant nitrogen flux to preserve it from degradation.

Each sample was cut in $5\times5cm^2$ and afterwards etched in HCl 5%wt for 1 min to remove the CdS capping layer, just before the Zn(O,S) deposition. After the ALD growth, the window layer was completed depositing 70nm of un-doped ZnO and 350 nm of Al-doped ZnO, both by RF-sputtering in $5\times10^{-3}$ mbar argon pressure at a power density of 200 and 300 $W/cm^2$, respectively. The samples were processed at room temperature. For AZO, a target with composition of $ZnO:Al_2O_3$ 1%wt is used and results in films with sheet resistance of about 40 $\Omega/cm^2$. On the top, a 50nm-Ni/2µm-Al/50nm-Ni fork-like grid was then deposited by means of electron-beam evaporation, through a shadow mask. In the end, each sample was mechanically scribed into 16 $0.5cm^2$ solar cells. The QE of the devices was first measured to accurately calibrate the solar simulator and to determine the correct current of devices, taking in account 2.5% current loss due to grid shading. The QE illumination spot size is 1 $mm^2$ and the wavelength step of 2nm or 5nm was chosen, starting the sweep at 300 nm and ending it at 1200 nm. No voltage bias was applied and no light bias as well. Then, IV curves were taken under AM 1.5g simulated illumination,

starting from -0.5 V until +1 V, with 0.005 V voltage step (301 points). The samples temperature was controlled with a cooling plate, ranging between 297 K and 300 K. For both QE and IV measurements, two golden tips soldered to wires were used as probes: the first tip is connected to the front aluminium contact, the other one to an indium contact previously soldered on the naked molybdenum all along the perimeter of the sample. Note that no potassium treatment of CIGS surface was carried out and no anti-reflection coating was applied; moreover, the measurements were conducted without any post-fabrication annealing or light soaking treatment of solar cells.

The $Zn(O_{1-x},S_x)$ compositional study was conducted testing precursors ratio $H_2S/(H_2S+H_2O)$ from 0.13 to 0.20, corresponding to nominal S content from 0.23 to 0.47, at a constant cycles number of 175, i.e. about 40nm-thick films. The trends of $V_{oc}$, $J_{sc}$, FF and efficiency of samples mean values are displayed in Figure 7.12. Few devices were accidentally scratched and resulted in shunted solar cells, which were excluded by the mean-values calculation of device parameters.

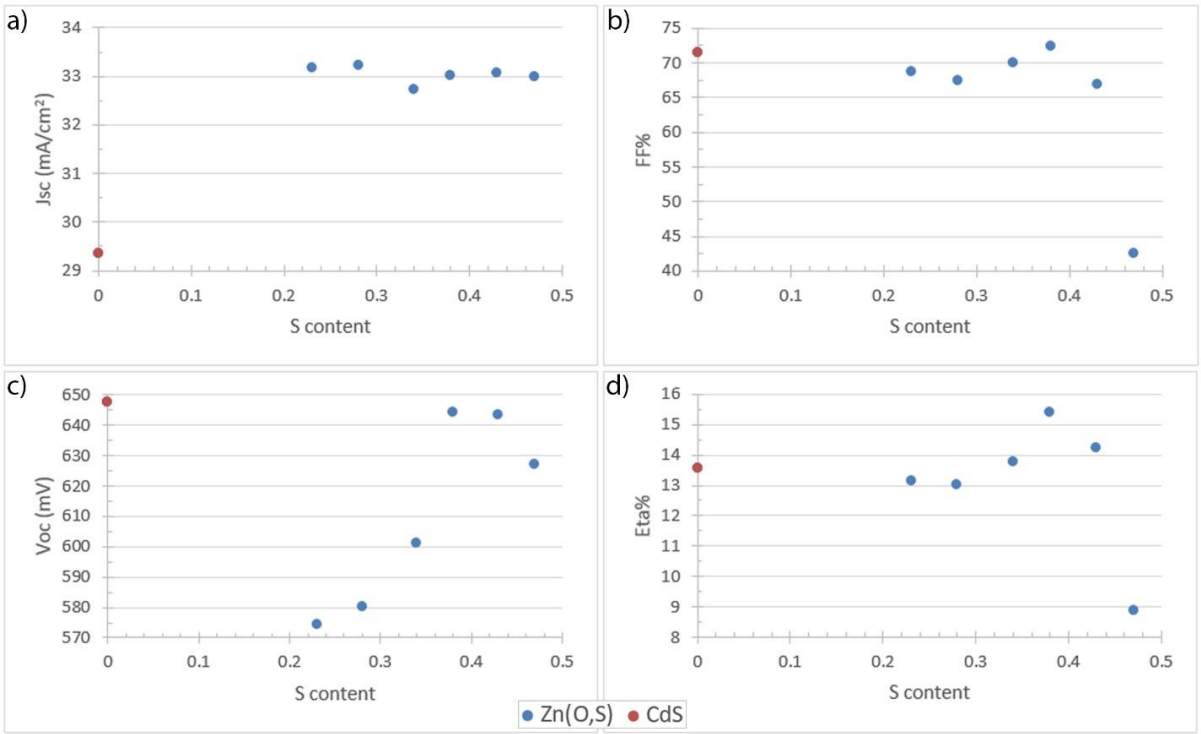


*Figure 7.12 – Mean values of $J_{sc}$ (a), FF (b), $V_{oc}$ (c) and η (d) in function of $Zn(O_{1-x},S_x)$ composition x.*

The device short-circuit current density is nearly constant with the S content and about 3.5 $mA/cm^2$ larger than the CdS samples. As pointed out by QE analyses shown in Figure 7.13, the current gain with the alternative buffer is mainly due to the extended transparency region. CdS (red line in Figure 6.13) absorption kills the device response below 516 nm, which correspond to the CdS band gap of 2.4 eV, and so the QE drops. Indeed, the larger bandgap of Zn(O,S), coupled with its lower thickness, allows more photons of that spectral region to reach the CIGS. Moreover, the QE curves of Zn(O,S) buffers are higher even in the rest of the spectra, symptom of improved interface quality. Average $V_{oc}$ rapidly increases with the S dose until $x$=0.38, almost reaching the same CdS value of about 648mV, then

remains constant for a small interval and eventually starts to decrease as the S content is further enhanced. Similarly, FF shows a small peak at *x*=0.38 and then it drops abruptly because of a blocking behaviour. The efficiency of the devices follows the same trend as FF, but due to the $V_{oc}$ increment, η is more peaked on the *x*=0.38 value. Zn(O,S) with *x*=0.38 corresponds to the best sample of the present study and is obtained by the precursor ratio of 0.17. The CIGS sample buffered with $Zn(O_{0.62},S_{0.38})$ is even the most homogeneous one among the composition series: standard deviation on 7cm$^2$ sample (14 devices) is 0.4 mA/cm$^2$ for $J_{sc}$, 6 mV for Voc, 1.6% absolute in FF and then 0.5% absolute in efficiency.

The trend of the most efficient solar cell of each sample is in accordance with the mean values, although to some extent more scattered and obviously shifted towards higher values: $J_{sc}$ slightly bigger, FF is 3-4 points larger, $V_{oc}$ gains 5-20 mV and, in the end, η is 0.5-1.5% greater.

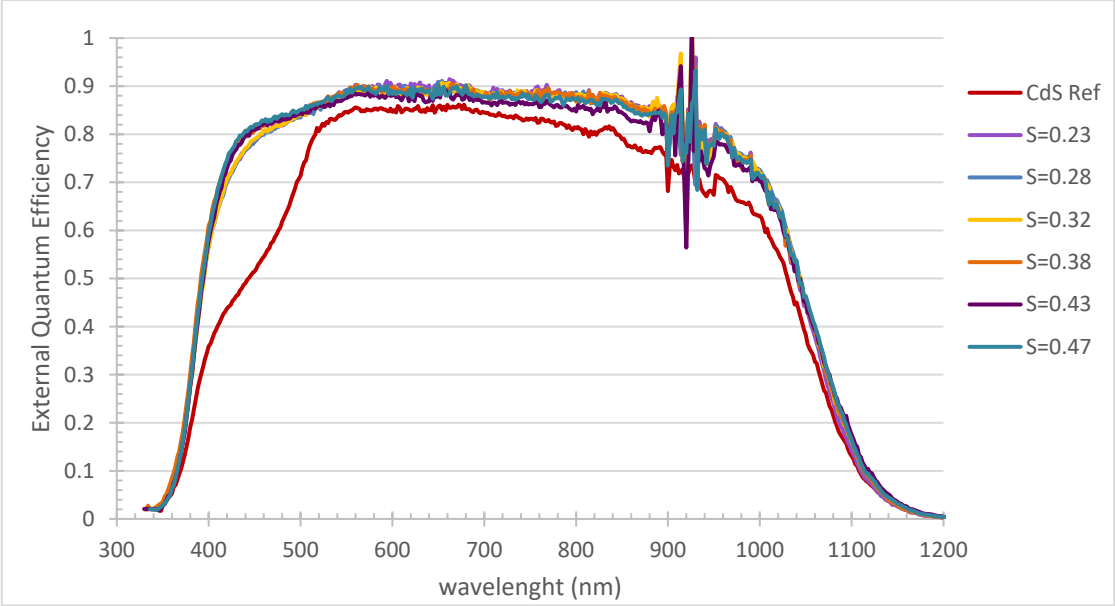


*Figure 7.13 – External quantum efficiency spectra of CIGS solar cells buffered with $Zn(O_{1-x},S_x)$ at different composition x and with CdS (red line). The curves are related to the best solar cell of each sample. The spikes occurring between 900nm and 945nm are interferences due to experimental setup.*

Subsequently the compositional study, a thickness series was carried out. From previous calibration, a GPC of 0.23 nm/cycle was determined on glass and confirmed on CIGS. The thickness of Zn(O,S) buffer layer was varied from 6nm (corresponding to 24 cycles) to 69 nm (350 cycles) and the results are shown in Figure 7.14. For classic CIGS solar cell structure, with i-ZnO and AZO by sputtering as TCO (blue spots in the graphs), the average performances of solar cells reveals $J_{sc}$ is fairly scattered with the buffer width but almost constant between 33 mA/cm$^2$ and 33.5 mA/cm$^2$, with the exception of the thicker buffer sample whose mean current density is more than 1 mA/cm$^2$ larger.

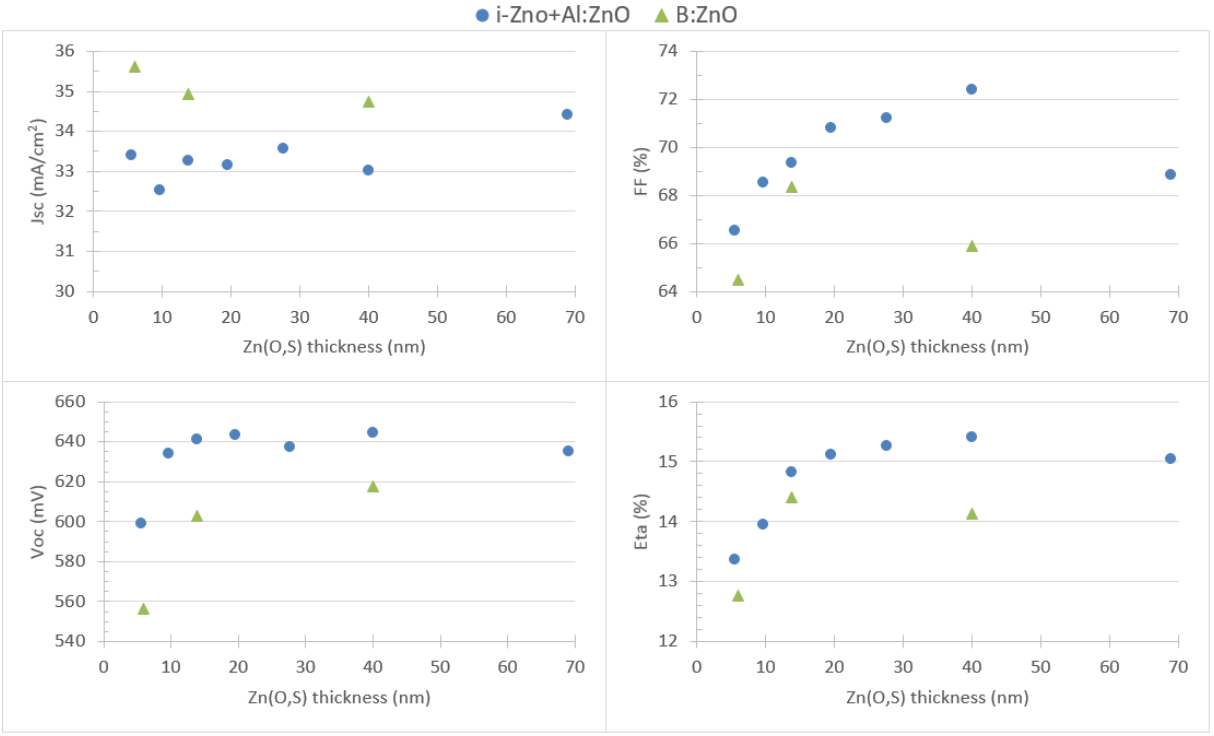


*Figure 7.14 - Mean values of $J_{sc}$ (a), FF (b), $V_{oc}$ (c) and η (d) in function of $Zn(O_{1-x},S_x)$ thickness at fixed composition x=0.38, with different TCO: the classic sputtered intrinsic-ZnO/aluminium-doped-ZnO structure (blue spots) and the boron-doped ZnO by CVD (green triangles).*

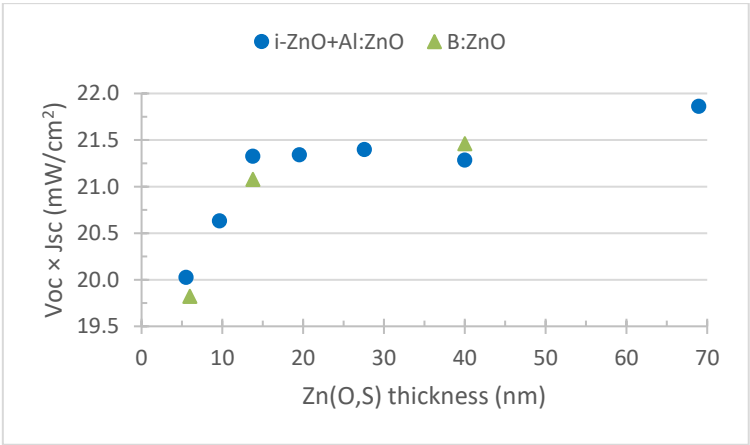


*Figure 7.15 - Average $J_{sc}$ × $V_{oc}$ value in function of $Zn(O_{1-x},S_x)$ thickness at fixed composition x=0.38, for classic TCO structure (blue spots) and for boron-doped ZnO by CVD (green triangles).*

$V_{oc}$ seems to saturate above 640 mV after a thickness of about 14nm, and then slightly decrease for the thickest film. The product between $J_{sc}$ and $V_{oc}$ exhibits basically the same trend as $V_{oc}$ with the plateaux after 14nm, but a higher mean power-density for 69nm-thick buffer (see Figure 7.15). Fill factor exhibits a parabolic behaviour with a maximum for 40nm-thick Zn(O,S). Correspondingly, the mean-efficiency trend is maximized for buffer layer thickness of about 40nm or slightly higher.

While the $V_{oc}$ is expected to be lower for thinner films, the FF is assumed not to dramatically decrease thinning the buffer layer. A FF loss is expected thickening the Zn(O,S) film, due to increased series resistance, but the trend was not clear for the thinner buffers. Until the ALD process provided a total

covering of the substrate, the FF would be constant. Only when the buffer is no longer conformal, the FF is expected to drop. Since the $V_{oc}$ was almost constant until 14nm-thick buffers, the film was expected to be conformal until such thickness. Therefore, the FF loss was first attributed to a sputtering damage caused by the ZnO deposition on the top of the buffer. Very-thin films could be sensitive to ion implantation during the energetic deposition of sputtering process. To verify this hypothesis, samples with different Zn(O,S) thickness were completed with a non-sputtered TCO. Boron-doped ZnO by chemical vapour deposition (CVD) was then grown by Solibro Research AB Company. B:ZnO has higher carrier mobility and less free-carrier density than Al:ZnO, resulting in more transparent film but with larger resistivity. Consequently, a 1200nm-thick B:ZnO film is necessary to achieve the same sheet resistance ($40\Omega/cm^2$) as the 350nm-thick Al:ZnO. The transparency of the chemically-deposited TCO is anyway higher than the sputtered one, resulting in greater current (green triangles in Figure 7.14a), as confirmed by EQE analyses (Figure 7.16).

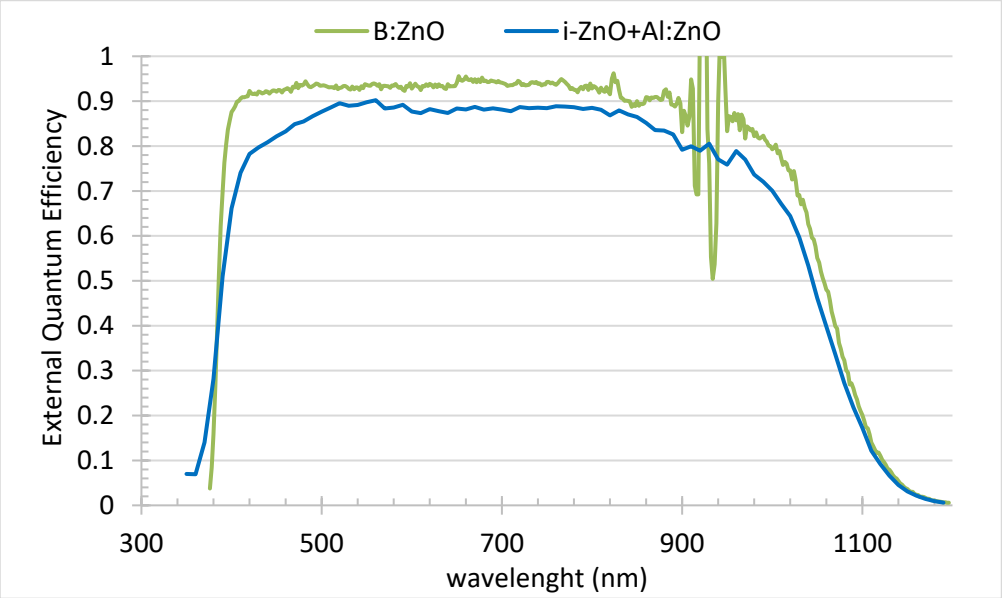


*Figure 7.16 – Examples of external quantum efficiency spectra of CIGS solar cells buffered with Zn(O,S) at same sulphur content of 0.38 and thickness of 5.5nm, with the classic sputtered ZnO-based TCO (blue line) and the CVD-grown boron-doped ZnO (green curve). The spikes occurring between 900nm and 945nm are interferences due to experimental setup.*

Since B:ZnO was not optimized for the present study and no resistive layer was deposited to avoid sputtering process, $V_{oc}$ and FF resulted lower than for the classic TCO, mainly due to lower shunting resistance. A heat effect may be the cause. However, the FF trend was confirmed even with the chemical TCO (see Figure 7.14b, green triangles), thus excluding sputtering damage to be the main cause for the FF dip in thinner-buffer devices.

Another proposed mechanism that can explain the FF loss is the thinning of the resistive layer between absorber and Al:ZnO, which is due to the buffer thinning. Zn(O,S) and i-ZnO total thickness is lowered for thinner buffer layers and this may increase the shunt of the device. This phenomenon was excluded because no appreciable variation in shunt resistance was observed. To confirm it, samples with different

i-ZnO thickness were realized, in order to maintain the resistive layer thickness at 110nm for each buffer thickness. From the measured solar cells, the variation in FF was still an issue thus exonerating the thinner resistive layer of affecting FF. The FF trend remained an open question to be further investigated.

To test if and how the Zn(O,S) growth is conditioned by S content at the interface with CIGS, pure-ZnS depositions were carried out, providing only $H_2S$ during the ALD growth, i.e. without water. ZnS thickness was varied between 2 nm (12 cycles) and 7.2 nm (42 cycles), with a GPC of about 0.17nm/cycle, as previously determined. Since the first layer of ALD-grown Zn(O,S) is expected to be more S-rich than the rest of the buffer, this experiment would be a simulation of how the interface layer (few ALD cycles) of Zn(O,S) grows onto CIGS in the extreme S-rich case (no oxygen). Results are shown in Figure 7.17: FF maximum was reached for 4nm-thick ZnS (c), while the $V_{oc}$ increases with ZnS thickness (d). For the thickest film, a blocking behaviour causing a roll-over effect in the JV (see Figure 7.17a, blue curve) dramatically affected the FF and even lowers $J_{sc}$ and $V_{oc}$. It was probably caused by the CBO of pure ZnS, which acted as a high potential barrier and was too thick to be tunnelled by the electrons. Indeed, the thinnest sample showed a bad FF and an extremely poor $V_{oc}$ mostly due to both increased shunt and recombination (see Figure 7.17a, orange curve). These results suggest that 12 ALD-cycles are probably not enough to fully cover the CIGS surface. An islands nucleation could be the cause: if it occurred, creating very-thin and scattered spots of ZnS, most of the CIGS area would be in contact with the sputtered ZnO thus explaining the low parameters. The most efficient sample of the series, obtained for 5.6nm-thick ZnS, shows a FF already affected by the blocking behaviour (see Figure 7.17a, green curve), even if not so greatly and not yet resulting in an evident roll-over effect.

The trends of the ZnS thickness series, show a clear trade-off between two phenomena: the fully covering of the CIGS surface, necessary for high output voltage and good FF, versus the thickness of ZnS buffer, which causes high CBO towards CIGS and hinders the electrons flow. Unfortunately, the compromise was not satisfying the requirement for good efficiency devices: when the FF was maximized, it was still too low to allow good performance (FF<60%) and the $V_{oc}$ was not yet maximized. A possible explanation could be the island nucleation itself: at the beginning of the growth, for few ALD cycles, the ZnS may nucleate in some points and not over the whole CIGS surface. Later, these ZnS areas increase their thickness and width quickly thanks to a heterogeneous growth. But, since the centre is formed before the edges, ZnS islands always have thinner borders. After more cycles, the island would be large enough to merge each other and to provide a fully covering layer. Following the described mechanism, when the complete coating of CIGS is reached, the ZnS islands are probably already too thick in a wide zone close to their centre and that would explain the FF chopped down by the buffer blocking. At the same time, the trend of $V_{oc}$ suggests the total CIGS surface covering was not yet achieved even for 7nm-thick ZnS films or that tunnelling recombination was still affecting it, due to a very-thin buffer region.

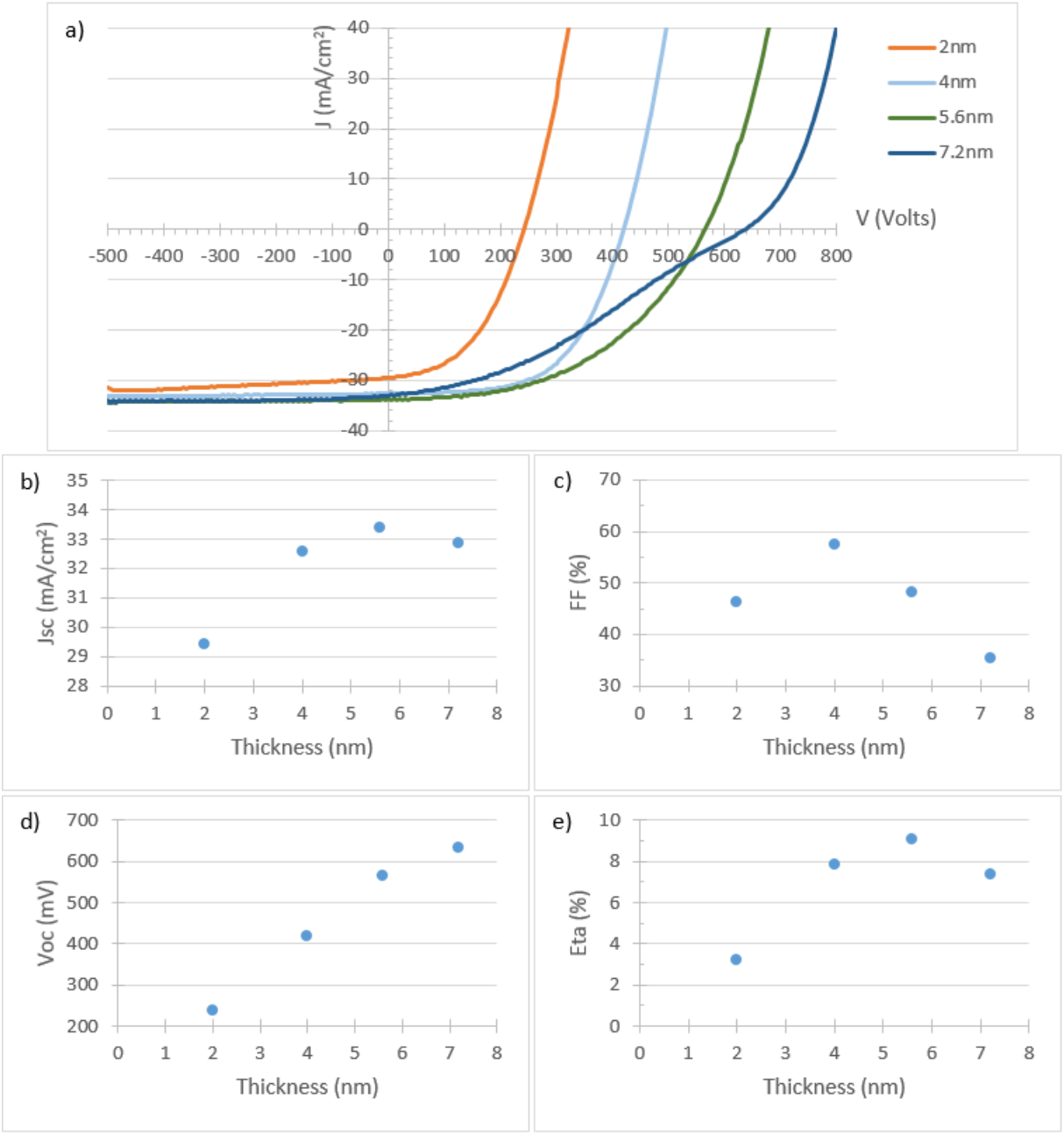


*Figure 7.17 - Behaviour of solar cells buffered with ZnS at different thickness: a) JV curves of a 0.5 cm² solar cells, representative of the average behaviour of the sample; b), c), d) and e) mean $J_{sc}$, FF, $V_{oc}$ and efficiency values of the samples, respectively.*

Considering that issues such as nucleation process and blocking behaviour could affect Zn(O,S) deposition and device functioning, we tried to apply a gradient in the buffer composition in order to understand how the interface layer influences the junction properties. First, graded buffer layers were grown moving gradually from ZnS at the CIGS interface to a S-poor buffer (or ZnO) in the top layer. This study did not improve the FF since even 5-10 ALD cycles of pure ZnS, corresponding to about 1nm-2nm, were already enough to block, although only lowering the FF of 1-2%. At the same time, the $V_{oc}$ gain was negligible. Subsequently, the interface composition of the buffer layer was varied

fabricating samples with ALD buffer recipe changing the $H_2S$:$H_2O$ ratio of the first 25 cycles, from the O-richer 1:7 to the S-richer 1:4. The buffers were then completed by 150 cycles of 1:5 recipe, corresponding to 175 total cycles. In this way, the samples were grown accurately as the best solar cell of the whole project (1:5 recipe, 175 cycles), except for the composition of the interface layer on the top of CIGS. The effects of the interface composition on the solar cells parameters are shown in Figure 7.18. A clear trend was observed for the $V_{oc}$, which increased with the sulphur content and was not yet saturated for the 1:4 recipe, and the FF, with a maximum for the interface composition corresponding to the 1:6 recipe. The 1:6 interface, thanks to both higher FF and current, lead to the best average efficiency of the present series: $\eta_{average}$=15.2%. The best results were related to the same 1:6 interface recipe reaching $\eta_{best}$=16.1% ($FF_{best}$=74%), slightly higher than the $\eta_{best}$=16.0% of the standard 1:5 recipe, in which the $H_2S$:$H_2O$ ratio was equivalent for the interface and the bulk layers (not changed during the whole growth). Since this study was conducted several months after the previous ones, although on capped absorber from the same batch, the 1:5 standard sample was repeated. It resulted in higher $J_{sc}$ (+0.4mA/cm$^2$) but lower $V_{oc}$ (-15mV) than the previous samples with the same deposition parameters. The FF mean value was lower (-1%) too, but the best one of the sample was exactly equivalent to the best from the composition and thickness series (73.9%). The same for the efficiency: the average η of the study was 0.4 absolute-% lower than the previous one, but the best sample had almost the same behaviour ($\eta_{best}$=16.0% instead of 16.1%).

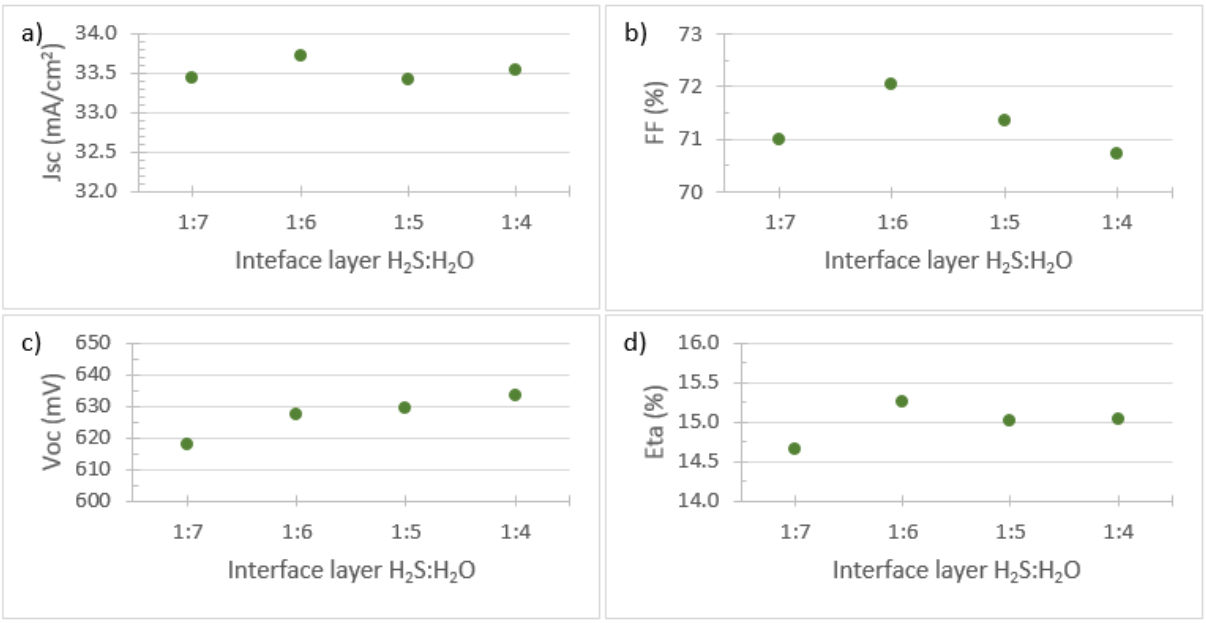


*Figure 7.18 - a), b), c) and d) shows the average $J_{sc}$, FF, $V_{oc}$ and efficiency in function of the interface layer recipe applied, with a constant 1:5 $H_2S$:$H_2O$ bulk composition of the buffer. The number of interface-layer and bulk-layer ALD cycles are the same for each sample, 25 and 150 respectively, in order to have the same amount of deposited material as the best device from the thickness series (about 40nm).*

These preliminary results about S-graded buffers suggest the interface layer plays a key role in the junction behaviour and therefore it must be optimized tuning the ALD precursor ratio. Extremely high

S-content caused FF loss even for few cycles, and so S must be slightly reduced at the interface to increase the FF by lowering the CBO. On the contrary, in respect to the standard recipe, the O-richer interface lowered the $V_{oc}$, meaning that the thickness of the interface layer had still to be optimized. Moreover, in addition to the ALD recipe applied, the composition of the buffer bulk at the beginning probably depends even on the S content of the interface layer: the nucleation might be different, extending the S-rich interface phase for a larger thickness than expected. If this statement is true, it would be necessary to grow buffers with S-richer but thinner interface layer applying then an oxygen-rich recipe between the interface layer and the bulk one. Basically, the new route consists in a first S-rich layer to properly passivate the CIGS surface, switching then to an intermediate S-poor layer to avoid undesired thick high-positive-CBO film, and in the end a top layer to finish the buffer and guarantee a homogeneous covering. This buffer structure should result in S-richer interface film but with a reduced thickness and is aimed to optimize FF and $V_{oc}$. The parameters to be taken in account are several and involve the composition and the thickness of each single layer. Experiments based on these concepts are being carried on.

In conclusion, from composition and thickness series onto CIGS absorber fabricated by means of co-evaporation by Solibro Research AB, the best ALD-Zn($O_{1-x}$,$S_x$) buffer layer turns out to be for sulphur content of $x$=0.38 at a thickness of 40nm. The compositional series results are in accordance with the previously-proposed theory of Zn(O,S) growth started by a mixture of hexagonal ZnO grains and amorphous S-rich regions. As a matter of fact, for a fixed surface Ga content of CIGS, the CBO barrier height should not change applying Zn($O_{1-x}$,$S_x$) buffer layers with composition within $0<x<0.45$, since in this range the Zn(O,S) conduction-band is pinned at a constant energy (as shown in Figure 6.3a). But experimental results presented in this thesis show a clear trend in FF and in $V_{oc}$ which could confirm the previous growth hypothesis: starting from extremely O-rich ALD-Zn(O,S) and increasing the sulphur content, the junction area with positive-CBO would be enlarged to detriment of ZnO density, pushing up both FF and Voc. Moreover, the results suggest the CIGS surface promotes a S-richer Zn(O,S) layer at the beginning of the ALD process: if the Zn(O,S) growth starts with a higher S-content than the one assumed by the ALD recipe applied, the amorphous S-rich phase occupies a larger area in contact with CIGS, thus the positive-CBO region is extended than expected. Increasing the S content, the ZnO grains are reduced and at a certain point almost the whole CIGS surface would be coated by the S-rich phase. Applying further larger S dose, the CBO would rise along with S, starting soon to block electrons. Taking in account a constant S content in the buffer, the blocking behaviour would be expected only for very large $x$, at which the CBO turns to be an insurmountable potential barrier. Indeed, in the presented data, the roll-over effect affects the FF already at about $x$=0.40 and becomes dramatic at $x$=0.47 (huge FF drop): this could be explained by a S-richer interface layer, whose outcome would be both higher CBO towards the CIGS, responsible for the FF trend, and improved passivation and reduced recombination, which boost the $V_{oc}$, until the blocking becomes the predominant effect. Actually, the

CBO value depends from both Zn(O,S) and CIGS compositions, in terms of S and Ga content, respectively. The best results are assumed to correspond about at the same CBO formed by CBD-CdS towards CIGS, i.e. +0.3 eV, and must vary in function of the absorber GGI at the surface.

Zn(O,S) thickness series shows an unexpected FF loss for thinner buffer layers. Sputtering damage and resistive layer thinning are cleared of the trend. A non-uniform covering of the absorber surface could be the cause since clues of nucleation growth started by islands was found in ZnS study.

## 7.5. ALD-Zn(O,S) buffer layer for CIGS grown by LTPED

Pulsed electron deposited CIGS were buffered with alternative Zn(O,S) buffer layers by means of atomic layer deposition. The absorber material was grown at IMEM-CNR of Parma as described in chapter 5. , on commercial Mo-coated substrates. No Ga-grading or sulfurization were applied during the LTPED CIGS growth. Devices with different Zn(O,S) composition and thickness were investigated seeking for the best matching with two different CIGS composition: GGI=37.5% and GGI=30%. The absorber material was chosen in these two composition since they are most commonly used by IMEM-CNR in Parma, and in order to study the matching with the Zn(O,S) buffer layer with respect to its composition.

The CIGS used was an un-optimized material but all the samples were deposited within few days, with the same NaF dose and annealing time. Each deposition produced 3 samples: 1 was completed with the standard CBD-CdS buffer and sputtered TCO in Parma, as described in section 5.3, and kept as solar cell reference, 2 where immediately capped by the same CdS process but with a shorter deposition time to grow a 40nm-thick layer. These capped samples were then sealed in low-vacuum bags and shipped to the Ångström Laboratory of Uppsala University. These precautions were used to preserve the CIGS from degradation during the transport. The samples were etched by means of HCl 5%wt for 1 min to remove the CdS, straight before the Zn(O,S) growth by ALD. Later, solar cells were completed as in the previous study (section 7.4): TCO layer consisted in 70nm of un-doped ZnO and 230nm of Al-doped ZnO, both deposited by RF-sputtering. In the end, the samples were mechanically scribed into 0.1$cm^2$ solar cells. No metal contact was deposited on the top of the solar cell. The QE of devices with alternative buffer were measured before the JV to accurately calibrate the solar cell current. The EQE illumination spot size is 1$mm^2$ and the wavelength step was chosen to be 2 nm or 5 nm, starting the sweep at 300 nm and ending it at 1200 nm. No voltage bias was applied and no light bias as well. Then, IV curves were measured by means of AM 1.5g simulated illumination, starting from -0.5 V until +1 V, with 0.005 V voltage step (301 points). The samples temperature was controlled with a cooling plate, ranging between 297 K and 300 K. For both EQE and IV measurements, two golden tips soldered to wires were used as probes: the first tip connected to the front Al:ZnO contact, the other one to the indium contact previously soldered on the naked molybdenum all along the perimeter of the sample.

Reference samples were fabricated depositing CdS by CBD and i-ZnO and Al:ZnO by RF-Magnetron Sputtering, following the same procedure described in chapter 5. . Al contacts were then deposited on the top of samples with CIGS GGI=37.5% by means of thermal evaporation. No metal contact was applied on the top of CIGS-GGI=30% devices. JV and QE measurements were carried out as described in chapter 5. .

Note that neither potassium treatment of CIGS surface nor anti-reflection coating was applied; moreover, the JV and QE measurements were conducted without any post-fabrication annealing or light soaking treatment of solar cells.

For the series on CIGS with GGI=37.5%, all the CdS references showed almost the same behaviour: the best solar cells of each batch had $J_{sc}$=30.5 mA/cm$^2$, $V_{oc}$=645 mV, FF=73.6% and η=14.5%. The composition study tested pure ZnO and Zn($O_{1-x}$,$S_x$) with *x* from 0.25 to 0.40, at a constant cycles number of 175, i.e. about 40nm-thick films. CIGS with GGI=30% were buffered with Zn(O,S) having S=0.30 and S=0.38, and their CdS reference had $J_{sc}$= 31.6mA/cm$^2$, $V_{oc}$=565 mV, FF=69.6% and η=12.4%. The trends of $J_{sc}$, FF, $V_{oc}$ and efficiency in function of Zn($O_{1-x}$,$S_x$) composition are shown in Figure 7.19, for the best solar cell of both LTPED-CIGS (blue squares for GGI=37.5% and green circles for GGI=30%).

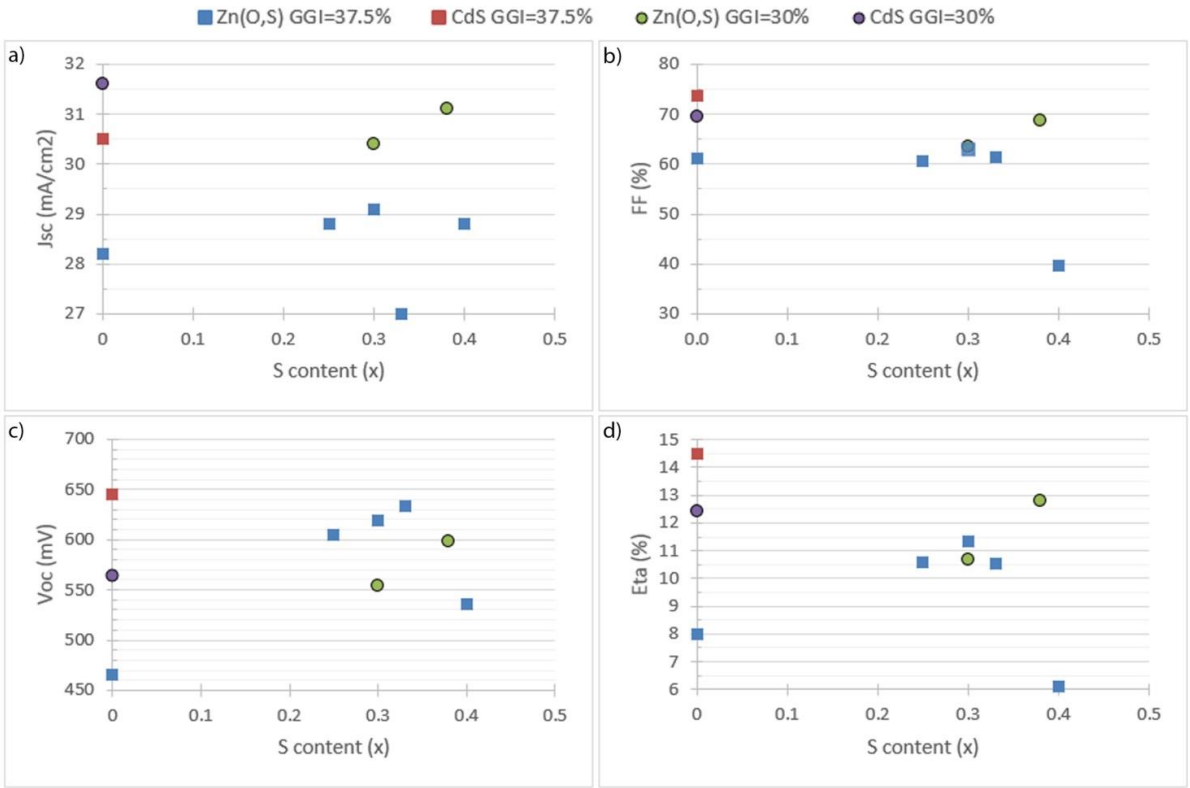


*Figure 7.19 – a), b), c) and d) shows $J_{sc}$, FF, $V_{oc}$ and efficiency of the best solar cells from samples buffered with Zn(O,S) onto CIGS having GGI=37.5% (blue squares) and GGI=30% (green circles), and relative CdS references (red squares and purple spots, respectively) on y-axis.*

The JV of solar cells fabricated using CIGS with GGI=37.5% are shown in Figure 7.20. Buffer with *x*=0.40 gave rise to a strong blocking behaviour (purple curve), while the FF is maximized at *x*=0.30.

The current is almost steady around 29 mA/cm$^2$, but the one corresponding to S=0.33, which was lower. The $V_{oc}$ grew until about S=0.33 and later dropped. The trends were similar to the series onto Solibro CIGS, shown in section 7.4, but shifted towards lower S content and with a great gap from the CdS reference. The devices current densities are expected to be higher since Zn(O,S) is the buffer, but in this series they were found rather lower than the one of CdS samples. EQE comparison of CIGS-GGI=37.5% buffered with different Zn(O,S) compositions is shown in Figure 7.21.

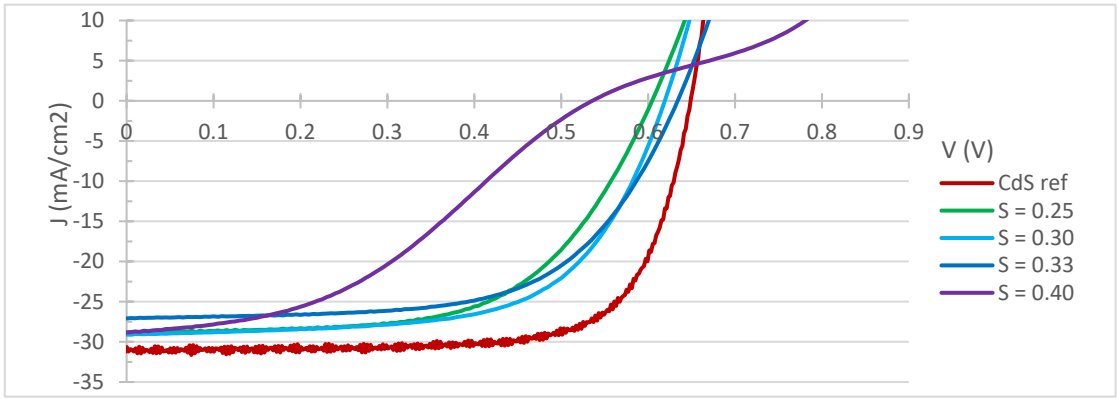


*Figure 7.20 – JV curves of best solar cells by CIGS GGI=37.5% buffered with CdS (red line) and different Zn(O,S) compositions.*

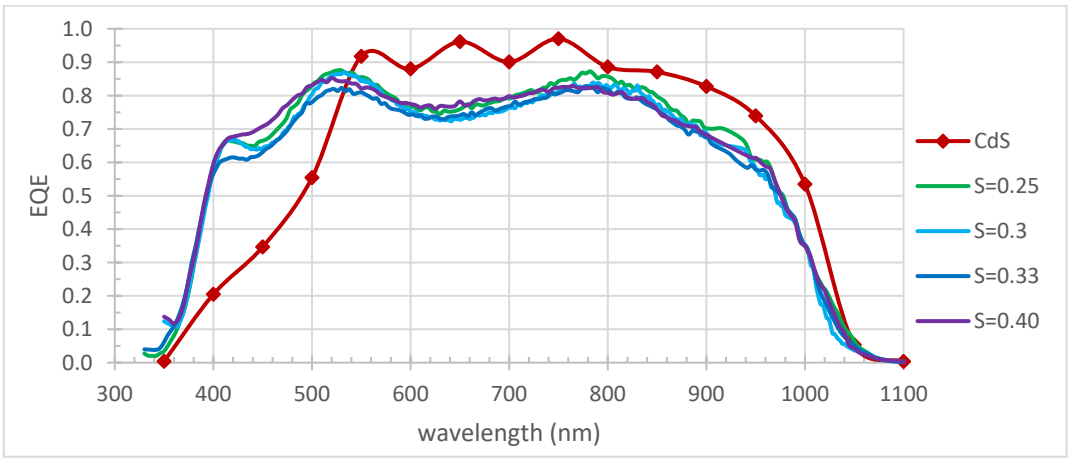


*Figure 7.21 – External quantum efficiency measurements of solar cells fabricated with CIGS GGI=37.5% and buffered with CdS (red line) or different Zn(O,S) compositions (other lines). The solar cells were neighbour devices of the best ones, with almost the same current. The CdS reference sample was measured with a wavelength step of 50nm, while for the Zn(O,S) samples the step was 2 or 4nm and curves smoothing was performed in the 900nm-950nm region to get rid of set-up interferences.*

The optical match between CIGS, Zn(O,S) and TCO resulted in high reflectivity, as highlighted by reflectance measurements. Internal QE was calculated to determine how much current the device is capable to provide in absence of reflection losses. Figure 7.22 compares EQE and reflectivity measurements along with calculated IQE of the samples with *x*=0.25 (a) and *x*=0.33 (b). The IQE gain in $J_{sc}$ for all the Zn(O,S) samples with GGI=37.5% is about 9.5-10.0%, corresponding to 2.6-3.0mA/cm$^2$, in respect of EQE. Thus, with a perfect anti-reflection coating, the current density would be increased up to 29.6 mA/cm$^2$ for the sample with *x*=0.33, and up to 31.6-31.9mA/cm$^2$ for the other S contents.

The sample with $x$=0.33 exhibited a poor current even in IQE data, probably due to a lower quality of the interface. Anyways, IQE-$J_{sc}$ values of the whole series are still lower than expected for Zn(O,S) buffer layer, for example the Solibro Research AB's CIGS series presented in section 7.4 (33-34mA/cm$^2$).

In the CdS references, the current-density gain calculated by means of IQE is around 6%, resulting in 32.3 mA/cm$^2$. With respect to the CdS, IQEs of Zn(O,S) devices are lower in the entire region above 500 nm (where the buffer absorption plays no role). Since the CIGS material was from the same batch, it may be imputed to different depletion width or interface conditions. Considering the $J_{sc}$ values obtained by IQE, the efficiency of LTPED-CIGS GGI=37.5% devices would increase by the same percentage as the current density enhancement, reaching η=12.4% for the best sample buffered with $Zn(O_{1-x},S_x)$ ($x$=0.30) and 15.4% for the references with CdS.

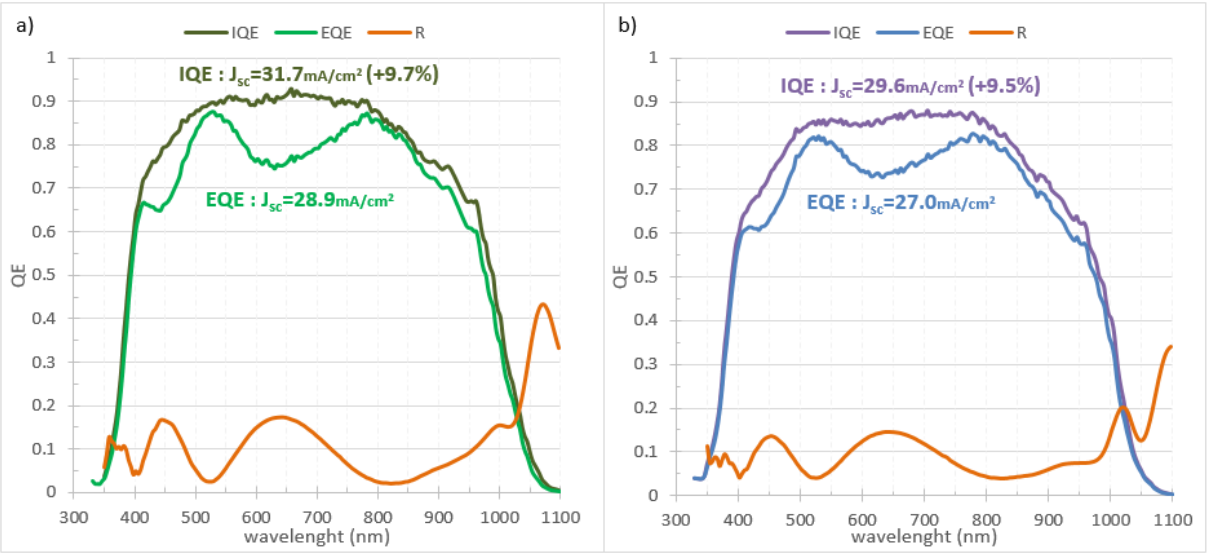


*Figure 7.22 - EQE (blue line), IQE (green line) and reflectivity (orange line) measurements of the best solar cell with CIGS GGI=37.5%, buffered with $Zn(O_{0.75},S_{0.25})$ (a) and with $Zn(O_{0.67},S_{0.33})$ (b). The current loss due to reflection were determined to be 2.9 mA/cm$^2$ and 2.6 mA/cm$^2$, respectively. EQE smoothing was performed between 900nm and 950nm to get rid of set-up interferences.*

Other than the current lower than expected, the very limiting parameter of solar cells with CIGS-GGI=37.5% was the FF. It was more than 11 points lower than the CdS reference. This variation can be only partially ascribed to the absence of Al contact in the devices with alternative buffers. Low-quality interface may be the main cause. To evaluate the ALD process, a pure ZnO buffer was grown by ALD, with the same number of cycles (175), onto CIGS-GGI=37.5%. Its FF resulted to be 61%, slightly lower than the Zn(O,S) samples but typical for a ZnO buffer layer. Consequent deduction was the ALD process had no role in the FF loss, in terms of contamination, and the CIGS preservation and etching were not deteriorating the CIGS surface. The sulphur interaction with the absorber may affect the buffer growth. The LTPED-CIGS with GGI=37.5% may nucleate Zn(O,S) differently than CIGS by co-evaporation

previously studied and so, probably, a good matching between the LTPED absorber and Zn(O,S) is not possible at the present ALD growth conditions.

FF and IQE data underlined once again the importance of the interface between absorber and buffer, which is strictly dependant from the materials used and the process applied.

Using the same absorber composition (GGI=37.5%), a thickness series was carried out at the buffer sulphur content *x*=0.30. Figure 7.23 shows FF in function of Zn(O,S) thickness. Interestingly, no important FF variation was observed, except for the 26nm-thick sample for which FF was 2-3 points higher than the other samples. $V_{oc}$ and $J_{sc}$ of devices was scattered, their product had a maximum at 40nm-buffer. Even in this series, the current density was affected by high reflection. Starting with 40nm-buffer and moving towards thicker or thinner Zn(O,S) did not improve the efficiency, so the solar cells with 40nm-thick Zn(O,S) was the best one of the series.

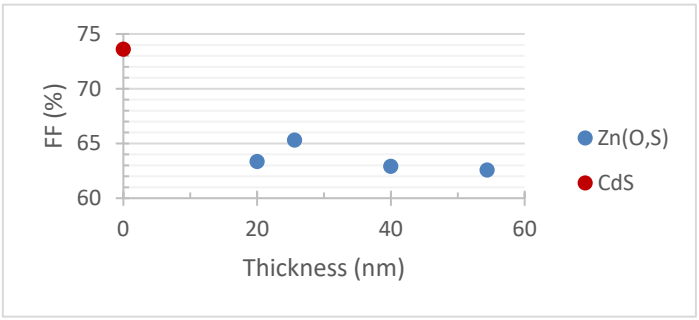


*Figure 7.23 – FF vs thickness composition of the Zn(O,S) buffer layer for PED-CIGS with GGI=37.5%.*

Alternative-buffered solar cells with CIGS-GGI=30% exhibited different behaviour than the ones with CIGS-GGI=37.5%. Few samples were fabricated for GGI=30% and only two buffer composition were investigated, so it is not possible to look for a trend. The buffer with sulphur content of *x*=0.38 gave rise to more efficient devices than buffer with *x*=0.30 (green spots in Figure 7.19), thanks to higher solar-cells parameters, which were even extremely close to or larger than the CdS reference (purple spot). $J_{sc}$ measured by EQE were still affected by reflectance issues, but IQE showed an enhancement of about 10.0-10.8%, achieving values of 34.2 mA/cm$^2$ in the best performing devices (CdS reference achieved $J_{sc}$=33.5 mA/cm$^2$ thanks an IQE gain of about 6% with respect to EQE). The FF was extremely close to CdS devices, just 1 point lower for *x*=0.38. Note that no metal-grid contact was deposited on the top of the TCO, whether the buffer material was CdS or Zn(O,S). The same composition turned out to have a $V_{oc}$ (599 mV) larger than the CdS reference (565 mV), even if CdS devices with higher $V_{oc}$ (590 mV) were found on the same sample but resulted in lower efficiencies due to poor current density.

In the end, the efficiency of the best solar cells on CIGS-GGI=30% and buffered with $Zn(O_{0.62},S_{0.38})$ was η=12.8% (14.1% with IQE-$J_{sc}$), higher than the CdS reference, η=12.4% (13.1% with IQE-$J_{sc}$). The JV curves of these two samples are shown in Figure 7.24. Considering the IQE currents plausible, with

a perfect AR coating the $Zn(O_{0.62},S_{0.38})$-buffered CIGS-GGI=30% would have an efficiency about 1 point larger than the CdS reference.

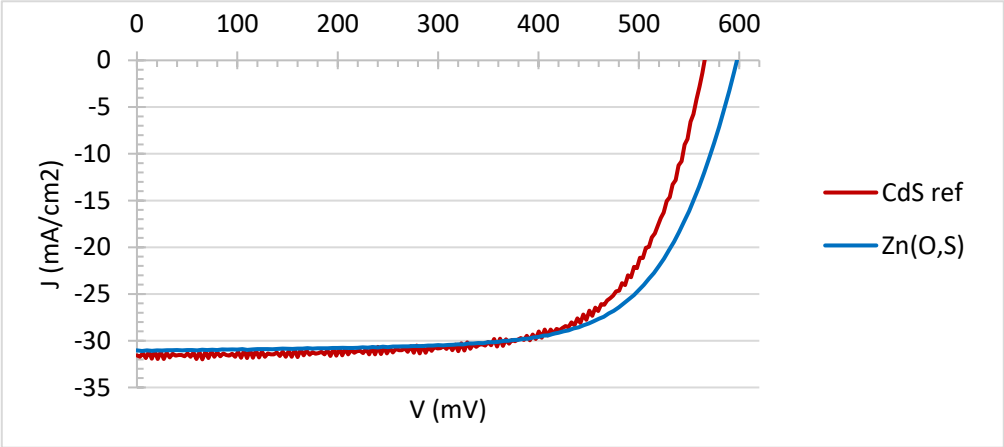


*Figure 7.24 – JV curves of PED-CIGS with GGI=30% buffered with $Zn(O_{0.62},S_{0.38})$ (blue curve) and CdS (red curve). Current densities are confirmed by EQE measurements. Because of the reflection loss, Zn(O,S) $J_{sc}$ can be push up by roughly 10% applying an anti-reflection coatings, confirmed by IQE.*

## 7.6. Conclusions

Important results have been obtained for solar cells with CIGS absorber and 40nm-thick buffer layer made by ALD with the 1:5 recipe, corresponding to $Zn(O_{0.62},S_{0.38})$. In this case, the alternative buffer demonstrated higher efficiency than CdS both on co-evaporated CIGS and on LTPED-grown CIGS with GGI=30%. For the latter, the efficiency gap between Zn(O,S) and CdS can be scaled up applying an AR coating. On the other hand, Zn(O,S) buffers were limited by important FF losses and lower $J_{sc}$ when coupled to LTPED-grown CIGS with GGI=37.5%. These issues may be related to a bad interface formation due to a different nucleation of Zn(O,S) onto CIGS with larger Ga content.

The interface layer of the buffer material deeply influences the device behaviour and usually the substrate plays an important role for its formation in the thin film technology, especially with chemical-based deposition methods. In our case, the Zn(O,S) interface composition strongly depends from ALD precursor ratio, but may change in function of CIGS surface composition too: diverse GGI may nucleate buffer film with more or less S content. Moreover, it is possible that different CIGS phases or grain orientations have different affinity for ZnS and ZnO growth, thus CIGS surface may bring to different reaction kinetics from point to point. This might explain the hypothesized island nucleation. So far, there is no direct experimental evidence of island nucleation, only the hints given by devices analysis. Anyways, to understand if and how CIGS affects the S content of the interface layer, it may be straightforward to find the right matching between absorber and buffer materials in function of the CIGS GGI. That seems to be mandatory to obtain the best results from solar cells with different absorber composition. The experiments suggest the Zn(O,S) growing mechanism could be really complex thus turning the matching with CIGS absorber a tough challenge. A possible solution to push up FF and $V_{oc}$

could be to apply a S gradient inside the buffer, using ALD recipes which changes the precursor ratio during the deposition. In this way, the S content at interface can be controlled and FF may be enhanced while the $V_{oc}$ is kept at the same level.

# 8. Conclusions and Perspectives

This thesis contributed to the advancement of the Low-Temperature Pulsed Electron Deposition (LTPED) process, a new technology developed by CNR-IMEM for the fabrication of CIGS thin film solar cells. The most relevant result of this work was a photovoltaic conversion efficiency up to 17% on laboratory-scale devices. The progress presented in this work is an important breakthrough towards the production of low-cost and highly-efficient solar cells suitable for innovative applications since LTPED allows the growth of CIGS thin films at very-low temperature (250 °C) and in a single stage process, from a quaternary target. The 17%-efficiency milestone is even more significant since neither intentional Ga-grading nor K-treatment of CIGS nor AR coating was applied, even if a small and unintentional Ga-grading was observed both by SIMS and by Raman spectroscopy. Since LTPED does not need any post-deposition treatment in hazardous gas and its power consumption is lower than co-evaporation, a cheaper fabrication of solar-cell absorber can be available. Furthermore, the low temperature process can permit the usage of plastic substrates, such as polyimides, thus enabling the production of flexible devices for building-integrated photovoltaics.

As innovative applications, bifacial solar cells were realized by depositing CIGS onto TCO-coated glass. This enabled light collection from both the front (mainly for direct and diffuse daylight) and the rear (albedo) sides. Fluorine-doped tin oxide demonstrated optimal interface properties with CIGS deposited by LTPED at 250 °C. With FTO as back contact, front-illumination efficiency was determined to be as high as the Mo reference, with a similar homogeneity, while under bifacial-illumination an equivalent efficiency of 17% was measured. Therefore, by means of LTPED, bifacial devices can be fabricated with an efficiency comparable to the state-of-the-art ones. Indium-tin oxide has also been tested as back contact for bifacial solar cells with very promising results but LTPED-grown solar cells so far exhibited a low FF due to the quality of the CIGS and an increased shunt behaviour. This feature is believed to be correlated to a higher density of electrically-active deep levels associated to the formation of an unintentional Ga-rich phase during the LTPED growth of CIGS on ITO. In fact, Raman spectroscopy revealed the Ga content of the absorber was larger at the CIGS/ITO interface and diminished towards the buffer layer. Thus, the GGI variation is supposed to be strain-driven due to the lattice mismatch

between CIGS and the ITO substrate, which is gradually relaxed with increasing CIGS thickness. Similar problems were also observed on Al-doped ZnO back contacts.

By reducing the thickness of the CIGS absorbers, from 1.6 μm to 1.2 μm, higher total current densities can be achieved by bifacial illumination, even if the efficiency drops because of lower FF and $V_{oc}$. However this is an important step towards another important application of thin-film technology for BIPV: semi-transparent solar cells for PV windows. This target could be reached by fabricating ultra-thin CIGS devices (~300 nm).

Finally, one of the main objectives of this thesis was to investigate the fabrication of Cd-free solar cells by using only vacuum-based techniques. For this purpose, Zn(O,S) deposited by atomic layer deposition was studied as an alternative buffer layer for LTPED-grown CIGS, in collaboration with the Ångström Laboratory at Uppsala University (Uppsala, Sweden). The performance of CIGS-based solar cells is strongly influenced by the interface layer of Zn(O,S), since both the conduction band offset and the defect density at the interface control FF and $V_{oc}$. Atomic layer deposited Zn(O,S) films are known to grow as a mixture of ZnO grains and a S-rich amorphous phase, with a larger sulphur content in the interface layer. In this thesis, from the characterization of devices with different Zn(O,S) composition and thickness, the ALD growth of Zn(O,S) appeared to be influenced by the CIGS composition. By analysing solar cells with LTPED-grown CIGS having GGI=30% and GGI=37.5% as a function of the Zn(O,S) composition, the FF trends suggested that the GGI strongly affects the device behaviour. First, the FF maxima were obtained at different sulphur content of the buffer layer, then, while for GGI=30% the FF was similar to the CdS reference, for GGI=37.5% it dropped by more than 10 points. The first result can be explained by a larger S content of the interface layer, while a generally lower interface quality could be responsible for the dramatic FF drop. Thereby, the Ga content of the CIGS surface is suspected to affect the formation of Zn(O,S) interface layer, promoting more S content and/or even a different nucleation. In fact, hints of island nucleation were found in ZnS buffer layer on co-evaporated CIGS. These hints are suspected to affect Zn(O,S) as well, in a way that depends on the surface composition of both CIGS and Zn(O,S). The phenomenon may result in poor morphology for very-thin films: only when the islands grow enough and merge together covering the whole CIGS surface, the interface recombination can be reduced, thus maximizing both FF and $V_{oc}$ maximized. Every absorber batch is expected to have a unique surface (in terms of GGI, grains dimension and orientations) which hence brings to a special nucleation of the interface layer of Zn(O,S) and to unique properties of the pn-junction.

With LTPED-CIGS having GGI=30%, Zn(O,S) buffers resulted in devices comparable or even more efficient than the CdS reference, whose efficiency can be extended by the application of a AR coating. The improvements must be confirmed by means of higher-quality absorber to test whether the ALD-Zn(O,S) can be alternative to CdS even for the most efficient ($\eta$>16%) solar cells.

In order to improve the robustness of LTPED process and the electrical performance of CIGS cells, some features of the absorber layer must be investigated in the near future. One of the most interesting aspects is the unintentional Ga-grading of the record device. It will be crucial to understand which is the driving force of this grading, in order to maximize its effect on the cell efficiency. Moreover, the model for the GGI calculation from the Raman depth profile is being further refined to improve the accuracy and the reliability of this non-destructive technique. Samples with intentionally-graded CIGS are being deposited by means of LTPED using targets with different compositions; they are intended to correlate the Raman-peak shift with the GGI and to lay the groundwork for LTPED-grown absorbers with optimized double Ga-grading, aiming to efficiency improvements.

According to literature, further improvements are then expected by introducing a post-deposition treatment of KF. In fact, it is widely accepted that KF treatments can improve the interface between CIGS and CdS as well as the buffer uniformity, thus resulting in higher $V_{oc}$ and FF due to lower surface recombination. Moreover, since a thinner CdS is needed to obtain a conformal coverage of K-doped CIGS, an indirect increase of the short-circuit current can also be obtained. Although the role of KF with alternative buffer materials is not yet clear, the advantages for LTPED-grown CIGS solar cells are potentially the same that has allowed several laboratories to overcome the 20% efficiency threshold over the last 2-3 years.

During the PhD, I was involved in other research projects, not presented in this thesis, aimed to the development of CIGS by LTPED.

An unconventional substrate heating by Joule effect (136) was developed to preserve the substrate from over-heating and to limit the heat losses during the CIGS growth. Joule-heating is based on the application of a DC electrical power directly through the Mo back contact of the cell: electrical energy is converted into heat by Joule effect and produces a localized heating of the sample surface, i.e. of the Mo layer only. Devices based on CIGS grown by LTPED with Joule-heating demonstrated the same device features than the one realized by conventional IR heating. This novel process is aimed to lower the energy cost for the manufacturing of thin-film solar cells and to enable the deposition onto polyimide or other thermolabile plastic substrates.

In another project, LTPED epitaxy of CIGS was explored and 1.6μm-thick single-crystal CIGS films were successfully grown by means of LTPED on Ge at very low temperature (270 °C), in order to compare the optical and electrical characteristics of poly- and mono-crystalline CIGS. The only defects found were twin boundaries along the (112) direction while photoluminescence spectra exhibited no $In_{Cu}$ peak and CV analysis revealed a free carrier concentration much larger than the Mo reference. Since the density of compensating defects is reduced in CIGS epilayer than in polycrystalline CIGS films, single-crystal CIGS promise better performances as absorber layer in single and multi-junction thin-film solar cells.

Eventually, roll-to-roll deposition of CIGS is currently being exploited to grow CIGS on flexible tapes, such as metal (steel, Mo, etc.), ultra-thin glass or even plastics like polyimide. A vacuum chamber has been specifically designed for the deposition of highly-efficient CIGS on flexible substrates by LTPED: an in-situ control of the film thickness by IR interference gives the feedback to activate two external motors which move the tape to realize the roll-to-roll deposition.

Summarizing, the present work confirmed LTPED technique is a desirable process for industrial manufacture of low-cost and high-quality CIGS. In fact, LTPED is the only known process able to fabricate CIGS for highly-efficient ($\eta$=17%) thin-film solar cells at low temperature (250 °C) and in a single-stage deposition.

# Appendix I - Thin-film characterization methods

## IR pyrometer and thermography

Infrared spectroscopy and thermo-imaging aims to provide in-situ and real-time measurement of the film thickness during the deposition. The temperature of a heated substrate during a thin-film deposition can be monitored analysing the emitted infrared radiation using a pyrometer. The exact temperature can be determined if the emissivity of the substrate material is known. During the CIGS deposition, if the growing material is transparent to the IR radiation emitted by the substrate, a temperature variation can be observed, due to the interference caused by the growing film. The optical path of the IR photons coming from the hot substrate is modified by the new interfaces between substrate and CIGS and between CIGS and vacuum, thus reaching the detector with a phase shift depending from the thickness CIGS film. This brings to constructive and destructive interference, which results in maxima and minima of the reflected light. The thickness than corresponds to them as determined by:

$$\text{maxima:} \quad d = \frac{(2m+1)\cdot\lambda}{4n}$$

$$\text{minima:} \quad d = \frac{(2m+2)\cdot\lambda}{4n}$$

where $n$ is the refractive index of the film, $\lambda$ is the wavelength detected by the pyrometer and $m$ the is the order of the maximum/minimum. In this thesis, a Raytek Marathon MM pyrometer, pointing perpendicular to the substrate surface, is used to detect the radiation with $\lambda$=8 μm.

The same can be done with a thermo-camera: in this case, thanks to two-dimensional images, the film thickness can be mapped on a wide area. The evolution of the deposition can be monitored in real-time for the whole sample extent.

## Secondary ions mass spectrometry

In secondary-ions mass spectroscopy (SIMS), high energy ions supplied by an ion gun are focused on the solid sample. The ejection of secondary atoms by the sputtering of the solid material allows a mass spectrometer to provide chemical analyses of the sample. With this technique, the sputtering erosion proceeds down through the material: SIMS can hence perform composition analyses in-depth and can be used to determine concentration gradients of the elements along the film thickness. Problems can occur by signal overlapping (ions with same mass/charge ratio) and erosion from the crater walls, which causes a memory effect. For SIMS analyses of CIGS devices of this thesis, an instrument model Cameca SC-Ultra was used, equipped with a primary ion gun of $Cs^+$ working at 8 kV. The ion-beam impact energy is 3 keV and its current 40 nA. During the measurements, the sample is kept at a voltage of 5 kV and the pressure is ~$10^{-9}$ mbar. The sputtering raster is 250μm×250μm and the ion beam diameter is

75μm, while the sputtering velocity is 0.3 nm/s. The following species have been monitored: $^{16}O$, $^{23}Na$, $^{32}S$, $^{63}Cu$, $^{69}Ga$, $^{80}Se$, $^{98}Mo$, $^{114}Cd$, $^{115}In$, with a mass resolution of 400. All the $MCs^+$ ion-signal profiles are normalized to the $Cs^+$ signal.

## Raman Spectroscopy

The Ga content of CIGS thin films can be determined by micro-Raman spectroscopy. In fact, the frequency of the chalcopyrite $A_1$ mode (representing the vibration of the anions in the x-y plane with cations at rest) has been observed to be linearly dependent from GGI: the phonon frequency shifted from 174 $cm^{-1}$ for CIS to 184 $cm^{-1}$ for CGS (99). Therefore, GGI of co-evaporated CIGS has been calculated by the Raman shift of the $A_1$-mode peak ($R_{shift}$) as:

$$GGI = 0.1 \cdot R_{shift} - 17.4$$

For this thesis, to investigate the CIGS composition along the growth axis, depth-resolved Raman measurements were made using a micro-Raman apparatus (Horiba Jobin–Yvon Labram) equipped with a confocal microscope (Olympus BH-4) with 4, 10, 50, ULWD 50 and 100 objectives (lateral spatial resolutions of approximately 25, 10, 2, 2 and 1μm). The spectrometer is fitted with a 20 mW He–Ne laser emitting at 632.8 nm, an edge filter, a 256×1024pixel CCD detector, a 1800 grooves/mm grating, and a density filter wheel. The spectrometer is calibrated at the silicon Raman peak of 520.6 $cm^{-1}$ before each measurement. The spectra were recorded at different sample depths using the 100 objective: each datum is the mean of 4 repetitions lasting 30 s each, or the average of 30 measurements of 10 s repeated 2 times each obtained mapping a 20μm×40μm sample area. Peak fitting was carried out using a Lorentzian function. For the samples of this thesis, the GGI calculated by Raman and SIMS analyses did not match perfectly. PED-grown CIGS may be characterized by slightly different constants in the equation shown above. Moreover, the $A_1$ mode is expected to shift in function of the copper content too. The correlation between the composition of PED-grown CIGS and the Raman $A_1$ peak is currently under investigation to optimize the GGI calculation.

## UV-Vis spectroscopy

Optical transmittance/absorbance and reflectance of thin film can be determined by means of ultra-violet and visible (UV-Vis) spectroscopy. Absorbance measurements allows the calculation of the energy gap of the semiconductor by its absorption edge. Due to the electrons excitation from the VB to the CB by the incoming photons, absorbance occurs only for those photons with energy higher than $E_G$, in first approximation. Hence, for a semiconductor with direct band-gap, $E_G$ can be derived by means of the Tauc plot from:

$$\alpha h\nu = A \cdot \sqrt{h\nu - E_G}$$

Reflectivity measurements are indeed used to find out the thickness of the films. Interference phenomena occur when the film thickness has the same order of magnitude of the incident wavelength, giving rise to intensity fringes of the reflected light. Knowing the refractive index of the material, the film thickness can be estimated by the positions of maxima and minima in the spectrum of the reflected radiation.

In this thesis, a Jasco V-530 spectrophotometer was used working in the range 350nm-1100nm.

### X-ray diffraction

The structural properties of thin films can be investigated by X-ray diffraction (XRD), to determine the crystal structure, the dimensions of the unit cell, the preferred crystallographic orientation of the grains and to detect the presence of unwanted phases. In a crystalline material, an incident X-ray beam is diffracted by the electrons of the lattice atoms in specific directions, thus constructive interference is obtained when the Bragg's Law is satisfied. By scanning the intensity in function of the diffraction angle, the atomic structure and the crystalline lattice of the sample can be determined.

For this thesis, a Siemens D500 (Siemens, Berlin, Germany) system in Bragg–Brentano geometry was used, equipped with a Cu Kα X-ray source ($\lambda$=1.54 Å).

### X-ray fluorescence

X-ray fluorescence (XRF) is an X-ray spectroscopy technique used for qualitative and quantitative analysis of materials. It is based on the excitation of electrons of the inner shells of an atom, obtained by bombarding with X-rays having a defined energy to excite only that element. After being promoted to excited states, the electrons recover their initial level emitting secondary (or fluorescent) X-rays, which have an energy unique for that element and an intensity related to its amount inside the sample. By analysing the sample for several elements, it is possible to calculate the concentration ratio between these elements.

In this thesis, a XRF spectrometer model Epsilon 5 by PANalytical is used to determine the S content in $Zn(O_{1-x},S_x)$ films.

### Scanning electron microscopy

Scanning electron microscopy (SEM) can investigate the morphological properties of the samples: surface roughness, grains dimension and shape, film thickness and density. SEM uses a low-current and high-voltage electron beam to scan a sample area and to produce images of it. The focused electrons interact with the atoms of the sample originating several kinds of signal (secondary electrons, X-rays, etc.), each one carrying information about surface topography and/or composition. Usually, the secondary electrons emitted by the surface are detected while the beam scans the sample. An image is reconstructed in function of the number of secondary electron reaching the detector: this number depends from the material and the angle between the surface and the beam direction. Therefore, it is

possible to distinguish different materials, in function of their electrical characteristic (like electron conductivity), and morphological variations.

Here, two different SEM models were used:

- Philips 515, working at 20kV, for cross-sectional images and energy dispersive X-ray spectroscopy;
- Carl Zeiss Auriga Compact, working at 3 kV, for cross-sectional images.

### Energy-dispersive X-ray spectroscopy

Energy-dispersive X-ray spectroscopy (EDS or EDX) allows to determine the elemental composition of the sample. It is mainly used in electron microscopes since it used an electron beam to cause the X-ray emission from the material. The highly-energetic electrons of the beam transfer energy to the electrons of the sample atoms promoting them to the outer shells. The following electron relaxation from the outer to the inner shell brings to the generation of a X photon. Thus, the detection of the X-ray emission of the material gives information about its chemical composition.

### Profilometry

A profilometer is an instrument used for detecting small vertical variation of the sample surface, moving a stylus across the sample and applying a specified force. It can measure both the sample roughness or the film thickness. For the latter purpose, a sharp step is needed: it can be realized by using a mask, in contact with the substrate during the thin-film deposition, or by means of a controlled etching after the material growth.

### Four-point probe

Four-point probe is a quick method to measure the sheet resistance of a semiconductor thin film. It uses four aligned contacts: current is flowing inside the sample through the two outer ones, while the two inner contacts measure the voltage. Knowing the film thickness, the resistivity can be easily calculated.

### Hall measurement

Hall measurement is a characterisation method based on the Hall effect used to determine the carrier density and the carrier mobility in semiconductors. It consists in the application of a magnetic field on a semiconductor thin-film in which a current is flowing. The system setup is assembled so that the force due to the magnetic field is acting on the electrons perpendicular to the current flow and thus the electrons are driven towards one side of the sample. The electrons gradient along this direction builds up an electric field whose force opposes to the one of the magnetic field. Once steady conditions are reached, the intensity of the voltage between the two edges of the sample depends on the strength of the magnetic field and on the type, density and properties of the charge carriers in the semiconductor.

# Appendix II - Solar-cells characterization methods

## Current-Voltage

The current-voltage (IV) characteristics of the solar cells are detected scanning the voltage and determining the corresponding current with or without any incident light. In this thesis, measurements in dark condition were carried out covering the sample to avoid any light exciting the device, while the illuminated IV characteristics were measured under AM1.5g spectrum with power density of 100mW/cm$^2$ produced by a solar simulator model ABET SUN 2000. In both cases, the temperature was kept constant at 25 °C by means of a cold plate and the IV tests were performed with a Keithley 2635 system. Current-density vs. voltage (JV) were then calculated dividing the current by the device active area. Only for solar cells with Zn(O,S) buffers, the JV curves were calculated with the total area of the device.

## Capacitance-Voltage

Capacitance-Voltage (CV) analysis reveals the electrical properties of the pn junction, such as the free-carrier density of the semiconductors, the width of the SCR and the energy and concentration of deep levels inside it. The technique applies a forward or inverse DC bias coupled to small AC signal ($\Delta V$=10-50mV, $f$=100Hz-1MHz) to the diode device and determine the variation of its capacitance due to restricted or extended SRC. The capacitance is calculated by the imaginary part of the admittance, which is measured by an impedance analyser. To determine the free-carrier density of semiconductors, CV analysis are usually carried out at low temperature and with high-frequency signal in order to avoid the excitation of deep levels and thus to determine the special charge due to the acceptor/donor states only.

## Quantum efficiency

Quantum efficiency (QE) provides information about the light collection in the solar cell that generates photocurrent. The external quantum efficiency (EQE) for a certain wavelength is defined as the percentage of incoming photons, with the corresponding wavelength, that are absorbed creating a free electron and a free hole which are separated by the electric field of the pn junction and then contribute to the power generation. EQE measurements are carried out with monochromatic light at low intensity, measuring the output short-circuit current of the solar cells and comparing it with the current produced by a calibration cells. The QE spectrum is obtained sweeping the wavelength from UV to IR range and its integration provides the $J_{sc}$ of the solar cell. For this thesis, EQE measurements were carried out under the solar simulator with a set of 16 narrow-band filters (Thorlabs FB350/1100-10) and a Silicon photodiode (Thorlabs FDS-1010-CAL), except for the devices with Zn(O,S) buffer layer.

Internal Quantum Efficiency (IQE) is an evaluation of the quantum efficiency of solar cells when no light power is reflected and all the irradiating light is propagating into the device: IQE simulates the EQE in the case of an anti-reflection layer deposited onto the top of the device. It can be calculated for each wavelength as:

$$IQE_{(\lambda)} = \frac{EQE_{(\lambda)}}{100 - R(\%)_{(\lambda)}}$$

where *R(%)* is the reflected intensity expressed as percentage of the illuminating intensity. *R(%)* is usually measured by UV-Vis and near-IR spectroscopy.

## Open-circuit voltage vs Temperature

The trend of the open-circuit voltage as a function of the sample temperature is used to determine the main recombination mechanism affecting the solar cell. The sample is illuminated as in IV measurement but the device is kept in vacuum, to avoid that water from the air condenses onto its surface, and the $V_{oc}$ of the solar cell is measured lowering the temperature. $V_{oc}$ of CIGS-based solar cells is expected to increase lowering the sample temperature until about 200 K and then to saturate. The extrapolation of the linear trend before the saturation allow to determine the activation energy ($E_A$) of the dominant recombination mechanism:

$$E_A = \frac{V_{oc}^{(T=0)}}{q} \quad [eV]$$

If $E_A$=$E_G$ the recombination takes place mainly in the quasi-neutral region of the absorber. Indeed, when $E_A$ is slightly lower than $E_G$ the recombination occurs in the SCR, while if $E_A$<<$E_G$ the high density of interface states plays a major role in the recombination.

## Electron-beam induced current

Electron-beam induced current (EBIC) is a SEM-based technique used to localise defects or buried junction in semiconductor devices and the properties of their minority carrier. Scanning with the electron beam, EBIC maps the electronic activity of the sample with a good lateral resolution, while the depth resolution is controlled by the SEM accelerating voltage. The electrons of the beam undergo to inelastic interactions with the semiconductor sample resulting in the generation of electron-hole pairs. The carriers are then separated by the electric field of pn junctions and collected by contacts. The resulting current (EBIC) is used to draw an image as the focused electron beam scans across the semiconductor device. The image contrast visualises defects of the device as dark areas while the depletion region of pn junction appears bright. It can detect electrical shorts, defects inside the SCR of diode, determine minority carrier property as diffusion length and surface recombination velocity.

# Acknowledgements

The PhD at IMEM-CNR of Parma was more than a simple academic/work experience. I must thank all my colleagues and in particular Edi for the opportunity of having a PhD in the PED-TEAM group and the support in several bureaucratical things, my supervisors Stefano and Francesco P. for the fruitful discussions and explanations, Matteo for the intensive fabrication of CIGS for my projects and for prioritizing my problems whenever I needed a help, and Massimo for the advises and suggestions and the nice dinners we had in Lille.

Additionally, I am thankful to all the other colleagues who contributed to cheer my period at IMEM: first of all, Davide D. in charge of keeping the spirits up and entertaining the colleagues of *studio 100* and neighbour offices with sophisticated songs; Francesco B. and Paola for sharing the office, distributing the desks in the most complicated way; Nicola Z. and Giacomo for the "Tecnopolo" experience, unfortunately very short but extremely exciting; Giulia and Davide C. for providing the PED-TEAM with cosy dinners; Greta, Benedetta, Martina, Maurizio, Marco, Matteo, Nicola Ca., Silvio, Manuele, Aldo, Nicola Co., Daniele, Fabio, Federico, Lucia and all the previous ones for the long interesting discussions during meals and/or coffee breaks, as well as all the lunches, dinners, vacations, basketball matches and nice times we had together.

Moreover, I am very glad I had the chance to work at Ångström Laboratory of Uppsala University, since during the internship I improved both my research and personal skills. Therefore, I would like to acknowledge my group at IMEM, the C.M. Lerici Foundation and Uppsala University for providing the financial support for my stay and research in Uppsala. *Tack så mycket* to Marika for hosting me in the CIGS group, for making me feel like at home and for always helping me with a large genuine smile. Then, I would like to express my deepest gratitude to Tobias for supervising my project at Ångström, introducing me to the MP3 and giving patient explanations. *Ett stort tack* even to Fredrik, Jan and Adam for contributions, assistances and aids: I most appreciated your cooperation in both cleanroom and pubs. Thanks to Uwe for supplying the Friday-afternoon meetings with the raw material and all the other PhD students, researchers and professors of the department of Solid State Electronics for their kind words and the Friday Fika: Long, Sasha, Lukas, Yi, Tove, Christopher, Katharina, Dorothea, Mandy, Syaiful, Indrek, Malkom, Patrik, Jonathan, Olof, Nils, Carl, Viktor, Nina, Jes, Lars, Jörgen and Lotten. A great thanks to Oleksander and Fredrik for the coffee-times and the extra-academic activities together, and *danke* to Lukas for hosting me and brewing that *Bud-Spencering* beer.

Special thanks to Murphy, for providing a Law which explains the most incomprehensible phenomena, and to Dedè, for working harder than anyone else and saving the world alone while I was busy with my PhD.

In the end, the greatest *grazie* to Lucia: you patiently waited me during each step of my doctoral studies, encouraging me even in the most tough periods; and to my family for your hard work and all the opportunities you gave me.

# References

1. Progress in thin film CIGS photovoltaics – Research and development, manufacturing and applications. T. Feurer, P. Reinhard, E. Avancini, B. Bissig, J. Löckinger, P. Fuchs, R. Carron, T.P. Weiss, J. Perrenoud, S. Stutterheim, S. Buecheler, A. N. Tiwari. 2016, Prog. Photovolt: Res. Appl., p. published online.

2. IEA. International Energy Outlook 2013 (IEO2013). [Online] 2013. [Riportato: 5 12 2016.] http://www.eia.gov/outlooks/archive/ieo13/.

3. U.S. Global Change Research Program. GlobalChange.gov. [Online] [Riportato: 5 12 2016.] https://health2016.globalchange.gov/.

4. United Nation. Adoption of the Paris Agreement. Conference of the Parties - 21st session. Paris : s.n., 2015.

5. International Energy Agency (IEA): Photovoltaic Power System (PVPS) programme. IEA-PVPS Editorial 27th October 2016 . [Online] [Riportato: 5 12 2016.] http://iea-pvps.org/index.php?id=267.

6. NREL. https://www.nrel.gov/pv/. [Online] 11 2016.

7. C. Ghezzi. Fisica dei semiconduttori. s.l. : Monte Università Parma, 2013.

8. M.Wolf, N. Holonyak, G.E. Stillman. Physical properties of semiconductors. s.l. : Prentice-Hall International Edition, 1989.

9. M.S. Tyagi. Intoductions to semiconductor materials and devices. s.l. : John Wiley & sons, 1991.

10. J. Nelson. The Physics of Solar Cells. s.l. : Imperial College Press, 2003.

11. Solar Frontier. Presented at IW-CIGSTech 7. [Online] 23 06 2016. [Riportato: 20 10 2016.] https://www.photovoltaic-conference.com/images/2016/2_Programme/parallel_events/7thInternationalWorkshopCIGS/Takuya_KATO.pdf.

12. Effects of heavy alkali elements in Cu(In,Ga)Se2 solar cells with efficiencies up to 22.6%. Jackson P., Wuerz R., Hariskos D., Lotter E., Witte W., Powalla M. 2016, physica status solidi (RRL) – Rapid Research Letters.

13. Potential of photovoltaic systems in countries with high solar irradiation. G. Makrides, B. Zinsser, M. Norton, G.E. Georghiou, M. Schubert, J.H. Werner. 14(2), 2010, Renewable and Sustainable Energy Reviews, p. 754-762.

14. Energy payback time (EPBT) and energy return on energy invested (EROI) of solar photovoltaic systems: A systematic review and meta-analysis. K.P. Bhandari, J.M. Collier, R.J. Ellingson, D.S. Apul. 2015, Renewable and Sustainable Energy Reviews, Vol. 47, p. 133-141.

15. http://cigs-pv.net/cigs-white-paper-initiative/. CIGS white paper initiative – CIGS thin-film photovoltaics. [Online]

16. Wieting, R. 1999, AIP Conf. Proc., Vol. 462, p. 3-8.

17. Thin-film CIGS PV modules with more than 3000 h damp heat stability: Breakthrough time property of the B-Dry® edge sealant and its characterization. A. Bonucci, S. Rondena, A. Gallitognotta, P. Gallina, O. Salomon, W. Wischmann, S. Hiss. 2012, Solar Energy Materials and Solar Cells, Vol. 98, p. 398-403.

18. Phase equilibria of Cu-In-Se. I. Stable states and nonequilibrium states of the In2Se3-Cu2Se subsystem. T. Godecke, T. Haalboom, F. Ernst. 2000, Zeitschrift für Metallkunde, Vol. 91, p. 622-634.

19. W.N. Shafarman, L. Stolt. Cu(InGa)Se2 Solar Cells. [aut. libro] A. Luque and S. Hegedus. Handbook of photovoltaic science and engineering. s.l. : John Wiley & Sons Ltd., 2003, Vol. 2, p. 546-599.

20. Highly efficient Cu(In,Ga)Se2 solar cells grown on flexible polymer films. A. Chirilă, S. Buecheler, F. Pianezzi, P. Bloesch, C. Gretener, A.R. Uhl, C. Fella, L. Kranz, J. Perrenoud, S. Seyrling, R. Verma, Shiro Nishiwaki, Y.E. Romanyuk, G. Bilger, A.N. Tiwari. 2011, Nature Materials, Vol. 10, p. 857–861.

21. M.A. Green. Solar Cells. Kensington : The University of New South Wales, 1992. p. 89.

22. Electronic properties of CuGaSe 2 -based heterojunction solar cells. Part I. Transport analysis. V. Nadenau, U. Rau, A. Jasenek, H. W. Schock. 2000, Journal of Applied Physics, Vol. 87(1), p. 584-593.

23. ZnO/CdS/CuInSe2 thin-film solar cells with improved performance. L. Stolt, J. Hedström, J. Kessler, M. Ruckh, K.O. Velthaus. H.W. Schock. 62, 1993, Appl. Phys. Lett, p. 597.

24. Effects of Na on the Growth of Cu(In,Ga)Se2 Thin Films and Solar Cells. D. Rudmann, A.F. Da Cunha, M. Kaelin, F.J. Haug, H. Zogg, A.N. Tiwari. 763, 2003, Materials Research Society Symposium - Proceedings, p. 53-66.

25. Sodium incorporation strategies for CIGS growth at different temperatures. D. Rudmann, D. Brémaud, A.F. da Cunha, G. Bilger, A. Strohm, M. Kaelin, H. Zogg, A.N. Tiwari. 2005, Thin Solid Films, Vol. 480-481, p. 55–60.

26. Development of rear surface passivated Cu(In,Ga)Se2 thin film solar cells with nano-sized local rear point contacts. B.Vermang, V. Fjällström, J. Pettersson, P. Salomé, M. Edoff. 2013, Solar Energy Materials and Solar Cells, Vol. 117, p. 505-511.

27. Surface passivation of Cu(In,Ga)Se2 using atomic layer deposited Al2O3. W.W. Hsu, J.Y. Chen, T.H. Cheng, S.C. Lu, W.S. Ho, Y.Y. Chen, Y.J. Chien, C.W. Liu. 2012, Appl. Phys. Lett. , Vol. 100, p. 023508.

28. Reducing interface recombination for Cu(In,Ga)Se2 by atomic layer deposited buffer layers. A. Hultqvist, J.V. Li, D. Kuciauskas, P. Dippo, M.A. Contreras, D.H. Levi, S.F. Bent. 2015, Applied Physics Letters, Vol. 107(3), p. 33906.

29. Designing CIGS solar cells with front-side point contacts. G. Sozzi, D. Pignoloni, R. Menozzi, F. Pianezzi, P. Reinhard, B. Bissig, S. Buecheler, A.N. Tiwari. 2015, In Photovoltaic Specialist Conference (PVSC) 2015 IEEE 42nd, p. 1-5.

30. Role of incorporated sulfur into the surface of Cu(InGa)Se2 thin-film absorber. Y. Nagoya, K. Kushiya, M. Tachiyuki, O. Yamase. 2001, Solar Energy Materials and Solar Cells, Vol. 67, p. 247–253.

31. Compositional investigation of potassium doped Cu(In,Ga)Se2 solar cells with efficiencies up to 20.8%. P. Jackson, D. Hariskos, R. Wuerz, W. Wischmann, M. Powalla. 2014, Physica status solidi: rapid research letters, Vol. 8, p. 219–222.

32. The effect of Ga-grading in CIGS thin film solar cells. O. Lundberg, M. Edoff, L. Stolt. 2005, Thin Solid Films, Vol. 480-481, p. 520–525.

33. Development of thin-film Cu(In,Ga)Se2 and CdTe solar cells. A. Romeo, M. Terheggen, D. Abou-Ras, D.L. Bätzner, F.-J. Haug, M. Kälin, D. Rudmann, A.N. Tiwari. 2004, Prog. Photovolt: Res. Appl., Vol. 12, p. 93–111.

34. Graded band-gap Cu(In,Ga)Se2 thin-film solar cell absorber with enhanced open-circuit voltage. M. Contreras, J. Tuttle, D. Du, Y. Qi, A. Swartzlander, A. Tennant, R. Noufi. 1993, Applied Physics Letters, Vol. 63(13), p. 1824-1826.

35. High-efficiency CuInxGa1-xSe2 solar cells made from (Inx,Ga1-x)2Se3 precursor films. A.M. Gabor, J.R. Tuttle, D.S. Albin, M.A. Contreras, R. Noufi, A.M. Hermann. 1994, Applied Physics Letters, Vol. 65(2), p. 198-200.

36. Phases, morphology, and diffusion in CuInxGa1-xSe2 thin. M. Marudachalam, R.W. Birkmire, H. Hichri, J.M. Schultz, A. Swartzlander, M.M. Al-Jassim. 1997, Journal of Applied Physics, Vol. 82(6), p. 2896-2905.

37. Dynamics of a pulsed-electron beam induced plasma: application to the growth of zinc oxide thin films. S. Tricot, C. Boulmer-Leborgne, M. Nistor, E. Millon and J. Perrière. 2008, J. Phys. D: Appl. Phys., Vol. 41, p. 175205.

38. Magnetic anisotropy in composite CoFe2O4-BiFeO3 ultrathin films grown by pulsed-electron deposition. R. Comes, M. Khokhlov, H. Liu, J. Lu, S.A. Wolf. 2012 : s.n., J. Appl. Phys., Vol. 111, p. 07D914.

39. Time resolved spectroscopic study of a pulsed electron beam ablation plasma. M. Nistor, F. Gherendi, M. Magureanu, N. B. Mandache. 2005, Journal of optoelectronics and Advanced Materials, Vol. 7 (2), p. 979-984.

40. Pulsed electron beam deposition of oxide thin film. M. Nistor, N.B. Mandache, J. Perrière. 2008, J. Phys. D: Appl. Phys., Vol. 41, p. 165205.

41. Deposition of iron pyrite via pulsed electron ablation. R. Henda, O. Al-Shareeda, A. McDonald, A. Pratt. Appl. Phys. A, Vol. 108 (4), p. 967-974.

42. Deposition of YBa2Cu3O7−x thin films by channel-spark pulsed electron beam ablation. Q.D. Jiang, F.C. Matacotta, M.C. Konijnenberg, G. Müller, C. Schultheiss. 1994, Thin Solid Films, Vol. 241, p. 100-102.

43. Parameters that control pulsed electron beam ablation of materials and film deposition processes. Strikovski, K. S. Harshavardhan and M. 2003, Applied Physics Letters, Vol. 82 (6), p. 853-855.

44. Deposition by means of pulsed electron beam ablation. G. Muller, M. Konijnenberg, G. Krafft, C. Schultheiss. s.l. : World Scientific, 1995, Science and Technology of Thin Films, p. 89-119.

45. Growth of Cu(In,Ga)Se2 thin films by a novel single-stage route based on pulsed electron deposition. S. Rampino, F. Bissoli, E. Gilioli, F. Pattini. 2013, Prog. Photovolt: Res. Appl., Vol. 21, p. 588–594.

46. M. D. Strikovski, J. Kim, S. H. Kolagani. Plasma Energetics in Pulsed Laser and Pulsed Electron Deposition. [a cura di] K. Byrappa, V. Prasad, M. Dudley G. Dhanaraj. Handbook of Crystal Growth - Part E Epitaxial Growth. s.l. : Springer, 2010, p. 1193-1211.

47. ZnO sublimation using a polyenergetic pulsed electron beam source: numerical simulation and validation. S. Tricot, N. Semmar, L. Lebbah and C. Boulmer-Leborgne. 2010, J. Phys. D: Appl. Phys., Vol. 43, p. 065301.

48. Simple model for the desorption of hydrogen from Ni surfaces. David, G. Comsa and R. 1977, Chem. Phys. Lett, Vol. 49, p. 512-515.

49. Observation of two distinct components during pulsed laser deposition of high T c superconducting films. T. Venkatesan, X.D. Wu, A. Inam, J.B. Wachtman. 14, 1988, Appl. Phys. Lett., Vol. 52, p. 1193.

50. Catalytic oxidation of CO on Pt(111): The influence of surface defects and composition on the reaction dynamics. J. Segner, C.T. Campbell, G. Doyen, G. Ertl. 2-3, 1984, Surface Science, Vol. 138, p. 505-523.

51. Angular distribution of laser-ablated species from a Pr0.67Sr0.33MnO3 target. Quin, H.dang and Q. 1999, Phys. Rev. B, Vol. 60, p. 11187.

52. Dynamics of evaporation from CuGaSe2 targets in pulsed electron deposition technique. F. Pattini, M. Bronzoni, F. Mezzadri, F. Bissoli, E. Gilioli, S. Rampino. 2013, J. Phys. D: Appl. Phys., Vol. 46, p. 245101 (7pp).

53. Role of substrate temperature on the structural, morphological and optical properties of CuGaSe2 thin films grown by Pulsed Electron Deposition technique. M. Bronzoni, M. Stefancich, S. Rampino. 2012, Thin Solid Film, Vol. 520, p. 7054-7061.

54. Na-induced efficiency boost for Se-deficient Cu(In,Ga)Se2 solar cells. C.H Hsu, Y.S. Su, S.Y. Wei, C.H. Chen, W.H. Ho, C. Chang, Y.H. Wu, C.J. Lin, C.H. Lai. 2015, Prog. Photovolt. Res. Appl., Vol. 23, p. 1621–1629.

55. Progress on Low-Temperature Pulsed Electron Deposition of CuInGaSe2 Solar Cells. M. Mazzer, S Rampino, E. Gombia, M. Bronzoni, F. Bissoli, F. Pattini, M. Calicchio, A. Kingma, F. Annoni, D. Calestani, N. Cavallari, V.T. Vijayan, M. Lomascolo, A. Cretì, E. Gilioli. 2016, Energies, Vol. 9(3) 207.

56. W.N. Shafarman, S. Siebentritt, L. Stolt. Cu(InGa)Se2 Solar Cells. [aut. libro] S. Hegedus A. Luque. Handbook of Photovoltaic Science and Engineering, 2nd ed. New York, NY, USA : Wiley, 2011, p. 547.

57. Fabrication of high-efficiency Cu(In,Ga)Se2 solar cells by Pulsed Electron Deposition technique. Bronzoni, M. 2014, PhD Thesis in Science and Technology of Innovative Materials - University of Parma.

58. Atom probe study of sodium distribution in polycrystalline Cu (In, Ga) Se 2 thin film. E. Cadel, N. Barreau, J. Kessler, P. Pareige. 2010, Acta Materialia, Vol. 58, p. 2634-2637.

59. Solar cell efficiency tables (Version 45). M.A. Green, K. Emery, Y. Hishikawa, W. Warta, E.D. Dunlop. 2015, Prog. Photovolt. Res. Appl., Vol. 23, p. 1-9.

60. Charge and doping distributions by capacitance profiling in Cu(In,Ga)Se2 solar cells. M. Cwil, M. Igalson, P. Zabierowski, S. Siebentritt. 103, J. Appl. Phy. : s.n., 2008.

61. Thin-film solar cells: device measurements and analysis. Shafarman, S.S. Hegedus and W.N. 12, Prog. Photovolt. Res. Appl. : s.n., 2004, p. 155-176.

62. Characterization of the Cu(In,Ga)Se2/Mo interface in CIGS solar cells. T. Wada, N. Kohara, S. Nishiwaki, T. Negami. 1-2, 2001, Thin Solid Films, Vol. 387, p. 118–122.

63. Formation and characterisation of MoSe2 for Cu(In,Ga)Se2 based solar cells. D. Abou-Ras, G. Kostorz, D. Bremaud, M. Kälin, F.V. Kurdesau, A.N. Tiwari, M. Döbeli. 2005, Thin Solid Film, Vol. 480-481, p. 433–438.

64. Electrical impact of MoSe2 on CIGS thin-film solar cells. K.J. Hsiao, J.D. Liu, H.H. Hsieha, T.S. Jianga. 2013, Phys. Chem. Chem. Phys., Vol. 15, p. 18174-18178 .

65. Metal contacts to CuInSe2. R.J Matson, O. Jamjoum, A.D. Buonaquisti, P.E. Russell, L.L. Kazmerski, P. Sheldon, R.K. Ahrenkiel. 1984, Sol. Cells, Vol. 11, p. 301-305.

66. Studio degli effetti del Na nelle celle a film sottile di Cu(In,Ga)Se2 realizzate mediante Pulsed Electron Deposition (PED). Annoni, F. 2013, Master Thesis in Material Science - University of Parma.

67. 15% efficient Cu(In,Ga)Se2 solar cells obtained by low-temperature pulsed electron deposition. S. Rampino, N. Armani, F. Bissoli, M. Bronzoni, D. Calestani, M. Calicchio, N. Delmonte, E. Gilioli, E. Gombia, R. Mosca, L. Nasi, F. Pattini, A. Zappettini, M. Mazzer. 2012, Appl. Phys. Lett., Vol. 101, p. 245101.

68. Comparative study about Al-doped Zinc Oxide thin films deposited by Pulsed Electron Deposition and Radio Frequency Magnetron Sputtering as Transparent Conductive Oxide for Cu(In,Ga)Se2-based solar cells. F. Pattini, F. Annoni, F. Bissoli, M. Bronzoni, J.P. Garcia, E. Gilioli, S. Rampino. 2015, Thin Solid Film, Vol. 582, p. 317–322.

69. Combinatorial Pulsed Laser Deposition of Fe, Cr, Mn, and Ni-substituted SrTiO3 films on Si substrates. D.H. Kim, N.M. Aimon, P. Jiang, G.F. Dionne, C.A. Ross. 14 (3), 2012, Comb. Sci., p. 179-190.

70. Combinatorial atmospheric pressure Chemical Vapor Deposition of graded TiO2–VO2 mixed-phase composites and their dual functional property as self-cleaning and photochromic window coatings. M. Wilkinson, A. Kafizas, S.M. Bawaked, A.Y. Obaid, S.A. Al-Thabaiti, S.N. Basahel, C.J. Carmalt, I.P. Parkin. 2013, Comb. Sci., Vol. 15 (6), p. 309-319.

71. Transparent and conducting Zn-Sn-O thin films prepared by combinatorial approach. J.H. Ko, I.H. Kim, D. Kim, K.S. Lee, T.S. Lee, B. Cheong, W.M. Kim. 2007, Applied Surface Science, Vol. 253 (18), p. 7398-7403.

72. Deposition and Testing of Combinatorial Libraries of Photovoltaic Devices. T.D. Hatchard, N.J. Gerein, M.Y. Versavel, G.A. Gelves, J.A. Haber. 2005, 208th ECS Meeting, Abstract #881.

73. U. Avachat, T. Chiang, C. Hunter, J. Li, G. Zhang. Combinatorial methods for making CIGS solar cells. US8927322 B2 6 1 2015.

74. The role of the CdS buffer layer in CuGaSe2-based solar cells. R. Caballero, C.A. Kaufmann, M. Cwil, C. Kelch, D. Schweigert, T. Unold, M. Rusu, H.W. Schock, S. Siebentritt. 2007, Journal of Physics: Condensed Matter, Vol. 19, p. 356222.

75. Bifacial CIGS solar cells grown by Low Temperature Pulsed Electron Deposition. M. Mazzer, S. Rampino, G. Spaggiari, F. Annoni, D. Bersani, F. Bissoli, M. Bronzoni, M. Calicchio, E. Gombia, A. Kingma, F. Pattini, E. Gilioli. 2016, Solar Energy Materials & Solar Cells, p. http://dx.doi.org/10.1016/j.solmat.2016.10.048.

76. Building-integrated PV modules. J. Benemann, O. Chehab, E. Schaar-Gabriel. 2001, Sol. Energy Mater. Sol. Cells, Vol. 67, p. 345-354.

77. 50% more output power from an albedo-collecting flat panel using bifacial solar cells. A. Cuevas, A. Luque, J. Eguren, J. Del Alamo. 1982, Sol. Energy, Vol. 29, p. 419-420.

78. Mori, H. U.S. patent No. 3,278,811 October 1966.

79. Bifacial silicon solar cells with 21.3% front efficiency and 19.8% rear efficiency. H. Ohtsuka, M. Sakamoto, K. Tsutsui, Y. Yazawa. 2000, Prog. Photovolt. Res. Appl., Vol. 8, p. 385–390.

80. A novel low-cost method for fabricating bifacial solar cells. S. Saha, R.A. Rao, L. Mathew, M. Ainom, S.K. Banerjee. 2013, http://dx.doi.org/10.1109/PVSC.2013.6744929.

81. Bifacial dye-sensitized solar cells: a strategy to enhance overall efficiency based on transparent polyaniline electrode. J. Wu, Y. Li, Q. Tang, G. Yue, J. Lin, M. Huang, L. Meng. 2014, Sci. Rep., Vol. 4, p. 4028.

82. Low-temperature-processed efficient semi-transparent planar perovskite solar cells for bifacial and tandem applications. F. Fu, T. Feurer, T. Jäger, E. Avancini, B. Bissig, S. Yoon, S. Buecheler, A.N. Tiwari. 2015, Nat. Commun., Vol. 6, p. 8932.

83. Efficient bifacial Cu2ZnSnSe4 solar cells. M. Espindola-Rodriguez, Y. Sanchez, S. Lopez-Marino, H. Xie, V. Izquierdo-Roca, D. Sylla, M. Neuschitzer, O. Vigil-Galan, E. Saucedo, M. Placidi. 2015, Proceedings of IEEE, p. 1-3.

84. Bifacial solar cell with SnS absorber by vapor transport deposition. A. Wangperawong, P.-C. Hsu, Y. Yee, S.M. Herron, B.M. Clemens, Y. Cui, S.F. Bent. 2014, Appl. Phys. Lett., Vol. 105, p. 173904.

85. Bifacial solar photovoltaics – A technology review. R. Guerrero-Lemus, R. Vega, T. Kim, A. Kimm, L.E. Shephard. 2016, Renewable and Sustainable Energy Reviews, Vol. 60, p. 1533-1549.

86. ITRPV - International Technology Roadmap for Photovoltaic: 2013 Results. 24th March 2014.

87. A new method to characterize bifacial solar cells. J.P. Singh, T.M. Walsh, A.G. Aberle. 2014, Prog. Photovolt.: Res. Appl., Vol. 22, p. 903–909.

88. Future of bifacial Si solar cells for space applications. G.M. Grigorieva, M.B. Kagan,K.N. Zviagina,V. Kulicauscas, L. Kreinin,N. Bordin, et al. Valencia, Spain : s.n., 2008, Proc. of the 23rd European photovoltaic solar energy conference, p. 756-761.

89. Industrial production of bifacial solar cells: design principles and latest achievements. L. Kreinin, N. Bordin, N. Eisenberg, P. Grabitz, S. Hasenauer, D. Obhof, et al. Konstanz : s.n., 2012, Bifi Workshop.

90. Characteristics of bifacial solar cells under bifacial illumination with various intensity levels. H. Ohtsuka, M. Sakamoto, M. Koyama, K. Tsutsui, T. Uematsu, Y. Yazawa. 2001, Prog. Photovolt.: Res. Appl., Vol. 9, p. 1-13.

91. Novel device structure for Cu(In,Ga)Se2 thin film solar cells using transparent conducting oxide back and front contacts. T. Nakada, Y. Hirabayashi, T. Tokado, D. Ohmori, T. Mise. 2004, Sol. Energy, Vol. 77, p. 739-747.

92. Effect of the ITO substrate on the growth of Cu(In,Ga)Se2, CuGa3Se5, CuGa5Se8 and CuIn3Se5 thin films by flash evaporation. E.J. Friedrich, J.F. Trigo, J. Ramiro, C. Guillén, J.M. Merino, M. León. 2009, J. Phys.: Appl. Phys., Vol. 42, p. 085401.

93. Microstructural and diffusion properties of CIGS thin film solar cells fabricated using transparent conducting oxide back contacts. Nakada, T. 2005, Thin Solid Films, Vol. 480-481, p. 419-425.

94. Printable, wide band-gap chalcopyrite thin films for power generating window applications. S.H. Moon, S.J. Park, Y.J. Hwang, D.-K. Lee, Y. Cho, D.-W. Kim, B.K. Min. 2014, Sci. Rep., Vol. 4, p. 4408.

95. Fabrication of optimized aluminum-doped zinc oxide films as front contacts for Cu(In,Ga)Se2-based solar cells via RF magnetron sputtering. J.P.B. Garcia. 2013, SERP-Chemistry Master Thesis.

96. 21.9% efficient silicon bifacial solar cells. C.Z. Zhou, P.J. Verlinden, R.A. Crane, R.M. Swanson, R.A. Sinton. 1997, Proceedings of IEEE, p. 287–290.

97. Cu(In1−xGax)Se2 thin film solar cells using transparent conducting oxide back contacts for bifacial and tandem solar cells. T. Nakada, Y. Hirabayashi, T. Tokado, D. Ohmori. 2003, Proceedings of 3rd World Conference on Photovoltaic Energy Conversion, Vol. 3, p. 2880-2884.

98. Kodigala, S.R. Cu(InGa)Se2 Based Thin Film Solar Cells. London : Academic Press, 2009. p. 276-294.

99. Influence of the Ga content on the Mo/Cu(In,Ga)Se2 interface formation. W. Witte, R. Kniese, A. Eicke, M. Powalla. 2006, Proceeding of the 2006 IEEE 4th World Conference on Photovoltaic Energy Conversion, Vol. 1.

100. Characterization of CuGaxSey/ZnO for superstrate solar cells. F.J. Haug, M. Krejci, H. Zogg, A.N. Tiwari, M. Kirsch, S. Siebentritt. 2000, Thin Solid Films, Vol. 361-362, p. 239-242.

101. Cu(In,Ga)Se2 superstrate solar cells: prospects and limitations. M.D. Heinemann, V. Efimova, R. Klenk, B. Hoepfner, M. Wollgarten, T. Unold, H.W. Schock, C.A. Kaufmann. 2015, Prog. Photovolt. Res. Appl., Vol. 23, p. 1228-1237.

102. Low-temperature growth of single-crystal Cu(In,Ga)Se2 films by pulsed electron deposition technique. S. Rampino, M. Bronzoni, L. Colace, P. Frigeri, E. Gombia, C. Maragliano, F. Mezzadri, L. Nasi, L. Seravalli, F. Pattini, G. Trevisi, M. Motapothula, T. Venkatesan, E. Gilioli. 2015, Sol. Energy Mater. Sol. Cells, Vol. 133, p. 82-86.

103. Application of a substrate bias to control the droplet density on Cu(In,Ga)Se2 thin films grown by Pulsed Electron Deposition. S. Rampino, F. Pattini, C. Malagù, L. Pozzetti, M. Stefancich, M. Bronzoni. 2014, Thin Solid Film, Vol. 562, p. 307-313.

104. Solar Frontier. Solar Frontier achieves world record thin-film solar cells efficiency: 22.3%. Solar Frontier Company webpage. [Online] 8 12 2015. [Riportato: 16 10 2016.] http://www.solar-frontier.com/eng/news/2015/C051171.html.

105. Improved Photocurrent in Cu(In,Ga)Se2 Solar Cells: From 20.8% to 21.7% Efficiency with CdS Buffer and 21.0% Cd-Free. Friedlmeier TM, Jackson P, Bauer A, Hariskos D, Kiowski O, Wuerz R, Powalla M. s.l. : IEEE Journal of Photovoltaics, 2015, Vol. 5, pp. 1487–1491.

106. CIGS cells and modules with high efficiency on glass and flexible substrates. M. Powalla, W. Witte, P. Jackson, S. Paetel, E. Lotter, R. Wuerz, F. Kessler, C. Tschamber, W. Hempel, D. Hariskos, R. Menner, A. Bauer, S. Spiering, E. Ahlswede, T.M. Friedlmeier, D. Blázquez-Sánchez, I. Klugius, W. Wischmann. 2014, IEEE J. Photovolt., Vol. 4, p. 440-446.

107. Cadmium-free CIGS mini-modules with ALD-grown Zn(O, S)-based buffer layers. U. Zimmermann, M. Ruth, M. Edoff. Dresden : s.n., 2006, Proceeeding of 21st European Photovoltaic Solar Energy Conference, p. 1831-1834.

108. Growth and characterization of ZnO-based buffer layers for CIGS solar cells. Törndahl T., Hultqvist A., Platzer-Björkman C., Edoff M. 2010, SPIE Proceedings, Vol. 7603, p. 76030D–76030D–9.

109. Inline Cu(In,Ga)Se co-evaporation for high-efficiency solar cells and modules. Lindahl J., Zimmermann U., Szaniawski P., Törndahl T., Hultqvist A., Salomé P., Platzer-Björkman C., Edoff M. 2013, IEEE Journal of Photovoltaics, Vol. 5(5), p. 1100-1105.

110. Junction formation by Zn(O,S) sputtering yields CIGSe-based cells with efficiencies exceeding 18%. Klenk R., Steigert A., Rissom T., Greiner D., Kaufmann C.A., Unold T., Lux-Steiner M.C. 2014, Progress in Photovoltaics: Research and Applications, Vol. 22(2), p. 161-165.

111. Buffer layers and transparent conducting oxides for chalcopyrite Cu(In, Ga)(S, Se)2 based thin film photovoltaics: present status and current developments. N. Naghavi, D. Abou-Ras, N. Allsop, N. Barreau, S. Bücheler, A. Ennaoui, C.-H. Fischer, C. Guillen, D. Hariskos, J. Herrero, R. Klenk, K. Kushiya, D. Lincot, R. Menner, T. Nakada, C. Platzer-Björkman, S. Spiering, A.N. Tiwari, T. Törndahl. 2010, Prog. Photovolt. Res. Appl., Vol. 18, p. 411.

112. Theoretical analysis of the effect of conduction band offset of window/CIS layers on performance of CIS solar cells using device simulation. T. Minemoto, T. Matsui, H. Takakura, Y. Hamakawa, T. Negami, Y. Hashimoto, T. Uenoyama, M. Kitagawa. 1-4, 2001, Solar Energy Materials and Solar cells, Vol. 67, p. 83–88.

113. Oxygenation and air-annealing effects on the electronic properties of Cu(In,Ga)Se2 films and devices. Rau U., Braunger D., Herberholz R., Schock H., Guillemoles J., Konik L., Cahen D. 1999, J Appl Phys, Vol. 86(1), p. 497-505.

114. Defect chalcopyrite Cu(In1-xGax)3Se5 materials and high-Ga-content Cu(In,Ga)Se2 based solar cells. Contreras M., Wiesner H., Niles D., Ramanathan K., Matson R., Tuttle J., Keane J., Noufi R. Washington D.C. : s.n., Proc. of the 25th IEEE Photovoltaic Specialists Conference, Vol. 1996, p. 809-812.

115. Defect chemical explanation for the effect of air anneal on CdS/CuInSe2 solar cell performance. R., Cahen D. and Noufi. 1989, Appl. Phys. Lett., Vol. 54, p. 558-560.

116. Direct evidence of a buried homojunction in Cu(In,Ga)Se2 solar cells . C.S. Jiang, F.S. Hasoon, H.R. Moutinho, H. A. Al-Thani, M.J. Romero and M.M. Al-Jassim. 127, 2003, Appl. Phys. Lett., Vol. 82.

117. Direct evidence of Cd diffusion into Cu(In, Ga)Se2 thin films during chemical-bath deposition process of CdS films. T. Nakada and A. Kunioka. 1999, Appl. Phys. Lett., Vol. 74, p. 2444.

118. Nano-structural investigations on Cd-doping into Cu(In, Ga)Se2 thin films by chemical bath deposition process. T. Nakada. 2000, Thin Solid Films, Vol. 361-362, p. 346.

119. Chalcopyrite/defect chalcopyrite heterojunctions on the basis of CuInSe2. D. Schmid, M. Ruckh, F. Grunwald, H.W. Schock. 73, 1993, J. Appl. Phys., p. 2902.

120. Control of conduction band offset in wide-gap Cu(In,Ga)Se2 solar cells. T. Minemoto, Y. Hashimoto, W. Shams-Kolahi, T. Satoh, T. Negami, H. Takakura, Y. Hamakawa. 1-2, 2003, Solar Energy Materials and Solar Cells, Vol. 75, p. 121–126.

121. Strong Valence-Band Offset Bowing of ZnO1−xSx Enhances p-Type Nitrogen Doping of ZnO-like Alloys. Persson C., Platzer-Björkman C., Malmström J., Törndahl T., Edoff M. 2005, Phys. Rev. Lett., Vol. 97, p. 146403.

122. Zn(O,S) buffer layers by atomic layer deposition in Cu(In,Ga)Se2 based thin film solar cells: Band alignment and sulfur gradient. Platzer-Björkman C., Törndahl T., Abou-Ras D., Malmström J., Kessler J., Stolt L. 2006, J. Appl. Phys., Vol. 100, p. 044506.

123. Energy band alignment in chalcogenide thin film solar cells from photoelectron spectroscopy. A. Klein. 13, 2015, Journal of Physics: Condensed Matter, Vol. 27, p. 134201.

124. A. Hultqvist. Cadmium Free Buffer Layers and the Influence of their Material Properties on the Performance of Cu(In,Ga)Se2 Solar Cells. PhD thesis, Uppsala University, Uppsala (Sweden) : Acta Universitatis Upsaliensis, 2010.

125. High-efficiency Cu(In,Ga)Se2 thin-film solar cells with a CBD-ZnS buffer layer. T. Nakada, M. Mizutani, Y. Hagiwara, A. Kunioka. 2001, Solar Energy Materials and Solar Cells, Vol. 67 (1-4), p. 255-260.

126. Improved CIGS thin-film solar cells by surface sulfurization using In2S3 and sulfur vapor. D. Ohashi, T. Nakada, A. Kunioka. 2001, Solar Energy Materials and Solar Cells, Vol. 67 (1-4), p. 261-265.

127. Improved efficiency of Cu(In,Ga)Se2 thin film solar cells by surface sulfurization using wet process. T. Nakada, K Matsumoto, M. Okumura. 2003, Conference Record of the Twenty-Ninth IEEE Photovoltaic Specialists Conference, 2002.

128. Zinc oxysulfide thin films grown by atomic layer deposition. B.W. Sanders and A. Kitai. 1992, Chem. Mat., Vol. 4, p. 1005.

129. Atomic layer deposition of Zn(O,S) buffer layers for high efficiency Cu(In,Ga)Se2 solar cells. Platzer-Bjorkman C., Kessler J., Stolt L. 2003, Proceedings of 3rd World Conference on Photovoltaic Energy Conversion, Vol. 1, p. 461-464.

130. CuGaSe2 Solar Cells Using Atomic Layer Deposited Zn(O,S) and (Zn,Mg)O buffer layers. A. Hultqvist, C. Platzer-Björkman, J. Pettersson, T. Törndahl, M. Edoff. 2009, Thin Solid Film, Vol. 517, p. 2305-2308.

131. The effect of Zn1-xMgxO buffer layer deposition temperature on Cu(In,Ga)Se2 solar cells: A study of the buffer/absorber interface. T. Törndahl, E. Coronel, A. Hultqvist, C. Platzer-Björkman, K. Leifer, M. Edoff. 2009, Progress in Photovoltaics: Reasearch and Applications, Vol. 17, p. 115-125.

132. Growth and characterization of ZnO-based buffer layers for CIGS solar cells. T. Törndahl, A. Hultqvist, C. Platzer-Björkman, M. Edoff. San Francisco : s.n., 2010, Proceedings of the SPIE - The International Society for Optical Engineering, Vol. 7603, p. 7603D-1-9.

133. Band gap engineering of ZnO for high efficiency CIGS based solar cells. C. Platzer-Björkman, A. Hultqvist, J. Pettersson, T. Törndahl. 2010, Proceedings of the SPIE - The International Society for Optical Engineering, San Francisco, Vol. 7603, p. 76030F-1-9.

134. Impact of the Band Offset for n-Zn(O,S)/p-Cu(In,Ga)Se2 Solar Cells. Sites, S. Sharbati and J.R. 2, 2014, IEEE Journal of Photovoltaics, Vol. 4, p. 697-702.

135. Experimental investigation of Cu(In1−x,Gax)Se2/Zn(O1−z,Sz) solar cell performance. A. Hultqvist, C. Platzer-Björkman, E. Coronel, M. Edoff. 2, 2011, Solar Energy Materials and Solar Cells, Vol. 95, p. 497-503.

136. Joule heating-assisted growth of Cu(In,Ga)Se2 solar cells. S. Rampino, F. Annoni, M. Bronzoni, M. Calicchio, E. Gombia, M. Mazzer, F. Pattini, and E. Gilioli. 2015, Journal of Renewable and Sustainable Energy, Vol. 7, p. 013112.

# Abbreviations

| | |
|---|---|
| a | Incongruent-evaporation coefficient in PED |
| AC | Alternated current |
| ALD | Atomic layer deposition |
| AM | Air mass |
| AR | Antireflective |
| AZO | Aluminium-doped zinc oxide |
| BFSC | Bifacial solar cell |
| BIPV | Building-integrated photovoltaic |
| CBD | Chemical bath deposition |
| CBO | Conduction band offset |
| CGI | [Cu]/[Ga+In] |
| CGS | $CuGaSe_2$ |
| CIGS | $Cu(In_{1-x},Ga_x)Se_2$ |
| CIS | $CuInSe_2$ |
| CV | Current vs Voltage |
| CVD | Chemical vapour deposition |
| CZTS | $Cu_2ZnSnSe_4$ |
| D | Adatom diffusion length |
| D(θ) | Film-thickness distribution for PED |
| DC | Direct current |
| DEZ | Di-ethyl zinc: $Zn(C_2H_5)_2$ |
| $E_A$ | Activation energy |
| $E_B$ | Energy of CB minimum |
| EBIC | Electron-beam induced current |
| EDX | Energy dispersive X-ray spectroscopy |
| $E_F$ | Fermi level energy |
| $E_G$ | Energy gap |
| EQE | External quantum efficiency |
| $E_V$ | Energy of VB maximum |
| f | Incongruent-evaporated mass during PED |
| F(θ) | Angular distribution of evaporation in PED |
| FF | Fill factor |
| FTO | Fluorine-doped tin oxide |
| GB | Grain boundaries |
| GGI | [Ga]/[Ga+In] |
| GPC | Growth per cycle in ALD process |
| $I_m$ | Current corresponding to $P_M$ |
| IQE | Internal quantum efficiency |
| IR | Infra-red |
| $I_{sc}$ | Short-circuit current |
| ITO | Indium-tin oxide |
| IV | Current vs Voltage |
| i-ZnO | Intrinsic zinc oxide |
| J | Current density |
| $J_{sc}$ | Short-circuit current density |
| JV | Current density vs Voltage |
| $k_B$ | Boltzmann's constant |
| LEC | Liquid encapsulated Czochralski |
| LTPED | Low-temperature pulsed electron deposition |
| M | Plasma velocity in Mach number |
| $N_A$ | Density of acceptor |
| $N_{CB}$ | Effective density of states in CB |
| $N_D$ | Density of donor |
| $N_{VB}$ | Effective density of states in VB |
| ODC | Ordered defect compound |
| p | Exponent of cosine for PED ablation contribute |
| PED | Pulsed electron deposition |
| PL | Photoluminescence |
| PLD | Pulsed laser deposition |
| $P_M$ | Maximum output power of solar cell |
| PV | Photovoltaic |
| P(z) | Power density along the electron range |
| q | Electron energy |
| QE | Quantum efficiency |
| QNR | Quasi neutral region |
| RF | Radio frequency |
| $R_s$ | Series resistance |
| $R_{sh}$ | Shunt resistance |
| $R_{sheet}$ | Sheet resistance |
| RT | Room temperature |
| SCR | Space charge region |
| SEM | Scanning electron microscope |
| SHR | Shockley-Read-Hall recombination |
| SIMS | Secondary ions mass spectrometry |
| SLG | Soda lime glass |
| T | Temperature |
| TCO | Transparent conductive oxide |
| TFSC | Thin-film solar cell |
| u | Plasma expansion velocity |
| UV | Ultraviolet |
| v | Velocity of plasma particles |
| $V_B$ | Breakdown voltage for PED pulse |
| VB | Valence band |
| $V_{bi}$ | Built-in potential |
| $V_m$ | Voltage corresponding to $P_M$ |
| $V_{oc}$ | Open-circuit voltage |
| W | Work function |
| XRD | X-ray diffraction |
| XRF | X-ray fluorescence |
| YBCO | $YBa_2Cu_3O_7$ |
| α | Absorption coefficient |
| γ | Ratio between $C_P$ and $C_V$ |
| δ | Penetration range of electron beam |
| $\delta_T$ | Thermal diffusion length |
| $\varepsilon_D$ | Activation energy for adatom diffusion |
| η | Conversion efficiency |
| θ | Deposition angle |
| λ | Photon wavelength |
| ρ | Density |
| τ | PED pulse duration |